Chapter 4: Future global climate: scenario-based projections and near-term information

Coordinating Lead Authors:
June-Yi Lee (Republic of Korea), Jochem Marotzke (Germany)

Lead Authors:
Govindasamy Bala (India/USA), Long Cao (China), Susanna Corti (Italy), John Dunne (USA), Francois Engelbrecht (South Africa), Erich Fischer (Switzerland), John Fyfe (Canada), Christopher Jones (UK), Amanda Maycock (UK), Joseph Mutemi (Kenya), Ousmane Ndiaye (Senegal), Swapna Panickal (India), Tianjun Zhou (China)

Contributing Authors:
Kyle Armour (USA), Michael Byrne (UK/Ireland), Christophe Cassou (France), Hannah Christensen (UK), Sybren Drijfhout (Netherlands), Christopher Fletcher (Canada/UK), David Keller (Germany), Ben Kravitz (USA), Matthew Menary (France/UK), William Merryfield (Canada/USA), Dirk Notz (Germany), Emilia Sanchez-Gomez (France/Spain), Javier García-Serrano (Spain), Aimée Slangen (Netherlands), Malte F. Stuecker (Republic of Korea/Germany), Danila Volpi (Italy), Giuseppe Zappa (UK/Italy)

Review Editors:
Krishna Kumar Kanikicharla (Qatar/India), Vladimir Kattsov (Russia), Masahide Kimoto (Japan)

Chapter Scientists:
Sebastian Milinski (Germany), Kyung-Sook Yun (Republic of Korea)

Date of Draft: 29 April 2019

Note: TSU compiled version

Table of Contents

Executive Summary

This chapter assesses simulations of indicators of future global climate change, spanning time horizons from the near-term (2021–2040) out to year 2300. Change is assessed relative to both the recent past (1995–2014) and the approximation to the pre-industrial period (1850–1900). The chapter provides the global reference for the later chapters covering processes and regional change.

[Note: Major quantitative results in this chapter are preliminary, because they are based on the subset of five CMIP6 models (BCC-CSM2-MR, CanESM5, CNRM-CM6-1, IPSL-CM6A-LR, and MRI-ESM2-0) that are available for this first order draft (FOD).]

The projections results assessed here are mainly based on a new range of scenarios, Shared Socio-economic Pathways (SSPs), as used in the Coupled Model Intercomparison Project Phase 6 (CMIP6). Among the SSPs, we focus on the four priority scenarios SSP1-2.6, SSP2-4.5, SSP3-7.0, and SSP5-8.5. Where appropriate, this chapter will also assess results from CMIP5, which used scenarios based on Representative Concentration Pathways (RCPs). {4.2.2}

Globally averaged surface air temperature

Based on results from the five models that have thus far contributed to the CMIP6 exercise, we conclude that global surface air temperature (GSAT) for 2081–2100, relative to 1995–2014, shows a 5–95% range of 0.7°C–1.7°C under SSP1-2.6 where CO_2 concentrations peak between 2040–2060 (*medium confidence* because of the limited number of models available). The corresponding range under the highest overall emissions scenario (SSP5-8.5) is 2.9°C–6.1°C (*medium confidence*). The ranges for the intermediate emissions scenarios (SSP2-4.5 and SSP3-7.0), where CO_2 concentrations increase to 2100 but less rapidly than SSP5-8.5, are 1.6°C–3.1°C and 2.4°C–4.8°C, respectively (*medium confidence*). {4.3.1}

Based on results from the five CMIP6 models, we note that there is unanimity across all of the available model simulations that GSAT change relative to pre-industrial (1850–1900) will rise above: 1) 1.5°C following any of the priority SSPs (on average around 2025); 2) 2.0°C following either SSP2-4.5, SSP3-7.0, or SSP5-8.5 (on average around 2040), and 3) 3.0°C following either SSP3-7.0 or SSP5-8.5 (on average around 2061). In summary, it is *very likely* that within the near-term (2021–2040) or mid-term (2041–2060), GSAT rise will exceed 1.5°C relative to pre-industrial under all of the priority SSPs, above 2.0°C under most of the priority SSPs, and above 3.0°C under the highest forcing scenarios (*medium confidence* because of the limited number of models available). {4.3.1}

Referenced against 1850–1900, the available CMIP6 simulations project future globally averaged warming that until around 2060 largely falls within the warming range inferred from the *very likely* range in equilibrium climate sensitivity (ECS, 2°C–5°C) that is assessed in Chapter 7. After 2060, some models stay within this range and some other models lie above. The stronger-warming models are expected to have an ECS above the Chapter 7-assessed *very likely* range (expert judgement, *medium confidence*). {Box 4.1, Chapter7}

The uncertainty in projecting GSAT that arises from the ECS *very likely* range is substantially larger than the irreducible uncertainty arising from internal variability, from the mid-term period (2041–2060) onward (*high confidence*). By contrast, the GSAT uncertainty arising from the ECS *likely* range is similar to the irreducible uncertainty arising from internal variability (*medium confidence*). Predictions initialized from recent observations simulate GSAT for the period 2019–2028 that lie toward the lower end of both the CMIP6 range and the warming range inferred from the ECS *very likely* range (expert judgement, *low confidence* owing to limited data availability). {Box 4.1, Chapter7}

For the latter portion of the 21st century, the range of regional climatic states that might be expected in the RCP8.5 scenario is significantly and detectably further removed from today's climate state than the RCP4.5 scenario even in the presence of internal variability (*high confidence*). {4.6.3}

Initial results from targeted numerical experiments are inconclusive whether the Zero Emissions Commitment (ZEC, the GSAT rise after all emissions cease) on decadal timescales is either positive or negative, with values spanning from approximately -0.4°C to 0.2°C. There is therefore *low confidence* in the sign and magnitude of ZEC and its potential impact on the assessed remaining carbon budgets for 1.5°C or 2°C. {4.7.2}

Precipitation

Based on results from the five CMIP6 models available, it is *very likely* that global land precipitation will be higher during the period 2081–2100 than during the period 1995–2014, under all scenarios considered here (*medium confidence* due to limited data availability). {4.3.1}

Based on results from the five CMIP6 models available, it is *virtually certain* that, in the long term, global mean precipitation will increase with GSAT rise. It will *likely* increase by 1–3% $°C^{-1}$ for the SSP5-8.5 scenario. Precipitation will *likely* increase in monsoon regions and high latitudes (*medium confidence*). {4.5.1, Chapter 8}.

Based on the three CMIP6 models (BCC-CSM2-MR, IPSL-CM6A-LR, and MRI-ESM2-0), it is *very likely* that global precipitation will increase as the level of global warming increases. Precipitation increase on land will be higher at 3°C and 4°C warming level compared with 1.5°C warming level. It is *very likely* that extreme precipitation events will increase with GSAT rise (*medium confidence*). {4.6.1, Chapter 11}

Global monsoon precipitation and circulation

In the near-term period, the global monsoon precipitation tends to increase in all four SSP scenarios, based on the five models available in the CMIP6. However, there is no consensus on the near-term projected change of global monsoon circulation against multi-decadal natural variability (*medium confidence*). {4.4.1}

In the long-term period (2081–2100), the global monsoon precipitation index is projected to increase by 0.9–1.7% per 1°C GSAT rise (5–95% range of available projections), and the global monsoon circulation index is projected to decrease by 10.4–19.4% per 1°C GSAT rise based on all of the priority SSPs from five available CMIP6 simulation (*medium confidence*). {4.5.1}

Sea level pressure and large-scale atmospheric circulation

Mean sea level pressure is projected to decrease in high latitudes and increase in the mid-latitudes for SSP5-8.5, except over some land areas. On average, models project a poleward shift in the mid-latitude jets in both hemispheres by the end of the 21st century under SSP5-8.5 (*low confidence* owing to the current small number of CMIP6 models), but there is large spread amongst projections from individual models. In austral summer, it is *very likely* that the influence of stratospheric ozone recovery will oppose the poleward expansion of the mid-latitude circulation in the Southern Hemisphere (SH) due to GHGs, though internal variability could overwhelm forced trends in the Southern Annular Mode (SAM) on decadal timescales. It is *likely* that wind speeds associated with extratropical cyclones will intensify in the SH storm track for high emission scenarios (*high confidence*). Substantial uncertainty and thus *low confidence* remain in projecting changes in Northern Hemisphere (NH) storm tracks and blocking, especially for the North Atlantic basin in winter. {4.5.1}

Cryosphere, ocean, and biosphere

From the three available CMIP6 models, we conclude that it is *very likely* that following any one of the priority SSPs, the Arctic will become effectively permanently ice-free (coverage below 1 million km^2) in September by the end of the 21st century (*low confidence* because of the very limited number of models available). {4.3.2}

In the three available CMIP6 models, thermosteric global sea level rises from present to the end of the 21st century by about 0.15 m under SSP1-2.6 (taken as the minimum rise across the three models) to a maximum of about 0.45 m under SSP5-8.5 (taken as the maximum rise between the three models). We conclude that it is *very likely* that under any one of the priority SSPs, there will be monotonic rise in global sea level through the end of the 21st century (*low confidence* because of the very limited number of models available). {4.3.2}

In the two available CMIP6 models, cumulative ocean carbon uptake rises from 1850 to the end of the 21st century by about 250 PgC under SSP1-2.6 (taken as the minimum rise across the two models) to a maximum of about 600 PgC m under SSP5-8.5 (take as the maximum rise between the two models). In the one model that has so far contributed surface pH as part of the CMIP6 exercise, increasing in ocean carbon uptake translates into increasing surface acidity. We conclude that it is *very likely* that under any one of the priority SSPs, there will be a monotonic rise in ocean carbon uptake and ocean acidification through the end of the 21st century (*low confidence* because of the very limited number of models available). {4.3.2}

Modes of variability

Based on results from the five available CMIP6 models, we conclude that future boreal wintertime Northern Annular Mode (NAM) is *very likely* to become slightly more positive in the future under SSP5-8.5, and that the SAM is *likely* to weaken under all of the priority SSPs as stratospheric ozone recovers through the mid-21st century (*medium confidence* because of the limited number of models available). {4.3.3}

Results from the five available CMIP6 models suggest that El Niño-Southern Oscillation (ENSO) variability is *likely* to weaken under the SSP1-2.6 and SSP2-4.5 beginning in the near-term (2021–2040) while there is no consensus on the ENSO variability change in the SSP3-7.0 and SSP5-8.5 (*low confidence* because of the limited number of models available). {4.3.3}

It is *very likely* that ENSO-related rainfall variability over the Niño3.4 region will increase significantly regardless of ENSO amplitude changes by the latter half of the 21st century (*medium confidence*). {4.5.3}

Climate response to mitigation, carbon dioxide removal, and solar radiation modification

There is *high confidence* that mitigation through reduced greenhouse gas (GHG) emissions would slow and limit the degree of climate change relative to high emissions reference scenarios by the middle and late 21st century. There would be a lag between emission peak, CO_2 concentration peak, and peak in surface temperature. There is *medium confidence* that the delay in detectability of the climate benefits of mitigation is mainly due to the inertia and internal variability of the physical climate system rather than the global carbon cycle. Recent modelling results and our improved understanding suggest that over the near term, it is possible that global mean surface temperature (GSAT) might rise at a faster rate than during the most recent past despite emissions reductions (*medium confidence*). {4.6.3}

Even when applied continuously and at scales as large as currently represented in the RCP8.5 scenario as reference, all carbon dioxide removal (CDR) methods are individually either relatively ineffective with limited (8%) warming reductions, or they have potential severe side effects (*medium confidence*). Termination of CDR schemes is expected to cause increasing warming trends, associated with outgassing of CO_2 upon termination of CDR (*medium confidence*). {4.6.3}

Modelling studies have consistently suggested that Solar Radiation Modification (SRM) can markedly diminish global and regional climate change from increasing CO_2 concentrations. There is *high confidence* that all SRM schemes would reduce global precipitation if they were implemented to offset global mean temperature change. However, a combination of stratospheric aerosol injection and cirrus cloud thinning is expected to offset global temperature and precipitation changes simultaneously. Model simulations suggest that by injecting aerosols into the stratosphere at multiple latitudes and by adjusting the annual rate of injections, multiple temperature targets such as GSAT, equator-to-pole temperature gradient and inter-hemispheric temperature gradient can be met simultaneously (*low confidence* owing to the large uncertainty in simulating aerosol forcing). {4.6.3}

There is *high confidence* that sudden termination of SRM would cause a rapid increase in temperature, but a gradual phase-out of SRM combined with mitigation and CDR could avoid the risk from sudden SRM termination. {4.6.3}

4.1 Scope and Overview of this Chapter

This chapter is the first in the WGI contribution to the IPCC Sixth Assessment Report (AR6) to assess simulations of future climate change, covering both near-term and long-term global changes. The chapter will assess simulations of scientific indicators of global climate change, such as global surface air temperature (GSAT), global land precipitation, Arctic sea ice area (SIA), and global mean sea level (GMSL). Furthermore, the chapter will cover indices and patterns of properties and circulation that have global significance. The choice of quantities to be assessed is summarized in Box 2.1 and comprises a subset of the quantities covered in Chapters 2 and 3. This chapter provides consistent coverage from near-term to long-term global changes and provides the global reference for the later chapters covering important processes and regional change.

Essential input to the simulations assessed here is provided by future scenarios of concentrations or anthropogenic emissions of relevant substances; the scenarios represent plausible sets of decisions by humanity, without any implication that one set of decisions is more probable to occur than any other set. As in previous assessment reports, these scenarios are used for projections of future climate using global atmosphere-ocean general circulation models (AOGCMs) and Earth system models (ESMs) (e.g., Flato, 2011). This chapter thus provides a comprehensive assessment of the future global climate response to plausible future anthropogenic perturbations to the climate system.

A crucial element of this chapter is a comprehensive assessment of the sources of uncertainty of future projections. Uncertainty can be broken down into scenario uncertainty, model uncertainty involving both model biases and model spread, and the uncertainty arising from internal variability (Cox and Stephenson, 2007; Hawkins and Sutton, 2009). Assessment of uncertainty relies on multi-model ensembles such as the Coupled Model Intercomparison Project Phase 6 (CMIP6, Eyring et al., 2016a), large initial-condition ensembles (Kay et al., 2015), and ensembles initialized from the observed climate state (Marotzke et al., 2016; Meehl et al., 2014). Ensemble evaluation methods include assessment of model performance and independence (Abramowitz et al., 2019; Boe, 2018; Knutti et al., 2017); emergent and other observational constraints (Allen and Ingram, 2002; Cox et al., 2018; Hall and Qu, 2006); and the uncertainty assessment of equilibrium climate sensitivity in Chapter 7. The ensemble evaluation assessed throughout the WGI contribution to the AR6, including the implications for potential model weighting in the projection ensembles, is synthesized in BOX 4.1:.

The uncertainty assessment in this chapter builds on one particularly noteworthy advance since the IPCC fifth Assessment Report (AR5). Internal variability, which constitutes irreducible uncertainty over much of the time horizon considered here (Hawkins et al., 2016; Marotzke, 2019), can be diagnosed precisely even in a changing climate through the use of large initial-condition ensembles (Kay et al., 2015). Compared to the forced climate change signal, internal variability is dominant in any individual realization – including the one that will unfold in reality – in the near term (Kirtman et al., 2013; Marotzke and Forster, 2015), is substantial in the mid-term, and is still recognizable in the long term in many quantities (Deser et al., 2012a; Marotzke and Forster, 2015). This chapter will use the enhanced information on internal variability throughout.

The expanded treatment of uncertainty allows this chapter a more comprehensive assessment than in the AR5 of the benefits from mitigation as well as the climate response to Carbon Dioxide Removal (CRD) and Solar Radiation Modification (SRM) and how to detect them against the backdrop of internal variability. Important advances since the AR5 have been made in the detection and attribution of mitigation, CDR, and SRM (Bürger and Cubasch, 2015; Lo et al., 2016); exploring the “time of emergence” (ToE) of responses to assumed mitigation (Hawkins et al., 2014; Lehner et al., 2017; Tebaldi and Friedlingstein, 2013); and the attribution of decadal events to forcing changes reflecting mitigation (Marotzke, 2019).

Intimately related to the benefits of mitigation is the question of the potential threshold crossing relative to climate targets (Geden and Loeschel, 2017); a prerequisite is an assessment of how robustly magnitudes of warming can be defined (Millar et al., 2017). This chapter provides an update to the IPCC Special Report on 1.5°C warming (SR1.5, Masson-Delmotte et al., 2018) and constitutes a reference point for later chapters on the benefits of mitigation, including a robust uncertainty assessment.

The chapter is organized as follows. After Section 4.2 on the methodologies used in the assessment, Section 4.3 assesses projected changes in key global climate indices throughout the 21st century, relative to the period 1995–2014, which comprises the last twenty years of the historical simulations of CMIP6 (Eyring et al., 2016a) and hence the most recent past simulated with the observed atmospheric composition. The global climate indices assessed include GSAT, global land precipitation, Arctic SIA, GMSL, the Atlantic Meridional Overturning Circulation (AMOC), global mean ocean surface pH, the Northern and Southern Annular Modes (NAM and SAM), and the El Niño–Southern Oscillation (ENSO).

Section 4.4 covers near-term climate change, defined here as the period 2021–2040 and taken relative to the period 1995–2014. Section 4.4 focuses on global and large-scale climate indices, including rainfall and circulation indices and important modes of variability, as well as on the spatial distribution of warming. Potential role of short-lived climate forcers (SLCFs) and volcanic eruptions on near-term climate change is also discussed. Section 4.4 synthesizes information from initialized predictions and non-initialized projections for the near-term change.

Section 4.5 then covers mid-term and long-term climate change, defined here as the periods 2041–2060 and 2081–2100, respectively, and again relative to the period 1995–2014. The mid-term period is thus chosen as the twenty-year period following the short-term period and straddling the mid-century point, year 2050; it is during the mid-term that differences between different scenarios are expected to emerge against internal variability. The long-term period is defined, as in the AR5, as the twenty-year period at the end of the century. Section 4.5 assesses the same set of indices as Section 4.4 but additionally changes in internal variability and in large-scale patterns, both of which are expected to emerge in the mid- to long-term. The chapter sub-division according to time slices (near term, mid-term, and long-term) is thus to a large extent motivated by the different roles that internal variability plays in each period, compared to the expected forced climate-change signal.

Section 4.6 assesses the implications of climate policies, as simulated with climate models. First, Section 4.6 assesses patterns of climate change expected for various levels of GSAT rise including 1.5°C, 2°C, 3°C, and 4°C, compared to the proxy for the pre-industrial period 1850–1900 to facilitate immediate connection to the SR1.5 and the temperature targets specified in the Paris agreement (COP21, 2015). Section 4.6 continues with climate targets, path-dependence, and overshoot, as well as the climate response to mitigation, CDR, and SRM.

Section 4.7 assesses changes in selected global climate indices including GSAT, GMSL, and AMOC beyond 2100, emphasizing the period out to 2300. Section 4.7 continues with climate-change commitment and the potential for irreversibility and abrupt climate change.

This chapter concludes with Section 4.8 on the potential for low-probability–high-impact changes, followed by a discussion of key knowledge gaps. Answers to three frequently asked questions (FAQs) are assembled at the end of the chapter.

The assessment of concrete projection results is severely limited in this first order draft (FOD), because they are available for only a few CMIP6 models at this time. Most of the figures, tables, and quantitative assessments are thus placeholders indicating the planned approach and structure, to be updated in the Second Order Draft (SOD).

4.2 Methodology

4.2.1 Models, Model Intercomparison Projects, and Ensemble Methodologies

Similar to the AR5 (Flato et al., 2013), this chapter primarily relies on comprehensive climate models, AOGCMs and ESMs; the latter differ from AOGCMs by including representations of various biogeochemical cycles. We will here also exploit inputs from Earth system models of intermediate complexity (EMICs, Claussen et al., 2002; Eby et al., 2013) and other types of model where appropriate. To establish robustness of results or lack thereof, it is vital to assess the performance of these models in mean state, variability, and response to external forcings. This evaluation, using the 'Diagnostic, Evaluation and Characterization of Klima' (DECK) and historical simulations, is performed extensively in AR6 Chapter 3.

This chapter focuses on a particular set of coordinated multi-model experiments known as model intercomparison projects (MIPs). These recommend and document standards for experimental design for running AOGCMs and ESMs to minimise the chance of differences in results being misinterpreted. The CMIP is an activity of the World Climate Research Programme (WCRP), and the latest generation is CMIP6 (Eyring et al., 2016a). This chapter draws mainly on future projections referenced both against the period 1850–1900 and the recent past, 1995–2014, performed primarily under ScenarioMIP (O'Neill et al., 2016). Other MIPs also target future scenarios with a focus on specific processes or feedbacks (see Table 4.1:).

Other MIPs that are used throughout this chapter are summarised in Table 4.1:. The coupling between climate and the carbon cycle is represented in C4MIP, the implications of land use and cover change for climate and carbon is explored in LUMIP, the detection and attribution of chemistry processes and climate response is explored in AerChemMIP, SRM and CDR solutions to climate warming are explored in GeoMIP and CDRMIP, respectively.

[START TABLE 4.1 HERE]

Table 4.1: MIPs utilized in Chapter 4. *Details of models and sub-sections to be completed once CMIP archive is more populated and results shown in this chapter are more fully developed*. [Placeholder for FOD, entries to be confirmed and expanded]

MIP / experiment	Why?	Where used?	Number of models	Number of simulations	Reference
DECK, 1%, 4×CO_2	TCR, ECS	Ch7, Ch4	TBD	TBD	(Eyring et al., 2016a)
CMIP6 Historical	Evaluation, baseline	Ch3, Ch4	TBD	TBD	(Eyring et al., 2016a)
ScenarioMIP	Future projections	Ch.4, WGI AR6	TBD	TBD	(O'Neill et al., 2016)
C4MIP	Carbon cycle/budgets	Ch5, Ch4	TBD	TBD	(Jones et al., 2016a)
LUMIP	Land use/change	Ch5, Ch4	TBD	TBD	(Lawrence et al., 2016)
AerChemMIP	Aerosols and trace gases	Ch6, Ch4	TBD	TBD	(Collins et al., 2017)
GeoMIP	Solar Radiation Modification	Ch6, Ch4	TBD	TBD	(Kravitz et al., 2015)
CDRMIP	Carbon Dioxide Removal	Ch5, Ch4	TBD	TBD	(Keller et al., 2018)
VolMIP	Response to volcanic eruptions	Ch4	TBD	TBD	(Zanchettin et al., 2016)

[END TABLE 4.1 HERE]

Such multi-model ensembles provide the central focus of projection assessment. While single-model experiments are of great value especially for exploring new results and theories, multi-model ensembles allow an assessment of the robustness and reproducibility of results and to quantify the uncertainty that comes from models' internal structure and representation of processes variability (Hawkins and Sutton, 2009) (see subsection 4.2.5). However, these multi-model 'ensembles of opportunity' with their mixture of related and dissimilar models and uneven number of simulations per model are suboptimal in terms of quantifying the individual sources of uncertainty in model projections of future climate change. Progress has been made since the AR5 in understanding the interdependence of the growing number of models contributing to CMIP (Boe, 2018). Techniques to weight model output based on performance and dependence have been made (Abramowitz et al., 2019; Knutti et al., 2017; Olson et al., 2018) but there is no consensus on how to do this optimally. Techniques underlying the combination of evaluation and weighting that are applied in this chapter are synthesised in BOX 4.1:, drawing on assessments across the WGI AR6.

Perturbed-physics ensembles (Murphy et al., 2004) can account for parameter uncertainty in a given model. Two types of perturbed-physics ensembles have been used: (a) where model parameters are perturbed, and (b) where stochastic physics are incorporated. In the perturbed-parameter approach, uncertain model parameters are changed between ensemble members to systematically sample the impact of parameter uncertainty on climate (Johnson et al., 2018; Regayre et al., 2018). Different ensemble members in a perturbed-parameter ensemble have different climate biases and climate sensitivities. It is possible to weight ensemble members according to some performance metric or emergent constraint (Fasullo et al., 2015; Murphy et al., 2004) to improve the ensemble distribution. In the stochastic-physics approach, a stochastic term is included into the model formulation to account for unresolved small-scale processes (Berner et al., 2017). The inclusion of stochastic physics can influence the climate sensitivity of a model (Seiffert and von Storch, 2008; Strømmen et al., 2019). However, members in a stochastic physics ensemble are statistically indistinguishable from each other, so a stochastic ensemble in itself cannot indicate a range in long-term climate sensitivity. Stochastic physics can correct long-standing mean-state biases in climate models (Sanchez et al., 2016). Stochastic physics can also improve the representation of internal variability, including the Madden-Julian Oscillation (Wang et al., 2016), ENSO (Christensen et al., 2017; Yang et al., 2019), the Indian Summer Monsoon (Strømmen et al., 2018), precipitation variability (Davini et al., 2017; Watson et al., 2017) and variability in the mid-latitudes (Dawson and Palmer, 2015),with impacts for near-term projections. While only the UK Met Office CMIP6 contribution includes stochastic physics (Walters et al., 2017), the approach is expected to become more widely used in future intercomparisons.

Large initial-condition ensembles, where the same model is run repeatedly under identical forcing but with initial conditions varied through small perturbations or by sampling different times of a pre-industrial control run, have substantially grown in their use since the AR5 (Deser et al., 2012a; Hedemann et al., 2017; Kay et al., 2015; Maher et al., 2019; Rodgers et al., 2015; Selten et al., 2004; Stolpe et al., 2018). Internal variability makes it hard to identify forced climate signals, especially when considering regional climate signals over short timescales (up to a few decades), such as local trends over the satellite era (Deser et al., 2012a; Hawkins and Sutton, 2009; Lovenduski et al., 2016; Suárez-Gutiérrez et al., 2017; Xie et al., 2015). Such large ensembles can therefore be used to quantify uncertainty due to internal variability (Hawkins et al., 2016; Lehner et al., 2017; Marotzke, 2019; McCusker et al., 2016; McKinnon et al., 2017; Sigmond and Fyfe, 2016) and thereby unpick the forced signal from the internal noise; moreover, they allow the investigation of forced changes in internal variability (e.g., Maher et al., 2018).

4.2.2 Scenarios

The IPCC AR5 (across all WGs) drew heavily on four main scenarios, known as Representative Concentration Pathways (RCPs, Meinshausen et al., 2011; van Vuuren et al., 2011), and simulation results from CMIP5 (Taylor et al., 2012, see Subsection 4.2.1). The RCPs were labelled by the approximate radiative forcing reached at the year 2100, going from 2.6, 4.5, 6.0 to 8.5 W m^{-2}.

This chapter will draw on model simulations from CMIP6 (Eyring et al., 2016a) using a new range of scenarios based on Shared Socio-economic Pathways (SSPs, O'Neill et al., 2016) and RCPs. The set of SSPs is described in detail in Chapter 1 and recognizes that global radiative forcing levels can be achieved by different pathways of CO_2, non-CO_2 greenhouse gases (GHGs), aerosols, and land use; the set of SSPs therefore establishes a matrix of global forcing levels and socio-economic storylines. ScenarioMIP (O'Neill et al., 2016) identifies four priority (tier-1) scenarios that participating modelling groups are required to perform, SSP1-2.6 for sustainable pathways, SSP2-4.5 for middle-of-the-road, SSP3-7.0 for regional rivalry, and SSP5-8.5 for fossil-fuel-rich development. This chapter will focus its assessment on these, plus also the SSP1-1.9 scenario, which is directly relevant to assessment of the 1.5°C climate target.

Complete backward comparability between CMIP5 and CMIP6 scenarios cannot be established for detailed regional assessments, because the SSP scenarios include regional forcings especially from land use and aerosols that are different from the CMIP5 RCPs. At a global level, however, a quantitative comparison is possible between corresponding SSP and RCP radiative forcing levels. The RCP scenarios assessed in the AR5 all showed similar, rapid reductions in SLCFs and emissions of SLCF precursor species over the 21st century; the CMIP5 projections hence did not sample a wide range of possible trajectories for future SLCFs. The SSP scenarios assessed in the AR6 offer more scope to explore SLCF pathways as they sample a broader range of air quality policy options (Gidden et al., 2018). Other MIPs (see Subsection 4.2.1) have been designed to explicitly explore some of the implications of the different socio-economic storylines for a given radiative forcing level. While here we focus on scenarios out to 2040 as the near term and 2100 as the long term, we also include extensions out to 2300 as described in ScenarioMIP (O'Neill et al., 2016) for CO_2 concentrations and C4MIP (Jones et al., 2016a) for CO_2 emissions.

4.2.3 Sources of Near-Term Information

This subsection describes the three main sources of near-term information used in Chapter 4. These are 1) the projections from the CMIP6 multi-model ensemble introduced in Section 4.2.1 (Eyring et al., 2016a; O'Neill et al., 2016), 2) observationally constrained projections (Gillett et al., 2013; Stott et al., 2013) , and 3) the initialized predictions contributed to CMIP6 from the Decadal Climate Prediction Project (DCPP, Boer et al., 2016)). The projections under 1) and the observational constraints under 2) are used for all time horizons considered here, whereas the initialization information under 3) is applied only in the near term.

Observationally constrained projections (Gillett et al., 2013; Stott et al., 2013) use detection and attribution (D&A) methods to correct for systematic model bias and thus provide improved projections of near-term change. Notable advances have been made since the AR5, illustrated through the example of observationally constrained estimates of Arctic sea-ice loss when global average surface temperature is stabilized at 1.5°C, 2.0°C and 3.0°C warming above pre-industrial (Jahn, 2018; Screen, 2018; Screen and Williamson, 2017; Sigmond et al., 2018). There is *high confidence* that these approaches can reduce the uncertainties involved in such estimates.

The AR5 was the first IPCC report to assess decadal climate predictions initialized from the observed climate state (Kirtman et al., 2013), and assessed with *high confidence* that they contribute positively to near-term averaged surface temperature information, globally and over large regions, for up to ten years. Substantially more experience has been gained since the AR5; the remainder of this subsection assesses the advances made.

Because the "memory" that potentially enables prediction of multi-year to decadal internal variability resides mainly in the oceans, some systems initialize the ocean state only (e.g., Yeager et al., 2018), whereas others incorporate observed information in the initial atmospheric states (e.g., Knight et al., 2014; Pohlmann et al., 2013) or other non-oceanic drivers providing further sources of predictability (Bellucci et al., 2015a). Ocean initialization techniques generally use one of two strategies. Under full-field initialization, estimates of observed climate states are represented directly on the model grid. A potential drawback is that because models are imperfect, their climates differ from that of the real world, so predictions initialized using the full-field approach tend to drift toward the climate preferred by the model (Bellucci et al., 2015b; Kröger et al., 2018; Smith et al., 2013a). Such drifts can be as large as or larger than the climate anomaly being predicted and may obscure predicted climate anomalies unless corrected through post-processing. By contrast, anomaly initialization adds observed anomalies (deviations from mean climate) to the mean climate of the model in order to reduce drifts (Cassou et al., 2018; Pohlmann et al., 2013; Smith et al., 2013a; Thoma et al., 2015b). For either approach, unrealistic features in the data used for initialization may further induce unrealistic transient behavior (Pohlmann et al., 2017; Teng et al., 2017). As yet, none of these strategies has been shown clearly to be superior to the others (Hazeleger et al., 2013; Magnusson et al., 2013; Marotzke et al., 2016; Smith et al., 2013a), although such comparisons may be sensitive to the model, region, and details of the initialization and forecast assessment procedures considered (Bellucci et al., 2015b; Polkova et al., 2014).

There is also a wide range of techniques employed to assimilate observed information into models. These range in complexity from simple relaxation towards observed time series of sea surface temperature (SST) (Mignot et al., 2016) or wind stress anomalies (Thoma et al., 2015a, 2015b), to relaxation toward three-dimensional values from ocean and sometimes atmospheric state estimates from various sources (e.g., Knight et al., 2014; Pohlmann et al., 2013), to sophisticated data assimilation methods such as the ensemble Kalman filter (Karspeck et al., 2015; Msadek et al., 2014) and the initialization of sea ice (Guemas et al., 2016; Kimmritz et al., 2018). In addition, decadal predictions necessarily consist of ensembles of forecasts in order to quantify uncertainty as discussed in Section 4.4. A common way to generate such an ensemble is through sets of initial conditions whose differences lead to different subsequent climate trajectories. A variety of methods has been employed to generate initial-condition ensembles for decadal prediction (e.g., Cassou et al., 2018; Marini et al., 2016). As yet there is no clear consensus as to which initialization and ensemble generation techniques are most effective, and evaluations of their comparative performance within a single modelling framework are needed (Cassou et al., 2018).

A consequence of model imperfections and resulting model systematic errors or biases is that estimates of these errors must be removed from the prediction in order to isolate the predicted climate anomaly. Because of the tendency for systematic drifts to occur following initialization, bias corrections generally depend on time since the start of the forecast, often referred to as lead time. In practice, the lead-time-dependent biases are calculated using ensemble retrospective predictions, also known as hindcasts, and recommended basic procedures for such corrections are provided in previous studies (Boer et al., 2016; Goddard et al., 2013). Besides mean climate as a function of lead time, further aspects of decadal predictions may be biased, and additional correction procedures have thus been proposed to remove biases in representing long-term trends (Balaji et al., 2018; Kharin et al., 2012; Kruschke et al., 2016), as well as more general dependences of drift on initial conditions (Fučkar et al., 2014).

Many skill measures exist that describe different aspects of the correspondence between predicted and observed conditions, and no single one should be considered exclusively. Important aspects of forecast performance captured by different skill measures include ability to predict the sign and phase of future climate variability, the typical magnitude of differences between predicted and observed values, forecast reliability and resolution (Corti et al., 2012) and whether the forecast ensemble appropriately represents uncertainty in the predictions. A framework for skill assessment (also called verification) that encompasses each of these aspects of forecast quality has been proposed by Goddard et al. (2013).

Considerable skill, especially for temperature, can be attributed to external forcings such as changes in GHG and aerosol concentrations. This contribution to skill has been found to exceed that from the prediction of internal variability except in early stages of the forecast (Corti et al., 2015), though idealized potential skill measures suggest that improving the prediction of internal variability could extend this crossover to longer lead times (Boer et al., 2013). And although the skill added by initialization tends to be modest particularly over land and at longer lead times, an alternative approach of assessing how well initialized predictions forecast observed variability that is not captured by uninitialized simulations suggests the value added by initialization may be greater than previously thought (Scaife and Smith, 2018).

One additional aspect of forecast quality assessment is that skill can be degraded by errors in observational datasets used for verification, in addition to errors in the predictions (Massonnet et al., 2016). This suggests that skill may tend to be underestimated, particularly for climate variables whose observational uncertainties are relatively large, and that predictions are in turn useful for assessing the quality of observational datasets.

Skill assessments have shown that initialized predictions generally out-perform their uninitialized counterparts, although such comparisons are sensitive to the region and variable considered, and that multi-model predictions are generally more skilful than individual models (Doblas-Reyes et al., 2013; Smith et al., 2013b). Initialized predictions of near-surface temperature are particularly skilful over the North Atlantic, a region of high potential and realised predictability (Boer et al., 2013; Pohlmann et al., 2009; Yeager and Robson, 2017) (*high confidence*). Much of this predictability is associated with the North Atlantic subpolar gyre (Wouters et al., 2013), where skill in predicting ocean conditions is typically high (Hazeleger et al., 2013) and shifts in ocean temperature and salinity potentially affecting surface climate can be predicted up to several years in advance (Hermanson et al., 2014; Robson et al., 2012) although such assessments remain challenging due to incomplete knowledge of the state of the ocean during the hindcast evaluation periods (Menary and Hermanson, 2018).

In contrast to the North Atlantic, near-surface temperature forecast skill is low or even negative throughout much of the central and northeastern Pacific (Doblas-Reyes et al., 2013), although some evidence for multi-year skill in forecasting shifts in the Interdecadal Pacific Oscillation and its impacts on global temperature has been found (Guemas et al., 2013b; Meehl et al., 2016). Skill for multi-year to decadal precipitation forecasts is generally much lower than for temperature, although one exception is Sahel rainfall (Sheen et al., 2017) due to its dependence on predictable variations in North Atlantic SST (Martin and Thorncroft, 2014a). In addition, decadal predictions having large ensemble sizes appear able to predict multi-annual precipitation anomalies over certain land regions (Yeager and Robson, 2017) although with ensemble-mean magnitudes that are much weaker than observed. This discrepancy may be symptomatic of an apparent deficiency in climate models that causes predictable signals to be much weaker than in nature (Eade et al., 2014; Scaife and Smith, 2018).

Evidence is accumulating that additional properties of the Earth system that relate to ocean variability may be skilfully predicted on multi-annual time scales. These include levels of Atlantic hurricane activity (Caron et al., 2017), drought and wildfire (Chikamoto et al., 2017), and variations in the ocean carbon cycle including CO_2 uptake (Li et al., 2016b, 2019).

In summary, there is *high confidence* that information from initialized predictions reduces the uncertainty of projections of future temperature on the global and large scales; for a recent application of a multi-model prediction ensemble to the question of whether global warming of 1.5°C above pre-industrial levels will be exceeded in the near future, see (Smith et al., 2018). By contrast, there is *medium* or *low confidence* for similar uncertainty reductions for other climate quantities.

4.2.4 Pattern Scaling

The CMIP6 projections of future climate change under different SSPs are representative of a range of transient and stabilization scenarios (O'Neill et al., 2016). Projected climate change futures are typically represented for specific periods in the future, for example in this chapter projections are presented for near-term (2021–2040), mid-term (2041–2060) and long-term (2081–2100) periods. One important source of uncertainty in projections presented for fixed future time-slabs is the underlying mitigation scenario used to force the GCMs. Presenting projections and associated measures of uncertainty for specific future time-slabs (see Sections 4.4 and 4.5) remains the most widely applied methodology towards informing climate change impact studies. It is becoming increasingly important, however, from the perspective of climate change and mitigation policy, to present projections of future climate change not only as a function of different periods in the future but also as a function of the increase in GSAT. In particular, the IPCC SR1.5 report assessed the regional patterns of warming for increase in GSAT of 1.5°C and 2°C above pre-industrial levels. The report compared impacts of global warming at 1.5°C of global warming to impacts at 2°C of global warming. For such an analysis, it is important to develop an understanding of the spatial variations of temperature and other climate variables for a particular increase in the GSAT. The techniques used to represent the spatial variations in climate at a given increase in the GSAT are referred to as pattern scaling.

In the original (or traditional) methodology, also applied in the AR5 (Collins et al., 2013), patterns of climate change in space are calculated as the product of the change in GSAT at a given point in time and a spatial pattern of change that is constant over time and mitigation scenario, and which may or may not depend on a particular climate model (Allen and Ingram, 2002; Andrews and Forster, 2010; Bony et al., 2013; Lambert and Allen, 2009; Lopez et al., 2014; Mitchell, 2003). This approach thus assumes that external forcing does not affect the internal variability of the climate system, which may be regarded a stringent assumption when taking into account decadal and multi-decadal variability (Lopez et al., 2014) and the potential nonlinearity of the climate change signal. Moreover, pattern scaling is expected to have lower skill for variables with large spatial variability (Tebaldi and Arblaster, 2014) and is less accurate for strong mitigation scenarios such as RCP2.6 (May, 2012). Scaling fails to capture changes in sea ice extent and snow cover (Collins et al., 2013), which behave more like a boundary that moves poleward than a pattern that scales. Pattern scaling also fails for certain quantities such as frost days that decrease under warming but are bounded at zero. Spatial patterns are expected to be different between transient and equilibrium simulations because of the long adjustment time scale of the deep ocean.

Modifications of the AR5 approach have since explored the role of aerosols in modifying regional climate responses at a specific degree of global warming and also the effect of different GCMs and mitigation scenarios on the scaled spatial patterns (Frieler et al., 2012; Levy et al., 2013). Furthermore, the modified forcing-response framework (Kamae and Watanabe, 2012, 2013; Sherwood et al., 2015), which decomposes the total climate change into fast adjustments and slow response, identifies the fast adjustment as forcing-dependent and the slow response as forcing-independent, scaling with the change in GSAT.

For precipitation change, there is suppression during the fast-adjustment phase for CO_2 and black-carbon radiative forcing (Andrews et al., 2009; Bala et al., 2010; Cao et al., 2015), but there is near-zero fast adjustment for solar forcing. By contrast, the slow response in precipitation change is independent of the forcing. This indicates that pattern scaling is not expected to work well for climate variables that have a large fast-adjustment component. Even in such cases, pattern scaling still works for the slow response component, but a correction for the forcing-dependent fast adjustment would be necessary to apply pattern scaling to the total climate change signal. In a multi-model setting, it has been shown that temperature change patterns conform better to pattern scaling approximation than precipitation patterns (Tebaldi and Arblaster, 2014).

Most recently, Herger et al. (2015) have explored the use of multiple predictors for the spatial pattern of change at a given degree of global warming, following the approach of Joshi et al. (2013) that explored the role of the land-sea warming ratio as a second predictor. They found that the land-sea warming contrast changes in a non-linear way with GSAT, and that it approximates the role of the rate of global warming in determining regional patterns of climate change. The inclusion of the land-sea warming contrast as the second predictor provides the largest improvement over the traditional technique. However, as pointed out by Herger et al. (2015), multiple-predictor approaches still cannot detect nonlinearities (or internal variability), such as the apparent dependence of spatial temperature variability in the mid to high latitudes on GSAT (e.g. Screen, 2014; Fischer and Knutti, 2014).

An alternative to the traditional pattern scaling approach is the time-shift method described by (Herger et al., 2015), and this methodology (also called the epoch approach, see Section 4.6.1) is the one applied in this chapter. When applied to a transient scenario such as SSP5-8.5, a future time-slab is identified for which the average temperature equals a particular increase in the GSAT (e.g., 1.5°C or 2°C of global warming above pre-industrial levels). The spatial patterns that result represent a direct scaling of the spatial variations of climate change at the particular level of global warming, irrespective of the scenario. An important advantage of this approach is that it ensures physical consistency between the different variables for which changes are presented (Herger et al., 2015). The internal variability does not have to be scaled and is consistent with the GSAT change. The time-shift method furthermore allows for a partial comparison of how the rate of increase in GSAT influences the regional spatial patterns of climate change. For example, spatial patterns of change for global warming of 2°C can be compared across the SSP2-4.5 and SSP5-8.5 scenarios. Direct comparisons can also be obtained between variations in the regional impacts of climate change for the case where global warming stabilizes at, say, 1.5°C or 2°C of global warming, as opposed to the case where the GSAT reaches and then exceeds the 1.5°C or 2°C thresholds. An important potential caveat is that forcing mechanisms such as aerosol radiative forcing are represented differently in different models, even for the same SSP. This may imply different regional aerosol direct and indirect effects, implying different regional climate change patterns. Hence it is important to consider the variations in the forcing mechanisms responsible for a specific increase in the GSAT, towards understanding the uncertainty range associated with the variations in regional climate change. A minor practical limitation of this approach is that stabilization scenarios at 1.5°C or 2°C of global warming, such as SSP1-2.6, do not allow for spatial patterns of change to be calculated from these scenarios at higher levels of global warming in scenarios such as SSP5-8.5 (Herger et al., 2015).

In this chapter the spatial patterns of change as a function of increase in the GSAT are thus constructed using the time-shift approach to consider various nonlinearities and internal variability that influence the projected climate change signal. This implies a reliance on large ensemble sizes to quantify the role of uncertainties in regional responses to different degrees of global warming. The assessment in Section 4.6.1 also explores how the rate of global warming (as represented by different SSPs), aerosol effects, and transient as opposed to stabilization scenarios influence the spatial variations in climate change at specific levels of global warming.

4.2.5 Quantifying Various Sources of Uncertainty

The spread across individual runs within a multi-model ensemble represents a combination of different sources of uncertainties, specifically scenario uncertainties, parametric and structural model uncertainty and internal variability (e.g., Hawkins and Sutton, 2009; Kirtman et al., 2013). This sub-section assesses methods to disentangle different sources of uncertainties and quantifies their contributions to the overall ensemble spread.

The AR5 uncertainty characterisation (Kirtman et al., 2013) followed Hawkins and Sutton (2009) and diagnosed internal variability through a high-pass temporal filter. But it has since become clear that internal variability manifests itself substantially also on the multi-decadal timescale (Deser et al., 2012a; Marotzke and Forster, 2015). Large initial-condition ensembles have revealed that the AR5 approach underestimates the role of internal variability and overestimates the role of model uncertainty (Maher et al., 2018; Stolpe et al., 2018). The availability of large initial-condition ensembles thus represents a crucial step towards a cleaner separation of model uncertainty and internal variability (Deser et al., 2014, 2016; Saffioti et al., 2017). For time horizons beyond the limit of decadal predictability (Branstator and Teng, 2010; Marotzke et al., 2016; Meehl et al., 2014), internal variability constitutes an uncertainty that is irreducible and that at best can be accurately quantified.

Scenario uncertainty cannot be quantified within the remit of WGI, because the scenarios have no probability attached to them, owing to the current impossibility of attaching probabilities to societal decisions (Schneider, 2001). More comprehensive representation of SSPs induces additional uncertainties such as the response to land use changes and others (Ciais et al., 2013; O'Neill et al., 2016).

An additional uncertainty is highlighted by the contrast between emission-driven and concentration-driven simulations, which introduces carbon-cycle feedbacks as a source of uncertainty (Friedlingstein et al., 2014; Hewitt et al., 2016) that strongly influences the transient climate response to emission (TCRE). This uncertainty is crucial for the assessment of remaining carbon budgets consistent with temperature targets (Masson-Delmotte et al., 2018; Millar et al., 2017) and is be covered in Chapter 5 of this report.

The relative magnitudes of model uncertainty and internal variability depend on the time horizon of the projection, location, spatial and temporal aggregation, variable, and signal strength (Deser et al., 2014; Fischer et al., 2013; Saffioti et al., 2017). New literature published after the AR5 systematically discusses the role of different sources of uncertainty and shows that the relative contribution of internal variability is larger for short than long projection horizons (Marotzke and Forster, 2015), larger for high latitudes than low latitudes, larger for land than ocean variables, larger at station level than continental than global means, larger for annual maxima/minima than for multi-decadal means, larger for dynamic quantities (and, by implication, precipitation) than for temperature (Fischer et al., 2014), and larger for weak than for strong signals.

Some uncertainties are not or only partially accounted for in the CMIP6 experiments, such as long-term Earth system feedbacks including missing land-ice feedbacks or some long-term carbon-cycle feedbacks (Fischer et al., 2018). Where appropriate, this chapter will use results from non-CMIP ESMs or EMICs to assess the role of these feedbacks.

As discussed extensively already in the AR5 (Collins et al., 2013), differences between projections performed with different climate models account for only part of the entire model uncertainty, even when considering only the uncertainty in the radiative forcing in projections (Vial et al., 2013) or in the forced response. The true uncertainty is larger than the model spread, because the entire CMIP ensembles are known to share certain biases in simulations of the past (Flato et al., 2013) and because climate models are expected to share errors in simulating future climates. Assessing these shared errors in projections remains fundamentally very difficult, because observational tests are elusive. Emergent constraints (e.g., Cox et al., 2018; Hall and Qu, 2006) introduce observable quantities as proxies of projected quantities, but in each case the validity of the proxy rests on untested connections established by the climate model. Obtaining a full assessment of the uncertainty in an ensemble of projections thus continues to pose a fundamental epistemological challenge (Baumberger et al., 2017; Frisch, 2015; Parker, 2009).

4.2.6 Display of Model Agreement and Spread

Maps of multi-model mean changes provide an average estimate for the forced model response to a certain forcing. However, they do not include any information on the robustness of the response across models nor on the significance of the change with respect to unforced internal variability (Tebaldi et al., 2011). Models can consistently show absence of significant change, in which case they should not be expected to agree on the sign of a change (e.g., Fischer et al., 2014; Tebaldi et al., 2011). In a multi-model mean map of precipitation where the median shows no change it is unclear whether the models consistently project both small and insignificant increases and decreases or whether projections span both substantial increases and substantial decreases (McSweeney and Jones, 2013; Tebaldi et al., 2011). Therefore, a set of different methods have been introduced in the literature to display model robustness and to put a climate change signal into the context of internal variability. The AR5 Box 12.1 provides a detailed assessment of different methods of mapping model robustness.

The combination of several large initial-condition (e.g., Kay et al., 2015) and multi-model ensembles (Eyring et al., 2016a; Taylor et al., 2012) provides new opportunities to separate internal variability from model uncertainty and to better understand whether individual model realizations disagree due to internal variability or model differences. Most methods of quantifying robustness assume, however, that only one realization from each model is applied. There are new challenges that arise from having inhomogeneous multi-model ensembles with many members for some models and single members for others (Olonscheck and Notz, 2017). Furthermore, the methods that map model robustness usually ignore that sharing parametrizations or entire components across coupled models can lead to substantial model interdependence (Abramowitz et al., 2019; Annan and Hargreaves, 2017; Boe, 2018; Fischer et al., 2011; Kharin et al., 2012; Knutti et al., 2013a, 2017; Leduc et al., 2015; Sanderson et al., 2015, 2017a) This may lead to an overestimation of model agreement if a substantial fraction of models are interdependent. However, quantifying and accounting for model dependence in a robust way remains challenging (Abramowitz et al., 2019).

Furthermore, absence of significant mean change in a certain climate variable does not imply absence of substantial impact, because there may be substantial change in variability, which is typically not mapped (McSweeney and Jones, 2013).

The following chapter will be using the same methodology as the AR5 to map model robustness and significance of the signal. This approach represents a compromise between transparency and comprehensiveness of the diverse mapping methodologies and has the advantage that a broad community is used to interpret this mapping methodology. That maps of mean changes ignore potential changes in variability addressed by a more comprehensive assessment of changes in temperature variability and modes of internal variability.

The degree to which climate change drivers and processes are known and formulated in the various models is very important in the display of projections. This display makes it straightforward to extract long-term policy-relevant information (magnitudes, robustness, significance, and certainty levels). Recent developments in climate change modelling including more physically consistent schemes used in CMIP6 runs and new analysis methods applied to both CMIP5 and CMIP6 have brought out information with smaller spread and increased convergence of change evidence at specific warming levels (Knutti et al., 2017; Notz and Stroeve, 2016). These are substantial advancements of the AR6 above AR5 in the display and assessment of model agreement.

[START BOX 4.1 HERE]

BOX 4.1: Ensemble Evaluation and Weighting

Box 4.1 provides the synthesis required for a robust assessment of projection ensembles, in part using material from other WGI AR6 Chapters.

The IPCC AR5 used a pragmatic approach to quantifying the uncertainty in CMIP5 climate projections (Collins et al., 2013). One realization per model per scenario was picked and defined the ensemble. For most quantities, the 5–95% ensemble spread was used to characterize the uncertainty, but the 5–95% spread was interpreted as the 16–83% (*likely*) range. The uncertainty was thus explicitly assumed to contain sources not represented by the model spread. While straightforward and clearly communicated, this approach had several drawbacks, and there has been substantial progress since the AR5 on how to assess the uncertainty of projections.

i) The uncertainty breakdown into scenario uncertainty, model uncertainty, and internal variability (Cox and Stephenson, 2007; Hawkins and Sutton, 2009) in the AR5 followed (Hawkins and Sutton, 2009) and diagnosed internal variability through a high-pass temporal filter (Kirtman et al., 2013). But it has since become clear that interval variability manifests itself substantially also on the multi-decadal timescale (e.g., (Deser et al., 2012a; Marotzke and Forster, 2015)); hence a more comprehensive approach is needed.
ii) The uncertainty characterization ignores observation-based information about internal climate variability during the recent past. This may matter less for the long-term projections (Collins et al., 2013) but becomes very important for the near-term future (Kirtman et al., 2013). It was necessary to include additional uncertainty quantification for the near-term projections in the AR5 but this characterization of uncertainty was inconsistent with that of the long-term projections.
iii) The ensemble-spread-based uncertainty characterization for equilibrium climate sensitivity (ECS) was distinct from the *likely* range assessed for ECS in the AR5 (Collins et al., 2013), and while the CMIP5 spread in ECS and the AR5 ECS *likely* range did not differ much, this did create an inconsistency. Furthermore, WGIII in the AR5 used the assessed *likely* range for ECS in their calculations of carbon budgets (IPCC, 2014), and as the recent discussion has shown (e.g., Millar et al., 2017, 2018a, 2018b; Schurer et al., 2018), small uncertainties matter a great deal when assessing remaining carbon budgets consistent with a given climate target.

Another important consideration concerns the potential weighting of model contributions to an ensemble, based on model independence, model performance during the historical period, or both. Such model weighting (in fact, model selection) was performed in the AR5 for the projections of Arctic sea ice (Collins et al., 2013), but the method applied has, for this case, been shown by Notz (2015) to be contaminated by internal variability, making the resulting weighting questionable (see also Stroeve and Notz, 2015). For a general cautionary note see Weigel et al. (2010). More robust approaches, taking into account internal variability and model independence, have been proposed since the AR5 (Abramowitz et al., 2019; Boe, 2018; Knutti et al., 2017).

Chapter 4 will apply all available information, stemming from (i) the CMIP6 multi-model ensemble (Eyring et al., 2016a), augmented if appropriate by the CMIP5 ensemble (Taylor et al., 2012); (ii) single-model large initial-condition ensembles (e.g., Kay et al., 2015; Maher et al., 2019; Sigmond and Fyfe, 2016) and combinations of control runs with CMIP transient simulations (e.g., Olonscheck and Notz, 2017; Thompson et al., 2015) to characterize internal variability; (iii) climate predictions initialized from recent observations (e.g., Kirtman et al., 2013) and the Decadal Climate Prediction Project (DCPP) contribution to CMIP6 (Boer et al., 2016); (iv) assessed ranges of climate sensitivity based on multiple lines of evidence (e.g., Chapter 7, Collins et al., 2013); (v) diagnosed model independence (e.g., Boe, 2018) and performance in simulating the past (e.g., Abramowitz et al., 2019; Knutti et al., 2017); (vi) emergent constraints (e.g., Cox et al., 2018; Hall and Qu, 2006); and (vii) information from perturbed-physics ensembles (e.g., Murphy et al., 2004), to produce a robust method for quantifying the uncertainty in climate projections, including a breakdown into sources of uncertainty. Not all proposed methods are already available for the FOD; furthermore, the FOD comprises a mix of CMIP5 and CMIP6 models and a mix of RCP and SSP radiative forcings, because CMIP6 projections and SSP radiative forcings are not yet sufficiently available.

0 shows GSAT simulated by CMIP6 models for both the historical period and forced by scenario SSP2-4.5 until 2100, combined with various characterizations of uncertainty. First, internal variability is estimated with the 100-member Max Planck Institute Grand Ensemble (MPI-GE, Maher et al., 2019), forced by scenario RCP4.5 (0, left); note that no large ensemble is currently available that is driven by an SSP scenario. Second, GSAT implied by the Chapter 7 *likely* and *very likely* ECS ranges are simulated with an energy balance model (EBM) as an emulator, using the RCP4.5 radiative forcing information (0). Third, the initialized-prediction ensemble from the CMIP6 model MPI-ESM-HR (Müller et al., 2018) is shown for the years 2019–2028 (purple, 0, right); the predictions have been produced through the MiKlip project (Marotzke et al., 2016) and contribute to DCPP (Boer et al., 2016).

Referenced against 1850–1900, the available CMIP6 simulations project future warming that until around 2060 largely falls within the emulated GSAT range that is based on the Chapter 7-assessed ECS *very likely* range of 2°C–5°C. After 2060, some models stay within this range and some other models lie above. The stronger-warming models are expected to have an ECS above the Chapter 7-assessed *very likely* range (expert judgement, *medium confidence*).

The GSAT uncertainty arising from the ECS *very likely* range is substantially larger than the irreducible uncertainty arising from internal variability, from the mid-term period (2041–2060) onward (*high confidence*). By contrast, the ECS *likely* range is similar to the irreducible uncertainty (*medium confidence*). The initialized predictions simulate GSAT toward the lower end of both the CMIP6 range and the emulator ECS *very likely* range (expert judgement, *low confidence* owing to limited data availability).

[START BOX 4.1, FIGURE 1 HERE]

Box 4.1, Figure 1: CMIP6 GSAT simulations and various contributions to uncertainty in the projections ensemble. The top row shows the period 1850–2100, referenced to 1850–1900; the bottom row shows a cut-out for the period 1995–2040, which encompasses the most recent past in CMIP6 (1995–2014) and the near-term future (2021–2040). All panels show for 1850–2100 one CMIP6-forced simulation each with BCC-CSM2-MR (cyan), CanESM5 (light green), IPSL-CM6A-LR (yellow), MRI-ESM2-0 (light purple), and UKESM1 (ochre); and GSAT simulated with an emulator driven by the AR5 radiative forcing, using RCP4.5 from the WGI AR5 Annex II after 2005 (black). The emulator is a two-layer time-dependent energy-balance model (EBM) following (Held et al., 2010), with ocean heat uptake efficiency κ = 0.8 W m^{-2} $°C^{-1}$ and efficacy 1.0. Results are shown for ECS = 2.5°C and 3.5°C, the lower and upper limits, respectively, of the Chapter 7 ECS *likely* range (solid black), as well as for 2°C and 5°C, the lower and upper limits, respectively, of the Chapter 7 ECS *very likely* range (dashed black). For the historical period, all panels show the observations (HadCRUT4, (Morice et al., 2012), red) and the CMIP5-forced simulations from the 100-member Max Planck Institute Grand Ensemble (MPI-GE, (Maher et al., 2019), dark blue for ensemble mean, light blue for individual realizations), Left: The MPI-GE simulations are extended from 2006–2100 following the RCP4.5 scenario. Right: For the years 2019–2028, the initialized-prediction ensemble from the CMIP6 model MPI-ESM-HR (Müller et al., 2018) is shown (dark purple), produced through the MiKlip project (Marotzke et al., 2016) and contributing to DCPP (Boer et al., 2016). The MiKlip results are drift-removed and referenced to the time-averaged hindcasts for 1995–2014 lead-year by lead-year; then the HadCRUT4 difference between the means over 1995–2014 and 1850–1900 is added. [Placeholder figure, to be updated with the full CMIP6 ensemble and CMIP6/AR6/SSP forcing for the EBM.]

[END BOX 4.1, FIGURE 1 HERE]

[END BOX 4.1 HERE]

4.3 Projected Changes in Global Climate Indices in the 21st Century

Here we assess the latest simulations of representative indicators of global climate change at the surface considered as simple time series and tabulated values over the 21st century and across the main realms of the global climate system. In the atmospheric realm (see Section 4.3.1), we assess simulations of GSAT (see Figure 4.1:) and global land precipitation (see Figure 4.1:). Across the cryospheric, oceanic, and biospheric realms (see Section 4.3.2), we assess simulations of Arctic SIA (see Figure 4.1:), GMSL (see Figure 4.1:), the AMOC, cumulative ocean carbon uptake, and pH. Finally, in Section 4.3.3 we assess simulations of a several indices of climate variability, namely, the indices of the NAM, SAM, and ENSO.

The quantities assessed here comprise a subset of the variables assessed in Chapters 2 and 3; selected so as to illustrate the range of connected changes simulated over the entirety of the 21st century and spanning much of the global climate system (see Figure 4.1:). From the CMIP6 multi-model ensemble we consider historical simulations with observed external forcings to 2014 and extensions to 2100 based on the four priority SSPs; namely, SSP1-2.6 (sustainable), SSP2-4.5 (middle-of-the-road), SSP3-7.0 (regional rivalry), and SSP5-8.5 (fossil-fuel-rich development). In tabular form, we show ensemble-mean changes and uncertainties for the near-term (2020–2041), mid-term (2041–2061) and the long-term (2081–2100), relative to present-day (1995–2014) and/or pre-industrial (1850–1900). Changes of selected variables near 1.5°C, 2.0°C, and 3.0°C of global warming relative to pre-industrial are also assessed.

[START FIGURE 4.1 HERE]

Figure 4.1: Selected indicators of global climate change from historical and scenario simulations. (a) Global surface air temperature changes relative to averages from 1995–2014 (left axis) and relative to averages from 1850–1900 (right axis). (b) Arctic sea-ice area. (c) Global land precipitation changes relative to averages from 1995–2014. (d) Global sea level change (due to thermal expansion alone) relative to averages from 1995–2014. (a), (b) and (d) are annual averages, (c) are September averages. The curves plotted here are based on results from the models that have thus far contributed to the CMIP6 exercise. In (a) and (b), the models are BCC-CSM2-MR, CanESM5, CNRM-CM6-1, IPSL-CM6A-LR, and MRI-ESM2-0. In (c) and (d), the models are CanESM5, CNRM-CM6-1, and IPSL-CM6A-LR. The number inside panel indicates the total number of models used. Eventually this figure will be updated using single simulations from the full CMIP6 ensemble plotted as ensemble means with shaded uncertainties.

[END FIGURE 4.1 HERE]

Assessments of the regional manifestations of the changes discussed in this section are undertaken in Section 4.4 (for the near-term) and Section 4.5 (for the mid- to long-term). Detailed physical understanding of the changes documented here are undertaken in Chapters 5 to 11.

4.3.1 Atmosphere

4.3.1.1 Surface Air Temperature

The AR5 assessed from CMIP5 simulations that GSAT will continue to rise over the 21st century if GHGs continue increasing (Collins et al., 2013). The GHG trajectories, or RCPs, considered in the AR5 ranged from RCP2.6 which assumes that GHG emissions peak between 2010 and 2020, with emissions declining substantially thereafter, to RCP8.5 where emissions continue to rise throughout the 21st century. The AR5 concluded that GSAT for 2081–2100, relative to 1986–2005 will *likely* be in the 5–95% range of 0.3°C–1.7°C under RCP2.6 and 2.6°C–4.8°C under RCP8.5. The corresponding ranges for the intermediate emissions scenarios with emissions peaking around 2040 (RCP4.5) and 2060 (RCP6.0) are 1.1°C–2.6°C and 1.4°C–3.1°C, respectively. The AR5 further assessed that GSAT averaged over the period 2081–2100 are projected to *likely* exceed 1.5°C above 1850–1900 for RCP4.5, RCP6.0 and RCP8.5 (*high confidence*), and are *likely* to exceed 2°C above 1850–1900 for RCP6.0 and RCP8.5 (*high confidence*). Global surface temperature changes above 2°C under RCP2.6 were deemed *unlikely* (*medium confidence*).

Here, for continuity's sake, we assess the CMIP6 simulations of GSAT in a fashion similar to the AR5 assessment of the CMIP5 simulations. For each CMIP6 model, we show one historical realization of GSAT from 1950–2014 and one scenario realization from 2015–2100 for each priority SSP (see Figure 4.1:). These are displayed as anomalies relative to 1995–2014 and 1850–1900. We tabulate the 5–95% range of anomalies from 1995–2014 averaged over 2021–2040 (near-term), 2041–2060 (mid-term) and 2081–2100 (long-term) for each priority SSP (Table 4.1:). Based on results from the five models that have thus far contributed to the CMIP6 exercise, we conclude that GSAT for 2081–2100, relative to 1995–2014, shows a 5–95% range of 0.7°C–1.7°C under SSP1-2.6 where CO_2 concentrations peak between 2040–2060 (see Table 4.2:; *medium confidence* because of the limited number of models available). The corresponding range under the highest overall emissions scenario (SSP5-8.5) is 2.9°C–6.1°C (*medium confidence*). The ranges for the intermediate emissions scenarios (SSP2-4.5 and SSP3-7.0), where CO_2 concentrations increase to 2100 but less rapidly than SSP5-8.5, are 1.6°C–3.1°C and 2.4°C–4.8°C, respectively (*medium confidence*).

We will compare and contrast the changes in GSAT across the three reference periods and the four SSPs in terms of differences in the underlying time-evolving emissions. The changes we find will be related to the estimated radiative forcing for the scenarios and models, with reference to the assessment in Chapter 7. Changes in area-weighted land, ocean, tropical (30°S–30°N), Arctic (67.7°N–90°N), and Antarctic (90°S–55°S) surface air temperature will be evaluated (see Table 4.2:).

[START TABLE 4.2 HERE]

Table 4.2: CMIP6 annual mean surface air temperature anomalies (°C) from the 1995–2014 reference period for selected time periods, regions and SSPs. The multi-model mean ±1 standard deviation ranges across the individual models are listed and the 5–95% ranges from the models' distribution (based on a Gaussian assumption and obtained by multiplying the CMIP6 ensemble standard deviation by 1.64) are given in brackets. The values tabulated here are for single simulations from the five models that have thus far contributed to the CMIP6 exercise. The models are BCC-CSM2-MR, CanESM5, CNRM-CM6-1, IPSL-CM6A-LR, and MRI-ESM2-0. Eventually this table will be updated using single simulations from the full CMIP6 ensemble.

		SSP1-2.6 (°C)	SSP2-4.5 (°C)	SSP3-7.0 (°C)	SSP5-8.5 (°C)
Global :	2021–2040	0.8 ± 0.1 (0.6, 1.0)	0.8 ± 0.2 (0.5, 1.1)	0.8 ± 0.2 (0.5, 1.2)	0.9 ± 0.2 (0.6, 1.2)
	2041–2060	1.2 ± 0.2 (0.8, 1.5)	1.4 ± 0.3 (1.0, 1.9)	1.7 ± 0.3 (1.1, 2.2)	1.9 ± 0.4 (1.3, 2.5)
	2081–2100	1.2 ± 0.3 (0.7, 1.7)	2.3 ± 0.5 (1.6, 3.1)	3.6 ± 0.7 (2.4, 4.8)	4.5 ± 1.0 (2.9, 6.1)
Land :	2081–2100	1.6 ± 0.4 (0.9, 2.3)	3.0 ± 0.6 (2.0, 4.1)	4.8 ± 1.0 (3.1, 6.4)	6.0 ± 1.4 (3.8, 8.3)
Ocean :	2081–2100	1.1 ± 0.2 (0.7, 1.5)	2.0 ± 0.4 (1.4, 2.7)	3.1 ± 0.6 (2.1, 4.1)	3.9 ± 0.9 (2.5, 5.3)
Tropics :	2081–2100	1.0 ± 0.3 (0.6, 1.4)	2.0 ± 0.4 (1.4, 2.6)	3.1 ± 0.6 (2.1, 4.1)	3.9 ± 0.8 (2.6, 5.3)
Arctic :	2081–2100	3.4 ± 1.8 (0.5, 6.4)	5.9 ± 2.2 (2.3, 9.5)	8.8 ± 2.5 (4.7, 12.8)	10.6 ± 2.8 (6.0, 15.2)

Antarctic: 2081-2100	1.4 ± 0.4 (0.8, 2.0)	2.4 ± 0.4 (1.7, 3.0)	3.6 ± 0.5 (2.8, 4.4)	4.4 ± 1.0 (2.8, 6.0

[END TABLE 4.2 HERE]

Based on results from the five CMIP6 models, we note that there is unanimity across all of the available model simulations that GSAT change relative to pre-industrial (1850–1900) will rise above: 1) 1.5°C following any of the priority SSPs (on average around 2025); 2) 2.0°C following either SSP2-4.5, SSP3-7.0, or SSP5-8.5 (on average around 2040), and 3) 3.0°C following either SSP3-7.0 or SSP5-8.5 (on average around 2061). In summary, we conclude that it is *very likely* that within the near-term (2021–2040) or mid-term (2041–2060), global temperature rise will exceed 1.5°C relative to pre-industrial under all of the priority SSPs, above 2.0°C under most of the priority SSPs, and above 3.0°C under the highest forcing scenarios (*medium confidence* because of the limited number of models available).

Here, we will also assess the main sources of uncertainty in 21st century GSAT projections, including the relative importance of internal variability, model response uncertainty, and scenario uncertainty (as introduced in Subsection 4.2.5). Context will be provided by the assessment of equilibrium climate sensitivity (ECS) and transient climate response (TCR) in Chapter 7. In our concluding paragraph, we will compare and contrast the AR5/CMIP5 and AR6/CMIP6 assessments of simulations of projected GSAT change.

4.3.1.2 Precipitation

The AR5 assessed from the CMIP5 simulations that it would be *virtually certain* that global mean precipitation will increase by more than 0.05 mm day^{-1} (about 2% of global precipitation) and 0.15 mm day^{-1} (about 5% of global precipitation) by the end of the 21st century under the RCP2.6 and RCP8.5 scenarios, respectively (Collins et al., 2013). The AR5 also assessed that global mean precipitation will *likely* increase at a rate per degree Celsius in the range of 1–3% °C^{-1} for scenarios other than RCP2.6. For RCP2.6 in the CMIP5 models the range was 0.5– 4% °C^{-1} at the end of the 21st century.

Unlike the AR5, our focus here is on land rather than global precipitation because land precipitation has greater societal relevance. As with GSAT we show from each CMIP6 model one historical realization from 1950 to 2014 and one scenario realization from 2015 to 2100 for each priority SSP. These are displayed as anomalies relative to 1995–2014 (see Figure 4.1:). In tabular form we show the 5–95% range of global precipitation anomalies relative to 1995–2014 averaged over 2021–2040 (near-term), 2041–2060 (mid-term) and 2081–2100 (long-term) for each priority SSP. Based on results from the five models that have thus far contributed precipitation information to the CMIP6 exercise, we conclude it is *very likely* that global land precipitation will be larger during the period 2081–2100 than during the period 1995–2014, under all scenarios considered here (see Table 4.3:). We show global land precipitation anomalies when GSAT rise exceeds 1.5°C, 2.0°C, and 3.0°C relative to pre-industrial, indicating the percentage of simulations for which each exceedance is true (Table 4.3:). We will also contrast the AR5/CMIP5 and AR6/CMIP6 assessments of simulations of projected global precipitation change in absolute terms, and in relation to the rate of increase in GSAT.

[START TABLE 4.3 HERE]

Table 4.3: CMIP6 annual land precipitation anomalies (mm day^{-1}) relative to averages over 1995–2014 for selected future periods, regions and SSPs. The multi-model mean ±1 standard deviation ranges across the individual models are listed and the 5 to 95% ranges from the models' distribution (based on a Gaussian assumption and obtained by multiplying the CMIP6 ensemble standard deviation by 1.64) are given in brackets. Also shown are land precipitation anomalies at the time when global temperature rise exceeds 1.5°C, 2.0°C, and 3.0°C, and the percentage of simulations for which such exceedances are true. The values tabulated here are for single simulations from the five models that have thus far contributed to the

CMIP6 exercise. The models are BCC-CSM2-MR, CanESM5, CNRM-CM6-1, IPSL-CM6A-LR, and MRI-ESM2-0. Eventually this table will be updated using single simulations from the full CMIP6 ensemble.

		SSP1-2.6 (mm day^{-1})	SSP2-4.5 (mm day^{-1})	SSP3-7.0 (mm day^{-1})	SSP5-8.5 (mm day^{-1})
Land :	2021–2040	0.05 ± 0.04 (-0.02, 0.12)	0.04 ± 0.04 (-0.03, 0.10)	0.03 ± 0.04 (-0.04, 0.09)	0.05 ± 0.05 (-0.03, 0.13)
	2041–2060	0.07 ± 0.05 (-0.02, 0.16)	0.07 ± 0.05 (-0.01, 0.14)	0.07 ± 0.05 (-0.02, 0.15)	0.09 ± 0.06 (0.00, 0.18)
	2081–2100	0.08 ± 0.05 (-0.01, 0.17)	0.12 ± 0.07 (0.00, 0.23)	0.15 ± 0.07 (0.03, 0.26)	0.19 ± 0.09 (0.05, 0.34)
Land :	ΔT > 1.5°C	0.03 ± 0.02 (100%)	0.03 ± 0.01 (100%)	0.02 ± 0.01 (100%)	0.02 ± 0.02 (100%)
	ΔT > 2.0°C	0.05 ± 0.01 (60%)	0.04 ± 0.02 (100%)	0.04 ± 0.02 (100%)	0.06 ± 0.02 (100%)
	ΔT > 3.0°C	------ (0%)	0.09 ± 0.03 (60%)	0.08 ± 0.02 (100%)	0.09 ± 0.03 (100%)
Global :	2081–2100	0.09 ± 0.03 (0.04, 0.14)	0.13 ± 0.04 (0.06, 0.20)	0.16 ± 0.04 (0.09, 0.23)	0.21 ± 0.07 (0.10, 0.32)
Ocean :	2081–2100	0.09 ± 0.03 (0.04, 0.14)	0.14 ± 0.04 (0.07, 0.20)	0.17 ± 0.05 (0.09, 0.25)	0.22 ± 0.07 (0.11, 0.33)

[END TABLE 4.3 HERE]

We also compare and contrast the time-evolving anomalies of precipitation for the Northern Hemisphere (NH) extratropics (30°N–90°N) and the tropics (30°S–30°N) from 1950–2100 (see Figure 4.2:). We will highlight the different precipitation regimes projected for these two regions, which will underpin the detailed pattern analyses in subsequent sections of this chapter.

[START FIGURE 4.2 HERE]

Figure 4.2: Annual mean precipitation changes from historical and scenario simulations. (a) Northern Hemisphere (NH) extratropics (30°N–90°N). (b) North Atlantic (NAT) subtropics (5°N–30°N, 80°W–0°). Changes are relative to averages from 1995–2014. The number inside panel indicates the total number of models used. The curves here are for single simulations from the five CMIP 6 models including BCC-CSM2-MR, CanESM5, CNRM-CM6-1, IPSL-CM6A-LR, and MRI-ESM2-0. Eventually this figure will be updated using single simulations from the full CMIP6 ensemble plotted as ensemble means with shaded uncertainties.

[END FIGURE 4.2 HERE]

4.3.2 Cryosphere, Ocean, and Biosphere

4.3.2.1 Arctic Sea Ice

The AR5 assessed from the CMIP5 simulations that there will be year-round reductions of Arctic sea ice coverage by the end of this century (Collins et al., 2013). These range from between 43% for RCP2.6 and 94% for RCP8.5 in September, and from between 8% for RCP2.6 and 34% for RCP8.5 in March (*medium confidence*). Based on a five-member selection of CMIP5 models, the AR5 further assessed that for RCP8.5, Arctic sea-ice coverage in September will drop below 1 million km^2 at some point between 2040 and 2060.

With regards to the model selection in the AR5, model evaluation studies have since identified shortcomings of the CMIP5 models to match the observed distribution of sea-ice thickness in the Arctic (Shu et al., 2015; Stroeve et al., 2014) and the observed evolution of albedo on seasonal scales (Koenigk et al., 2014). It was also found that many models' deviation from observed sea ice cover climatology cannot be explained by internal variability, whereas the models' deviation from observed sea ice cover trend (over the satellite period) can often be explained by internal variability (Olonscheck and Notz, 2017). This hinders a selection of models according to their simulated trends, which additionally has been shown to only have a weak impact on the quality of simulated future trends (Stroeve and Notz, 2015). In our assessment of the CMIP6 models, we will consider one realization from each available model, possibly without subsetting or weighting.

Here, we show from each CMIP6 model, one historical realization of September Arctic SIA from 1950–2014 and one scenario realization from 2015–2100 for each priority SSP (see Figure 4.1:). In tabular form we will show the 5–95% range of September and March Arctic SIA averaged over 2021–2040 (near-term), 2041–2060 (mid-term) and 2081–2100 (long-term) for each priority SSP (see Table 4.4:). The Arctic is considered ice-free with coverage below 1 million km^2. For the three models that have so far contributed sea-ice variables as part of the CMIP6 exercise (CanESM5, CNRM-CM6, and IPSL-CM6A-LR), we conclude that it is *very likely* that following any one of the priority SSPs, the Arctic will become effectively permanently ice-free in September by the end of the 21st century (*low confidence* because of the very limited number of CMIP6 simulations currently available).

[START TABLE 4.4 HERE]

Table 4.4: CMIP6 Arctic sea ice area for selected months, time periods, and across the four priority SSPs. The multi-model mean ±1 standard deviation range across the individual models are listed and the 5 to 95% ranges from the models' distribution (based on a Gaussian assumption and obtained by multiplying the CMIP6 ensemble standard deviation by 1.64) are given in parentheses. One ensemble member is used from each model and the number of models differs for each SSP. Presently, this table is empty because only three models have so far contributed sea-ice variables to the CMIP6 exercise. Eventually, this table will be filled using the full CMIP6 ensemble.

	SSP1-2.6 (10^6 km^2)	**SSP2-4.5 (10^6 km^2)**	**SSP3-7.0 (10^6 km^2)**	**SSP5-8.5 (10^6 km^2)**
September : 2021–2040				
2041–2060				
2081–2100				
March : 2021–2040				
2041–2060				
2081–2100				

[END TABLE 4.4 HERE]

Studies focusing on the relationship of sea ice cover and changes in the external drivers have consistently found a much-reduced likelihood of a near ice-free Arctic Ocean during summer for a global warming compared to pre-industrial levels of 1.5°C compared to 2.0°C (Jahn, 2018; Niederdrenk and Notz, 2018; Notz and Stroeve, 2018; Screen and Williamson, 2017; Sigmond et al., 2018). This is shown here in a large initial-condition ensemble of observationally-constrained model simulations where global mean surface temperatures are stabilized at 1.5°C, 2.0°C and 3.0°C warming relative to pre-industrial in the RCP8.5 scenario (see Figure 4.3:). In these simulations, Arctic sea ice coverage in September is simulated, on average, to drop below 1 million km^2 around 2040, consistent with the AR5 models as a group (Sigmond et al., 2018). The individual model simulations, for which there are twenty for each stabilized temperature level, show that the probability of the Arctic becoming ice free (i.e. with area less than 1 million km^2) at the end of the 21st century is significantly higher for 2°C warming than for 1.5°C warming above pre-industrial levels. Estimates, such as these are possibly conservative, as they neglect the possible future reduction in atmospheric aerosol load, which models suggest will contribute to additional future sea-ice loss (Gagné et al., 2015; Wang et al., 2018b).

[START FIGURE 4.3 HERE]

Figure 4.3: Arctic sea ice extent in September in a large initial-condition ensemble of observationally-constrained simulations of an Earth System Model (CanESM2). The black curve is the average over twenty simulations following historical forcings to 2015 and RCP8.5 extensions to 2100. The coloured curves are averages over twenty simulations after GSAT has been stabilized at the indicated degrees of warming relative to preindustrial. The coloured circles on the right are individual values at 2100. On an individual simulation basis, the probability of the Arctic becoming ice free (i.e. with less than 1 million km^2 coverage) is significantly higher for 2°C warming than for 1.5°C warming (Sigmond et al., 2018).

[END FIGURE 4.3 HERE]

4.3.2.2 Sea Level

The AR5 assessed from CMIP5 process-based simulations that it is *very likely* that the rate of global mean sea level (GMSL) rise during the 21st century will exceed the rate observed during 1971–2010 for all RCP scenarios due to increases in ocean warming and loss of mass from glaciers and ice sheets (Church et al., 2013). Further, the AR5 concluded that for the period 2081–2100, compared to 1986–2005, GMSL rise is *likely* (*medium confidence*) to be in the 5–95% range of projections from process-based models, which give 0.26–0.55 m for RCP2.6, 0.32–0.63 m for RCP4.5, 0.33–0.63 m for RCP6.0, and 0.45–0.82 m for RCP8.5. For RCP8.5, the rise by 2100 is 0.52–0.98 m with a rate during 2081–2100 of 8–16 mm yr^{-1}.

There have been significant modelling advances since the AR5, including the development of semi-empirical models (SEMs) into a broader emulation-based approach (Kopp et al., 2014; Mengel et al., 2016; Nauels et al., 2017) that is partially based on the results from more detailed process-based modelling. A *low confidence* was assigned to SEMs because these models assume that the relation between climate forcing and GMSL is the same in the past and future (Church et al., 2013). Probable future changes in the relative contributions of thermal expansion, glaciers and ice sheets (in particular) invalidate this assumption. However, more recent emulation-based studies have overcome this shortcoming by considering GMSL contributors separately, and they will therefore be employed in this assessment.

Here, we show from each CMIP6 model, one historical realization of annual-mean GMSL from 1950–2014 and one scenario realization from 2015–2100 for each priority SSP (see Figure 4.1:). These are displayed as anomalies relative to 1995–2014, and based on contributions to GMSL rise from thermal expansion alone. For the three models that have so far contributed global sea level as part of the CMIP6 exercise (CanESM5, CNRM-CM6-1, and IPSL-CM6A-LR), thermosteric global sea level rises from present to the end of the 21st century by about 0.15 m under SSP1-2.6 (taken as the minimum rise across the three models) to a maximum of about 0.45 m under SSP5-8.5 (taken as the maximum rise between the three models) (see Figure 4.1:). We conclude that it is *very likely* that under any one of the priority SSPs, there will be monotonic rise in global sea level through the end of the 21st century (*low confidence* because of the very limited number of models available).

We will tabulate the different contributions to future GMSL change (coordinated with Chapter 9), such as thermal expansion and melt from glaciers and ice sheets (see Table 4.5:). We will also summarize and update the key findings on projected GMSL rise from the SR1.5 and the Special Report on Ocean and Cryosphere in a Changing Climate (SROCC).

[START TABLE 4.5 HERE]

Table 4.5: CMIP6 annual mean global sea level anomalies (m) from the 1995–2014 reference period for selected time periods, regions and SSPs. The multi-model mean ±1 standard deviation ranges across the individual models are listed and the 5–95% ranges from the models' distribution (based on a Gaussian assumption

and obtained by multiplying the CMIP6 ensemble standard deviation by 1.64) are given in brackets. Only one ensemble member is used from each model and the number of models differs for each SSP. Presently, this table is empty as only three models have so far contributed sea-level variables to the CMIP6 exercise. Eventually, this table will be filled using the full CMIP6 ensemble.

		SSP1-2.6 (m)	SSP2-4.5 (m)	SSP3-7.0 (m)	SSP5-8.5 (m)
Total :	2021–2040				
	2041–2060				
	2081–2100				
Steric :	2081–2100				
Glaciers :	2081–2100				
Ice sheets :	2081–2100				
Storage :	2081–2100				

[END TABLE 4.5 HERE]

4.3.2.3 Atlantic Meridional Overturning Circulation

The AR5 assessed from the CMIP5 simulations that it is *very likely* that the AMOC will weaken over the 21st century (Collins et al., 2013). Best estimates and ranges for the reduction from CMIP5 are 11% (1–24%) in RCP2.6 and 34% (12–54%) in RCP8.5. As assessed in the AR5, the projected weakening of the AMOC is consistent with CMIP5 projections of an increase of high-latitude temperature and high-latitude precipitation, with both effects causing the surface waters at high latitudes to become lighter and more stable.

Time series of CMIP6 projections of the AMOC strength at 30°N from 1850 through to the end of the priority SSP extensions will be shown in Chapter 9 of the AR6. Chapter 9 will also detail the physical understanding of the changes in the strength of the AMOC over this time period, including the projected weakening through the 21st century in most models and priority SSPs.

Here, we will assess the 5–95% of CMIP6 projections of the AMOC strength at 30°N averaged over 2081–2100 (long-term) for each priority SSP. We will also describe potential future evolutions of the AMOC in a large 50-member initial-condition ensembles of ESM (CanESM2) simulation where GMST is stabilized at 1.5°C, 2.0°C and 3.0°C warming relative to pre-industrial after following the RCP8.5 scenario (see Figure 4.4:). In this model, following the RCP8.5 scenario, the AMOC average over 2081–2100 is about 10% weaker than the average over 1995–2014 (i.e., 13.5 Sv down from 15.0 Sv). After temperature stabilization at 1.5°C and 2.0°C global warming above pre-industrial levels there is continued weakening for one to two decades, followed by strengthening. After temperature stabilization at 3.0°C warming, the AMOC strength plateaus for about two decades and then the AMOC begins to strengthen. Five-member extensions to 2600 indicate that under stabilization at either 1.5°C, 2.0°C and 3.0°C global warming, the strength of the AMOC recovers to less than its pre-industrial value (see Section 4.7).

[START FIGURE 4.4 HERE]

Figure 4.4: AMOC in large initial-condition ensembles of simulations of an Earth System Model (CanESM2). The black curve is the average over fifty simulations following historical forcings to 2005 and RCP8.5 extensions to 2100. The coloured curves are averages over fifty simulations (each) after GSAT has been stabilized at the indicated degree of warming relative to pre-industrial (Sigmond et al., 2018). The dashed lines indicate the AMOC strength at the point of emissions cessation.

[END FIGURE 4.4 HERE]

4.3.2.4 Cumulative ocean carbon uptake and pH

The AR5 assessed from the CMIP5 simulations that it is *virtually certain* that increasing storage of carbon by the ocean under all four RCPs through to 2100 will increase ocean acidification in the future (Ciais et al., 2013). Specifically, the AR5 reported that the CMIP5 models project increased ocean acidification globally to 2100 under all RCPs, and that the corresponding model-mean and model-spread in the decrease in surface ocean pH by the end of 21st century would be 0.065 (0.06–0.07) for RCP2.6, 0.145 (0.14–0.15) for RCP4.5, 0.203 (0.20–0.21) for RCP6.0 and 0.31 (0.30–0.32) for RCP8.5.

Here, we will show from each CMIP6 model one historical realization of cumulative ocean carbon uptake and pH from 1950 to 2014 and one scenario realization from 2015 to 2100 for each priority SSP (see Figure 4.5:). We will also assess the 5–95% ranges of cumulative ocean carbon uptake and pH averaged over 2081–2100 (long-term) for each priority SSP. For the two models that have so far contributed surface ocean carbon fluxes as part of the CMIP6 exercise (IPSL-CM6A-LR and CanESM5), cumulative ocean carbon uptake rises from 1850 to the end of the 21st century by about 250 PgC under SSP1-2.6 (taken as the minimum rise across the two models) to a maximum of about 600 PgC under SSP5-8.5 (taken as the maximum rise between the two models; Figure 4.5:). In the one model that has so far contributed surface pH as part of the CMIP6 exercise (IPSL-CM6A-LR), ocean carbon uptake translates into increasing surface acidity. We conclude that it is *very likely* that under any one of the priority SSPs, there will be a monotonic rise in cumulative ocean carbon uptake and ocean acidification through the end of the 21st century (*medium confidence* because of the very limited number of models available).

[START FIGURE 4.5 HERE]

Figure 4.5: Cumulative ocean carbon uptake and surface pH from historical and scenario simulations. (a) Cumulative ocean carbon uptake since 1850. (b) Surface pH. The curves plotted here are for single simulations from (a) two CMIP6 models (IPSL-CM6A-LR and CanESM5) and (b) one model (IPSL-CM6A-LR). Eventually the figure will be updated using single simulations from the full CMIP6 ensemble, plotted as ensemble means with shading.

[END FIGURE 4.5 HERE]

4.3.3 Modes of Variability

4.3.3.1 Northern and Southern Annular Modes

The NAM and SAM are the leading modes of climate variability in the NH and SH extratropics, respectively. They involve opposing fluctuations in sea level pressure (SLP) between about 40°N and 65°N (Li and Wang, 2003) and between 40°S and 65°S (Gong and Wang, 1999), respectively. These fluctuations reflect changes in the latitudinal position and strength of the mid-latitude westerly jets in both hemispheres. The AR5 assessed from CMIP5 simulations that the future boreal wintertime NAM is *very likely* to exhibit large natural variations and trend of similar magnitude to that observed in the past and is *likely* to become slightly more positive in the future (Collins et al., 2013). On the other hand, the positive trend in the austral summer SAM observed in the past is *likely* to weaken as stratospheric ozone recovers through the mid-21st century.

Here, we show from each CMIP6 model, one historical realization of boreal wintertime NAM and austral summertime SAM from 1950 to 2014 and one scenario realization from 2015 to 2100 for each priority SSP (see Figure 4.6:). We will also compare and assess the salient features of the 5–95% ranges of the NAM and SAM anomalies averaged over 2021–2040 (near-term), 2041–2060 (mid-term) and 2081–2100 (long-term) for each priority SSP. Based on results from the five CMIP6 models, we conclude that future boreal wintertime NAM is *very likely* to become slightly more positive in the future under SSP5-8.5, and that the SAM is *likely* to weaken under all of the priority SSPs as stratospheric ozone recovers through the mid-21st century (see Figure 4.6:; *medium confidence* because of the limited number of models available).

[START FIGURE 4.6 HERE]

Figure 4.6: Simulations of boreal wintertime Annular Mode indices: (a) NAM and (b) SAM. The NAM is defined as the difference in zonal mean SLP at 35°N and 65°N (Li and Wang, 2003) and the SAM as the difference in zonal mean SLP at 40°S and 65°S (Gong and Wang, 1999). All anomalies are relative to averages from 1850 to 1900. The curves here are for single simulations from the five CMIP6 models that are BCC-CSM2-MR, CanESM5, CNRM-CM6-1, IPSL-CM6A-LR, and MRI-ESM2-0. Eventually this figure will be updated using single simulations from the full CMIP6 ensemble, and ensemble means and shaded uncertainties will be displayed.

[END FIGURE 4.6 HERE]

4.3.3.2 El Niño-Southern Oscillation

The El Niño-Southern Oscillation (ENSO) reflects quasi-periodic fluctuations in the wind and SST over the tropical central to eastern Pacific, affecting much of the tropics, subtropics, and beyond. El Niño and La Niña refer to periods of anomalously warm and cold SST in the equatorial central to eastern Pacific, respectively. The AR5 assessed from CMIP5 simulations that ENSO variability will continue in the future and that associated precipitation variability on regional scales is likely to intensify (Collins et al., 2013). However, confidence in CMIP5 projected changes in ENSO variability itself in the 21st century is low due to a strong component of natural internal variability.

Here, we consider the evolution of the amplitude of ENSO variability projected by the five CMIP6 models over the 21st century. The Niño 3.4 index represents the average equatorial SST across the Pacific from about the dateline to the South American coast (5°S–5°N, 170°W–120°W). The amplitude of ENSO is defined by the standard deviation of the monthly Niño 3.4 index after removing the climatological monthly mean and long-term trend. Here, we display the amplitude of the simulated ENSO variability for maximally overlapping 50-year periods from 1950 to 2100. Results from the five models that have thus far contributed to the CMIP6 exercise suggest increasing and then decreasing ENSO variability over the period from 1950 to 2100 in the SSP1-2.6 (Figure 4.7:) and SSP2-4.5 (not shown). This is consistent with findings from a subset of CMIP5 model simulations following the RCP2.6 and 8.5 scenarios (Kim et al., 2014b). However, there is no robust change in the ENSO amplitude during the latter half of the 21st century in the SSP3-7.0 (not shown) and SSP5-8.5 scenarios (Figure 4.7:) obtained from five CMIP6 models. Based on results from the five models, we conclude that ENSO variability is *likely* to weaken under the SSP1-2.6 and SSP2-4.5 beginning in the near-term (2021–2040) while there is no consensus on the ENSO variability change in the SSP3-7.0 and SSP5-8.5 scenarios (see Figure 4.7:; *low confidence* because of the limited number of models available).

[START FIGURE 4.7 HERE]

Figure 4.7: Historical simulation and future projection of the amplitude of the ENSO under (a) SSP1-2.6 and (b) SSP5-8.5. The amplitude is defined as the standard deviation of the monthly Niño 3.4 index after removing climatological monthly mean and long-term trend. The amplitude is shown for maximally-overlapping fifty-year periods with the end-year shown on the horizontal axis. The thick curves are the mean of individual model's ENSO amplitude. The curves here are for single simulations from the five CMIP6 models that are BCC-CSM2-MR, CanESM5, CNRM-CM6-1, IPSL-CM6A-LR, and MRI-ESM2-0. Eventually this figure will be updated using single simulations from the full CMIP6 ensemble, and ensemble means and shaded uncertainties will be displayed.

[END FIGURE 4.7 HERE]

4.4 Near-term Global Climate Changes

In this section we present the raw CMIP6 range of near-term projections along with a range of observational estimates of the most recent past (Figure 4.8:). The sensitivity of that range to the choice of reference period (Hawkins and Sutton, 2016) will be assessed, together with the influence of internal variability on the estimated range and in comparison with observational estimates (Marotzke and Forster, 2015). The section will further assess the recent literature on producing calibrated projection ranges for the near future based on initialized predictions (Marotzke et al., 2016; Meehl et al., 2014), D&A results (Stott et al., 2013; Stott and Jones, 2012), and potential model weighting (BOX 4.1:, Abramowitz et al., 2019).

4.4.1 Atmosphere

4.4.1.1 Global Surface Air Temperature

We will assess how the GSAT is projected to evolve over the near-term period under different SSPs. The AR5 showed that the near-term GSAT is relatively insensitive to the particular RCP emissions scenario. Here we will assess whether this result is robust under different SSP scenarios, and we will quantify the relative roles of different scenarios – reflecting various levels of mitigation – and internal variability in influencing near-term GMST change. As a result, we will be able to assess the likelihood of exceeding 1.5°C and 2°C global warming above pre-industrial levels, respectively, during the near term and under a given scenario (e.g., Smith et al., 2018). This assessment will be influenced by the uncertainty in the different observational datasets over the historical period that form the baselines for the near-term changes.

Then we will assess the relative contributions of different external forcings on GSAT change. Changes in GSAT can be attributed to variations in external climatic forcing, such as volcanic eruptions or aerosol and GHG emissions.

[START FIGURE 4.8 HERE]

Figure 4.8: Projections and predictions of global-mean annual-mean surface air temperature, referenced to 1850–1900. The figure shows for 1995–2040 one CMIP6-forced simulation each with BCC-CSM2-MR (cyan), CanESM5 (light green), IPSL-CM6A-LR (yellow), MRI-ESM2-0 (light purple), and UKESM1 (ochre); and GSAT simulated with an emulator driven by the AR5 radiative forcing, using RCP4.5 from the WGI AR5 Annex II after 2005 (black). The emulator is a two-layer time-dependent energy-balance model (EBM) following (Held et al., 2010), with ocean heat uptake efficiency $\kappa = 0.8$ W m^{-2} °C^{-1} and efficacy 1.0. Results are shown for ECS = 2.5°C and 3.5°C, the lower and upper limits, respectively, of the Chapter 7 ECS *likely* range (solid black), as well as for 2°C and 5°C, the lower and upper limits, respectively, of the Chapter 7 ECS *very likely* range (dashed black). For the historical period, all panels show the observations (HadCRUT4, (Morice et al., 2012), red) and the CMIP5-forced simulations from the 100-member Max Planck Institute Grand Ensemble (MPI-GE, (Maher et al., 2019), dark blue for ensemble mean, light blue for individual realizations), For the years 2019–2028, the initialized-prediction ensemble from the CMIP6 model MPI-ESM-HR (Müller et al., 2018) is shown (dark purple), produced through the MiKlip project (Marotzke et al., 2016) and contributing to DCPP (Boer et al., 2016). The MiKlip results are drift-removed and referenced to the time-averaged hindcasts for 1995–2014 lead-year by lead-year; then the HadCRUT4 difference between the means over 1995–2014 and 1850–1900 is added. [Placeholder figure, copied from Box 4.1, Figure 1, bottom right; to be updated with the full CMIP6 ensemble and CMIP6/AR6/SSP forcing for the EBM.]

[END FIGURE 4.8 HERE]

We will further assess different published methods of estimating the probability of a zero trend (hiatus, see also Cross-Chapter Box 3.1) depending on the time horizon and scenario (Fyfe et al., 2013; Marotzke and Forster, 2015), as well as the probability of experiencing accelerated GSAT increase despite falling emissions (Marotzke, 2019). Finally, this section will assess the literature to what extent differences in SSPs can be detected in near-term projections of GSAT.

4.4.1.2 Spatial Patterns of Surface Warming

Figure 4.9: shows maps of seasonal mean surface air temperature changes in the near-term (2021–2040) in the SSP1-2.6 and SSP5-8.5 scenarios. Consistent with the findings of the AR5 and earlier assessments, these show the largest warming occurs at high latitudes, particularly in winter in the Arctic (see Section 4.5.1.1), and larger warming over land than over the oceans in both winter and summer seasons (see also Section 4.5.1.1). In both scenarios, the increase in seasonal mean surface temperatures over many NH land regions exceeds 1°C relative to 1995–2014. In the near-term, the two scenarios show surface temperature changes that are similar in magnitude. The projected trajectories for well-mixed GHGs, and as a consequence the effective radiative forcing, in the scenarios has not yet diverged that much (O'Neill et al., 2016; Riahi et al., 2017). Based on the currently available CMIP6 models, regions that do not show significant warming in the near-term include the northern North Atlantic, India, parts of North America and Eurasia in winter, and the subtropical eastern Pacific. These regional aspects will be evaluated and assessed in detail as results from more CMIP6 models become available.

The pattern of effective radiative forcing (ERF) from aerosols is distinct from that for well-mixed GHGs (Chapter 7). When comparing scenarios, one question therefore concerns the dependence of patterns of near-surface warming on the precise mix of forcing agents in the scenarios. The spatial efficacies – the change in surface temperature per unit ERF – for CO_2, sulphate and black carbon aerosols and solar forcing have been recently evaluated in a set of climate models (Richardson et al., 2019). It has been found that, on average, the spatial patterns of near-surface warming are largely similar for different external drivers (Samset et al., 2018b; Xie et al., 2013), despite the patterns of forcing being different, but there is large spread across different models (Richardson et al., 2019) .

Internal variability in near-surface temperature change is large in many regions, particularly in mid-latitudes and polar regions (Hawkins and Sutton, 2012). Projections from individual realizations can therefore show divergent regional responses in the near-term in areas where the amplitude of a forced signal is relatively small compared to internal variability (Deser et al., 2012b, 2014, 2016).

[START FIGURE 4.9 HERE]

Figure 4.9: CMIP6 multi-model mean change (°C) in (top) DJF and (bottom) JJA near-surface air temperature in 2021–2040 from SSP1-2.6 and SSP5-8.5 relative to 1995–2014 [Figure produced with ESMValTool (Eyring et al., 2016b) based on the five CMIP6 models: BCC-CSM2-MR, CanESM5, CNRM-CM6-1, IPSL-CM6A-LR, and MRI-ESM2-0. Figure will be updated with more CMIP6 models]

[END FIGURE 4.9 HERE]

4.4.1.3 Precipitation

The AR5 projections of the spatial patterns of precipitation change in the near-term showed consistency between models on the largest scales with zonal mean precipitation will *very likely* increase in high and some of the mid latitudes, and will *more likely than not* decrease in the subtropics. Similar to the AR5 pattern, projected changes in the near-term from five CMIP6 models (based on available CMIP6 model projections) showed *very likely* increase at high latitudes and in wet regions and decrease in dry regions (including large parts of the subtropics), as presented in Figure 4.10:. Precipitation changes are robust mainly at high latitudes; larger uncertainty is seen especially in regions located on the borders between regions of increases and regions of decreases. Much of the non-robustness is attributable to natural internal variability (Deser et al., 2012b; Hawkins and Sutton, 2011, 2016; Hoerling et al., 2011; Power et al., 2012). The AR5 assessment indicated that the magnitude of projected changes in mean precipitation in the near-term is considerably small compared to the magnitude of natural internal variability. Considering the uncertainty in near-term projections, internal variability contributes to more than 80% of total uncertainty in precipitation in the first decades and remained more than 50% at the end of the century (Hingray and Saïd, 2014). Based on large ensembles of climate change experiments, it was shown that on regional scales, anthropogenic changes in decadal precipitation mean state are distinguishable, outside the range expected from natural variability (Zhang and Delworth, 2018). The other sources of uncertainty, model uncertainty and scenario uncertainty, are generally small compared to internal variability.

[START FIGURE 4.10 HERE]

Figure 4.10: CMIP6 multi-model mean change (%) in (top) DJF and (bottom) JJA precipitation in 2021–2040 from SSP1-2.6 and SSP5-8.5 relative to 1995–2014 [Figure produced with ESMValTool (Eyring et al., 2016b) based on the five CMIP6 models: BCC-CSM2-MR, CanESM5, CNRM-CM6-1, IPSL-CM6A-LR, and MRI-ESM2-0. Figure will be updated with more CMIP6 models. Figure will be updated with more CMIP6 models]

[END FIGURE 4.10 HERE]

There has been considerable progress in understanding the factors contributing to changes in patterns of precipitation. Precipitation changes were interpreted as a wet-get-wetter and dry-get-drier pattern with a moistening trend in high latitudes and tropics and a drying trend in subtropics to middle latitudes (Held and Soden, 2006). Recent studies suggest that the dry-get-drier argument might not hold, because reduced precipitation appears along the outer flanks of the subtropics due to the poleward expansion of the subtropical dry zones (Scheff and Frierson, 2012). Large-scale circulation changes associated with expansion of the Hadley cell extend subtropical dry zones poleward, and a poleward displacement in storm tracks contributes to subtropical drying and moistening poleward regions (Scheff and Frierson, 2012). Studies have also indicated that precipitation response in the subtropics is also driven by the fast adjustment to CO_2 forcing, including land-sea warming contrast and direct CO_2 radiative forcing (He and Soden, 2017). In the tropics, a weakening of the circulation leads to a wet-gets-drier and dry-gets-wetter pattern (Chadwick et al., 2013). Factors governing changes in large-scale precipitation patterns are discussed in detail in Chapter 8.

Precipitation changes are determined by the increased moisture flux along with changes in atmospheric circulation. The sensitivity of global precipitation change is smaller (2% $°C^{-1}$) as compared to the sensitivity of water vapour concentration change (7% $°C^{-1}$). Reduced convective mass flux as part of weakening atmospheric circulation strength is one way in which the atmosphere adjusts in reconciling the water vapour and precipitation changes (Bony et al., 2013; Vecchi and Soden, 2007).

In the tropics, climate model agreement for precipitation change is lower than for other regions, with large areas of little model consensus on the sign and magnitude of change (Knutti et al., 2013b; McSweeney and Jones, 2013). Sources of inter-model uncertainty in regional tropical rainfall projections arise from circulation changes (Chadwick, 2016; Kent et al., 2015), SST pattern uncertainty over the tropical oceans and over land, and the response to uniform SST warming, with a secondary contribution from the response to direct CO_2 forcing (Chadwick, 2016).

In addition to the response to GHG forcing, forcing from natural and anthropogenic aerosols exert impacts on regional patterns of precipitation change (Bollasina et al., 2011; Krishnan et al., 2016; Liu et al., 2018a; Polson et al., 2014; Ramanathan et al., 2005). In contrast to the GHG changes, aerosol changes induce a drying in the SH tropical band compensated by wetter conditions in the NH counterpart (Acosta Navarro et al., 2017). The spatially uneven distribution of the aerosol forcing may also induce changes in tropical precipitation caused by shifts in the mean location of the intertropical convergence zone (ITCZ) (Hwang et al., 2013; Ridley et al., 2015; Voigt et al., 2017). Because of the large uncertainty in the aerosol forcing, there is *low to medium confidence* in the impacts of aerosols on projected changes in precipitation.

4.4.1.4 Global Monsoon Precipitation and Circulation

The global monsoon (GM) as a system comprises a hierarchy of regional and local monsoons, including the Asian-Australian monsoon, the African monsoon, and the American monsoon. The GM concept helps to dissect the mechanisms and controlling factors of monsoon variability at various temporal-spatial scales (Wang et al., 2017c; Wang and Ding, 2008). In the AR5, there was no specific assessment on global monsoon changes in the near term, but information can be derived from the AR5 projections of the spatial patterns of precipitation change. While the basic pattern of wet regions including global monsoon regions tending to get wetter and dry regions tending to get dryer is apparent, large response uncertainty is evident in the substantial spread in the magnitude of projected change simulated by different climate models, highlighting the large amplitude of the natural internal variability of mean precipitation. Over the global land monsoon regions, mean projected precipitation changes are almost everywhere smaller than the estimated standard deviation of natural internal variability.

Since the AR5 there has been considerable progress in understanding the factors that affect the decadal changes of GM. Decadal variability of the GM precipitation from 1901 to 2014, in particular over the Northern Hemisphere (NH), is rooted primarily in the north-south hemispheric thermal contrast modulated by the phase of AMV and an east-west thermal contrast in the Pacific modulated by the Interdecadal Pacific Oscillation (IPO) (Wang et al., 2018a). The GM precipitation has shown an enhanced trend during the satellite era (Lin et al., 2014), and can be explained by the phase change of AMV (Deng et al., 2018; Wang et al., 2013). It is suggested that both IPO and AMV should contribute to noise (irreducible uncertainty) in climate projections. Since the forcing uncertainty is generally negligible for near-term projections, internal variability including the contributions of IPO and AMV is the most important source of uncertainty for global monsoon projection. [Note: This part will assess the contribution of forcing uncertainty, model uncertainty, and internal variability to GM land precipitation and circulation changes, to be updated with CMIP6 data].

The boreal summer monsoon precipitation is projected in the near-term and in the multi-model mean to increase in the South Asian monsoon area, East Asian monsoon area, and part of the West African monsoon area (Figure 4.10:). A decrease of precipitation is projected in the multi-model mean in the Australian monsoon area (Figure 4.10:). The projected changes of precipitation in North and South American monsoon regions, and South African monsoon area are not significant. The global land monsoon precipitation index, defined as the accumulated precipitation falling in the global land monsoon domain, tends to increase in all priority SSPs (Figure 4.11:). The tropical monsoon circulation index, defined as the vertical shear of zonal winds between 850 and 200 hPa averaged in a zone stretching from Mexico eastward to the Philippines (0°–20°N, 120°W–120°E), tends to decrease associated with the weak increase of monsoon precipitation under four scenarios (Figure 4.12:). The projected changes of both monsoon precipitation and circulation are weak relative to natural variability and statistically insignificant. [To be updated based on the availability of new CMIP6 data].

[START FIGURE 4.11 HERE]

Figure 4.11: Changes of global land monsoon precipitation index (defined as the accumulated precipitation falling in the global land monsoon domain as defined by (Wang et al., 2013) in the historical climate simulation and four SSPs projections of five CMIP6 (BCC-CSM2-MR, CanESM5, CNRM-CM6-1, IPSL-CM6A-LR, MRI-ESM2-0) models. Each line in each SSP represents one model realization. Anomalies are relative to the 1995–2014 mean. Time series are normalized by climate mean values and smoothed with a 20-yr running-mean filter (Unit: %). Eventually this figure will be updated using single simulations from the full CMIP6 models, plotted as multi-model ensemble with shading of model spread.

[END FIGURE 4.11 HERE]

[START FIGURE 4.12 HERE]

Figure 4.12: Changes of tropical monsoon circulation index (defined as the vertical shear of zonal winds between 850 and 200 hPa averaged in a zone stretching from Mexico eastward to the Philippines (0°–20°N, 120°W–120°E) (Wang et al., 2013)in the historical climate simulation and two SSPs projection of five CMIP6 (BCC-CSM2-MR, CanESM5, CNRM-CM6-1, IPSL-CM6A-LR, MRI-ESM2-0). Each line in each SSP represents one model realization. Anomalies are relative to the 1995–2014 mean. Anomalies are relative to the 1995–2014 mean. Time series are smoothed with a 20-yr running-mean filter (Unit: m/s). Eventually this figure will be updated using single simulations from the full CMIP6 models, plotted as multi-model ensemble with shading of model spread.

[END FIGURE 4.12 HERE]

4.4.2 Cryosphere, Ocean, and Biosphere

4.4.2.1 Arctic Sea Ice

Since the AR5, there has been substantial progress in understanding the response of Arctic sea ice to changes in external forcing. In particular, it is *very likely* that different trajectories of the near-term evolution of anthropogenic forcing cause distinctly different likelihood ranges for very low sea-ice coverage to occur over the next two decades. This is most directly described in terms of the range of cumulative anthropogenic CO_2 emissions over the period 2020–2040, which ranges from around 500 Gt CO_2 in RCP2.6 to more than 1000 Gt CO_2 in RCP 8.5. This results in an *unlikely* drop of September Arctic sea-ice coverage to below 1 million km^2 before 2040 for RCP 2.6, and a *likely* drop of September Arctic sea-ice coverage to below 1 million km^2 before 2040 for RCP 8.5 (*medium confidence*), based on a single study (Notz and Stroeve, 2018) but consistent with estimates from temperature-based studies cited below. These estimates are derived from an observed loss of about 3 m^2 of September sea-ice area per tonne of CO_2 emissions (Notz and Stroeve, 2016) and an estimated internal variability of standard deviation < 0.5 million km^2 of September sea-ice coverage as given by CMIP5 simulations and the observational record (Notz and Marotzke, 2012; Olonscheck and Notz, 2017).

The much higher likelihood of a virtually sea-ice free Arctic Ocean during summer before 2040 in RCP8.5 compared to RCP2.6 is consistent with related studies that find a substantially increased likelihood of an ice-free Arctic Ocean for 2.0°C mean global warming relative to pre-industrial levels compared to 1.5°C mean global warming relative to pre-industrial levels (Jahn, 2018; Niederdrenk and Notz, 2018; Screen and Williamson, 2017; Sigmond et al., 2018).

Here, we will consider the range of September Arctic sea ice cover trends for all 10-year and 20-year periods ending in the near-term (2021–2040). Despite the substantial importance of anthropogenic forcing on the evolution of Arctic sea-ice cover, internal variability may mask its impact over the near-term. Here, an ensemble of simulations from one CMIP6 model, CanESM5, suggests that under all four SSP scenarios there is a significant chance of positive 10-year trends ending in the near-term (see Figure 4.13:). In this CMIP6 model, known for its high climate sensitivity, all 20-years trends are negative (see Figure 4.13:). For either 10- or 20-year periods ending in the near-term, the median trend is negative across all priority SSPs.

[START FIGURE 4.13 HERE]

Figure 4.13: September Arctic sea ice area trends for periods ending in the near-term period from 2021–2040 following the various priority SSPs. (a) 10-year periods. (b) 20-year periods. Plotted are the minimum and maximum trends, the lower and higher trend quartiles and the median trend. The percentage of positive trend values is indicated to the right of the maximum value. [The values plotted here are for 10 simulations from one CMIP6 model, CanESM5. Eventually the figure will be updated using single simulations from the full CMIP6 ensemble.]

[END FIGURE 4.13 HERE]

4.4.2.2 Ocean Carbon Uptake

Here we will follow a similar presentation as in the previous section, in that we will summarize the AR5 assessment of the CMIP5 simulations followed by an assessment of the CMIP6 simulations. Until the full CMIP6 ensemble is available we utilize a 10-member ensemble of simulations from one CMIP6 model, CanESM5. This CMIP6 model shows a much larger response in ocean carbon uptake over the near-term in the SSP5-8.5 forcing scenario than in the SSP1-2.6 forcing scenario (see Figure 4.14:). For 10-year trends ending in the near-term (2021–2040) following SSP1-2.6, equal numbers of trends in ocean carbon uptake are positive and negative.

[START FIGURE 4.14 HERE]

Figure 4.14: Annual-mean ocean carbon uptake trends for all periods ending in the near-term (2021–2040). (a) 10-year periods. (b) 20-year periods. Plotted are the minimum and maximum trends, the lower and higher trend quartiles and the median trend. The percentage of negative trend values is indicated to the left of the minimum value. [The values plotted here are for 10 simulations from on CMIP6 model, CanESM5. Eventually the figure will be updated using single simulations from the full CMIP6 ensemble.]

[END FIGURE 4.14 HERE]

4.4.3 Modes of Variability

In this sub-section the near-term evolution of the large-scale climate modes of variability and their associated teleconnections is assessed. Discussions of the physical mechanisms and the individual feedbacks involved in the future change of each mode are provided in Chapters 8–10.

4.4.3.1 Northern and Southern Annular Modes

The NAM and NAO

The NAM is the leading mode of climate variability in the NH extratropics. The NAM involves opposing fluctuations in sea level pressure (SLP) between about 40°N and 65°N (Li and Wang, 2003). A NAM index computed from the latitudinal gradient in SLP is strongly correlated with variations in the latitudinal position and strength of the mid-latitude westerly jets, and with the spatial distribution of Arctic sea ice (Caian et al., 2018).

The AR5 report elected to refer to the NAM, and its synonym the Arctic Oscillation (AO), through its regional counterpart the North Atlantic Oscillation (NAO). Here, we use the term NAM to refer also to the AO and NAO. Climate models were found to simulate the gross features of the NAM with reasonable fidelity. However, models underestimated the magnitude of the large positive trend in winter NAM observations over 1960–2000, and this was attributed more to natural variability than to anthropogenic influences. The AR5 reported that the underestimated trends in the NAM could be related to missing or poorly represented processes in climate models, including the representation of the stratosphere (Scaife et al., 2012).

The AR5 assessed from CMIP5 simulations that there is only *medium confidence* in near-term projections of a northward shift of NH storm track and westerlies, and an increase of the NAM because of the large response uncertainty and the potentially large influence of internal variability.

Significant progress has been made since the AR5 in understanding the physical mechanisms responsible for changes in the NAM, although large uncertainties remain. It is now clear from the literature that the NAM response, and the closely-related response of the mid-latitude storm tracks, to anthropogenic forcing in CMIP5-era climate models is determined by a "tug-of-war" between two opposite processes (Screen et al., 2018a). First, Arctic amplification (see Section 4.5.1.1) is associated with warming concentrated in the lower troposphere that initiates a chain of responses. The warming decreases the meridional temperature gradient, and reduces baroclinicity on the poleward flank of the eddy-driven jet, shifting the storm tracks equatorward and leading to a *negative* NAM (Hoskins and Woollings, 2015; Screen et al., 2018a). Second, warming in the tropical upper-troposphere, due to GHG increases and associated water vapour feedback, is expected to increase the meridional temperature gradient aloft, which tends to cause a poleward shift of baroclinicity in the northern extratropics, an associated poleward shift of the storm tracks and a *positive* NAM (Vallis et al., 2015). That the CMIP5 multi-model ensemble exhibits such large diversity, even in the sign (Gillett and Fyfe, 2013), of NAM projections appears to be explained by the relative importance of the two mechanisms in any particular model (McCusker et al., 2017; Oudar et al., 2017; Vallis et al., 2015). For instance, the degree of projected Arctic amplification in a model is related to a complex interplay of atmospheric circulation, sea ice dynamics, hydrologic change in all three phases, clouds, and surface/atmospheric radiation (Harvey et al., 2015). A paradigm appears to be emerging in the literature whereby models producing larger Arctic amplification also tend to produce larger equatorward shifts of the mid-latitude jets and storm tracks, and associated negative NAM responses (Barnes and Polvani, 2015; Harvey et al., 2015; Screen et al., 2018a).

Another line of research concentrates on the impact on the NH jet streams from quasi-stationary Rossby waves, and the subsequent impact on regional circulation patterns in the extratropics. Established theory predicts that Arctic amplification is associated with a decrease in Rossby wavelength, and an increase in wave amplitude (Hoskins and Woollings, 2015). These arguments have been used to link Arctic amplification due to sea ice loss and a change in the likelihood of extreme climate events at mid-latitudes, which would include large-amplitude NAM events (Francis and Vavrus, 2012), although that link remains controversial (Barnes and Screen, 2015). While changes to Rossby wavelength and amplitude may be expected from simple theoretical arguments (Mbengue and Schneider, 2017), the picture in observations and modelling results is much less clear (Simpson et al., 2014; Vallis et al., 2015). An important complicating factor is that changes to the characteristics and propagation of Rossby waves are driven much more readily by lower latitude perturbations than higher latitude ones (Hoskins and Karoly, 1981). A considerable body of literature has shown that changes to the NAM on seasonal and climate change timescales can be driven by variations in the wavelength and amplitude of Rossby waves, mainly of tropical origin (Cattiaux and Cassou, 2013; Ding et al., 2014; Fletcher and Kushner, 2011; Goss et al., 2016). Other studies report a robust negative NAM response driven by Arctic sea ice loss (Kim et al., 2014a; Screen et al., 2018b) that may be modified significantly by dynamical coupling with the stratospheric circulation (McKenna et al., 2018; Sun et al., 2015).

Near-term projections of anthropogenically-forced changes to the NAM and associated mid-latitude storm tracks indicate that, while there may be a positive trend present, it is weak in magnitude compared to the multi-model and/or multi-realization variability within the ensemble (Figure 4.15:, and Barnes and Polvani, 2015). On such short timescales, it is apparent that any forced signal of change in the NAM, which will be subject to considerable model uncertainty arising from imperfect representation of the physical processes described above, is expected to be of comparable magnitude to interannual or decadal variability in the NAM that is unrelated to anthropogenic forcing (Li et al., 2018a). A tendency to a near-term change towards a more positive NAM during the boreal winter is apparent in Figure 4.15:, where the near-term (2021–2040) changes in NAM from the 10-member ensemble CanESM5 under the SSP5-8.5 scenario is shown. [Note: This is a one-scenario single-model result. We will assess other scenarios and multi-model ensemble when CMIP6 data will become available.]

[START FIGURE 4.15 HERE]

Figure 4.15: Simulated Annular Mode index change (hPa) from present-day to the near-term: (a) NAM and (b) SAM. The NAM is defined as the difference in zonal mean sea-level pressure (SLP) at 35°N and 65°N (Li and Wang, 2003) and the SAM as the difference in zonal mean SLP at 40°S and 65°S (Gong and Wang, 1999). Present-day

values are averages over the period from 1995–2014. Near-term values are averages over the period from 2021–2040. The vertical lines are ensemble-means and the shaded bars are 5–95% confidence intervals on the ensemble means. [These calculations are based on a ten-member ensemble of simulations from one CMIP6 model, CanESM5. Eventually, the figure will be updated using single simulations from the full CMIP6 ensemble.]

[END FIGURE 4.15 HERE]

The SAM

The SAM describes the leading mode of variability in the Southern Hemisphere (SH) extratropical circulation, which influences climate across many regions including South America, southern African countries, Australia, New Zealand and Antarctica. In its positive phase, the SAM characterizes anomalously low pressure over the polar cap and high pressure in southern mid-latitudes (Marshall, 2003). While there are some zonal asymmetries to the structure of the SAM, most notably a canonical wavenumber-3 pattern (Raphael, 2004), it is more symmetric than its Northern Hemisphere (NH) counterpart (Fyfe et al., 1999). The SAM is closely tied to the behaviour of the mid-latitude eddy-driven jet and captures variations in both jet strength and jet latitude (Barnes and Polvani, 2013; Solomon and Polvani, 2016), as well as variations in the southern extent of the Hadley circulation (Ceppi et al., 2013). The changes in the SH circulation associated with the SAM impact on surface wind stress (Wang et al., 2014) and hence affect the Southern ocean.

The impact of ozone depletion and recovery on SH circulation exhibits a strong seasonality, with the largest influence in austral summer (Barnes et al., 2014; Gillett and Fyfe, 2013) following the peak of the Antarctic ozone hole in September-October. The AR5 concluded that in the future it is *likely* that increases in GHGs and the projected recovery of the Antarctic ozone hole will be the principal drivers of SAM trends and these will have competing effects on the SAM in austral summer and autumn. They further concluded that the positive trend in austral summer/autumn SAM observed over the past several decades is *likely* to weaken considerably as ozone depletion recovers through to the mid-21st century. Based on current scenarios for the future decline of ozone depleting substances in the atmosphere, the Antarctic ozone hole in October is projected by chemistry-climate models to recover by around 2060 (Dhomse et al., 2018), so this is the period over which the effect of ozone recovery on the SH circulation is expected to be greatest (Barnes et al., 2014). GHGs, on the other hand, influence the SH circulation year round (Gillett and Fyfe, 2013; Grise and Polvani, 2014) and are therefore *likely* to be the dominant driver of projected circulation changes in austral winter (Barnes et al., 2014; Gillett and Fyfe, 2013; Solomon and Polvani, 2016). An influence of other forcing agents, such as anthropogenic aerosols, on the SAM has been reported in some climate models (Rotstayn, 2013), but the response across a larger set of CMIP5 models is not robust (Steptoe et al., 2016) and depends on the details of the tropospheric temperature response to aerosols (Choi et al., 2019); this gives *low confidence* in the potential influence of anthropogenic aerosols on the SAM in the future.

Owing to the competing effects of changing GHG concentrations and ozone recovery on the SH circulation over the next several decades, SAM projections vary across different forcing scenarios. The CMIP5 models simulate a weak negative SAM trend in austral summer for the RCP4.5 scenario by the end of the century (Zheng et al., 2013a), while for a higher GHG forcing scenario (RCP8.5) they simulate a weak positive SAM trend (Zheng et al., 2013a). For a low GHG emissions scenario (RCP2.6) the effect of ozone recovery on the SAM may dominate over that of GHGs in austral summer (Eyring et al., 2013).

Since the AR5, there have been advances in understanding the role of internal climate variability for SH circulation trends over the recent past (Garfinkel et al., 2015) and over the 21st century (Solomon and Polvani, 2016). A large initial condition ensemble following the RCP4.5 scenario showed a monotonic positive SAM trend in JJA over the 21st century. In DJF, the SAM trend over the first half of the 21st century is weaker compared to the strongly positive trend observed and simulated over the late 20th century. In that model, the number of realizations required to identify a significant change in decadal mean SAM from its year 2000 state decreases to below 5 by around 2025 (Solomon and Polvani, 2016). In DJF, the same criterion was not met until around 2070 owing to the opposing effects of ozone recovery and GHGs on the summer SAM in the near-term. Figure 4.15: shows near-term (2021–2040) changes in the SAM in DJF from a 10-member ensemble from a single climate model (CanESM5) under the SSP5-8.5 scenario. This result shows a tendency toward a more positive SAM in the next two decades, with similar changes apparent in all seasons. [Note: We will also assess this for SSP1-2.6 when more CMIP6 simulations become available.]

In models that do not explicitly represent stratospheric ozone chemistry, which includes the majority of the CMIP6 model ensemble, an ozone dataset must be prescribed that properly captures the characteristics of ozone depletion and recovery in order to capture the effects of ozone on the tropospheric circulation (Neely et al., 2014; Young et al., 2014).

4.4.3.2 El Niño-Southern Oscillation and its Teleconnections

The AR5 assessed that it is *very likely* that the El Niño-Southern Oscillation (ENSO) will remain the dominant mode of interannual variability in the future. Moreover, due to increased moisture availability the associated precipitation variability on regional scales was assessed to *likely* intensify. An eastward shift in the patterns of temperature and precipitation variations in the North Pacific and North America related to El Niño and La Niña teleconnections was projected for the future with medium confidence. The stability of teleconnections to other regional implications including those in Central and South America, the Caribbean, Africa, most of Asia, Australia and most Pacific Islands were assessed to be uncertain.

A detection of robust near-term changes of ENSO SST variability in response to anthropogenic forcing is difficult to achieve due to pronounced unforced low-frequency modulations of ENSO (Maher et al., 2018; Wittenberg, 2009). However, a subset of CMIP5 models that simulate the ENSO Bjerknes index most realistically show an increase of ENSO SST amplitude in the near-term future and decline thereafter (Kim et al., 2014b) as shown as Figure 4.16:. The ENSO Bjerknes index is the most commonly used linear metric that captures the essential ocean-atmosphere coupled processes leading to either positive feedback (enhancement by zonal advective, thermocline, and Ekman feedbacks) or negative feedback (damping by mean advection and damping by thermodynamics) in the genesis of ENSO (Kim et al., 2014b).

[START FIGURE 4.16 HERE]

Figure 4.16: Time variation of simulated ENSO amplitude and ENSO stability [Placeholder figure from (Kim et al., 2014b), to be replaced in later drafts].

Simulating different ENSO flavours (characterized by varying zonal location of maximum SST anomalies) realistically was a significant challenge for the CMIP5 models (Timmermann et al., 2018); and thus, potential changes in ENSO flavours in response to anthropogenic forcing in the near-term future cannot be established with confidence based on the CMIP5 ensemble. Recently, the SST variance associated with Eastern Pacific (EP) ENSO events have been shown to increase in the CMIP5 ensemble, if taking into account that models simulate the centroid of this variability in different locations (Cai et al., 2018a). At the time of composing the FOD of Chapter 4, the ability of CMIP6 models in simulating different ENSO flavours as well as projected changes in SST variability in the near-term remain to be explored.

[END FIGURE 4.16 HERE]

4.4.3.3 Pacific Decadal Variability

Climate variability of the Pacific Ocean on decadal and interdecadal timescales is described in terms of a number of quasi-oscillatory SST patterns such as the Pacific Decadal Oscillation (PDO) (Mantua et al., 1997) and the Interdecadal Pacific Oscillation (IPO) (Folland, 2002), which are referred to as the Pacific Decadal Variability (PDV) (Newman et al., 2016). PDV comprises an inter-hemispheric pattern that varies at decadal-to-interdecadal timescales. One important feature of PDV is indeed the strong covariance between the tropics and extratropics (Liu, 2012), which has proved difficult to simulate accurately by climate models (see Newman et al. (2016) for a review). Yet, the IPO and the PDO are not identical. While the North Pacific and South Pacific centres of action in the IPO pattern have similar amplitude, the North Pacific centre in the PDO pattern is clearly enhanced. However, although the spatial domains to derive the IPO and PDO indices differ, and uncertainty applies to trend removal and time-filtering (Newman et al., 2016; Tung et al., 2019), the IPO and PDO are highly correlated in time and are often used interchangeably.

The AR5 assessed that near-term predictions of PDV (then referred to as PDO or IPO) were largely model dependent (Mochizuki et al., 2012; van Oldenborgh et al., 2012), not robust to sampling of initialization start-dates, overall not statistically significant, and worse than persistence (Doblas-Reyes et al., 2013), although some studies showed positive skill for PDV (Chikamoto et al., 2013; Mochizuki et al., 2010). Consistently, the CMIP5 decadal-prediction ensemble yielded no prediction skill of SST over the key PDV centres of action in the Pacific Ocean, both at 2–5 year and 6–9 year forecast averages (Doblas-Reyes et al., 2013; Guemas et al., 2013a).

Since the AR5, the processes causing the multi-decadal variability in the Pacific Ocean have become better understood. It now seems accepted that the IPO represents the low-frequency component of ENSO, driven by both interannual and decadal ENSO variability that is coherent between the North and South Pacific (Di Lorenzo et al., 2013, 2015), which may include both atmospheric and oceanic teleconnection mechanisms. Whether the IPO is a distinct mode of climate variability (Henley et al., 2017) or not (Tung et al., 2019) remains to be further assessed and clarified. A better-defined variability appears to be associated with the PDO. It is thought to be driven by atmospheric forcing linked to changes in the Aleutian Low and integrated by mixed layer dynamics and related re-emergence processes (interannual-to-decadal), as well as subpolar-subtropical gyre dynamics and related westward-propagating oceanic waves (decadal-to-interdecadal) (see Newman et al. (2016) for a review). The relative importance of tropical and extratropical processes underlying PDV remains unclear; although it seems to be stochastically driven rather than self-excited (Liu, 2012; Liu and Di Lorenzo, 2018).

Because PDV represents not one but many dynamical processes, it represents a challenge as a target for near-term climate predictions and projections. The new generation of decadal forecast systems keeps showing no multi-year prediction skill for PDV (Shaffrey et al., 2017), although there is the potential for forecasting capabilities in case studies (Meehl et al., 2014; Meehl and Teng, 2012). For the near-term, it is predicted a transition of PDV from the current negative phase towards a positive phase in the coming years (Meehl et al., 2016).

The PDV has been shown to influence the pace of global warming (Cai et al., 2015; Dai et al., 2015; Douville et al., 2015; England et al., 2014; Kosaka and Xie, 2013; Meehl et al., 2011, 2016; Watanabe et al., 2014); but the extent to which PDV is externally forced or internally generated and how it will evolve in a future climate remain open questions (Deser and Phillips, 2017).

4.4.3.4 Indian Ocean Basin and Dipole Modes and their Teleconnections

Important modes of interannual climate variability with pronounced climate impacts in the Africa-Indo-Pacific areas of the globe are the Indian Ocean Dipole (IOD), which is closely related to- and often coincides with ENSO phases (Stuecker et al., 2017), and the Indian Ocean Basin (IOB) mode, which is often described as a capacitor effect in response to ENSO (Du et al., 2013; Xie et al., 2009).

The projected climate mean state changes in the tropical Indian Ocean resemble a positive IOD state, with faster warming in the west compared to the east. This mean state change will potentially lead to a reduction in the amplitude difference between positive and negative IOD events, however with no robust change in IOD frequency (Cai et al., 2013). Currently, no new studies and evidence exist that would suggest a cessation of IOD variability and robust change in the IOB mode in the near-term to long-term future. This means that we can also expect that the ENSO-IOD and connection with phenomena of important climate implications like the Afro-Asian monsoons alongside other Indian Ocean Basin relationships observed in the current climate will persist in the near-term future.

4.4.3.5 Atlantic Multidecadal Variability

The Atlantic Multi-decadal Variability (AMV) is a large-scale climate mode accounting for the main fluctuations in North Atlantic SST on multi-decadal time scales. The AMV influences air temperatures and precipitation over adjacent and remote continents, and its undulations can partially explain the observed variations in the NH mean temperatures (Steinman et al., 2015). The origin of this variability is still uncertain. Ocean dynamics (e.g., changes in the AMOC), external forcing, and local atmospheric forcing all seem to play a role (Brown et al., 2016; Cassou et al., 2018; Menary et al., 2015; Ruprich-Robert and Cassou, 2015).

The AR5 assessed with *high confidence* that initialized predictions can improve the skill for temperature over the North Atlantic, in particular in the sub-polar branch of AMV, compared to the projections, for the first five years (see WG1 AR5 Figures 11.3 and 11.4). However, non-initialized predictions showed positive correlation over the same time-range as well, consistent with the notion that part of this variability is caused by external forcing.

Since the AR5, near-term initialized predictions, both multi-model (Bellucci et al., 2015a) and single-model ensembles (Marotzke et al., 2016; Yeager et al., 2018), confirm substantial skill in hindcasting North-Atlantic SSTs anomalies on a time range of 8–10 years. Yet, skill in predicting the AMV is not always translated into equally successful predictions of temperature and precipitations over the nearby land. This might be related to systematic model errors in the simulation of the spatial and temporal structure of the AMV and too weak associated teleconnections (see Section 3.7.7). However, preliminary analyses from large-ensemble decadal prediction systems such as the Community Earth System Model decadal prediction large ensemble (CESM-DPLE) (Yeager et al., 2018) show an improvement with respect to the CMIP5 decadal hindcasts (Martin and Thorncroft, 2014b) in forecasting Sahel precipitation over three to seven years, which is consistent with the current understanding of AMV impact over Africa (Mohino et al., 2016). CESM-DPLE predicts drought conditions over the Sahel through 2020, which is compatible with a shift towards a negative phase of AMV as a result of a weakening of the AMOC, advocated by a number of studies (Hermanson et al., 2014; Robson et al., 2014; Yeager et al., 2015).

However, since the AMOC-AMV relationship varies considerably from model to model in terms of amplitudes, spatial properties, preferred time scales and associated teleconnections (Ba et al., 2014; Peings et al., 2016; Ruiz-Barradas et al., 2013), and recent studies have even argued about the active role of the ocean dynamics in generating the AMV, that could be consequently attributed to random atmospheric forcing (Cane et al., 2017; Clement et al., 2015; O'Reilly et al., 2016; Zhang et al., 2016), the confidence in the predictions of AMV impacts is low. On the other hand, there is *high* confidence that the AMV skill over 5–8-year lead time is improved by using initialized predictions (compared to non-initialized ones).

4.4.3.6 Tropical Atlantic Modes and their Teleconnections

Interannual variability of the tropical Atlantic can be described in terms of two main climate modes: the Atlantic Equatorial Mode and the Atlantic Meridional Mode (AMM). The Atlantic Equatorial Mode, also commonly referred to as the Atlantic Niño or Atlantic Zonal Mode, is associated with SST anomalies near the equator, peaking in the eastern basin, while the AMM is characterized by an inter-hemispheric gradient of SST and wind anomalies. Both modes are associated with changes in the ITCZ and related winds and exert a strong influence on the climate in adjacent and remote regions.

Despite considerable improvements made in CMIP5 with respect to CMIP3, most of the climate models are not able to correctly simulate the main aspects of Tropical Atlantic Variability (TAV) and associated impacts. This is presumably the main reason why there is a lack of specific studies dealing with near-term changes in tropical Atlantic modes. Nevertheless, the AR5 reported that the ocean is more predictable than continental areas at the decadal timescale. In particular, the predictability in tropical oceans is mainly associated with decadal variations of the external forcing component. Since the AMV affects the tropical Atlantic, near-term variations of the AMV can modulate the Equatorial Mode and the AMM as well as associated impacts. The AR5 reported with *high confidence* that the skill of predicting the AMV index increases with initialization for the early forecast ranges.

There are no specific studies focusing on near-term changes in tropical Atlantic modes; nevertheless, decadal predictions show that although the North Atlantic stands out in most CMIP5 models as the primary region where skill might be improved because of initialization, encouraging results have also been found in the tropical Atlantic (Meehl et al., 2014). The impact of the initialization in the tropical Atlantic is not only visible in surface temperature but also in the subsurface ocean (Corti et al., 2015). In particular, initialization improves the skill via remote ocean conditions in the North Atlantic subpolar gyre and tropical Pacific, which influence the tropical Atlantic through atmospheric teleconnections (Dunstone et al., 2011; García-Serrano et al., 2015; Vecchi et al., 2014). Improvements of some aspects of climate prediction systems (initialization techniques, large ensembles, increasing model resolution) have also led to skill improvements over the tropical Atlantic (Monerie et al., 2017; Pohlmann et al., 2013; Yeager and Robson, 2017).

Recent studies have shown that the AMV can modulate not only the characteristics of the Atlantic Niños, but also their inter-basin teleconnections (Indian and Pacific). In particular, the Atlantic Niño–ENSO relationship is strongest during negative AMV phases (Losada and Rodríguez-Fonseca, 2016; Martín-Rey et al., 2014) when equatorial Atlantic SST variability is enhanced (Lübbecke et al., 2018; Martín-Rey et al., 2017).

Based on CMIP5 and CMIP6 [to be confirmed when more data is available] results, we conclude that there is a clear lack of studies on the near-term evolution of TAV and associated teleconnections. However, some studies show that despite severe model biases there are skilful predictions in the mean state of tropical Atlantic surface temperature several years ahead (*medium confidence*), though skill in simulated variability has not been assessed yet.

Decadal changes in the Atlantic Niño spatial configuration and associated teleconnections might be modulated by the AMV, but there is *low confidence* in these results.

4.4.4 Response to Short-Lived Climate Forcers and Volcanic Eruptions

The influence of SLCFs (methane, aerosols, ozone) on near-term climate (see also Sections 6.6.3 and 6.6.4) has been discussed extensively in the context of the climate targets set out by the Paris Agreement in 2015 (COP21, 2015). Comparisons have been made between current air quality legislation targets and the maximum feasible phase-out of SLCFs based on current technological options. The rate of reduction of SLCFs may influence near-term surface warming rates (Chalmers et al., 2012; Shindell et al., 2017) and have a modest influence on warming levels by mid-century up to a few tenths of a degree Celsius (Hienola et al., 2018; Smith and Mizrahi, 2013; Stohl et al., 2015), but there are only small differences in long-term GSAT trends by the end of century as a consequence of varying the SLCF pathway (Hienola et al., 2018). The estimated additional warming for scenarios of anthropogenic methane and black carbon emissions by mid-century, compared to a scenario for maximum technical reduction, is several times lower than an earlier estimate (UNEP, 2011).

Distinguishing the role of SLCFs for climate from that of long-lived GHGs is complicated by the fact that many short-lived species are co-emitted with CO_2 through combustion; hence policies aimed at reducing carbon emissions implicitly capture some SLCF reductions. For example, considering SLCFs separately from long-lived GHG emissions artificially inflates the potential control that SLCFs can exert on climate under ambitious mitigation and stabilization strategies (Rogelj et al., 2014). In scenarios consistent with meeting the 2°C target, additional measures to reduce anthropogenic black carbon emissions have little effect, because the key emissions are already ruled out through the implicit CO_2 controls. Nevertheless, other approaches may aim to tackle poor air quality through legislation, which would influence the abundance of

SLCFs (Shindell et al., 2017).

A complete phase-out of anthropogenic SO_2, black carbon, and organic carbon are expected to lead to additional surface warming for a climate stabilization scenario (0.5°C–1.1°C; *low confidence*) (Samset et al., 2018b). There may be a larger sensitivity of surface temperatures to aerosol in northern mid-latitudes and over land (*low confidence*). The additional warming at high northern latitudes associated with projected reductions in aerosol emissions over the 21st century are expected to have knock-on effects on other parts of the climate system, including a more rapid reduction in Arctic sea ice extent (Gagné et al., 2015). Furthermore, a removal of anthropogenic aerosols could increase global mean precipitation (2–4.6%; *low confidence*; (Richardson et al., 2018; Samset et al., 2018b)). Climate change and projected reductions in ozone-depleting substances interact in a complex way to determine future ozone radiative forcing by the end of the century (Banerjee et al., 2018; Young et al., 2018).

The major uncertainties around the climate impacts of SLCFs in the future come from: (i) the uncertainty in anthropogenic aerosol ERF (Chapter 7) and the representation of aerosols in the models used to make projections; (ii) uncertainty in co-emissions of long- and short-lived species; (iii) uncertainty in the relative changes to different SLCFs that have warming and cooling effects in the current climate (Chapter 7); and (iv) physical uncertainty. For example, the shortwave radiative forcing from methane was substantially underestimated in previous calculations (Etminan et al., 2016), which affects understanding of future methane effective radiative forcing (ERF). Methane levels have continued to rise since the AR5, and the current trajectory for methane lies between the RCP4.5 and RCP8.5 scenarios (Nisbet et al., 2019). Should the growth in methane emissions continue at its current rate until the end of century, it would contribute an estimated additional 0.5 W m^{-2} to the Paris targets (Nisbet et al., 2019).

[Note: Once available, we will use output from AerChemMIP future simulations in which SSP3-7.0 "Regional Rivalry" without climate policy is compared to SSP3-7-lowNTCF having "Strong" levels of air quality policy to 2055. Thus we will be able to assess in CMIP6 models the influence of alternative SLCF pathways on near-to-mid-term climate (Collins et al., 2017). See also Sections 6.6.3 and 6.6.4 for an assessment of the contribution from individual species to GSAT projections.]

Another factor that could substantially alter projections in the near term would be the occurrence of a large explosive volcanic eruption, or even a decadal to multi-decadal sequence of small-to-moderate volcanic eruptions as witnessed over the early 21st century (Santer et al., 2014). An eruption similar to the last large tropical eruption, Mount Pinatubo in the Philippines in June 1991, is expected to cause substantial Northern Hemisphere (NH) cooling, peaking between 0.09°C and 0.38°C and lasting for three to five years, as indicated by climate model simulations over the past millennium (e.g., Jungclaus et al., 2010). The response to changes in multi-decadal volcanic forcing shows similar cooling in both simulations and reconstructions of NH temperature. Volcanic eruptions generally result in decreased global precipitation (Iles and Hegerl, 2014, 2015; Man et al., 2014), with climatologically wet regions drying and climatologically dry regions wetting, which is opposite to the response under global warming (Held and Soden, 2006; Iles et al., 2013). In the AR5, uncertainty due to future volcanic activity was generally not considered in the assessment of the CMIP5 21st-century climate projections (O'Neill et al., 2016; Taylor et al., 2012).

Since the AR5, there has been considerable progress in quantifying the impacts of volcanic eruptions on decadal climate prediction and longer-term climate projections (Bethke et al., 2017; Meehl et al., 2015; Timmreck et al., 2016). By exploring 60 possible volcanic futures under RCP4.5, it has been demonstrated that the inclusion of volcanic forcing may enhance climate variability on annual-to-decadal timescales (Bethke et al., 2017). The interannual uncertainty range in annual-mean GSAT is about 50% higher (from 0.3°C to 0.5°C) in simulations with volcanoes relative to simulations without volcanoes (Figure 4.17:). Consistent with a tropospheric cooling response, the change in ensemble spread in the volcanic cases is skewed towards lower GSAT relative to the non-volcanic cases (see Figure 4.17:). In these simulations with multiple volcanic forcing futures there is: 1) an increase in the frequency of extremely cold years; 2) an increased likelihood of decades with negative GSAT trend; and 3) later anthropogenic signal emergence.

[START FIGURE 4.17 HERE]

Figure 4.17: Annual-mean GSAT. a, Ensemble mean (solid) of VOLC (blue), VOLC-CONST (magenta) and NO-VOLC (red/orange) with 5–95% range (shading) and ensemble minima/maxima (dots) for VOLC and NO-VOLC; evolution of the most extreme member (black). b, Probability density function (PDF) of the 2016–2035 mean relative to pre-industrial (PI), with 5–95% bootstrap confidence bounds. c, PDF of the time when GSAT change relative to PI (20-year running average) exceeds 1.5°C. d, PDF of annual anomalies with anthropogenic trend removed. The spread of VOLC-CONST is linearly shifted relative to NO-VOLC, and therefore not shown in a–c. These calculations are based on three 21st-century simulation ensembles with the Norwegian Earth System Model (NorESM), which use the same mid-range anthropogenic forcing scenario RCP4.5 but differ in their volcanic forcing: a 60-member ensemble using plausible stochastic volcanic forcing (VOLC); a 60-member reference ensemble using zero volcanic forcing (NO-VOLC); and a 20-member ensemble using 1850–2000 averaged volcanic forcing (VOLC-CONST). [This figure is adopted from (Bethke et al., 2017).]

[END FIGURE 4.17 HERE]

Volcanic forcing can also influence modes of interannual variability such as ENSO (see Figure 4.18:). The impact of northern, tropical, and southern volcanic eruptions on Pacific sea surface temperature (SST), and the different response mechanisms arising due to differences in the volcanic forcing structure, have been investigated using the Community Earth System Model Last Millennium Ensemble (CESM-LME) (Zuo et al., 2018). The Pacific features a significant El Niño-like SST anomaly five to ten months after northern and tropical eruptions, with a weaker tendency after southern eruptions. The Niño3 index peaks with a lag of 1.5 years after northern and tropical eruptions. Two years after all three types of volcanic eruptions, a La Niña–like SST anomaly pattern over the equatorial Pacific is simulated, forming an ENSO-like cycle (Zuo et al., 2018). Large tropical eruptions are associated with co-occurring El Niño and positive Indian Ocean Dipole (IOD) events in the ensemble mean that peak 6–12 months after the volcanic forcing maximum, marking a significant increase in the likelihood of each event occurring in the SH spring/summer following the eruption (Maher et al., 2015). Such responses in tropical variability are expected to follow future volcanic eruptions, too.

[START FIGURE 4.18 HERE]

Figure 4.18: (a) Evolution of the composite Niño-3 index with zonal mean removed (units: 8°C) after northern eruptions (blue line), tropical eruptions (red line), and southern eruptions (green line). The spreads of the individual volcanic eruptions are denoted by the blue, red, and green shading, respectively. (b) The lead–lag correlation between the Niño-3 index (5°S–5°N, 150°–90°W) and the 850-hPa zonal wind in the western-to-central equatorial Pacific (5°S–5°N, 110°E–150°W) following northern (blue line), tropical (red line), and southern eruptions (green line). The positive value of the horizontal axis indicates that the Niño-3 index lags the 850-hPa zonal wind. [This figure is adopted from (Zuo et al., 2018).]

[END FIGURE 4.18 HERE]

Volcanic forcing is a source of uncertainty in the CMIP6 projections assessed in this chapter. We will quantify this uncertainty in the near-term by utilizing existing large ensembles of natural-forcing-only simulations, as well as targeted simulations under CMIP6 VolMIP (Zanchettin et al., 2016).

4.5 Mid- to Long-term Global Climate Change

4.5.1 Atmosphere

In the following we assess how the global indicators discussed in Section 4.3 manifest themselves in large-scale spatial atmospheric patterns of mid- to long-term climate change. The patterns of change in any given future period represent a combination of unforced internal variability and a forced response. The role of internal variability is much larger at the local to regional scale than in the global mean projections. We here assess multi-model mean patterns, which represent an estimate of the forced response. It is important to note that this estimate of the forced response is a more homogeneous pattern than the 20-yr mean change patterns in any individual model realization (Knutti et al., 2010). The forced response is put into the context of internal variability by hatching the areas where the signal is smaller than 2 standard deviations of 20-year means in local variability (see Section 4.2.5 for details).

4.5.1.1 Near-Surface Air Temperature

Patterns of near-surface air temperature changes show wide-spread warming by 2041–2060 and 2081–2100 for all SSPs with respect to 1995–2014. The area fraction experiencing warming increases with the level of global mean warming. As GSAT continues to increase, it is *very likely* that by the middle and the end of the 21st century most of the global land and ocean areas will be warmer than in 1995–2014 (*high confidence*) (see also Section 4.3.1.1).

The temperature change pattern can be interpreted as a combination of unforced internal variability of the coupled climate system acting at synoptic to multi-decadal time scales and forced response pattern to forcings such as changes in atmospheric GHG and aerosol concentrations or in land use or land management (Deser et al., 2012b, 2016). The higher the level of global warming and the longer the period averaged across, the more the sign of the regional temperature change is dominated by the forced response. Figure 4.19: illustrates the CMIP6 multi-model mean estimate of this forced response for two different SSPs. The multi-model mean pattern shows some robust key characteristics such as a land-ocean warming contrast or amplified warming over the Arctic region assessed below. Changes in aerosol concentrations and land use and land management can furthermore have a direct imprint on the regional warming pattern.

[START FIGURE 4.19 HERE]

Figure 4.19: Multi-model mean change in annual mean near-surface air temperature (°C) in 2041–2060 and 2081–2100 in (top) SSP1-2.6 and (bottom) SSP5-8.5 relative to 1995–2014. [Figure produced with ESMValTool (Eyring et al., 2016b) based on the five CMIP6 models, BCC-CSM2-MR, CanESM5, CNRM-CM6-1, IPSL-CM6A-LR, and MRI-ESM2-0 will be updated with more CMIP6 models.]

[END FIGURE 4.19 HERE]

Land-Ocean Warming Contrast

It is *virtually certain* that average warming will be higher over land than over the ocean. This so-called land-ocean warming contrast is a striking feature of observed trends (Byrne and Schneider, 2018; Lambert and Chiang, 2007) and projected changes in surface-air temperature (Bayr and Dommenget, 2013; Byrne and O'Gorman, 2013b; Dong et al., 2009; Drost et al., 2012; Izumi et al., 2013; Joshi et al., 2013; Joshi and Gregory, 2008; Lambert et al., 2011; Sutton et al., 2007). Between 1979 and 2016, average temperature over continents increased by 42% more than over oceans (Byrne and Schneider, 2018); a similar warming contrast is found in CMIP5 projections though with large differences across models and latitudes (Byrne and O'Gorman, 2013b; Drost et al., 2012; Joshi et al., 2013; Sutton et al., 2007). The land-ocean warming contrast is typically quantified as an amplification factor defined as the ratio of land-to-ocean warming: A = δT_{Land} / $\delta T_{\mathrm{Ocean}}$ (Byrne and O'Gorman, 2013a). The amplification factor is greater than one for almost all regions and is larger for dry subtropical continents (about 1.5) than for moist regions in the tropics and mid-latitudes (about 1.2) (Byrne and O'Gorman, 2013a), suggesting a link between the land-ocean warming contrast and surface dryness.

It has long been recognized that the warming contrast is not caused by the differences in effective heat capacity between land and ocean (e.g., Sutton et al., 2007). However, only since the AR5 has a robust physical understanding of the warming contrast been developed. A simple theory based on atmospheric dynamics and moisture transport shows that surface-air temperature and relative humidity over land are strongly coupled, and demonstrates that the warming contrast occurs because air over land is drier than over oceans (Byrne and O'Gorman, 2013a, 2013b, 2018; Joshi et al., 2008). The warming contrast causes land relative humidity to decrease (Byrne and O'Gorman, 2016, 2018; Chadwick et al., 2016) and this feeds back on and strengthens the warming contrast. Decomposing the mechanisms controlling the tropical land-ocean warming contrast (Byrne and O'Gorman, 2013b), it is found that for the median CMIP5 model approximately 40% of the warming contrast is due to continents being drier, the feedback due to decreases in land relative humidity under global warming accounts for another 40%, and the remaining contribution comes from modest increases in near-surface ocean relative humidity (Schneider et al., 2010). Differences in land relative humidity responses across models are the primary cause of uncertainty in the land-ocean warming contrast (Byrne and O'Gorman, 2013b). These land relative humidity changes are ultimately controlled by moisture transport between the land and ocean boundary layers (Byrne and O'Gorman, 2016; Chadwick et al., 2016) and are also sensitive to characteristics of land surfaces that are challenging to model, including stomatal conductance and soil moisture (Berg et al., 2016).

Polar Amplification

It is *very likely* that under global warming the Arctic is warming stronger than the global average (*high confidence*). Since the AR5 the understanding of the physical mechanisms driving the Arctic Amplification has improved.

The Arctic surface is projected to warm by more than the global average over the 21st century, with annual-average Arctic warming of about 3°C (SSP1-2.6) to 12°C (SSP5-8.5) by 2081–2100 (Figure 4.19:). This phenomenon, known as polar or Arctic amplification, is a ubiquitous feature of the response to GHG forcing simulated by climate models (Hansen et al., 1984; Holland and Bitz, 2003; Manabe et al., 1991; Manabe and Stouffer, 1980; Manabe and Wetherald, 1975, 1980; Pithan and Mauritsen, 2014; Robock, 1983; Winton, 2006) and has been observed over recent decades concurrent with Arctic sea-ice loss (Serreze and Barry, 2011) (Chapter 2). Based on robust scientific understanding and agreement across multiple lines of evidence (Section 7.6), there is *high confidence* that warming will continue to be Arctic amplified over the 21st century on timescales longer than several decades.

A variety of mechanisms contribute to Arctic amplification (see Section 7.6.2). While surface-albedo feedbacks associated with the loss of sea ice and snow have long been known play important roles (Arrhenius, 1896; Hall, 2004; Manabe and Stouffer, 1980; Robock, 1983), it is now recognized that temperature (lapse-rate and Planck) feedbacks also contribute substantially to Arctic amplification with longwave radiative damping to space with warming being less efficient at high latitudes (Goosse et al., 2018; Pithan and Mauritsen, 2014; Winton, 2006). Changes in poleward atmospheric and oceanic heat transports are thought to contribute to Arctic warming (Bitz et al., 2006; Holland and Bitz, 2003; Lee et al., 2011, 2017, Marshall et al., 2014, 2015; Nummelin et al., 2017; Oldenburg et al., 2018; Singh et al., 2017; Woods and Caballero, 2016), but the primary drivers of polar amplification within models appear to be polar feedback processes rather than heat transport changes (Pithan and Mauritsen, 2014; Stuecker et al., 2018). However, quantifying the role of individual factors in the coupled climate system is complicated by interactions between polar climate feedbacks and heat transports and between the different climate feedbacks (Section 7.6.2). Projected reduction in the strength of the AMOC over the 21st century is expected to reduce Arctic warming, but even a strong AMOC reduction would not eliminate Arctic amplification entirely (Liu et al., 2017, 2018c; Wen et al., 2018) (*medium confidence*).

There remains substantial uncertainty in the magnitude of projected Arctic amplification with the Arctic warming by a factor of two to four times the global average in models (Holland and Bitz, 2003; Nummelin et al., 2017). This uncertainty primarily stems from different representations of polar surface-albedo, lapse-rate, and cloud feedbacks, and from different projected poleward energy transport changes (Bonan et al., 2018; Crook et al., 2011; Holland and Bitz, 2003; Mahlstein and Knutti, 2011; Pithan and Mauritsen, 2014). The magnitude of Arctic amplification may also depend on the mix of radiative forcing agents (Najafi et al., 2015; Sand et al., 2016), with tropospheric aerosol emissions reducing simulated Arctic warming over the middle of the 20th century (Gagné et al., 2017) and with aerosol emission reductions enhancing simulated Arctic warming over recent and future decades (Acosta Navarro et al., 2016; Gagné et al., 2015; Wang et al., 2018b; Wobus et al., 2016).

Climate models project weakly polar amplified warming in the Southern Hemisphere (SH) under transient warming (Figure 4.19:) with a similar pattern to that observed over the 20th century (Armour et al., 2016; Jones et al., 2016c; Manabe et al., 1991; Marshall et al., 2014). Model simulations (Danabasoglu and Gent, 2009; Hall, 2004; Li et al., 2013) and paleoclimate proxies indicate polar amplification in both hemispheres near equilibrium, but generally with less warming in the Antarctic than the Arctic (Section 7.6). The primary driver of delayed warming of the southern high latitudes is the upwelling of unmodified water from depth in the Southern Ocean and associated ocean heat uptake that is then transported away from Antarctica by northward flowing surface waters (Armour et al., 2016; Frölicher et al., 2015; Liu et al., 2018b; Marshall et al., 2015) (Section 7.2; Section 7.6.2; Section 9.2). Changes in westerly surface winds over the Southern Ocean have the potential to affect the rate of sea-surface warming, but there is currently *low confidence* in even the sign of the effect based on a diverse range of climate model responses to wind changes (Ferreira et al., 2015; Kostov et al., 2017; Marshall et al., 2014). A substantial increase in freshwater input to the ocean from the Antarctic ice sheet could further slow the emergence of SH polar amplification by cooling the Southern Ocean surface (Bronselaer et al., 2018), but this process is not represented in current climate models which lack dynamic ice sheets. Thus, while there is *high confidence* that the SH high latitudes will warm by more than the tropics on centennial timescales, there is *low confidence* that such a feature will emerge this century (Section 7.6).

Seasonal Warming Patterns

The warming pattern also shows distinct seasonal characteristics. The majority of models show a stronger warming poleward of about 60° in hemispheric winter than summer conditions and thereby a reduced amplitude of the temperature cycle (Donohoe and Battisti, 2013; Dwyer et al., 2012). Over the subtropics and mid-latitudinal land and ocean regions most of the models project stronger warming in hemispheric summer than winter (Donohoe and Battisti, 2013; Sanchez and Simon, 2018; Santer et al., 2018), leading to an amplification of the seasonal cycle, a phenomenon that has been studied particularly in the case of the Mediterranean region (Brogli et al., 2019; Kröner et al., 2017; Seager et al., 2014).

Changes in Temperature Variability

It has long been recognized that along with mean temperatures also variance and skewness of the temperature distribution may be changing (Gregory and Mitchell, 1995; Mearns et al., 1997). By amplifying or dampening changes in the tail of temperature distribution such changes are potentially highly relevant extremes and pose a serious challenge to adaptation measures. Changes in temperature variability can occur from diurnal to multi-decadal time scales and from the local to the global scale.

Changes in GSAT variability are poorly understood. Based on model experiments it has been suggested that unforced variability of global mean temperatures tend to decrease in warmer world as a result of reduced albedo variability in high latitudes resulting from melting snow and sea ice (Brown et al., 2017; Huntingford et al., 2013), but *confidence* remains *low*. An assessment of changes in global temperature variability is inherently challenging due to the interplay of unforced internal variability and forced changes.

Changes in tropical temperature variability may arise from changes in the amplitude of the El Niño Southern Oscillation (ENSO) (Section 4.3.3.2). However, even the sign of the changes in ENSO amplitude remains inconsistent across models (Zheng et al., 2016). Large single-model initial-condition ensembles cover most of the range of changes in ENSO variance found in CMIP5 (Maher et al., 2018; Zheng et al., 2018), suggesting that internal variability accounts for most of the uncertainty. However, even if the forced response in ENSO amplitude is derived as the average of these large ensembles, the sign of the changes remain inconsistent (Maher et al., 2018).

Over the extratropics, several studies have identified robust large-scale patterns of changes in variability of annual and particularly seasonal mean temperature, including (a) a reduction in high latitudinal winter temperature variability and (b) an increase in summer temperature variability over land in tropics and subtropics (Holmes et al., 2016; Huntingford et al., 2013) as shown in Figure 4.20:. There is growing evidence that year-to-year and daily temperature variability decreases in winter over mid- to high-latitudes (Borodina et al., 2017; De Vries et al., 2012; Fischer et al., 2011; Holmes et al., 2016; Screen, 2014), which implies that the lowest temperatures rise more than the respective seasonal mean temperatures. Reduced high-latitude temperature variability may result from disproportionally large warming in source region of cold-air advection due to Arctic amplification and land-sea contrast (De Vries et al., 2012; Holmes et al., 2016; Screen, 2014). It has further been argued that a reduction in snow and sea-ice coverage from partly to completely snow- and ice-free ocean and land surface would substantially reduce cold-season temperature variability (Borodina et al., 2017; Fischer et al., 2011; Gregory and Mitchell, 1995).

On the other hand, enhanced summer temperature variability is projected over some land regions in the mid-latitudes and subtropics. In particular an increase in daily to interannual summer temperature variability has been projected over central Europe as a result of larger year-to-year variability in soil moisture conditions varying between a wet and dry regime and leading to enhanced land-atmosphere interaction (Fischer et al., 2012b; Holmes et al., 2016; Seneviratne et al., 2006). Furthermore, the amplified warming in the source region of warm-air advection due to land-ocean warming contrast and amplified Mediterranean warming (Brogli et al., 2019; Seager et al., 2014), may lead to disproportionally strong warming of the hottest days and summers and thereby increased variability.

[START FIGURE 4.20 HERE]

Figure 4.20: Relative change in variability of (left) JJA and (right) DFJ mean temperature in three large initial condition ensembles. Changes are shown as percentage changes of standard deviation across local seasonal mean temperatures. Changes are shown MPI 100-member grand ensemble by 2081–2100 (Maher et al., 2019), CanESM2 50-member ensemble (Kirchmeier-Young et al., 2017) and NCAR-CESM 30-member ensemble (Kay et al., 2015) for RCP8.5. [Figure may later be updated based on large initial-condition ensembles or large multi-model ensembles such as CMIP6 showing changes in standard deviation of seasonal mean temperatures in 2081–2100 (SSP5-8.5) relative to 1995–2014].

[END FIGURE 4.20 HERE]

4.5.1.2 Annual Mean Atmospheric Temperature

This subsection will assess the vertical and zonal structure of the temperature change (Figure 4.21:). Changes in lapse rate and zonal temperature gradients will be assessed in relation to changes in atmospheric dynamics discussed below (e.g., Perlwitz et al., 2015; Santer et al., 2017).

[START FIGURE 4.21 HERE]

Figure 4.21: Change in annual atmospheric temperature (°C) in 2081–2100 in (left) SSP1-2.6 and (right) SSP5-8.5 relative to 1995–2014 for the IPSL-CM6A-LR model from CMIP6. [To be updated with more CMIP6 models as they become available].

[END FIGURE 4.21 HERE]

4.5.1.3 Near-Surface Humidity

The relative humidity (RH) is expected to remain approximately constant on climatological time scales and planetary space scales, as indicated from modelling studies prior to the AR5. The AR5 noted the regional differences in long-term changes in RH, particularly on the contrast between land and ocean. Based on assessments from CMIP5 models, the AR5 concluded with *medium confidence* that 'reductions in near-surface RH over many land areas are *likely*'. The decrease in RH over most land areas is primarily contributed by the larger warming rates over land than over the ocean, and is termed the last-saturation-temperature constraint, as explained in the AR5.

Since the AR5, significant effort has been devoted to understanding the mechanisms for the decrease in land RH under global warming, and the relevance of the RH changes for land-sea warming contrast and water cycle. For the land RH decrease, both the moisture transport from the ocean and land-atmosphere feedback processes contribute. For specific humidity and its changes over land, the oceanic contribution is dominant while the role of evapotranspiration is secondary. However, the changes in land RH are also strongly influenced by evapotranspiration, which is suppressed by the drying soils under climate change (Berg et al., 2016; Byrne and O'Gorman, 2015; Chadwick et al., 2016). The combination of both oceanic and continental influences can explain the spatially diverse trends in RH over land in the observations for the recent decades, with a generally dominant negative trend at the global scale (Vicente-Serrano et al., 2018). The changes of land RH and temperature are not independent. There is a strong feedback between the land RH decrease and land-ocean warming contrast under future warming projections (see Section 4.5.1.1).

Changes in land RH can modulate the response of the water cycle to global warming (Byrne and O'Gorman, 2015; Chadwick et al., 2013). Most CMIP5 models project high precipitation associated with high near-surface RH and temperature under climate change (Lambert et al., 2017). Over land, the spatial gradients of fractional changes in RH contribute to a drying tendency in precipitation minus evapotranspiration with warming, which partly explains why the 'wet-gets-wetter, dry-gets-drier' principle does not hold over land (Byrne and O'Gorman, 2015). Terrestrial aridity is projected to increase over land, as manifested by a decrease in the ratio of precipitation to potential evapotranspiration, in which the decrease in land RH has a contribution of about 35% according to CMIP5 models under doubling CO_2 forcings (Fu and Feng, 2014). The aridity can be further amplified by the feedbacks of projected drier soils on land surface temperature, RH and precipitation (Berg et al., 2016).

The CMIP6 multi-model ensemble projects general decreases in near-surface relative humidity over most land areas, but moderate increases over the oceans (Figure 4.22:). The absolute change is weak and only on the order of a few percent. A seasonal-dependence of the response is projected. During boreal winter, significant decreases relative to natural variability are projected in the high latitudes of the NH, subtropical Eurasian continent, Amazonia, southern Africa and Europe. During boreal summer, significant decreases relative to natural variability are projected in the tropical and subtropical Eurasian continent, North America, South America, South Africa and Australia. Significant decrease is projected in the mid-latitude SH.

[START FIGURE 4.22 HERE]

Figure 4.22: Multi-model mean change (%) in seasonal (left) DJF and (right) JJA mean near-surface relative humidity in 2041–2060 and 2081–2100 in SSP5-8.5 relative to 1995–2014 based on two CMIP6 models, IPSL-CM6A-LR and MRI-ESM2-0. [Figure to be updated.]

[END FIGURE 4.22 HERE]

The AR5 assessed an increase in projected heat stress, dominated by increasing temperatures in spite of local decreases in RH. The AR5 identified hotspots of future heat stress increases in areas with abundant atmospheric moisture availability and high present-day temperatures, such as Mediterranean coastal regions.

Since the AR5, more comprehensive assessments on the future changes in heat stress have been conducted, concerning spatial variability (Kang and Eltahir, 2018; Pal and Eltahir, 2016), diurnal cycle (Buzan et al., 2015; Li et al., 2018b), extreme events (Pal and Eltahir, 2016), and different global warming targets (Russo et al., 2017). The detection of historical changes provides a sound physical basis for future projections. Already in the observed records, there is a detectable increase in wet-bulb globe temperature globally and over land regions since the 1970s that is attributable to human induced GHG emissions (Knutson and Ploshay, 2016; Li et al., 2017).

Continued increases in heat stress are expected over all land regions along with rising temperatures, as consistently projected by global (including CMIP5) and regional climate models based on different heat stress metrics (Fischer and Knutti, 2013; Li et al., 2017; Russo et al., 2017). The projections of heat stress indices are relatively robust across models, with smaller uncertainty than would be expected from temperature and humidity individually, because the projected greater warming is usually accompanied by larger decreases in RH in models (Fischer and Knutti, 2013). While multiple heat stress indicators are used in future projections, the uncertainty in projected changes in heat stress is to a larger extent induced by different climate models compared to that from different choices of indices (Zhao et al., 2015).

There is spatial variability of the heat stress responses. On the regional scale, extreme wet-bulb globe temperatures are expected to approach and even exceed the physiologic threshold for human adaptability (35°C) in hotspots such as southwest Asia and North China Plain in the late 21st century under RCP8.5, with possible interactions between humid coastal air masses and hot interior ones (Kang and Eltahir, 2018; Pal and Eltahir, 2016). These severe heat-related conditions located in low-elevation areas close to water bodies are consistent with those projected for southern Europe and Mediterranean coasts (Fischer and Schär, 2010). The exposure to humid heat waves is also expected to be high in some of the most densely populated regions, such as the Eastern United State and China (Russo et al., 2017). There is an urban amplification in heat stress changes compared to neighbouring rural areas directly related to the urban heat island effect, although weakly offset by the urban humidity deficit (Fischer et al., 2012a).

Due to the co-occurrence of temperature, humidity and wind speed conditions, the heat index will increase at a faster rate than atmospheric temperature alone (Horton et al., 2016; Li et al., 2018b). The increase in apparent temperature (referred to as heat index) is 0.17°C (0.12°C–0.25°C) per decade faster than that in air temperature under RCP8.5 projections from CMIP5 models throughout the 21st century, and is more remarkable in summer daytime than winter night-time (Li et al., 2018b). The elevated heat stress consequently results in future increases in heat-related morbidity and mortality (Li et al., 2018b) and reductions in labour capacity especially in peak months of heat stress (Dunne et al., 2013).

The CMIP6 multi-model ensemble projects robust increases in the mean wet-bulb globe temperature over land areas with distinct regional and seasonal characteristics (Figure 4.23:). Spatially, the increases in wet-bulb globe temperature are largest in the northern high latitudes, related to the polar amplification in atmospheric warming. This amplified increase in wet-bulb globe temperature is more pronounced in the boreal winter than summer. The forced climate change signal is significantly different from the internal variability over nearly all land regions under SSP5-8.5 in the mid- and long-term.

[START FIGURE 4.23 HERE]

Figure 4.23: Multi-model mean change (°C) in seasonal (left) DJF and (right) JJA mean wet-bulb globe temperature in 2041–2060 and 2081–2100 in SSP5-8.5 relative to 1995–2014 based on two CMIP6 models, IPSL-CM6A-LR and MRI-ESM2-0. [Figure to be updated.]

[END FIGURE 4.23 HERE]

4.5.1.4 Precipitation

The AR5 assessed that it is *virtually certain* that, in the long term, global precipitation will increase with GSAT rise. A gradual increase in global precipitation is projected over the 21st century with change exceeds 0.05 mm day^{-1} (about 2% of global precipitation) and 0.15 mm day^{-1} (about 5% of global precipitation) by 2100 in RCP2.6 and RCP8.5, respectively in CMIP5 models. Global maps of the percentage change in precipitation based on the five available CMIP6 models in the mid-term and long-term from SSP1-2.6 and SSP5-8.5 are presented in Figure 4.24:. Precipitation will *likely* increase by 1–3% $°C^{-1}$ for the SSP5-8.5 scenario. Precipitation is projected to increase in the CMIP6 models especially in monsoon regions and high latitudes. Changes in precipitation exhibit strong seasonal characteristics and, in many regions, the sign of the precipitation changes varies with season. Seasonal precipitation anomalies can provide a robust signal than annual mean (Huang et al., 2013; Lee et al., 2013). [Note: An assessment based on seasonal projections (JJA and DJF) will be presented with the availability of more CMIP6 projections.]

[START FIGURE 4.24 HERE]

Figure 4.24: Multi-model mean change (%) in annual mean precipitation in 2041–2060 (left) and 2081–2100 (right) relative to 1995–2014 from (top) SSP1-2.6 and (bottom) SSP5-8.5. [Figure produced with ESMValTool (Eyring et al., 2016b) based on the five CMIP6 models BCC-CSM2-MR, CanESM5, CNRM-CM6-1, IPSL-CM6A-LR, and MRI-ESM2-0. Figure to be updated with more CMIP6 models for JJA and DJF season.]

[END FIGURE 4.24 HERE]

The projected precipitation changes can be decomposed into a part that is related to atmospheric circulation referred to as dynamical component and a part related to water vapour changes, the thermodynamic component. There is *high confidence*, based on understanding and modelling (Fläschner et al., 2016; Samset et al., 2016), that global mean precipitation increases approximately 1–3% per °C of warming. However, regional precipitation changes also depend strongly on the atmospheric circulation. Model projections of circulation-related fields show a wide range of possible outcomes, which are primarily controlled by dynamics and exert a strong control on regional climate (Shepherd, 2014). The tropical circulation slows down with moisture and stratification changes, connecting to a poleward expansion of the Hadley cells and a shift of the ITCZ (Foltz et al., 2018). Circulation and precipitation changes are associated with weaker net radiative cooling of the atmosphere with higher atmospheric carbon dioxide levels (Bony et al., 2013).

Since the AR5, significant progress has been achieved in understanding changes in patterns and rates of precipitation with GSAT rise. Climate models disagree in their hydrological sensitivity, changes per degree Celsius of surface warming (Fläschner et al., 2016; Knutti et al., 2013b; Liu et al., 2014). The dependence of precipitation uncertainty on GSAT change indicates that dynamical uncertainty unrelated to climate sensitivity dominates precipitation change uncertainty across the globe (Kent et al., 2015). Most of the projected changes exhibit a sharp contrast between land and ocean, with surface temperature-driven (slow) sensitivity reaching 3–5% $°C^{-1}$ over the ocean and only 0–2% $°C^{-1}$ over land (Samset et al., 2018a). Based on Precipitation Driver Response Model Intercomparison Project (PDRMIP), temperature-driven intensification of land-mean precipitation during the twentieth century has been masked by fast precipitation responses to anthropogenic sulphate and volcanic forcing. As projected sulphate forcing decreases and warming continues, land-mean precipitation is expected to increase more rapidly and may become clearly observable by the mid-21st century (Richardson et al., 2018).

Precipitation exhibits a significant rapid adjustment in response to forcing. Rapid adjustments account for large regional differences in hydrological sensitivity across multiple drivers (Myhre et al., 2017; Samset et al., 2016). The rapid regional precipitation response to increased CO_2 is robust among models, implying that the uncertainty in long-term changes is mainly associated with the response to SST-mediated feedbacks (Richardson et al., 2016). The processes that govern large-scale changes in precipitation are discussed in Chapter 8.

Based on results from the 5 CMIP6 models available, we conclude that it is *virtually certain* that, in the long term, global precipitation will increase with GSAT rise. It will *likely* increase by 1–3% °C^{-1} for the SSP5-8.5 scenario. Precipitation will *likely* increase in monsoon regions and high latitudes.

4.5.1.5 Global Monsoon Precipitation and Circulation

In the AR5, the changes of the global monsoons were assessed in the context of long-term trends across the 21st century and the change by the end (2081–2100) of the 21st century. The AR5 showed that there is growing evidence of improved skill of climate models in reproducing the climatological features of the global monsoon. Taken together with identified model agreement on future changes, the global monsoon, aggregated over all monsoon systems, is *likely* to strengthen in the 21st century with increases in its area and intensity, while the monsoon circulation weakens. Monsoon onset dates are *likely* to become earlier or not to change much and monsoon retreat dates are *likely* to be delayed, resulting in lengthening of the monsoon seasons in many monsoon regions. In the CMIP5 models the global monsoon area (GMA), the global monsoon total precipitation (GMP), and the global monsoon precipitation intensity (GMI) are projected to increase by the end of the 21st century (2081–2100). In all RCP scenarios, GMA is *very likely* to increase, and GMI is *likely* to increase, resulting in a *very likely* increase in GMP, by the end of the 21st century (2081–2100) (Kitoh et al., 2013).

Since the AR5, there has been considerable progress in understanding the physical reasons governing the projected changes. The multi-model ensemble of the four best CMIP5 models for simulating GM properties projects that under the RCP4.5 scenario the NH monsoon precipitation is projected to increase much larger than the SH counterpart due to increase in temperature difference between the NH and SH, significant enhancement of the Hadley circulation, and atmospheric moistening, against stabilization of troposphere (Lee and Wang, 2014). It has been suggested that the dynamic effect plays more important role on regional differences in projected precipitation change among different monsoon regions than the thermodynamic effect. In the Asian monsoon regions, the monsoon circulation slows down at a much lower rate than in the other monsoon regions (Endo and Kitoh, 2014). Under the RCP4.5 scenario, the CMIP5 models project enhanced global monsoon activity, with the increases of GMA, GMP, and GMI by 1.9%, 3.2%, and 1.3%, respectively, per degree Celsius of surface warming. The increase in GMP is primarily attributed to the increase of moisture convergence, which comes mainly from the increase of water vapour concentration but is partly offset by the convergence effect (Hsu et al., 2013). Under RCP4.5, the interannual variability of monsoon rainfall is projected to intensify mainly over land, and the relationship between monsoon and El Niño is projected to strengthen (Hsu et al., 2013).

Based on the projections of changes in precipitation from CMIP6 under the four priority SSPs, the global monsoon precipitation, aggregated over all monsoon systems, is *likely* to strengthen in the 21st century with increases in its intensity (Figure 4.11:), while the monsoon circulation weakens (Figure 4.12:). Over the period of 2021–2040, the increase of precipitation for SSP1-2.6 is generally stronger than that of SSP5-8.5, while over the long-term period (2081–2100), the increase of monsoon precipitation under SSP5-8.5 is far stronger than that of SSP1-2.6. In the long-term period (2081–2100), the global monsoon precipitation index projected to increase by 0.9–1.7 % per 1°C GSAT rise (5–95% range of the available projections), but the global monsoon circulation index is projected to decrease by 10.4– 19.4 % per 1°C GSAT rise, based on all of the priority SSPs from five available CMIP6 simulation (*medium confidence* owing to limited data availability).

[We will further assess changes in GMA, GMI, and GMP for the four priority SSPs of CMIP6 once data becomes available.]

4.5.1.6 Sea Level Pressure, Large-scale Atmospheric Circulation, Storm Tracks and Blocking

In this subsection, we will assess projected long-term changes in aspects of the large-scale atmospheric circulation including sea level pressure patterns (Figure 4.25:), zonal wind changes (Figure 4.26:), storm track density and blocking. Here we will specifically address the robustness of projected changes and key uncertainties (Shepherd, 2014). We will also assess new understanding on key characteristics and mechanisms in atmospheric circulation (Ceppi et al., 2018; Zappa and Shepherd, 2017) including Hadley cell expansion (Nguyen et al., 2015) and poleward shift in storm tracks (Li et al., 2018a; Mbengue and Schneider, 2017; Shaw et al., 2016; Tamarin-Brodsky and Kaspi, 2017), changes induced by stratospheric ozone and water vapour (Maycock et al., 2013; Chiodo and Polvani, 2017) .

The AR5 assessed that mean sea level pressure is projected to decrease in high latitudes and increase in the mid-latitudes as GSAT rise. Such a pattern is associated with a poleward shift in the storm track and an increase in the annular mode index. Figure 4.25: shows seasonal mean sea level pressure changes for 2081–2100 in a low greenhouse emission scenario (SSP1-2.6) and a high GHG emissions scenario (SSP5-8.5). The broad pattern of increasing sea level pressure in mid-latitudes and decreasing pressure over polar regions is most pronounced for the high GHG forcing scenario. In SSP1-2.6, an opposite response is found at southern high latitudes, which in austral summer can be attributed to the relatively more important role of ozone recovery for the circulation in the absence of a larger global warming signal.

[START FIGURE 4.25 HERE]

Figure 4.25: Multi-model mean change (hPa) in JJA and DJF mean sea level pressure in 2081–2100 in SSP1-2.6 and SSP5-8.5 relative to 1995–2014 [Figure produced with ESMValTool (Eyring et al., 2016b) based on the five CMIP6 models BCC-CSM2-MR, CanESM5, CNRM-CM6-1, IPSL-CM6A-LR, and MRI-ESM2-0. More CMIP6 models will be added as they become available.]

[END FIGURE 4.25 HERE]

Storm tracks and mid-latitude westerly jets are dynamically related aspects of mid-latitude circulation. The AR5 assessed that a poleward shift of the Southern Hemisphere (SH) westerlies and storm track is *likely* by the end of the 21st century in the RCP8.5 scenario. In contrast, *low confidence* was assessed for the storm-track response in the Northern Hemisphere (NH).

Figure 4.26: shows changes in annual and zonal mean zonal wind at the end of the century (2081–2100) for the SSP1-2.6 and SSP5-8.5 scenarios. In both scenarios there is a strengthening and lifting of the subtropical jets in both hemispheres, consistent with the response to large-scale tropospheric warming found in earlier generations of climate models (Collins et al., 2013). In the SH, there is on average a weak equatorward shift of the mid-latitude jet in SSP1-2.6. This annual mean perspective masks the fact that changes in the SH mid-latitude jet are expected to show a seasonal variation owing to the relative importance of ozone recovery and GHGs as a driver of circulation changes in different seasons. This relative balance is further evident when examining the SSP5-8.5 scenario in Figure 4.27:, which shows a stronger poleward shift in the SH mid-latitude jet compared to the weak equatorward shift in SSP1-2.6 (Barnes and Polvani, 2013). In the NH, the changes in lower tropospheric zonal mean zonal winds by the end of the century are smaller than found in the SH and reflect an average over potentially divergent regional wind changes particularly over the major NH ocean basins (Simpson et al., 2014).

[START FIGURE 4.26 HERE]

Figure 4.26: Multi-model mean annual mean zonal wind change (m s^{-1}) in 2081–2100 in (left) SSP1-2.6 and (right) SSP5-8.5 relative to 1995–2014. Results are based on the IPSL-CM6A-LR and BCC-CSM models. The 1995–2014 climatology is shown in contours with spacing 10 m s^{-1}. [More CMIP6 models to be added as they become available.]

[END FIGURE 4.26 HERE]

[START FIGURE 4.27 HERE]

Figure 4.27: Multi-model mean change in winter (NH DJF, SH JJA) zonal wind at 850 hPa (*u850*) in 2081–2100 in (left) SSP1-2.6 and (right) SSP5-8.5 relative to 1995–2014. The 1995–2014 climatology is shown in contours with spacing 10 m s^{-1}. [More CMIP6 models to be added as they become available].

[END FIGURE 4.27 HERE]

CMIP5 models show a strong seasonal and regional dependence in the response to climate change of NH westerlies (Barnes and Polvani, 2013; Grise and Polvani, 2014; Simpson et al., 2014; Zappa et al., 2015). CMIP5 projections indicate a poleward shift of the westerlies in the North Atlantic in summer, and in both the North Pacific and North Atlantic in Autumn (Simpson et al., 2014). The shift of the westerlies is more uncertain in the other seasons, particularly in the North Atlantic in winter (Zappa and Shepherd, 2017). A poleward shift of the jets and storm tracks is expected in response to an increase in the atmospheric stratification and in the equator-to-pole meridional temperature gradient (Harvey et al., 2014; Shaw et al., 2016). Progress since the AR5 has better highlighted how different climate change aspects can drive different, and potentially opposite, responses in the mid-latitude jets and storm tracks. Potential drivers include the patterns in sea surface warming (Ceppi et al., 2018; Langenbrunner et al., 2015; Mizuta et al., 2014), land-sea contrast (Shaw and Voigt, 2015), the loss of sea ice (Deser et al., 2015; Harvey et al., 2015; Screen et al., 2018b), and the strength of the stratospheric vortex (Grise and Polvani, 2017; Manzini et al., 2014; Simpson et al., 2018). From an energetics perspective, the uncertainty in the response of the jet streams depends on the response of clouds, their non-spatially uniform radiative feedbacks shaping the meridional profile of warming (Ceppi and Hartmann, 2016; Ceppi and Shepherd, 2017; Voigt and Shaw, 2016). The influence from competing dynamical drivers and the absence of observational evidence suggests there is at most *medium confidence* on a poleward shift of the NH low-level westerlies in autumn and summer and *low confidence* in the other seasons.

As stated in the AR5, the number of extratropical cyclones (ETC) composing the storm tracks is projected to decline in the future projections, but by no more than a few percent. The reduction is mostly located on the southward flank of the storm tracks, which is associated with the Hadley cell expansion and a poleward shift in the mean genesis latitude of ETCs (Tamarin-Brodsky and Kaspi, 2017). Furthermore, the poleward propagation of individual ETCs is expected to increase with warming (Graff and LaCasce, 2014; Tamarin-Brodsky and Kaspi, 2017), thus contributing to a poleward shift in the mid-latitude transient-eddy kinetic energy. The increased poleward propagation results from the strengthening of the upper tropospheric jet and increased cyclone-associated precipitation (Tamarin-Brodsky and Kaspi, 2017), which are robust aspects of climate change.

The number of ETCs associated with intense surface wind speeds and undergoing explosive pressure deepening are projected to strongly decrease in the NH winter (Kar-Man Chang, 2018; Seiler and Zwiers, 2016). Some previous studies had found an increase in the frequency of extreme NH ETCs, but these conflicting results have been reconciled in the light of changes in the background pressure field rather than in dynamical aspects of ETCs (Chang, 2014). There are, however, regional exceptions such as in the northern North Pacific, where explosive and intense ETCs are projected to increase in association with the poleward shift of the jet and increased upper-level baroclinicity (Seiler and Zwiers, 2016). The weakening of surface winds of ETCs in the NH is attributed to the reduced low-level baroclinicity from SST and sea ice changes (Harvey et al., 2014; Seiler and Zwiers, 2016; Wang et al., 2017b). Eddy kinetic energy and intense cyclone activity is also projected to decrease in the NH summer in association with a weakening of the jet (Chang et al., 2016; Lehmann et al., 2014). However, it remains unclear how important a future increase in mesoscale latent heating could be for the dynamical intensity of ETCs (Li et al., 2014; Michaelis et al., 2017; Pfahl et al., 2015; Willison et al., 2015). Because mesoscale heating is presumably not properly represented at the spatial resolution of CMIP5 climate models, there is only *medium confidence* in the projected decrease in the frequency of intense NH ETCs.

In contrast to the NH, CMIP5 models indicate that the frequency of intense ETCs will increase in the SH (Chang, 2017). This response follows from both an increase in the meridional SST gradient, linked to the slower warming of the Southern Ocean, and from the poleward shift in the upper level jet (Grieger et al., 2014). The wind speeds associated with ETCs are therefore expected to intensify in the SH storm track for high emission scenarios (*high confidence*). The ozone hole and GHG increases have a similar impact on ETC tracks (Grise et al., 2014), so that the ozone hole recovery could largely compensate the GHG signal in low emission scenarios.

Regardless of dynamical intensity changes, the number of ETC associated with extreme precipitation is projected to greatly increase with warming (*high confidence*), due to the increase moisture-loading capacity of the atmosphere (Hawcroft et al., 2018; Yettella and Kay, 2017).

[We will further assess changes in characteristics of ETC in four SSPs from the CMIP6 models (Figure 4.28:) as more data becomes available.]

[START FIGURE 4.28 HERE]

Figure 4.28: Multi-model mean change in winter, extratropical storm track density (NH DJF, SH JJA in 2081–2100 in SSP5-8.5 relative to 1995–2014. [AR5 Figure 12.20, to be updated when high frequency output becomes available from CMIP6].

[END FIGURE 4.28 HERE]

Blocking is associated with a class of quasi-stationary high-pressure weather systems in the middle and high latitudes that disrupt the prevailing westerly flow. These events can persist for extended periods such as a week or longer, and can cause long-lived extreme weather conditions, from heat waves in summer to cold spells in winter. The AR5 assessed with *medium confidence* that the frequency of blocking would not increase under enhanced GHG concentrations, while changes in blocking intensity and persistence remained uncertain.

CMIP5 projections suggest that the response of blocking frequency to climate change might be quite complex (Dunn-Sigouin et al., 2013; Masato et al., 2013). An eastward shift of winter blocking activity in the NH is indicated (Kitano and Yamada, 2016; Lee and Ahn, 2017; Masato et al., 2013; Matsueda and Endo, 2017) while during boreal summer blocking frequency tends to decrease in mid-latitudes (Matsueda and Endo, 2017) and to increase in high latitudes (Masato et al., 2013). However, as shown in (Woollings et al., 2018), the spatial distribution and the magnitude of the suggested changes are sensitive to the blocking detection methods (Barriopedro et al., 2010; Davini et al., 2012; Schwierz et al., 2004). In the SH, blocking frequency is projected to decrease in the Pacific sector during austral spring and summer. However, seasonal and regional changes are not totally consistent across the models (Parsons et al., 2016).

To better understand the uncertainty in future blocking activity, a process-oriented approach has been proposed that aims to link blocking responses to different features of the global warming pattern. The upper-level tropical warming might be the key factor leading to a reduced blocking because of the strengthening of zonal winds (Kennedy et al., 2016). The more controversial influence of near-surface Arctic warming might lead to an increase blocking frequency (Francis and Vavrus, 2015; Mori et al., 2014).

The large differences among models and the large sensitivity to the blocking detection methods suggest that there is at most *medium confidence* in a shift of the major centres of blocking activities, with a decrease of blocking frequency in those regions with the largest frequencies during the historical period.

[We will further assess changes in atmospheric blocking frequencies in four SSPs from the CMIP6 models (Figure 4.29:) as more data becomes available.]

[START FIGURE 4.29 HERE]

Figure 4.29: Box plot showing wintertime (December to March) present-day (1986–2005) and future climate (2081–2100) atmospheric blocking frequencies over (a) the Greenland region (65°W–20°W, 62.5°N–72.5°N), (b) the Central European region (20°W–20°E, 45°N–65°N), (c) the North Pacific region (130°E–150°W, 60°N–75°N). Values show the percentage of blocked days per season following the (Davini et al., 2012) index. Median values are the black horizontal bar. The numbers below each bar report the number of models included. Observations are obtained as the average of the ERA-Interim Reanalysis, the JRA-55 Reanalysis and the NCEP/NCAR Reanalysis.

[END FIGURE 4.29 HERE]

4.5.2 Cryosphere, Ocean, and Biosphere

4.5.2.1 Ocean Temperature

This subsection assesses the vertical cross-sections of zonal and annual mean ocean temperature change (Figure 4.30:). We assess the robustness and uncertainties of the patterns as well as the key characteristics and underlying mechanisms (Exarchou et al., 2015), including an assessment of forced changes in the Southern Ocean (Frölicher et al., 2015; Swart et al., 2018).

Since the AR5, significant improvement has been made in the observation-based ocean heat content estimate by improving methods used to account for spatial and temporal gaps in ocean temperature measurements (Cheng et al., 2017, 2019). The newly estimated observation-based change in ocean heat content is larger than reported by the AR5 and consistent with the reconstruction of the radiative imbalance at the top of atmosphere starting in 1985 (Cheng et al., 2017). Also, the new ocean heat content estimate is in line with the mean of CMIP5 results, providing greater confidence in model-projected ocean temperature change in the future. For the mean of 2081–2100 relative to 1991–2005, CMIP5 models project an ocean heat content change (0–2000m) of 1037 ZJ (around 0.40°C) and 2020 ZJ (around 0.78°C) for RCP 2.6 and RCP 8.5, respectively (Cheng et al., 2019).

The redistribution of heat to the ocean interior is governed by a collection of complicated processes. Changes in different processes can either warm or cool the ocean. In the 70-year idealized $4\times CO_2$ experiments performed by three climate models, it is found that convective and mixed-layer processes, as well as eddy-related processes, tend to cool the subsurface ocean, whereas advective and diapycnically diffusive processes tend to warm the ocean interior (Exarchou et al., 2015). The Southern Ocean plays a dominant role in the global ocean heat uptake. CMIP5 model simulation shows that during the period 1861–2005, about 75% ocean heat uptake occurs in the Ocean south of 30°S (Frölicher et al., 2015). The observed warming of the Southern Ocean since 1950s is primarily attributed to increase in GHGs, and the effect of stratospheric ozone depletion is much smaller (Swart et al., 2018). It is *very likely* that the Southern Ocean will continue playing a major role in the ocean heat uptake.

The multi-model mean projection of zonally averaged ocean temperature change in 2081–2100 relative to 1995–2014 (Figure 4.30:) shows that excess heat has penetrated to the ocean interior as deep as about 2000 m. In the deep ocean, the warming is much more pronounced in the Southern Ocean. A slight cooling is observed in the deep ocean of the mid-to-high latitude Northern Hemisphere (NH), which might be associated with projected reduction in the strength of AMOC. [These aspects will be further assessed in the four priority SSPs from more CMIP6 models as more data becomes available.]

[START FIGURE 4.30 HERE]

Figure 4.30: Multi-model mean change (°C) in annual mean ocean temperature in 2081–2100 in (left) SSP1-2.6 and (right) SSP5-8.5 relative to 1995–2014. [AR5 Figure 12.12 lower panels, to be updated for FOD].

[END FIGURE 4.30 HERE]

4.5.2.2 Ocean acidification

It is *virtually certain* that continued penetration of anthropogenic CO_2 from the surface to the deep ocean will acidify the ocean interior. The continued acidification of the deep ocean can be demonstrated by the shoaling of the saturation horizon of calcium carbonate, which represents the interface below which seawater is undersaturated with calcium carbonate. At present, the calcium carbonate saturation horizon is much shallower in the subarctic Pacific and the Southern Ocean, compared to that of the North Atlantic (Feely et al., 2004). With continued CO_2 emission, the saturation horizon of both aragonite and calcite will move towards the surface (Figure 4.31:). More comprehensive assessment will be done on the future ocean acidification under the four priority SSPs from more CMIP6 models.

[START FIGURE 4.31 HERE]

Figure 4.31: Latitude-depth distribution of aragonite saturation state under RCP 8.5 in year 2100 for the Atlantic (upper panel) and Pacific Ocean (lower panel). Overplotted is the aragonite saturation horizon at year 2010 (dotted lines) and 2100 (solid lines). Results are shown for the median projection of CMIP5 model results (taken from Figure 6.29 of the AR5, to be updated with CMIP6 SSP1-2.6 and SSP5-8.5 results relative to 1995–2014).

[END FIGURE 4.31 HERE]

4.5.3 Modes of Variability

In this subsection the mid- to long-term evolution of the large-scale climate modes of variability and their associated teleconnections is assessed. Assessments of the physical mechanisms and the individual feedbacks involved in the future change of each mode are provided in Chapters 8–10.

4.5.3.1 Northern and Southern Annular Modes

The NAM and NAO

The AR5 assessed from CMIP5 simulations that the future boreal wintertime northern annular mode (NAM) is *very likely* to exhibit natural variability and forced trends of similar magnitude to that observed in the past and is likely to become slightly more positive in the future. Considerable uncertainty existed related to physical mechanisms to explain the observed and projected changes in the NAM, but it was clear that NAM trends are closely connected to projected shifts in the mid-latitude jets and storm tracks. It was reported that some debate existed in the literature as to whether the NAM is part of the forced response to anthropogenic influence, or an additional source of natural variability (e.g., Zhang et al., 2006).

NAM projections from climate models analysed since the AR5 reveal broadly similar results to the AR5 for the late 21st century, showing a positive trend with comparable magnitude to the multi-model or multi-realization variability. While CMIP5 models simulate interannual variability of the NAM that closely matches observations, the clear impression from literature is that decadal and multidecadal variability of the NAM are uniformly underestimated (Wang et al., 2017d).

In long-term projections under the SSP5-8.5 scenario for an ensemble of CanESM6 simulations the signature of NAM change becomes somewhat clearer above the variability (Figure 4.32:). The NAM becomes much more positive in all season excluding the boreal summer, where on the contrary it decreases. In boreal winter the central estimate for the NAM is more than four times higher than the current one. This estimate from CanESM6 is in partial contrast with the wintertime change in the CMIP5 multi-model ensemble, where it has been shown a considerable uncertainty even by 2100 (Gillett and Fyfe, 2013). This uncertainty provides further evidence that our inability to make more precise projections of changes to the NAM is primarily by a lack of physical understanding (Shepherd, 2014) and imperfect models (Lee et al., 2019; Zappa et al., 2014), rather than by internal climate variability.

The SAM

Figure 4.32: shows the long-term southern annular mode (SAM) changes under the SSP5-8.5 scenario for an ensemble of CanESM6 simulations. Under this forcing scenario, the SAM becomes substantially more positive by the end of the century relative to 1995–2014 than was found for the near-term, 2021–2040 (see Section 4.4.3.1). In austral winter and spring, the central estimate for the increase in SAM is more than four times larger than over 2021–2040. In austral autumn and winter, the increase in SAM is larger by around a factor of three to four compared to the projected near-term changes (see Section 4.4.3.1). The amplitude of the changes in SAM at the end of the century will depend strongly on the GHG forcing scenario being considered, with larger trends for a higher forcing scenario (Barnes et al., 2014; Barnes and Polvani, 2013).

[START FIGURE 4.32 HERE]

Figure 4.32: Simulated Annular Mode index change from present-day to the long-term: (a) NAM and (b) SAM. The NAM is defined as the difference in zonal mean SLP at 35°N and 65°N (Li and Wang, 2003) and the SAM as the difference in zonal mean SLP at 40°S and 65°S (Gong and Wang, 1999). Present-day values are averages over the period from 1995–2014. Near-term values are averages over the period from 2081–2100. The vertical lines are ensemble-means and the shaded bars are 5–95% confidence intervals on the ensemble means. [These calculations are based on a ten-member ensemble of simulations from one CMIP6 model, CanESM5. Eventually, the figure will be updated using single simulations from the full CMIP6 ensemble.]

[END FIGURE 4.32 HERE]

4.5.3.2 El Niño-Southern Oscillation and its Teleconnections

The El Niño Sourthern Oscillation (ENSO) influences global climate and is the dominant source of seasonal climate predictability (Timmermann et al., 2018), and will very likely remain so in the future (Cai et al., 2015). While pronounced low-frequency modulations of ENSO exist in unforced control simulations (Wittenberg, 2009), there is potential for anthropogenically forced changes in both ENSO SST variability and climate impacts in the mid-term to long-term future (Cai et al., 2015). While a subset of CMIP5 models that simulate linear ENSO stability realistically exhibit a decrease in ENSO amplitude by the latter half of the 21st century (Figure 4.16:), there is no strong consensus among models on long-term Niño 3.4 SST changes when considering all models (Cai et al., 2015) as shown in Figure 4.33:. However, an increase of Eastern Pacific (EP)-ENSO SST variance has been shown when taking into account the biases in the ENSO pattern simulation by different models (Cai et al., 2018a).

The ENSO characteristics depend on the climate mean state of the tropical Pacific; however, ENSO can also change the mean state through nonlinear processes (Cai et al., 2015; Timmermann et al., 2018). The response of the tropical Pacific mean state to anthropogenic forcing is characterized by a faster warming on the equator compared to the off-equatorial region, a faster warming of the eastern equatorial Pacific compared to the central tropical Pacific, and a weakening of the Walker circulation in most models. These changes are associated with enhanced precipitation on the equator, especially in the eastern part of the basin (Cai et al., 2015; Watanabe et al., 2012).

While there is no strong model consensus on how these mean state changes affect ENSO SST variability, consensus exist that these changes are conducive to an increase in extreme ENSO-associated rainfall even if ENSO SST variability itself remains unchanged (Cai et al., 2015; Power et al., 2013). Moreover, there is an indication that tropical cyclones will become more frequent during future El Niño events (and less frequent during future La Niña events) by the end of the 21st century (Chand et al., 2017), thus contributing to the projected increase in ENSO-associated hydroclimate impacts. These projected changes of ENSO impacts depend, however, critically on the projected climate mean state changes. For instance, one CMIP5 model that warms less in the eastern than in the western Pacific exhibits a pronounced decrease in extreme ENSO events (Kohyama and Hartmann, 2017). This example highlights the importance of constraining tropical Pacific mean state changes in order to enhance confidence in the projected response of Pacific climate variability, such as ENSO.

[START FIGURE 4.33 HERE]

Figure 4.33: Comparison between past and future probability distributions of ENSO SST anomalies computed using two different ENSO indices (Cai et al., 2015), namely Niño3 and Niño4 Indices. [A similar analysis based on the CMIP6 multi-model ensemble potentially will be shown in this subsection. Additionally, a figure for ENSO-associated hydroclimate changes will be shown.]

[END FIGURE 4.33 HERE]

4.5.3.3 Pacific Decadal Variability

The AR5 assessed that there is *low confidence* in projections of future changes in Pacific decadal variability (PDV) due to the inability of CMIP5 models to satisfactory represent the connection between PDV and Indo-Pacific SST variations. Because the PDV appears to encompass the combined effects of different dynamical processes operating at different timescales, its correct representation in CMIP5 climate models is still discussed and its long-term evolution under climate change is still uncertain.

On top of the challenge to narrow uncertainty in the future evolution of all potential mechanisms at play in PDV, it also remains unclear how the background state in the Pacific Ocean will change due to time-varying radiative forcing, and how this change will interact with variability at interannual and low-frequency timescales (Fedorov et al., 2019). Recent research suggests that PDV would have weaker amplitude and higher frequency with global warming (Geng et al., 2019; Xu and Hu, 2017; Zhang and Delworth, 2016). The former appears to be associated with a decrease in SST variability and the meridional gradient over the Kuroshio-Oyashio region, and with a reduction in North Pacific wind stress and the meandering of the subpolar/subtropical gyre interplay (Zhang and Delworth, 2016). The latter is hypothesized to rely on the enhanced ocean stratification and shallower mixed layer of a warmer climate, which would increase the phase speed of the westward-propagating oceanic waves, hence shortening the decadal-interdecadal component (Goodman and Marshall, 1999; Xu and Hu, 2017; Zhang and Delworth, 2016). The weakening of the PDV in a warmer climate may reduce the internal variability of global mean surface temperature, to which PDV seems associated (Kosaka and Xie, 2016; Zhang et al., 1997). Thus, a weaker and more frequent PDV could reduce the disturbance of the internal variability to the global warming trend and eventually lead to a reduced probability of global warming hiatus events.

Concerning secular variations, a multi-model projection suggests the PDV shift into a negative phase, particularly towards the end of the century for which the trend becomes statistically significant, although not absent of model diversity and uncertainty (Lapp et al., 2012). The influence of the anthropogenic climate change on PDV, however, is still unclear (Liu and Di Lorenzo, 2018)

On the basis of recent studies conducted using CMIP5 models, there is still low *confidence* on how PDV would change under global warming. [This statement should be confirmed (or not) when the new results from CMIP6 models will be available.]

4.5.3.4 Indian Ocean Basin and Dipole Modes and their Teleconnections

In the mid- to long-term period, the projected climate mean state changes in the tropical Indian Ocean resemble a positive Indian Ocean dipole (IOD) state, with faster warming in the west compared to the east (Cai et al., 2013; Zheng et al., 2013b). However, it was argued that this projected mean state change could be due to the large mean state biases in the simulated current climate and potentially not a realistic expectation (Li et al., 2016a). If the mean state change will indeed resemble a positive IOD state however, this would lead to a reduction in the amplitude difference between positive and negative IOD events, but with no robust change in IOD frequency (Cai et al., 2013). For a small subset of CMIP5 models that simulate IOD events best, a slight increase in IOD frequency was found under the CMIP5 RCP4.5 scenario (Chu et al., 2014) .

However, it was also found that the frequency of extreme positive IOD events, which exhibit the largest climate impacts, might increase by a factor of about three under the CMIP5 RCP8.5 scenario (Cai et al., 2014). An approximate doubling of these extreme positive IOD events was still found for global warming of 1.5 °C warming above pre-industrial levels, without a projected decline thereafter (Cai et al., 2018b). These results depend however on how realistic the projected mean state change is in the Indian Ocean and could thus potentially turn out to be spurious (Li et al., 2016a).

For a small subset of CMIP5 models that simulate IOB events best, a considerable decrease in IOB frequency was found under the CMIP5 RCP4.5 scenario (Chu et al., 2014). For a different subset of models however, it was found that ENSO-related IOB warming increases under the same CMIP5 RCP4.5 scenario (Tao et al., 2015).

Given the results that ENSO events in general (Cai et al., 2018a) and extreme El Niño events (Cai et al., 2014) are projected to increase in response to greenhouse warming, and given the close relationship between ENSO-IOD (Stuecker et al., 2017) and ENSO-IOB (Du et al., 2013; Xie et al., 2009), ENSO-related IOD and IOB variability might increase. Currently, no new studies and evidence exist that would suggest a disappearance of either IOD or IOB variability in the mid-term to long-term future. This means that we also expect that the ENSO-IOD and ENSO-IOB relationships observed in the current climate will persist in the future (*high confidence*).

4.5.3.5 Atlantic Multidecadal Variability

Based on paleoclimate reconstructions and model simulations, the AR5 assessed that AMV is *unlikely* to change its behaviour in the future. However, AMV fluctuations over the coming decades are *likely* to influence regional climates, enhancing or offsetting some of the effects of global warming. No new results on AMV projections have become available since the AR5. There is clearly a knowledge gap on long-term changes of the AMV under global warming.

4.5.3.6 Tropical Atlantic Modes and their Teleconnections

In spite of remarkable progresses made in CMIP5 with respect to CMIP3, climate models are generally not able to correctly simulate the main aspects of Tropical Atlantic variability (TAV) and associated impacts. This is *likely* the main reason why in the AR5 there are very few studies dealing with long-term changes in TAV. The models that best represent the Atlantic meridional mode (AMM) show a weakening for future climate conditions. However, model biases in the Atlantic Niños are too strong to properly assess changes. Nevertheless, there is robust evidence over multiple generations of models of a warming in the mean state of the Tropical Atlantic basin, though the impact of climatological changes on the variability is quite uncertain.

Long-term changes in TAV modes and associated teleconnections are expected as a result of global warming, but large uncertainties exist (Cai et al., 2019; Lübbecke et al., 2018). Observational analyses show large discrepancies in SST and trade winds strength (Mohino and Losada, 2015; Servain et al., 2014). Single-model sensitivity experiments show that Atlantic Niño characteristics at the end of twenty firsts century remain equal to those of the twentieth century, though changes in the climatological SSTs can lead to changes in the associated teleconnections (Mohino and Losada, 2015).

The weakening of the Atlantic Meridional Overturning Circulation (AMOC) expected from global warming (e.g., Jackson et al., 2016a; Robson et al., 2014) has been suggested to have an influence on the mean background state of tropical-Atlantic surface conditions, thereby enhancing equatorial Atlantic variability and resulting in a stronger tropical Atlantic–ENSO teleconnection (Svendsen et al., 2014). But again, based on CMIP5 and CMIP6 results [to be confirmed as more data becomes available], we conclude that there is a clear lack of model studies investigating the long-term evolution of TAV and associated teleconnections. Most of studies rely on a single model, and hence a large uncertainty exists. The strong model biases together with limitations in the observational record might explain this lack of progress.

4.6 Implications of Climate Policy

4.6.1 Patterns of Climate Change for Specific Levels of Global Warming

This section provides an assessment of changes in climate at 1.5°C, 2°C, 3°C, and 4°C of global warming above pre-industrial levels, including a discussion of the regional patterns of change in temperature (Section 4.6.1.1), precipitation (Section 4.6.1.2), aspects of atmospheric circulation (Section 4.6.1.3) and global modes of variability (Section 4.6.1.4). An assessment of changes in extreme weather events as a function of different levels of global warming is provided in Chapter 11, whilst corresponding analyses of regional changes in climate are provided in Chapter 12 and in the Atlas. This section builds upon assessments from the AR5 WGI report (Bindoff et al., 2013; Christensen et al., 2013; Collins et al., 2013; Hartmann et al., 2013) and Chapter 3 of the IPCC Special Report on Global Warming of 1.5°C (SR1.5; (Hoegh-Guldberg et al., 2018)), as well as a substantial body of new literature related to projections of climate at 1.5°C, 2°C and higher levels of global warming above pre-industrial levels.

Several methodologies have been applied to estimate the spatial patterns of climate change associated with a given level of global warming. These include performing model simulations under stabilisation scenarios designed to achieve a specific level of global warming (e.g. Dosio et al., 2018; Kjellström et al., 2018; Mitchell et al., 2017), the analysis of epochs identified within transient simulations that systematically exceed different thresholds of global warming (e.g. Hoegh-Guldberg et al., 2018), and analysis based on statistical methodologies that include empirical scaling relationships (ESR) (e.g., Dosio and Fischer, 2018; Schleussner et al., 2017; Seneviratne et al., 2018b) and statistical pattern scaling (e.g., Kharin et al., 2018). These different methodologies are discussed in some detail in Subsection 4.2.5 (see also James et al., 2017) and generally provide qualitatively consistent results regarding changes in the spatial patterns of temperature and rainfall means and extremes at different levels of global warming.

In this subsection we present the projected patterns of climate change obtained following the epoch approach (also called the time-shift method, see Section 4.2.4) under the transient SSP5-8.5 scenario. For each simulation considered, 11-year moving averages of the global average atmospheric surface temperature are first constructed, and this time series is used to detect the first year during which global warming exceeds the 1.5°C, 2°C, 3°C and 4°C threshold with respect to the pre-industrial (1850–1900) GSAT. A 21-year global climatology is subsequently constructed to represent each of the levels of global warming, centred on the year for which a particular threshold was first exceeded. Some of the complexities of scaling patterns of climate change with different levels of global warming are also discussed in the following sections, with supporting analysis that is provided in the Atlas. These include overshoot vs. stabilization scenarios and limitations of pattern scaling for strong mitigation and stabilization scenarios (Tebaldi and Arblaster, 2014).

Pattern scaling performance based on scenario experiments is generally better for near-surface temperature than for precipitation (Ishizaki et al., 2013). For precipitation, rapid adjustments due to different forcing agents must be accounted for (Richardson et al., 2016). Also important are possible non-linear responses to different forcing levels (Good et al., 2015, 2016). Pattern scaling does not work as well at high forcing levels (Osborn et al., 2018). It is also important to distinguish the forced response from internal variability when comparing similar warming levels (Suarez-Gutierrez et al., 2018). The purpose of this section is not to repeat the analysis for all the variables considered in Sections 4.4 and 4.5, but rather to show a selected number of key variables that are important from the perspective of understanding the response of the physical climate system to different levels of warming.

4.6.1.1 Temperature

A global warming of 1.5°C implies higher mean temperatures compared to the preindustrial levels across the globe, with generally higher warming over land compared to ocean areas (*virtually certain*) (Figure 4.34:). In addition, a global warming of 2°C versus 1.5°C results in robust increased in the mean temperatures in almost all locations, both on land and in the ocean (*virtually certain*), with subsequent further warming at almost all locations at higher levels of global warming (*virtually certain*). For each particular level of global warming, relatively larger mean warming is projected for land regions (*virtually certain*, see Figure 4.34:, also see (Christensen et al., 2013; Collins et al., 2013; Seneviratne et al., 2016)). The largest increase in mean temperature is found in the high latitudes of the Northern Hemisphere (NH) (*high confidence*; Figure 4.34:). This is due to substantial ice-snow-albedo-temperature feedbacks that constitute 'polar amplification' (Masson-Delmotte et al., 2013). In the Southern Hemisphere (SH) the relatively strong warming in subtropical southern Africa may be attributed to strong soil-moisture–temperature coupling and projected increased dryness under enhanced subsidence (Engelbrecht et al., 2015; Vogel et al., 2017). These projected changes at 1.5°C and 2°C global warming are consistent with the attribution of observed historical global trends in temperature (see Chapter 3), as well as with some observed changes under the recent global warming of 0.5°C (SR1.5; (Hoegh-Guldberg et al., 2018; Schleussner et al., 2017)).

[START FIGURE 4.34 HERE]

Figure 4.34: Projected spatial patterns of changes in annual mean temperature (°C) at 1.5°C, 2°C, 3°C, and 4°C of global warming compared to the pre-industrial period (1850–1900) (top), and the spatial differences of temperature change between 2°C, 3°C, and 4°C of global warming relative to 1.5°C of global warming (bottom). Cross-hatching highlights areas where at least two-thirds of the models (two out of three models at the time of the FOD; the models are BCC-CSM2-MR, IPSL-CM6A-LR, and MRI-ESM2-0) agree on the sign of change, as a measure of robustness. Values were assessed from the transient response over a 21-year period at a given warming level, based on SSP5-8.5 in CMIP6. Note that the responses for stabilization scenarios at 1.5°C and 2°C of global warming are similar (see Atlas, Section X.1). Maps depicting the effects of differential aerosol forcing on spatial patterns of temperature change at different levels of global warming are shown in Section X.2 of the Atlas.

[END FIGURE 4.34 HERE]

4.6.1.2 Precipitation

It is *virtually certain* that global precipitation will increase with increased global mean surface temperature. The AR5 assessment based on CMIP5 simulations showed that global-mean precipitation will increases with global temperature change across a range from 1% to 3% $°C^{-1}$. Percentage precipitation change at different levels of global warming based on three CMIP6 models from SSP5-8.5 are shown in Figure 4.35:. Precipitation increase with increase in global mean temperature, however, patterns of precipitation change does not scale linearly with surface air temperature increase. A number of recent studies have demonstrated that global hydrological sensitivity, the relative change of global-mean precipitation per degree of global warming, shows large diversity among models (Myhre et al., 2017; Samset et al., 2016, 2018a). The response of global mean precipitation to warming is constrained by global energy balance (O'Gorman et al., 2012; Pendergrass and Hartmann, 2014; Richardson et al., 2018). Precipitation response can be considered as a fast response due to atmospheric instability and correlates with radiative forcing associated with atmospheric absorption, whereas the slower response caused by changes in surface temperature correlates with radiative forcing at the top of the atmosphere (Samset et al., 2016). Differences in how the fast adjustment processes are represented within models are expected to explain a large fraction of the present model spread in the precipitation projections (Myhre et al., 2017).

[START FIGURE 4.35 HERE]

Figure 4.35: Projected spatial patterns of changes in annual precipitation (expressed as a % change) at 1.5°C, 2°C, 3°C and 4°C of global warming compared to the pre-industrial period (1850–1900). Stippling highlights areas where at

least two-thirds of the models (two out of three models at the time of the FOD; the models are BCC-CSM2-MR, IPSL-CM6A-LR, and MRI-ESM2-0) agree on the sign of change, as a measure of robustness. Values were assessed from the transient response over a 21-year period at a given warming level, based on SSP5-8.5 in CMIP6. Note that the responses for stabilization scenarios at 1.5°C and 2°C of global warming are similar (see Atlas, Section X.1). Maps depicting the effects of differential aerosol forcing on spatial patterns of temperature change at different levels of global warming are shown in Section X.2 of the Atlas.

[END FIGURE 4.35 HERE]

It is *very likely* that extreme precipitation events will increase with increased GSAT (Fischer and Knutti, 2016). Global warming of 1.5°C–2°C will result in increase in heavy precipitation events over several high-latitude regions, as well as in the tropics. The risks of increases in heavy precipitation events at 1.5°C global warming will be less as compared to 2°C global warming on global as well as on regional scale (*medium confidence*) (SR1.5; (Hoegh-Guldberg et al., 2018)). Statistically significant differences in heavy precipitation at 2°C versus 1.5°C global warming is found in several regions, aggregated over the global land area. However, there is *medium confidence* regarding global-scale differences in precipitation means and extremes at 2°C versus 1.5°C global warming. Similar assessment based on CMIP6 projections will be performed for precipitation response to 3°C and 4°C of global warming.

The AR5 assessed that with the increase in temperature, there is *high confidence* that contrast of annual mean precipitation between dry and wet regions and that the contrast between wet and dry seasons will increase over most of the globe. Recent studies have also shown that 1.5 °C and 2.0 °C global warming have regional implications; summer rainfall over the Asian monsoon regions will increase in both means and the extremes. Based on CMIP5 projections, area and population exposures to dangerous extreme precipitation events was shown to increase with warming over the global land monsoon regions (Zhang et al., 2018). The SR1.5 stated *low confidence* regarding changes in global monsoons at 1.5°C versus 2°C of global warming, as well as differences in monsoon responses at 1.5°C versus 2°C. Recent studies (Jacob et al., 2018; Kjellström et al., 2018; Vautard et al., 2014) have shown that 2°C of global warming was associated with a robust increase in mean precipitation over central and northern Europe in winter but only over northern Europe in summer, and with decreases in mean precipitation in central/southern Europe in summer. For change in regional annual average precipitation, 2.5°C–3°C is required for a statistically significant change (Tebaldi et al., 2015).

It is *virtually certain* that average warming will be higher over land than over the ocean. Precipitation variability in most climate models increases over a majority of global land area in response to warming. The global average sensitivity of the 20-year return value of the annual maximum daily precipitation increases with temperature increase, with large regional variations (Kitoh and Endo, 2016; Westra et al., 2013).

In summary, based on the available CMIP6 models it is *virtually certain* that global precipitation will increase with increased global mean surface temperature. Precipitation increase on land will be higher at 3°C and 4°C compared with 1.5°C warming (*high confidence*). It is *very likely* that extreme precipitation events will increase with increased global mean surface temperature.

4.6.1.3 Atmospheric Circulation

The AR5 assessed that under high levels of global warming (3°C or 4°C of global warming) there is *high confidence* of a poleward shift of the Southern Hemisphere (SH) storm tracks, even in the presence of ozone recovery (Stocker et al., 2013). A general southward shift of the low-level annually-averaged SH westerly winds are projected by the CMIP6 ensemble under 1.5°C and 2°C of global warming in the transient SSP5-8.5 scenario (Figure 4.36:) (*strong agreement* across the CMIP5 and available CMIP6 projections, *high confidence*). This pattern of change strengthens from 1.5°C to 2°C of global warming (*high confidence*), with further amplification of the pattern from 3°C to 4°C of warming (Figure 4.36:) *(high confidence)*. This poleward displacement of the westerlies is projected to occur in association with a decrease in the strength of the westerlies over the southern parts of South America, southern Africa and Australia (Figure 4.36:). Moreover, the circumpolar westerlies are projected to strengthen increasingly across increasing levels of global warming under SSP5-8.5, with an associated poleward shift in the mid-latitude jets and an intensification of extratropical cyclones under 3 and 4 ºC of global warming *(high confidence)*. Across all levels of global warming, the poleward expansion of the SH westerlies in summer is projected to be opposed by ozone recovery.

The AR5 assessed that under 3°C and 4°C of global warming there is low confidence in projections of poleward shifts of the Northern Hemisphere storm tracks (Stocker et al., 2013), and the available CMIP6 projections (Figure 4.36:) constitute a similar conclusion. A weakening of the Mediterranean storm track is expected already under low 1.5 and 2°C of global warming (Li et al., 2018a), with this signal strengthening under higher levels of global warming *(medium confidence).*

[START FIGURE 4.36 HERE]

Figure 4.36: Projected spatial patterns of change in near-surface winter zonal winds (m/s, 1000 hPa) at 1.5°C, 2°C, 3°C and 4°C of global warming compared to the pre-industrial period (1850–1900) for the SH (Panels a to d), and NH (Panels e to h). Cross-hatching highlights areas where at least two-thirds of the models (2 out of 3 models at the time of the FOD) agree on the sign of change, as a measure of robustness. Values were assessed from the transient response over a 21-year period at a given warming level, based on SSP5-8.5 in CMIP6 model simulations. Note that the responses for stabilization scenarios at 1.5°C and 2°C of global warming are similar (see Atlas, Section X.1). Maps depicting the effects of differential aerosol forcing on spatial patterns of temperature change at different levels of global warming are shown in Section X.2 of the Atlas.

[END FIGURE 4.36 HERE]

4.6.1.4 Global Modes of Variability

The AR5 assessed from CMIP5 simulations that there is *medium confidence* in near-term projections of an increase of the northern annular mode (NAM) and northward shift of the Northern Hemisphere (NH) storm tracks and westerlies, because of the large response uncertainty and the potentially large influence of internal variability (Collins et al., 2013). In particular, the AR5 assessed that the future boreal wintertime NAM is *very likely* to exhibit large natural variations and is *likely* to become slightly more positive in the future. NAM projections from climate models assessed since AR5 similarly indicate a positive trend through the 21st century (Wang et al., 2017d). Although there are currently not studies available that directly analyse changes in NAM as a function of the level of global warming, such an assessment can be obtained by translating projected changes in NAM in the near-term to the corresponding levels of global warming, and similarly so for long-term projections in NAM under transient low-mitigation scenarios. Based on results from one CMIP5 model, CanESM, it may be concluded that there is *medium confidence* for the boreal wintertime NAM to become more positive under 1.5 to 2 ºC of global warming. The same assessment can be made with *high confidence* under 3 or 4 ºC of global warming (Figure 4.37:).

The AR5 assessed that the positive trend observed in the southern annular mode (SAM) in recent decades is *likely* to weaken in the presence of stratospheric ozone recovery during the 21st century. Despite the current lack of studies that explicitly examine changes in SAM as a function of the level of global warming, such changes can still be deduced by comparing projections for the near-term and the medium- to long term, which, under transient low-mitigation scenarios such as SSP5-8.5, simulate relatively low levels of global warming in the near term and higher levels later on (Barnes et al., 2014; Barnes and Polvani, 2013). The competing effects of changing greenhouse gas concentrations and ozone recovery on the Southern Hemisphere circulation over the next several decades are *likely* to determine the response of SAM under different levels of global warming. Under stabilization scenarios, where global warming is 1.5 or 2 ºC by the end of the 21st century, it is *likely* for SAM to assume a week negative trend in the austral summer (but still with a positive trend for the remaining seasons). Under 3 and 4 ºC of global warming, however, the positive trend in the SAM is projected to persist even in the presence of stratospheric ozone recovery (Figure 4.37:) (*medium confidence*).

[START FIGURE 4.37 HERE]

Figure 4.37: Simulated Annular Mode index change under 1.5°C, 2°C, 3°C and 4°C of global warming. (a) Northern Annular Mode (NAM). (b) Southern Annular Mode (SAM). The NAM is defined as the difference in zonal mean sea-level pressure (SLP) at 35°N and 65°N (Li and Wang, 2003) and the SAM as the difference in zonal mean SLP at 40°S and 65°S (Gong and Wang, 1999). Values were assessed from the transient response over a 21-year period at a given warming level, based on SSP5-8.5 in CMIP6. The vertical lines are ensemble-means and the shaded bars are 5–95% confidence intervals on the ensemble means. [These calculations are based on a ten-member ensemble of simulations from one CMIP6 model, CanESM5. Eventually, the figure will be updated using single simulations from the full CMIP6 ensemble.]

[END FIGURE 4.37 HERE]

Recent studies suggest potential for continuous increase in the number of strong El Niño as the level of surface warming increases (Wang et al., 2017a). We will further assess ENSO mean and variability changes under different degree of warming (Figure 4.38:).

[START FIGURE 4.38 HERE]

Figure 4.38: Simulations of sea surface temperature (SST) averaged over the ENSO Nino 3.4 region under 1.5°C, 2°C, 3°C, and 4°C of global warming relative to the pre-industrial period (1850–1900). Values are assessed from transient simulations by averaging over a 21-year period centred at the given warming level, based on SSP1-2.6 and SSP5-8.5 from one CMIP6 model. The vertical lines are ensemble means, and the shaded bars are 5–95% confidence intervals on the ensemble means. [These calculations are based on a ten-member ensemble of simulations from one CMIP6 model, CanESM5. Eventually, the figure will be updated using single simulations from the full CMIP6 ensemble.]

[END FIGURE 4.38 HERE]

4.6.2 Climate Targets, Path-Dependence, and Overshoot

This subsection does not assess climate warming levels in the context of climate policy (assessed by WGIII) but will be informed by this literature (cf., SR1.5). The subsection will include assessment of when certain levels of warming such as 1.5°C and 2°C might be reached and assess levels of atmospheric CO_2 concentration consistent with given climate targets (e.g., (Betts and McNeall, 2018); see Section 4.3.1). We will assess how different scenarios alter these timings and also time of emergence (ToE) and benefits of mitigation (Hawkins et al., 2014; Mora et al., 2013; Tebaldi and Friedlingstein, 2013). [Note: A full assessment is not possible in this FOD owing to limited data availability from CMIP6].

There is strong evidence that climate response to increased CO_2 forcing is not linear (*high confidence*). It has been shown that the first 2°C of warming does not have the same characteristics as the second 2°C under idealized CO_2 simulations (Good et al., 2016). Simulations undertaken as part of the cloud feedback model intercomparison project (CFMIP, (Webb et al., 2017)(Webb et al., 2017)) will assess to what extent regional climate change for doubling of CO_2 is linear (state dependent). Climate sensitivity has been found to be state dependent (nonlinear) under different levels of forcing (Andrews et al., 2012; Knutti and Rugenstein, 2015). Hence it is *very likely* that patterns of climate change at 2°C will differ depending on the rate and timing of reaching this level and the combination of forcing within the scenario (Figure 4.39:).

[START FIGURE 4.39 HERE]

Figure 4.39: Projected changes in the global pattern of near-surface temperature and precipitation associated with a 2°C increase in global temperature achieved by different pathways. Example above shows the doubling difference and ratio from experiments to 2× and 4× CO_2 taken from (Good et al., 2016).

[END FIGURE 4.39 HERE]

There is *low confidence* in knowledge of the extent of reversibility of climate patterns following overshoot of a global temperature target. While global mean temperature is expected to decline approximately reversibly with reducing CO_2 (Section 4.7.2), regional patterns may not be the same as at the same level prior to overshoot. [We will draw on results from SSP5-3.4-overshoot scenarios.]

4.6.3 Climate Response to Mitigation, Carbon Dioxide Removal, and Solar Radiation Modification

Anthropogenic climate change can be limited by mitigation through reduced emissions of GHGs but also by intentional large-scale interventions in the climate system, sometimes referred to as geoengineering, climate engineering, or climate intervention (e.g., (National Research Council, 2015a, 2015b)). Two categories of climate intervention have been proposed, carbon dioxide removal (CDR) and solar radiation modification (SRM). SRM, also referred to as solar radiation management in the literature, refers to a range of radiation modification measures not related to greenhouse gas (GHG) mitigation that seek to limit global warming. There is some overlap between mitigation and CDR, but they are treated separately here, because mitigation refers to reducing emissions while CDR refers to methods that remove carbon already in the atmosphere. Most strong-mitigation scenarios assume the use of CDR in addition to emissions reductions; for example, RCP2.6 explicitly includes direct CDR from around 2025 onward and achieves net negative emissions by 2070 through a combination of bioenergy and carbon capture and storage (van Vuuren et al., 2011). Similarly, the emission profile of SSP1-1.9 is characterized by a rapid decline to zero and a long period of negative emissions for CO_2 (O'Neill et al., 2016).

Here we assess only the climate system response to mitigation and suggested methods of climate intervention; the technical, economic, and political feasibility will be assessed as part of the Working Group III Sixth Assessment Report (AR6).

4.6.3.1 Climate Response to Mitigation

Mitigation through reduced GHG emissions would slow and limit the degree of climate change relative to high emissions scenarios such as SSP5-8.5 (*very high confidence*). Because the peak warming depends on the cumulative carbon emissions (Allen et al., 2009; Frame et al., 2014; Matthews et al., 2018; Meinshausen et al., 2009), mitigation in the 21st century will help to avoid specific peak temperatures by 2100. Conversely, late mitigation could lead to overshoot of specific temperature levels.

Mitigation of GHGs is also associated with mitigation of short-lived climate forcing agents such as black carbon aerosols (Rogelj et al., 2014). Eliminating short-lived negative forcings from sulphate aerosols at the same time (e.g., by air pollution reduction measures) is *likely* to cause a temporary warming of a few tenths of a degree (Lelieveld et al., 2019; Matthews, 2011; Samset et al., 2018b). Regional patterns and rates of change are expected to vary with the type of emissions reduction; for example, black carbon aerosols and CH_4 emission reductions causing larger regional changes and acting faster than CO_2 reductions, because the forcing is more heterogeneous, and the lifetimes of these agents are substantially shorter than CO_2 (Chapter 6).

Mitigation would reduce CO_2 emissions but atmospheric CO_2 concentrations would continue to increase as long as emissions are larger than a few PgC per year (Matthews, 2010; Miyama and Kawamiya, 2009; Zickfeld et al., 2013). This implies a continued increase in surface temperature even when emissions are decreasing (Millar et al., 2017) and until emission rates fall below the threshold level of a few PgC per year *(high confidence*). The threshold depends on the specific levels of CO_2 stabilization. Even if anthropogenic greenhouses-gas emissions were halted now, the radiative forcing due to long-lived GHGs concentrations, and consequently surface temperatures, would decrease only slowly in the future, at a rate determined by the lifetime of the gas (Collins et al., 2013).

Because inertia and internal variability affect the physical climate system and the global carbon cycle, there would be a lag between emission peak, CO_2 concentration peak, and peak in GSAT (*high confidence*) (Ricke and Caldeira, 2014; Zickfeld and Herrington, 2015). This lag has implications for the timescale of detection of mitigation benefits. The inherent irreducible uncertainty due to internal variability has recently been quantified using a very large ensemble (100-member) from a single climate model (Marotzke, 2019). The trends in global surface air temperature (GSAT) were higher over the period 2021–2035 than over 2006–2020 in one-third of all realizations in the mitigation scenario RCP2.6, suggesting that the GSAT would rise at a faster rate with a probability of as much as one third. The probability was around one-half in the no-mitigation scenario RCP4.5. The climate response to RCP2.6 and RCP4.5 was nearly indistinguishable in the near term, 2005–2035 (Figure 4.40:). Further, mitigation was sufficient to cause a GSAT trend reduction with a low probability of only 0.40 and necessary with a further reduced probability of 0.33 (Marotzke, 2019). These recent results and our improved understanding suggest that in the near term, GSAT might rise at a faster rate than before despite emissions reductions (*medium confidence*).

[START FIGURE 4.40 HERE]

Figure 4.40: Near-term GSAT anomalies relative to the pre-industrial period (here, 1861–1880) in the 100-member Max Planck Institute Grand Ensemble (MPI-GE). (a) GSAT time series for each realization, scenario RCP2.6. (b) As (a) but for scenario RCP4.5. The thick blue, red, and green lines show, respectively, the RCP2.6 and RCP4.5 ensemble means and the observations. The climate response to RCP2.6 and RCP4.5 is nearly indistinguishable in the near term, here 2005–2035, indicating the irreducible uncertainty due to internal variability. [Placeholder figure from (Marotzke, 2019); will be updated using CMIP6.]

[END FIGURE 4.40 HERE]

The SR1.5 (Masson-Delmotte et al., 2018) assessed that climate models project robust differences in regional climate characteristics between present-day and global warming of 1.5°C, and between 1.5°C and 2°C above pre-industrial levels. These differences include increases in mean temperature in most land and ocean regions (*high confidence*), hot extremes in most inhabited regions (*high confidenc*e), heavy precipitation in several regions *(medium confidence*), and the probability of drought and precipitation deficits in some regions (*medium confidenc*e). This question was also recently addressed using an ensemble simulations from NCAR CESM, and it was found that the exceedance of historical record temperature occurs with 60% greater frequency in the 2°C climate than in a 1.5°C climate aggregated globally, and with twice the frequency in equatorial and arid regions, and extreme precipitation intensity is statistically significantly higher in a 2.0°C climate than a 1.5°C climate in some specific regions (Sanderson et al., 2017b). Further, the Benefits of Reduced Anthropogenic Climate changE (BRACE) project assessed the differences in impacts between the RCP4.5 and RCP8.5 scenarios using large ensembles simulated with the NCAR CESM. Clear benefits of mitigation have been found in the case of extremes in temperatures and precipitation (Fix et al., 2018; Lehner et al., 2018; O'Neill et al., 2016; Oleson et al., 2018; Sanderson et al., 2018). Reduction in the frequency of extreme precipitation events associated with tropical cyclones is also possible through mitigation from RCP8.5 to RCP4.5 (Bacmeister et al., 2018).

How many years it takes to detect the benefits of mitigation at global and regional scales was first investigated by Tebaldi and Friedlingstein (2013), analysing five CMIP5 models and a three-member initial-condition ensemble for each model. The emissions in scenarios RCP4.5 and RCP8.5 depart from the mitigation scenario RCP2.6 in 2020 and 2010, respectively, but the median time of detection for departure of CO_2 concentration in the RCP4.5 and RCP8.5 scenarios from the RCP2.6 scenario is about 10 years. For GMST the median detection time of mitigation was about 25-30 years (Tebaldi and Friedlingstein, 2013), which translates into detection of a mitigation signal by 2035 (RCP8.5) or 2045 (RCP4.5). The difference in detection time between CO_2 concentration and GSAT is related to the difference in signal-to-noise ratio between CO_2 and GSAT (*high confidence*).

The time of detection of mitigation depends on the seasons and the regions (Tebaldi and Friedlingstein, 2013). Generally, winter temperatures are more challenging for detection, adding a decade to the detection time *(high confidence*), whereas detection times for summer averages are similar to the annual temperature averages. This is mainly due to larger variability in winter temperatures. Detection happens later at regional CORDEX and Giorgi domains with a median detection time of 30–45 years after emission paths separate (Tebaldi and Friedlingstein, 2013). A stricter requirement of 95% confidence level induces a delay of several decades, bringing detection time toward the end of the 21st century at regional scales. There are also large uncertainties in detection times; the range for regional domains is up to 60 years (2020–2080) for RCP4.5 vs. RCP2.6 (Tebaldi and Friedlingstein, 2013). Such large uncertainties result from uncertainty in climate sensitivity and internal variability (*high confidence*).

Because the detection time for CO_2 concentration is only about 10 years, much shorter than that for physical climate quantities, the absence of early detectability of the climate benefits of mitigation is due to the inertia and internal variability of the physical climate system rather than the global carbon cycle (*medium confidence*). Moreover, based on results from traditional detection and attribution studies, the time to detection is expected to be further delayed for precipitation and sea level rise (Tebaldi and Friedlingstein, 2013) (*high confidence*). Using large ensembles, (Tebaldi and Wehner, 2018) recently found that statistically significant differences between RCP4.5 and RCP8.5 in extreme temperatures over all land areas become pervasive over the globe by 2050. A multi-model ensemble analysis of warm-season temperatures in the RCP2.6 and RCP8.5 scenarios (Ciavarella et al., 2017) also found that it takes less than 20 years of emissions reductions in many regions for the likelihood of extreme seasonal warmth to reduce by more than half following initiation of mitigation.

More recent studies (Sanderson et al., 2018) reach similar conclusions using single-model ensembles: while internal variability is *likely* a significant component of uncertainty for periods before 2050, there are significantly reduced extreme warm events in some regions as early as 2030 in RCP4.5 relative to RCP8.5. The period 2061–2080 *is likely* to see largely separate joint distributions of annual mean temperature and precipitation in most regions for the two scenarios. Hence, for the latter portion of the 21st century, the range of regional climatic states that might be expected in the RCP8.5 scenario is significantly and detectably further removed from today's climate state than the RCP4.5 scenario even in the presence of internal variability (*high confidence*).

4.6.3.2 Climate Response to Carbon Dioxide Removal

Chapter 5 discusses different CDR schemes and their implications for global biogeochemical cycles. In this sub-section, only the climate system response to CDR is assessed. CDR is also referred to as 'negative emissions'; the term 'net emissions' refers to the difference between anthropogenic carbon emissions and removal by CDR methods, and negative net emissions imply a scenario where CO_2 removal exceeds emissions. All CDR schemes would lead to a reduction in atmospheric CO_2 concentration relative to a scenario without CDR and hence lower global surface air temperature (GSAT); however, their maximum potential varies (*high confidence*; see Chapter 5). Furthermore, a delay would be expected between CDR deployment and net negative emissions (van Vuuren et al., 2011); mere deployment of CDR would not cause reduction in atmospheric CO_2 levels, and CO_2 removed by CDR should exceed emissions for CO_2 levels in the atmosphere to decrease. Hence, deployment of CDR is expected to precede net negative emissions and the consequent reduction in rate of warming by decades.

According to integrated assessment modelling studies, limiting global mean surface warming to 2°C above pre-industrial levels by 2100 is difficult without the use of CDR schemes (Rickels et al., 2018). As discussed in Chapter 5, when removal by CDR exceeds emissions, the net decrease in atmospheric CO_2 would be less than the net emissions because oceans and land are expected to outgas CO_2 when atmospheric CO_2 concentrations decrease (Cao and Caldeira, 2010; Jones et al., 2016b). This outgassing of CO_2 from the natural reservoirs is often referred to as the 'rebound effect'. Therefore, if temperatures were to be returned to pre-industrial levels, all anthropogenic carbon that is stored in the ocean, land, and atmosphere would have to be removed, not just the atmospheric anthropogenic carbon load. Even when applied continuously and at scales as large as currently represented in the RCP8.5 scenario as reference, all CDR methods are individually either relatively ineffective with limited (8%) warming reductions, or they have potential severe side effects (Keller et al., 2014) (*medium confidence*).

Because of the inertia, the climate system response is expected to lag behind the deployment of CDR (*high confidence*). Since the AR5, a growing number of studies have simulated the climate response to CDR, including the Carbon Dioxide Removal Model Intercomparison Project (CDRMIP). Key climate variables, including temperature, precipitation, the sea-ice area, the Atlantic Meriodional Overturning Circulation (AMOC), and sea level lag the deployment of CDR, as illustrated in multi-model simulations of CDR (Figure 4.41:). In particular, notwithstanding a decline in atmospheric CO_2, global mean thermosteric sea level would continue to rise for several decades and would not return to pre-industrial levels for over 1000 years after atmospheric CO_2 is restored to the pre-industrial concentration (Ehlert and Zickfeld, 2018).

[START FIGURE 4.41 HERE]

Figure 4.41: Simulated lag and irreversibility in global and annual mean climate variables against atmospheric CO_2. a) Normalized anomaly for key climate variables, b) surface air temperature, c) precipitation, d) Arctic sea ice area, e) Atlantic meridional overturning circulation, and f) thermosteric sea level rise as a function of atmospheric CO_2. Atmospheric CO_2 concentration increases at 1% per year to $4\times CO_2$ and then decreases at 1% per year again to return to pre-industrial levels. Multi-model mean (solid lines) and individual model results (thin lines) that participated in CDRMIP are shown. For surface air temperature, results are shown for 7 models (ACCESS1, BNU-ESM, CNRM1-ESM, Mk3L-COAL, NorESM, UVic, and OSCAR). For precipitation, results are shown for 4 models (ACCESS1, BNU-ESM, CNRM1-ESM, and NorESM). For sea-ice area, AMOC, and sea level rise, only UVic model results are shown.

[END FIGURE 4.41 HERE]

Global mean precipitation would increase initially in response to an abrupt CO_2 reduction (Cao et al., 2015). This is related to the fast adjustments (directly forcing-related changes) in the climate system, before global mean surface temperature increases. Several studies (Bala et al., 2010; Cao et al., 2012; Myhre et al., 2018; Richardson et al., 2016) have shown that when CO_2 in the atmosphere is abruptly increased, global mean precipitation is reduced before global mean surface temperature increases. An opposite initial change in precipitation was found in these studies for a CDR-related decline in CO_2.

The relationship between cumulative carbon emissions and surface temperature change becomes nonlinear during periods of negative emissions owing to the lagged response of the deep ocean to previously increasing CO_2 (Zickfeld et al., 2016). When corrected for this lagged response, or if the CO_2 decline is applied after the system has equilibrated with the previous CO_2 increase, the relationship between temperature change and cumulative carbon emissions is again close to linear during periods of net negative CO_2 emissions.

Termination of CDR schemes is expected to cause increasing warming trends, associated with outgassing of CO_2 upon termination of CDR (*medium confidence*). The rate of outgassing is conditional on the method of storage. For instance, (González et al., 2018) found that termination of alkalinity addition to oceans could cause regions of the Northern Hemisphere to warm at a rate that is 50% larger than those in RCP8.5, with rates similar to those caused by termination of SRM over the following three decades after cessation (up to 1.5°C per decade). In case artificially enhanced upwelling would be stopped, atmospheric CO_2 concentrations could rise rapidly, and hence warming would occur because carbon removed from the atmosphere and stored in soils in the cooler climate caused by artificial upwelling could be rapidly released back (Oschlies et al., 2010).

4.6.3.3 Climate Response to Solar Radiation Modification

By definition, solar radiation modification (SRM) schemes would intentionally use large or planetary scale engineering techniques to reduce the amount of sunlight absorbed by the planet by 1–2% (e.g., (Caldeira et al., 2013)). Several SRM schemes were discussed in detail in the AR5 and in the SR1.5. A short summary that updates these SRM proposals is listed in Table 4.6:. All schemes, except for cirrus cloud thinning, aim to cool the Earth by deflecting more solar radiation to space. Cirrus cloud thinning aims to cool the planet through increasing the longwave radiation to space, which could be achieved by reducing the amount of high clouds in the climate system (Storelvmo et al., 2014) (Mitchell and Finnegan, 2009). SRM could be considered as part of the overall strategy to limit global warming below 1.5°C (MacMartin et al., 2018).

In this sub-section, we assess the physical climate system response to SRM, whereas Chapter 5 assesses the biogeochemical implications. Since the AR5, substantial improvement has been made in SRM research. Many more modelling studies have been conducted on climate response to different SRM schemes, including those that participate in the Geoengineering Model Intercomparison Project (GeoMIP6, (Kravitz et al., 2015)), which started at the time of the AR5 (Kravitz et al., 2013a). Also, some studies have attempted to design novel SRM strategies to meet different climate goals simultaneously (Cao et al., 2017; Tilmes et al., 2018).

[START TABLE 4.6 HERE]

Table 4.6: A brief summary of the various SRM proposals

SRM scheme	How does the SRM scheme work?	Potential for countering a warming from a doubling of CO_2 (RF=3.5 W m^{-2})	Key side effects	References
Stratospheric Aerosol Injection (SAI)	Injection of sulphate aerosols into the stratosphere which scatter sunlight back to space; radiative forcing could be uniform	Achievable with 10 Mt S per year injection (equivalent to Mt. Pinatubo eruption)	Changes to stratospheric chemistry and circulation; increase in diffuse light at the surface; less intense global hydrological cycle	(Ferraro and Griffiths, 2016; Niemeier and Timmreck, 2015; Pitari et al., 2014)
Marine cloud brightening (MCB)	Injection of sea salt aerosols to increase the albedo of marine low clouds; heterogeneous radiative forcing	Achievable if nearly 75 % of ocean area is seeded but there are large uncertainties.	Uncertain regional changes in precipitation patterns; sea salt deposition on land	(Ahlm et al., 2017; Latham et al., 2012; Stjern et al., 2018)
Whitening the roofs	Painting the roof of buildings to increase the reflectivity; heterogeneous radiative forcing	Not achievable; max potential RF about 0.1 W m^{-2}	Potential changes to urban climate	(Seneviratne et al., 2018a)
Lightening the colour of the crops	Genetically modify the colour of crops to increase sunlight reflection; heterogeneous radiative forcing	Not achievable; max potential RF about 0.5 W m^{-2}	Uncertain changes to regional precipitation patterns	(Seneviratne et al., 2018a)
Ocean albedo increase	Add reflecting particles on the ocean surface or create microbubbles by stirring the ocean surface; land-sea radiative forcing contrast	RF of several Wm^{-2} is achievable	Runoff over land is *likely* to increase	(Gabriel et al., 2017; Kravitz et al., 2013b)
Cirrus cloud thinning (CCT)	Inject ice nuclei in the upper troposphere to reduce the amount of cirrus clouds to allow more longwave radiation to escape to space; heterogeneous radiative forcing	Uncertain	Increase in solar radiation at the surface; reduction in the intensity of the global hydrological cycle is *unlikely*	(Gasparini and Lohmann, 2016; Storelvmo et al., 2014)

Space sunshades	Place mirrors or reflecting particles in space between sun and earth to reflect sunlight back to space; uniform radiative forcing	Achievable by blocking about 2 % of the incoming solar radiation	Less intense global hydrological cycle	(Kalidindi et al., 2015; Kravitz et al., 2013a)

[END TABLE 4.6 HERE]

Recent SRM research has focused on offsetting large amounts of climate change through aerosol injection, which is expected to have several side effects and involves risks such as the termination effect. Recent research has also emphasized more nuanced treatment of SRM in the context of short-term action to complement emissions reductions and aid staying below short-term targets (Keith and MacMartin, 2015; Sugiyama et al., 2018) and limit warming to 1.5°C above pre-industrial levels using an ‘adaptive SRM’ approach (SR1.5) where SRM implementation could span only a few decades to hold warming to 1.5°C (Keith and MacMartin, 2015; MacMartin et al., 2018).

Modelling studies have consistently confirmed that SRM has the potential markedly diminish global and regional climate change from increasing CO_2 concentrations (Irvine et al., 2016) (*high confidence*). One of the key features of SRM is that in principle it can cool the planet rapidly; in highly idealised scenarios the cooling occurs with an e-folding time of only 4–5 years (MacMartin et al., 2017; Matthews and Caldeira, 2007; Tilmes et al., 2017). There is *high confidence* that the solar radiative forcing required to offset a CO_2-induced global surface air temperature (GSAT) change is larger than the CO_2-induced radiative forcing (Russotto and Ackerman, 2018; Schmidt et al., 2012). This is because the efficacy of solar forcing is less than one (meaning the warming effect is smaller than that of an equivalent CO_2 ERF), which has been explained on the basis of differing vertical profile of radiative forcing (Modak et al., 2016). The efficacy of stratospheric sulphate aerosol forcing has also been shown to be less than one (Duan et al., 2018) (*medium confidence*).

The spatial pattern of temperature and precipitation change relative to the corresponding baseline for space sunshading, stratospheric aerosol injection, marine cloud brightening, and cirrus cloud thinning are shown in Figure 4.42:. Each scheme is able to offset CO_2-induced warming, but with disparities in spatial pattern of temperature and precipitation change (Figure 4.42:). The spatial pattern of responses to marine cloud brightening and cirrus cloud thinning has large differences with space sunshading and aerosol injection because the former schemes are associated with large heterogeneous radiative forcing (Table 4.6:).

[START FIGURE 4.42 HERE]

Figure 4.42: The spatial pattern of changes in annual mean temperature (left panels) and precipitation (right panels) from CO_2 reduction, solar constant reduction, stratospheric sulphate aerosols, marine cloud brightening and cirrus cloud thinning experiments. The results are obtained from CESM slab ocean simulations. All geoengineering simulations are designed to offset global mean warming from an abrupt doubling of atmospheric CO_2. All results are shown relative to $2\times CO_2$. Correlation coefficient represent the spatial correlation between geoengineering case and $1\times CO_2$ case, and NRMS is the root-mean-square difference of geoengineering case normalized by that of $1\times CO_2$ case. The departure of the spatial patterns, relative to CO_2 change, is larger for marine cloud brightening and cirrus cloud thinning and less for solar constant reduction and stratospheric sulphate aerosols.

[END FIGURE 4.42 HERE]

There is *high confidence* that there is a trade-off between temperature and precipitation change in response to reduced solar radiation (Irvine et al., 2016; Kravitz et al., 2013a) because of different sensitivity of precipitation change to CO_2 and SRM forcings (Andrews et al., 2009; Bala et al., 2010; Duan et al., 2018; Jackson et al., 2016b). One manifestation of this is that SRM could cause a substantial reduction in global mean precipitation (Bala et al., 2008) and rainfall in the tropical monsoonal regions (Tilmes et al., 2013) if changes in global mean surface air temperature (GSAT) are offset. Further, regional SRM schemes such as

Arctic SRM are expected to have remote influence on the tropical monsoon precipitation by shifting the mean position of ITCZ (Nalam et al., 2018). CO_2-induced increases in extremes in temperature and precipitation and tropical cyclone intensity are expected to be reduced by SRM (Curry et al., 2014; Irvine et al., 2019; Muthyala et al., 2018b, 2018a).

SRM schemes such as marine cloud brightening, which use a highly heterogeneous radiative forcing to cool the climate system, are expected to cause large changes in regional precipitation patterns (Figure 4.42:). Compared to SRM schemes, however, cirrus cloud thinning are expected to intensify the global hydrological cycle (Cao et al., 2017; Kristjánsson et al., 2015; Muri et al., 2018). Therefore, changes in global mean temperature and precipitation are expected to be simultaneously offset by combining different RMMs such as stratospheric aerosol injection and cirrus cloud thinning (Cao et al., 2017) (*low confidence* owing to the large uncertainty in simulating aerosol forcing).

Major modelling results after the AR5 suggest that SRM can be designed to meet different temperature targets. For example, by interactively adjusting the rate of sulphate aerosol injection at different locations, multiple temperature stabilization targets, including global mean temperature, interhemispheric temperature gradient, and equator-to-pole temperature gradient, can be maintained simultaneously at the year 2020 level under the RCP 8.5 scenario (Figure 4.43:) (Kravitz et al., 2017; MacMartin et al., 2017). While these studies looked at broad-scale temperature features, there is still need for assessing the feasibility of meeting multiple targets for other key climate variables such as precipitation and regional features.

Simulations suggest that by offsetting CO_2-induced global mean warming, reduced solar irradiance largely returns Arctic sea ice to pre-industrial levels with modest changes in the seasonal cycle of sea ice extent (Moore et al., 2014). In a scenario where aerosol injection is used to limit radiative forcing at year 2020 levels, September sea ice extent still decreases from 2020 to 2070, presumably because of the high-latitude residual warming, but not as quickly as in the simulation without SRM (Berdahl et al., 2014). When aerosol injection is used to stabilize GSAT at 1.5°C above pre-industrial levels, Arctic sea ice loss is also stabilized (Jones et al., 2018). It is expected that SRM could stabilize the strength of AMOC under high-CO_2 scenarios over timescales from a few decades to thousands of years (Cao et al., 2016; Hong et al., 2017).

[START FIGURE 4.43 HERE]

Figure 4.43: Demonstration of the ability to meet three simultaneous temperature objectives in the state-of-the-art model CESM1(WACCM) via SO_2 injection at four independent locations (30°N, 15°N, 15°S, and 30°S, all at 180°E and 5 km above the annual mean tropopause), where the injection rate is adjusted every year based on feedback of the "observed" climate state. The objectives are to maintain, at 2020 levels, global mean temperature ($\Delta T0$), the interhemispheric temperature gradient ($\Delta T1$), and the equator-to-pole temperature gradient ($\Delta T2$). Top and middle panels show comparisons between the base state (RCP8.5) and the model with geoengineering implemented (referred to as "feedback"); 2020 values, which are the objectives, are indicated by dashed gray lines. Bottom panel shows the injection rate at each location, as well as the sum of all injections. Figure is reproduced from (Kravitz et al., 2017)

[END FIGURE 4.43 HERE]

Stratospheric aerosol schemes are expected to warm the lower stratosphere because of absorption of near-infrared solar and terrestrial longwave radiation by the aerosols, and alter the stratospheric ozone and water vapour concentrations thereby altering the stratospheric and tropospheric circulations (Niemeier and Schmidt, 2017). For instance, model simulations indicate stronger polar jets and weaker storm tracks and poleward shift of the tropospheric mid-latitude jets in response to stratospheric sulphate injections (Ferraro et al., 2015; Richter Jadwiga et al., 2018) as the meridional temperature is increased in the lower stratosphere by the aerosol-induced heating.

Because of internal variability, a full test of the climate system response to SRM is expected to be require a SRM forcing of the size produced by the 1991 Mount Pinatubo eruption (Robock et al., 2010). The effect of

SRM on global temperature and precipitation has been found to be detectable after one to two decades (Bürger and Cubasch, 2015; Lo et al., 2016). Detectability has been examined using the Geoengineering Large Ensemble Project (GLENS) in which SO_2 is injected at different locations starting in 2027 to maintain a 1.5°C target under RCP 4.5 (MacMartin et al., 2019). The analysis shows that for many regions the differences in temperature, precipitation change and precipitation minus evaporation at grid-scale between a climate state with GHG-induced 1.5° C global mean temperature change and another climate state with the same global mean temperature under RCP4.5 emissions and a limited deployment of SRM are not detectable by the end of this century. However, for higher emissions scenarios (the RCP8.5 scenario) and correspondingly larger SRM deployment for maintaining the same global mean temperature change of 1.5°C, the regional differences are detectable readily before the end of the century.

One of the most discussed risks of SRM is the sudden termination of the deployment of SRM because of engineering failure or the lack of agreement for the maintenance of SRM. A sudden termination would cause a rapid increase in global temperature and precipitation, and a reduction in sea ice area (Jones et al., 2013; McCusker et al., 2014) (*high confidence*). Sudden termination of SRM would increase both land and ocean temperature rise to an extent that far exceeds that predicted for future climate change without SRM (McCusker et al., 2014). However, a gradual phase-out of SRM combined with mitigation and CDR is *likely* to avoid the risk from sudden SRM termination (Keith and MacMartin, 2015; Tilmes et al., 2016).

4.7 Very-Long-Term Climate Changes

4.7.1 Change in Global Climate Indices Beyond 2100

This subsection will assess changes in global climate indices out to 2300 using Earth system models (ESM) and Earth system Models of Intermediate Complexity (EMICs) (Eby et al., 2013; Zickfeld et al., 2013). EMIC simulations under four CMIP5 RCP scenarios have shown consistent and complementary climate projections to 2300 with results from AOGCMs (Zickfeld et al., 2013). In these simulations the models followed RCP extensions from 2100–2300 known as Extended Concentration Pathways (ECPs). For example, ECP4.5 had a smooth transition towards a concentration stabilization level after 2150, while ECP8.5 had constant emissions after 2100, followed by a smooth transition to stabilized concentrations after 2250.

Here, a subset of the global climate indices will be assessed including global surface air temperature (GSAT), the Atlantic Meridional Overturning Circulation (AMOC), and probably global mean sea level (GMSL) with key figures similar to Figure 4.44:. Results beyond 2300 may also be shown if results are available.

[START FIGURE 4.44 HERE]

Figure 4.44: (a) Atmospheric CO_2 and projected (b) GSAT change and (c) AMOC change as simulated by EMICs for four RCPs up to 2300 [Placeholder Figure 12.42 from the AR5 – will be updated using more comprehensive EMIC and, if available, simulations with comprehensive ESMs. Other global climate indices may be included further.].

[END FIGURE 4.44 HERE]

4.7.1.1 Global Surface Air Temperature

It is *very likely* that the GSAT will exceed the 1.5°C–2°C target in all scenarios except for the RCP2.6 scenario at the year of 2300 (*high confidence*; Figure 4.44:). The multi-model mean ensemble projection under the RCP2.6 peaks at 1.7°C relative to preindustrial, and returns to 1.3°C by 2300. However, the high-emission scenario RCP8.5 shows continuous increase in GMST, with a multi-model ensemble-mean of 7.5°C temperature rise relative to preindustrial and a range of 4°C–9°C at 2300 (Zickfeld et al., 2013).

4.7.1.2 Global Land Precipitation

(Caesar et al., 2013) showed that under the CMIP5 extension simulations, HadGEM2-ES projected global land precipitation to remain roughly the same in RCP2.6, to increase about 4% in RCP4.5 and to increase about 7% in RCP8.5.

4.7.1.3 Arctic Sea Ice

It was shown that under the CMIP5 extension simulations, most models minimum (September) Arctic ice extent began to recover under RCP2.6 out to 2300, while RCP4.5 and RCP8.5 extensions became ice free in September (Hezel et al., 2014). They also found that under the RCP8.5 extension, the Arctic became ice-free nearly year-round by 2300.

4.7.1.4 Global Mean Sea Level

The AR5 and the SROCC assessed long-term GMSL. By using CMIP5 models out to 2100 and a model emulator out to 2300 to estimate the steric GMSL due to warming, it was found that even under the RCP2.6 extension, GMSL continued to rise out to 2300 (Palmer et al., 2018). Under the RCP4.5 extension, the steric component of GMSL rose from approximately 0.2 m at 2100 to 0.3–0.7 m by 2300. Under the RCP8.5 extension, the steric component of GMSL rose from approximately 0.3 m at 2100 to 0.8–1.6 m by 2300.

4.7.1.5 Atlantic Meridional Overturning Circulation

The AR5 assessed a small number of CMIP5 model simulations of the AMOC beyond 2100 and assessed that once radiative forcing is stabilized, the AMOC begins to recover, but in some models towards less than its pre-industrial level. This assessment was supported in simulations of EMICs following the same ECPs (Zickfeld et al., 2013).

Here, we will briefly assess the AMOC in the CMIP6 model simulations following the SSP extensions past 2100. A more detailed assessment will be undertaken in Chapter 9. We also present long-term simulations of the AMOC in an Earth system model (ESM) (CanESM2) after instantaneous cessation of anthropogenic emissions when global mean surface temperature reaches either 1.5°C, 2.0°C, or 3.0°C global warming relative to pre-industrial after following the RCP8.5 scenario (see Figure 4.45:). In these simulations, the AMOC generally overshoots when emissions are terminated (see Section 4.3), followed by recovery to less than its pre-industrial level. Averaged over the period from 2400–2600, the strength of AMOC is indistinguishable between individual realizations following the 1.5°C and 2.0°C global warming stabilization. On the other hand, following 3.0°C global warming stabilization, each individual simulation settles to a level less than any of the 1.5°C and 2.0°C stabilization simulations. These results raise the issue of the detectability of the long-term impact of different emissions scenarios (Marotzke, 2019).

[START FIGURE 4.45 HERE]

Figure 4.45: Atlantic Meridional Overturning Circulation (AMOC) in ensembles of simulations of an Earth system model (CanESM2). The black curve is the average over 50 simulations following historical forcings to 2005 and RCP8.5 extensions to 2100. The coloured curves are averages over five simulations (each) after global mean surface temperature (GMST) has been stabilized at the indicated degree of warming relative to pre-industrial. The vertical solid lines are the year at which all anthropogenic emissions were terminated and surface temperatures approximately stabilized. The dashed lines are ensemble-means averaged over 2400–2600. The open circles are individual averages over 2400–2600. Data based on (Sigmond et al., 2018).

[END FIGURE 4.45 HERE]

4.7.2 Climate-change Commitment and Irreversibility

While significant GHG emissions are taking place, the Transient Climate Response to cumulative carbon Emissions (TCRE) quantifies the warming up to the point of emission of a given cumulative amount of CO_2 emissions. Once the emissions or the warming stop, continued changes in the climate system occur, termed committed changes. We differentiate between:

(i) Zero Emissions Commitment (ZEC), the committed changes in global climate if we stop emitting GHGs. If emissions of CO_2 cease, the long-term continued uptake of carbon and heat into the ocean tend to offset each other, leading to an approximately constant climate. Deviations from this are the ZEC. Assessment of remaining carbon budgets requires an assessment of ZEC as well as of TCRE. Quantities that continue to evolve on long timescales after emissions cease include sea-level rise, the sea-ice area, the AMOC, some aspects of ocean biogeochemistry, and elements of the monsoon circulations.

(ii) Committed changes in components of the climate system under constant global temperature. For example, sea level would continue to rise for centuries, and ecosystems take many decades to respond to a stabilized climate.

Both the TCRE and the ZEC need to be known to relate carbon emissions to the eventual warming and thus to long-term climate targets. Introducing the TCRE concept was a major advance of the AR5 (Allen et al., 2009; Matthews et al., 2009; Meinshausen et al., 2009). Since the AR5 a considerable literature has developed on constraining the robustness of TCRE (Goodwin et al., 2015; MacDougall, 2016; Millar and Friedlingstein, 2018; Tachiiri et al., 2015) and its sensitivity to emissions trajectories (Krasting et al., 2014; Leduc et al., 2015; Steinacher and Joos, 2016) and ocean mixing (Ehlert et al., 2017).

By contrast, there has been relatively less literature on ZEC. It has been shown (e.g. Joos et al., 2013; Matthews and Caldeira, 2008; Solomon et al., 2009) that there is an offset of continued warming following stopping emissions by continued CO_2 removal by natural sinks. Some models continue the warming by up to 0.5°C after emissions cease at 2°C of warming (Frolicher et al., 2014; Frölicher and Paynter, 2015; Williams et al., 2017), while others simulate little to no additional warming (Nohara et al., 2015). This led the SR1.5 (Rogelj et al., 2018) to make the assumption that on the short-to-near term, ZEC was zero. Here we draw on new simulations to provide an assessment of ZEC from coordinated simulations using multiple ESMs and EMICs. Figure 4.46: shows preliminary results from five models. These initial results are inconclusive whether ZEC on decadal timescales is either positive or negative, with values spanning from approximately –0.4 to 0.2°C. There is therefore *low confidence* in the sign and magnitude of ZEC and its potential impact on the assessed remaining carbon budgets for 1.5°C or 2°C.

[START FIGURE 4.46 HERE]

Figure 4.46: Global CO_2 (top left) and temperature response (lower left) following a sudden cessation of emissions at three points on the 1% per year trajectory. Right hand panel shows collated temperature response from the point of departure after 1000 PgC cumulative emissions (hence the year varies for each model). Figure compiled from preliminary data from UKESM1, MPI-ESM, GFDL-ESM2M, CLIMBER and UVic simulations. Results to be updated from further ESMs and EMICs under the new ZEC-MIP activity quantifying the ZEC consistent with TCRE estimates. This will be a key input to Ch.5 assessment of carbon budgets.

[END FIGURE 4.46 HERE]

Understanding of reversibility of climate system components has advanced since the AR5. Some aspects of the physical climate changes induced by GHG warming have been demonstrated to be reversible (Boucher et al., 2012; Tokarska and Zickfeld, 2015). Others such as sea-level rise or terrestrial ecosystems continue to respond on long timescales (Clark et al., 2016; Pugh et al., 2018; Zickfeld et al., 2017). Reversibility can be defined in terms of the response to CO_2 or the response to global surface air temperature (GSAT). The latter itself is generally believed to be reversible with respect to CO_2 with a short lag. Reversibility with respect to other climate forcers is less commonly examined.

The Carbon Dioxide Removal Model Intercomparison Project (CDR-MIP) (Keller et al., 2018) comprises a set of 1% ramp-down simulations aimed at establishing a multi-model assessment of reversibility of Earth system components, although very little data is yet available. We will assess available literature as it emerges and synthesize a table of elements that do or do not exhibit irreversibility, including the speed of reversibility. Preliminary results from CDRMIP are presented in section 4.6.3. We will also assess results from the SSP5-3.4-Overshoot scenario and quantify spatial patterns of climate change at the same global mean temperature before and after a temperature peak.

[START TABLE 4.7 HERE]

Table 4.7: Synthesis table of components of the climate system which exhibit reversibility with respect to emissions.

quantity	Immediately reversible	Reversible with lag	Overshoots	Irreversible
Global Mean Air Temperature	Most models agree (Andrews and Ringer, 2014; Boucher et al., 2012; Nakashiki et al., 2006; Tsutsui et al., 2007; Zickfeld et al., 2013, 2016)			
Global Ocean Surface Temperature		Decades delay (Boucher et al., 2012; Cao et al., 2011)		
Global Land Surface Temperature	Closely follows air temperature except for permafrost (Boucher et al., 2012)	Permafrost delay (Schuur et al., 2008, 2015)		
Global Mean Precipitation		Decades delay (Boucher et al., 2012; Cao et al., 2011; Tsutsui et al., 2007; Wu et al., 2015)		
Global Land Precipitation		Inconsistent behaviour (Boucher et al., 2012)	Inconsistent behaviour (Boucher et al., 2012)	Inconsistent behaviour (Boucher et al., 2012)
Global Ocean Precipitation		Most models agree (Boucher et al., 2012)		
Sea Ice		Most models agree (Armour et al., 2011; Boucher et al., 2012)		
Ocean heat content				Long timescale of response (Nakashiki et al., 2006; Tsutsui et al., 2007; Zickfeld et al., 2013, 2016))
AMOC		In some models (Nakashiki et al., 2006; Palter et al., 2018)	In some models (Jackson et al., 2016a)	Under extreme Greenland ice melt (Rahmstorf and Ganopolski, 1999)
Land carbon		Long lag of soil/vegetation carbon		

store		stores (Boucher et al., 2012)		
Mixed layer depth			Increased mixing with interior warming (John et al., 2015; Nakashiki et al., 2006)	
permafrost		*Likely* reversible soil freezing (Boucher et al., 2012)		Irreversible loss of decomposed carbon (MacDougall, 2013)
Ocean Carbon Store				Long timescale of response(Cao and Caldeira, 2010; Zickfeld et al., 2013, 2016)
Ice sheets				Irreversible melt (Ganopolski and Rahmstorf, 2001; Rahmstorf and Ganopolski, 1999)

[END TABLE 4.7 HERE]

In their cataloguing of potentially mutually reinforcing climate feedbacks, (Steffen et al., 2015) provided a strawman against which to assess the scientific basis for the various vulnerabilities and associated climate feedbacks, including potential GHG implications of permafrost loss (Schuur et al., 2015). The sea-level rise implications are expected to be substantial. While (Steffen et al., 2015) were very successful in synthesizing the various feedback processes, they were unable to explain how the feedback strengths they provided might quantitatively translate to a very strong warming. As such, their assertion of risk is largely qualitative and speculative.

4.7.3 Potential for Abrupt Climate Change

The AR6 adopts a different definition of abrupt climate change from that used in the AR5. Here we take abrupt change to mean that the nonlinearity of the climate system may lead to abrupt climate changes, sometimes called rapid climate changes, abrupt events, or even surprises. The term abrupt refers to changes that occur faster than the rate of change of forcing (Alley et al., 2003). This definition includes shifts from one equilibrium state to another (tipping points), but also other non-linear responses of the climate system to external forcing (see Section 1.2.4.2 in Chapter 1). Abrupt climate changes typically involve a nonlinear process and its associated threshold.

Abrupt changes in the climate system will be assessed across multiple chapters. This section provides a synthesis, in an update to the AR5 Table 12.4. Classic examples of potential abrupt climate changes include AMOC, Greenland and Antarctic ice sheets, permafrost carbon, methane clathrates, tropical and boreal forests, sea ice, and hydrological cycles/monsoon circulations. AR5 Table 12.4 will be updated based on literature since the AR5 (Table 4.8:) (e.g., (Drijfhout et al., 2015)).

[START TABLE 4.8 HERE]

Table 4.8: Summary table of components in the Earth system that have been proposed in the literature as potentially being susceptible to abrupt or irreversible change. [Based on Table 12.4 from the AR5, to be updated for AR6. Content coordinated across Chapters 1, 4, 5, 8, 9, and 11. Projected changes not yet fully assessed.]

Earth System	Abrupt? (AR6 definition)	Irreversible? (AR6	Projected 21st century	See chapter/section

Component		definition)	change	
AMOC	Possible collapse		*Unlikely* collapse during 21st century	9.2.4.1
Ice Sheets				(Ch.9)
Glaciers	Yes	Yes		9.5.2.6
Permafrost	Yes. Via thermokarst	Yes		9.5.3.5
Snow		No, for seasonal cover. Possible for permanent cover due to snow albedo feedbacks		9.5.4.5 See also 8.6.2.3
Methane Clathrates	Possible CH4 release from clathrates	Yes	*Extremely unlikely* on large scale during 21st century	5.4.8.2, 5.4.8.3
Forest Dieback	Possible if climate threshold crossed	Postulated via feedbacks on rainfall	Partial loss of Amazon forest	5.4.8.1
Ocean Carbon Sink	Wind-induced reduction in Southern ocean carbon sink	No	Not yet assessed	5.4.8.4
Arctic Sea Ice		No		9.3.1.2
Drought	May be triggered by changes in land cover			Anthropogenic: 8.6.2.1 Land-surface feedbacks: 8.6.2.4
Extremes	Extreme events may be triggered by abrupt changes in ocean or atmosphere circulation			11.10.2

[END TABLE 4.8 HERE]

It has been postulated that ESMs may be prone to being too stable (Valdes, 2011), given palaeo evidence of abrupt events (Dakos et al., 2008; Klus et al., 2018; Sime et al., 2019). However, the CMIP5 archive did contain evidence of abrupt changes simulated by these models (Drijfhout et al., 2015).

4.8 Potential for Low-Probability–High-Impact Changes

4.8.1 Low-Probability High-Warming Storylines

Previous IPCC assessments have primarily assessed the projected *likely* or *very likely* range of changes (e.g., (Collins et al., 2013), see also Box 1.1). The focus on the *likely* range partly results from the design of model intercomparison projects that are not targeted to systematically assess the upper and lower bounds of projections, which in principle would require a systematic sampling of structural and parametric model uncertainties. The upper and lower bounds of model projections may further be sensitive to the missing representation of processes.

However, since risk is typically defined as likelihood × impact (Sutton, 2018), an integrated risk assessment requires taking into account high levels of warming. The climate-related risks have been argued to increase with increasing levels of global warming (O’Neill et al., 2017) even if their probability decreases. Thus, it has recently been argued that an assessment that is too narrowly focused on the *likely* range potentially ignores the changes in the physical climate system that are associated with the highest risks (Sutton, 2018).

Given that the CMIP experiments can be considered ensembles of opportunity that are not designed for probabilistic assessments of the tails of the distribution, alternative approaches such as physically plausible high-impact scenario (PPHIS) (Sutton, 2018) or storylines have been suggested (Kjellström et al., 2018; Lenderink et al., 2014; Shepherd et al., 2018; Zappa and Shepherd, 2017). Such storylines of very high warming are less probable to occur than the multi-model mean but are potentially associated with very high levels of impact. Such storylines of high warming can be used to test how well adaptation plans would cope if the impacts of climate change turned out to be more severe than suggested by the *likely* model range.

We here adapt an approach suggested in Sutton, 2018. Since changes increase with the level of warming (Section 4.6.1), a low-probability high-warming storyline is here illustrated based on the model that has a transient climate response to cumulative carbon emissions (TCRE) nearest to the upper bound of the assessed *very likely* range (90% quantile) in Chapter 7 [for the FOD we here select CanESM5 as an illustrative example]. Under SSP5-8.5, global surface air temperature (GSAT) is projected to increase by 6.3°C in 2081–2100 relative 1995–2014. Figure 4.47: illustrates the changes in annual mean temperature and precipitation consistent with this low-probability high-warming storyline. Annual mean temperatures by 2081–2100 are projected to increase by more than 8°C over large land fractions of North America, South America and most of Asia. Over large parts of the Arctic annual mean temperatures increase by more than 12°C. Annual mean precipitation is projected to increase by more than 50% across parts of Asia and Africa. Thereby the projected changes are much larger than the corresponding global mean changes and exceed them by a factor of up to two over large regions. This low-probability high-warming storyline does not correspond to a storyline of high changes in all variables and all regions. The model simulation illustrated in Figure 4.47: illustrates a high level of warming but not necessarily particularly large seasonal mean precipitation or changes in extremes over all regions. On the other hand, the representation of different variables represents a coherent physical climate state that is consistent with the assessed upper bound of TCRE. The changes projected here have not been specifically assessed at the regional scale.

[Note: For the SOD we will evaluate model performance during the historical period and the mean biases of annual mean temperature and precipitation, to assess whether the projection illustrated here can be considered plausible. Furthermore, we will assess the combination of a high TCRE and a strong-mitigation scenario, which has implications for the climate targets and the potential for abrupt changes even under strong mitigation.]

[START FIGURE 4.47 HERE]

Figure 4.47: Changes in annual mean temperature and precipitation in 2081–2100 relative to 1995–2014) in SSP5-8.5 and SSP1-2.6 for a storyline representing a physically plausible high-global-warming future.

[END FIGURE 4.47 HERE]

Knowledge Gaps

1) Lack of probabilities that can be assigned to scenarios (Schneider, 2001).

2) Translation of past performance into assessment of the quality of long-term projections (adequacy-for-purpose, (Parker, 2009)).

3) Potential for abrupt change – this is the perpetual 'unknown unknowns' question wherein a hitherto unquantified positive climate feedback mechanism may come to play (Steffen et al., 2018).

4) With respect to evaluating the robustness of projected future warming based on the historical climate response, uncertainty persists of aerosol and other radiatively active emissions and

concentrations (Lee et al., 2016), both in terms of preindustrial variability (Carslaw et al., 2017) and the early industrial era before strong observational constraints are available (Johnson et al., 2018).

5) Model projections continue to exhibit considerable structural uncertainty, and there is strong suggestion on multiple fronts that even though metrics of variability suggest that climate models are missing important observed modes (Guilyardi et al., 2016), models are overly uncertain in initialized predictions. Potential predictability determined by the ability of a model to predict itself on seasonal to interannual timescales (so called 'perfect model studies') is often lower than actual prediction skill of models in comparison to observations (Scaife and Smith, 2018). On multidecadal timescales, this question was raised in (Durack et al., 2012), because only the model ensemble mean demonstrates a strong spatial correlation with trends in sea surface salinity as reflecting large scale changes in precipitation minus evaporation over the oceans.

6) Lack of future scenario robustness with respect to land carbon projection and budgeting in the context of competing agricultural, biomass, reforestation, afforestation, CO_2 fertilization, nutrient down regulation, air quality, etc. Houghton et al. (2018) demonstrated a strong limitation in the ability to empirically constraining these budgets, much less turn them into a mechanistically robust, predictable modelling framework. Inability of current monitoring systems of carbon cycle to detect and attribute changes on less than multi-decadal timescales to inform historical and future scenario evaluation concentrations (Li et al., 2016c).

7) Detection and attribution of multidecadal variability versus forced change for a broader range of quantities and over scales smaller than continental. The advent of large initial-condition ensembles has recently brought considerable investigation into this field (e.g., Kay et al., 2015), but more work needs to be done.

8) There is a lack of studies investigating variability in the tropical Atlantic and Atlantic multidecadal variability in projections, possibly owing to the persistent climate-model biases especially in the tropical Atlantic.

Frequently Asked Questions

FAQ 4.1: What Can We Say about Climate Change in the Next Twenty Years?

For most climate quantities that have shown a clear trend over the most recent decades, we expect this trend to continue in the next twenty years. Our confidence derives from the increase in radiative forcing due to the expected continued emissions of greenhouse gases and from our scientific understanding and confidence in model simulations of the global-scale changes caused by this increased radiative forcing. However, the magnitude of the changes is much more uncertain, mainly because over a period of twenty years, natural internal variability can mask and for some quantities overwhelm the climate response to the increased radiative forcing. While it is virtually certain that global sea level will continue to rise in the next twenty years, we cannot say much about the change in precipitation averaged over all land areas. We expect that globally averaged surface temperature will continue to rise over the next twenty years, although another slowdown caused by natural internal variability cannot be excluded.

There is a clearly recognized societal need for information about climate change in the next twenty years, defined here as the near term. But this information is difficult to provide robustly. The difficulty arises chiefly because over twenty years, natural internal variability plays a major role relative to the changes expected from the increased radiative forcing. Natural internal variability is caused by chaotic processes in the atmosphere and the ocean, such as the changing weather systems, and even after averaging in time over twenty years, the time averages or calculated trends contain a substantial chaotic element.

In analogy to weather forecasting, natural internal variability can be predicted to some extent, provided that the prediction simulations are started from the observed climate state. These 'decadal predictions' do not attempt to forecast individual weather events, but instead they provide information such as how much warmer or colder future years will be on average, compared to the year just passed. Forecast quality or 'skill' is achieved because some elements of the climate system, primarily the oceans, vary on long timescales. Current models have some skill in predicting these slow variations, such that useful statements about the future state of natural internal variability can be made.

The AR5 was the first IPCC Assessment Report to include information from decadal predictions, and substantial experience has been gained since. But it has also been confirmed that for most climate quantities of interest, natural internal variability cannot presently be skilfully predicted beyond at most ten years into the future. Looking ahead for twenty years, there are indications that natural internal variability will never be predictable over this time horizon, implying that natural internal variability causes some uncertainty that is irreducible.

However, climate simulation results for the next twenty years are less sensitive to which of the emissions scenarios they are based on – in stark contrast to simulation results for the end of the 21st century. The reason for this is well understood; all scenarios show further greenhouse-gas emissions over the next twenty years, leading to increased greenhouse-gas concentrations and hence increased radiative forcing. Hence the globally averaged surface temperature is expected to continue to rise over the next twenty (*high confidence*). If the current rate continues, a warming of 1.5°C above the pre-industrial level is expected to be reached by around 2040, as already stated by the SR1.5.

The area of the Arctic sea ice will continue to reduce in the next twenty years (*high confidence*), and globally averaged sea level is *virtually certain* to rise further. By contrast, we cannot say much about how precipitation averaged globally over all land areas will change over the next twenty years, and there are indications that such a statement cannot ever be made with confidence.

[START FIGURE FAQ 4.1, FIGURE 1 HERE]

FAQ 4.1, Figure 1: Simulations over the period 1995–2040, encompassing the recent past and the near-term future, of four icons of global climate change, (a) globally averaged near-surface air temperature, (b) precipitation averaged globally over land, (c) the area of Arctic sea ice in September, and (d) globally averaged steric sea-level change, which arises purely from ocean warming. All quantities except the Arctic sea-ice area are shown as deviations from the average over the period 1995–2014. The black curves are for the historical period ending in 2014; the colours refer to various SSP scenarios as shown in the inlet. In (c), the dashed horizontal line is at 1 million km^2, the threshold conventionally used for designating an ice-free Arctic. [Placeholder figure, based on the CMIP6 model CanESM5. To be updated with other CMIP6 models and shading for indicating uncertainty. Sea-level change to be augmented by contributions from land-ice melt, something that is not included in the CMIP6 models.]

[END FIGURE FAQ 4.1, FIGURE 1 HERE]

FAQ 4.2: When Greenhouse-Gas Emissions Reduce, What Changes Will We See?

In the long run, reductions in greenhouse-gas (GHG) emissions will limit the surface warming and changes in many climate indicators. In the first few decades after emissions reductions begin, however, their effects on the climate system will be difficult to diagnose, because the combination of climate inertia and natural internal variability will mask the climate system response to the reductions. Emissions reductions are expected to leave a discernible fingerprint on atmospheric CO_2 concentrations after around 10 years, on global surface temperature after around 30 years, and on regional temperatures after around 40 years. An effect of mitigation on regional precipitation trends is expected only later in the 21st century.

Emissions reductions in long-lived GHG, especially in CO_2, will slow down the increase in atmospheric CO_2 concentrations but will over the first few decades not yet lead to a decrease in concentrations. This is a manifestation of one fundamental element of inertia in the climate system. As a consequence, the radiative forcing will also continue to increase, although after around 10 years at a detectably smaller rate. This smaller rate of increase in radiative forcing is expected to lead to a smaller rate of global surface warming. But this reduction in the rate of warming will be overlain by natural internal variability, which is caused by chaotic processes in the atmosphere and the ocean, such as the changing weather systems. Natural internal variability will thus make it difficult to detect in the next two decades whether surface warming has indeed slowed down as a response to the emissions reductions.

There has been some recent research on this difficult detection problem, but not enough for a broad quantitative consensus to have emerged. The difficulties arise at multiple levels. First, we are asking a question about something that will arise at some point in an assumed future, namely whether putative emissions reductions have shown an effect on the climate system. At present we thus have no direct observations to guide us in this juxtaposition of emissions reduction and climate response. Second, there is no unambiguous definition of a no-mitigation emissions pathway against which emissions reductions can be defined. Third, any quantitative answer must rely on climate models simulating the correct ratio of response to emissions reductions on the one hand and the magnitude of natural internal variability on the other hand. Fourth, this detection problem – in analogy to detecting anthropogenic climate change in the observed record of the past – becomes more difficult on the regional scale and for many quantities other than temperature. And fifth, even if a response has been detected through some advanced statistical method, there remains the communications challenge if detection has not yet been possible for one of the icons of global climate change. But despite the difficulty of detecting climate responses in the decades immediately after emissions reductions begin, there his *high confidence* that such a response will emerge clearly in the second half of this century in many quantities of interest.

[START FIGURE FAQ 4.2, FIGURE 1 HERE]

FAQ 4.2, Figure 1: Illustrating the difficulty of discerning mitigation benefit in the near term: Shown are results from 100 simulations with the same climate model that all assume the same reduction in greenhouse-gas emissions from 2020 onward. The difference between individual simulations arises solely through different manifestations of natural internal variability and represents an irreducible uncertainty. We want to assess quantitatively to what extent emissions reductions lead to a reduction in warming trend. Thus we compare, in each simulation separately, how the warming trend differs between the periods 2021–2035 and 2005–2020 (left), and between the periods 2036–2050 and 2005–2020 (right). The length of each bar indicates how often a trend difference of a certain size occurs among the 100 simulations. In the near term (left), we already see a preponderance of a slowdown in surface warming, occurring in two-thirds of the simulations. But as many as one-third of the simulations show faster warming in the near term, despite emissions reductions. By the mid-term (right), almost 90% of the simulations show a slowdown in warming compared to 2005–2020. [Placeholder figure, based on (Marotzke, 2019). Suggest replacing by 20-year trends and using the AR6 WGI definitions of near term and mid-term, as well as by CMIP6 results.]

[END FIGURE FAQ 4.2, FIGURE 1 HERE]

FAQ 4.3: At a Given Level of Warming, What Can We Say about Climate Change in the World's Regions?

Climate change does not unfold uniformly across the globe, and yet there are patterns of change that are robust. For example, the Arctic warms more than other regions, land areas warm more than the oceans, and the Northern Hemisphere warms more than the Southern Hemisphere. When such a robust pattern exists, we can infer the expected change in a region for each assumed level of global mean warming. Confidence in pattern robustness is highest for temperature-change patterns and for moderate levels of warming. By contrast, precipitation changes tend to show less robust patterns, because precipitation changes are more strongly influenced by regional forcing agents such as aerosol emissions and by natural internal climate variability; these influences are more pronounced under low levels of warming. Robust patterns cannot be established for changes in snow or sea-ice cover, because both snow and ice vanish completely if certain temperature thresholds are crossed.

Identifying a robust pattern of change for a given level of global warming offers two main advantages. First, it enables us to make statements about expected regional change that are largely independent of the forcing scenario. As long as different scenarios result in the same global warming level, irrespective of the time when this level is attained in each scenario, we can with high confidence specify the expected regional change resulting from this warming. And second, we can reliably interpolate and, with due caution, extrapolate to warming levels that have not been analysed or even simulated explicitly. Ideally a change pattern can be identified for every °C of global surface warming, and the expected regional change is readily found for every global warming level by simple multiplication ('scaling') of the pattern with this warming level. This approach can be highly efficient for studies of climate impacts at regional scales. When patterns of changes are robust, all impact assessments can readily be performed for all levels of global warming, for all future time periods, and for all scenarios.

Pattern scaling has some well-known strengths and weaknesses. It has been demonstrated to yield robust estimates for temperature changes at a given level of global warming. Limitations exist over areas of high natural internal variability that become particularly evident at low levels of warming and for seasonal changes, for areas with strong feedbacks due to melting snow or sea ice, and for areas with large differences between transient and very-long-term changes. Patterns are less robust for precipitation changes, for reasons that are likewise quite well understood. Global and regional changes in precipitation are not only a response to globally averaged surface warming, but also depend on the forcing agents such as anthropogenic aerosol emissions or land-use changes. Furthermore, regional precipitation changes are more strongly influenced by natural internal variability in the atmosphere, meaning that any given surface warming level can result in quite different patterns of precipitation change. Nevertheless, pattern scaling can be applied to precipitation changes, but the uncertainties are larger than for temperature changes.

Finally, there are climate variables for which pattern scaling is not appropriate. Sea-level change, for example, is expected to be more closely related to the entire past history of warming, rather than to the warming level at any given time. And changes in bounded variables such as sea-ice and snow cover are better described by whether a threshold is crossed or not, the threshold determining whether a region experiences a complete melt. Once the melt is complete, there can be no further melting, and the simple proportionality lying behind pattern scaling no longer applies.

[START FAQ 4.3 FIGURE 1 HERE]

FAQ 4.3, Figure 1: Example for a robust warming pattern, which is presented here for the CMIP6 model MRI-ESM2 and calculated from the scenario SSP3-7.0. Surface warming relative to 1850–1900 is shown here for time periods over which the globally averaged surface warming is 2°C. We recognise the strong warming over the Arctic, generally stronger warming over land than over the ocean, and a slight cooling over the central subpolar North Atlantic. [Placeholder figure, to be replaced by the average over more CMIP6 models.]

[END FIGURE FAQ 4.3, FIGURE 1 HERE]

References

Abramowitz, G., Herger, N., Gutmann, E., Hammerling, D., Knutti, R., Leduc, M., et al. (2019). ESD Reviews: Model dependence in multi-model climate ensembles: weighting, sub-selection and out-of-sample testing. *Earth Syst. Dynam.* 10, 91–105. doi:10.5194/esd-10-91-2019.

Acosta Navarro, J. C., Ekman, A. M. L., Pausata, F. S. R., Lewinschal, A., Varma, V., Seland, Ø., et al. (2017). Future Response of Temperature and Precipitation to Reduced Aerosol Emissions as Compared with Increased Greenhouse Gas Concentrations. *J. Clim.* 30, 939–954. doi:10.1175/JCLI-D-16-0466.1.

Acosta Navarro, J. C., Varma, V., Riipinen, I., Seland, Ø., Kirkevåg, A., Struthers, H., et al. (2016). Amplification of Arctic warming by past air pollution reductions in Europe. *Nat. Geosci.* 9, 277–281. doi:10.1038/ngeo2673.

Ahlm, L., Jones, A., Stjern, C. W., Muri, H., Kravitz, B., and Kristjánsson, J. E. (2017). Marine cloud brightening – as effective without clouds. *Atmos. Chem. Phys.* 17, 13071–13087. doi:10.5194/acp-17-13071-2017.

Allen, M. R., Frame, D. J., Huntingford, C., Jones, C. D., Lowe, J. A., Meinshausen, M., et al. (2009). Warming caused by cumulative carbon emissions towards the trillionth tonne. *Nature* 458, 1163–1166. doi:10.1038/nature08019.

Allen, M. R., and Ingram, W. J. (2002). Constraints on future changes in climate and the hydrologic cycle. *Nature* 419, 224–232. Available at: http://dx.doi.org/10.1038/nature01092.

Alley, R. B., Marotzke, J., Nordhaus, W. D., Overpeck, J. T., Peteet, D. M., Jr., R. A. P., et al. (2003). Abrupt Climate Change. *Science (80-.).* 299, 2005–2010.

Andrews, T., and Forster, P. M. (2010). The transient response of global-mean precipitation to increasing carbon dioxide levels. *Environ. Res. Lett.* 5, 1–6. doi:10.1088/1748-9326/5/2/025212.

Andrews, T., Forster, P. M., and Gregory, J. M. (2009). A surface energy perspective on climate change. *J. Clim.* 22, 2557–2570. doi:10.1175/2008JCLI2759.1.

Andrews, T., Gregory, J. M., Webb, M. J., and Taylor, K. E. (2012). Forcing, feedbacks and climate sensitivity in CMIP5 coupled atmosphere-ocean climate models. *Geophys. Res. Lett.* 39, L09712. doi:10.1029/2012GL051607.

Andrews, T., and Ringer, M. A. (2014). Cloud feedbacks, rapid adjustments, and the forcing--response relationship in a transient CO2 reversibility scenario. *J. Clim.* 27, 1799–1818.

Annan, J. D., and Hargreaves, J. C. (2017). On the meaning of independence in climate science. *Earth Syst. Dyn.* 8, 211–224. doi:10.5194/esd-8-211-2017.

Armour, K. C., Eisenman, I., Blanchard-Wrigglesworth, E., McCusker, K. E., and Bitz, C. M. (2011). The reversibility of sea ice loss in a state-of-the-art climate model. *Geophys. Res. Lett.* 38, n/a-n/a. doi:10.1029/2011GL048739.

Armour, K. C., Marshall, J., Scott, J. R., Donohoe, A., and Newsom, E. R. (2016). Southern Ocean warming delayed by circumpolar upwelling and equatorward transport. *Nat. Geosci.* 9, 549–554. doi:10.1038/ngeo2731.

Arrhenius, S. (1896). On the influence of carbonic acid in the air upon the temperature of the ground. *Philos. Mag. J. Sci.* 41, 237–276.

Ba, J., Keenlyside, N. S., Latif, M., Park, W., Ding, H., Lohmann, K., et al. (2014). A multi-model comparison of Atlantic multidecadal variability. *Clim. Dyn.* 43, 2333–2348. doi:10.1007/s00382-014-2056-1.

Bacmeister, J. T., Reed, K. A., Hannay, C., Lawrence, P., Bates, S., Truesdale, J. E., et al. (2018). Projected changes in tropical cyclone activity under future warming scenarios using a high-resolution climate model. *Clim. Change* 146, 547–560. doi:10.1007/s10584-016-1750-x.

Bala, G., Caldeira, K., and Nemani, R. (2010). Fast versus slow response in climate change: Implications for the global hydrological cycle. *Clim. Dyn.* 35, 423–434. doi:10.1007/s00382-009-0583-y.

Bala, G., Duffy, P. B., and Taylor, K. E. (2008). Impact of geoengineering schemes on the global hydrological cycle. *Proc. Natl. Acad. Sci. U. S. A.* 105, 7664–7669. doi:10.1073/pnas.0711648105.

Balaji, V., Taylor, K. E., Juckes, M., Lautenschlager, M., Blanton, C., Cinquini, L., et al. (2018). Requirements for a global data infrastructure in support of CMIP6. *Geosci. Model Dev. Discuss.* 11, 3659–3680. doi:10.5194/gmd-2018-52.

Banerjee, A., Maycock, A. C., and Pyle, J. A. (2018). Chemical and climatic drivers of radiative forcing due to changes in stratospheric and tropospheric ozone over the 21st century. *Atmos. Chem. Phys.* 18, 2899–2911. doi:10.5194/acp-18-2899-2018.

Barnes, E. A., Barnes, N. W., and Polvani, L. M. (2014). Delayed southern hemisphere climate change induced by stratospheric ozone recovery, as projected by the CMIP5 models. *J. Clim.* 27, 852–867. doi:10.1175/JCLI-D-13-00246.1.

Barnes, E. A., and Polvani, L. (2013). Response of the Midlatitude Jets, and of Their Variability, to Increased Greenhouse Gases in the CMIP5 Models. *J. Clim.* 26, 7117–7135. doi:10.1175/JCLI-D-12-00536.1.

Barnes, E. A., and Polvani, L. M. (2015). CMIP5 projections of arctic amplification, of the North American/North Atlantic circulation, and of their relationship. *J. Clim.* 28, 5254–5271. doi:10.1175/JCLI-D-14-00589.1.

Barnes, E. A., and Screen, J. A. (2015). The impact of Arctic warming on the midlatitude jet-stream: Can it? Has it? Will it? *Wiley Interdiscip. Rev. Clim. Chang.* 6, 277–286. doi:10.1002/wcc.337.

Barriopedro, D., García-Herrera, R., and Trigo, R. M. (2010). Application of blocking diagnosis methods to General Circulation Models. Part I: a novel detection scheme. *Clim. Dyn.* 35, 1373–1391. doi:10.1007/s00382-010-0767-5.

Baumberger, C., Knutti, R., and Hirsch Hadorn, G. (2017). Building confidence in climate model projections: an analysis of inferences from fit. *Wiley Interdiscip. Rev. Clim. Chang.* 8, e454. doi:10.1002/wcc.454.
Bayr, T., and Dommenget, D. (2013). The Tropospheric Land-Sea Warming Contrast as the Driver of Tropical Sea Level Pressure Changes. *J. Clim.* 26, 1387–1402.
Bellucci, A., Haarsma, R., Bellouin, N., Booth, B., Cagnazzo, C., Hurk, B., et al. (2015a). Advancements in decadal climate predictability: The role of nonoceanic drivers. *Rev. Geophys.* 53, 165–202. doi:10.1002/2014RG000473.
Bellucci, A., Haarsma, R., Gualdi, S., Athanasiadis, P. J., Caian, M., Cassou, C., et al. (2015b). An assessment of a multi-model ensemble of decadal climate predictions. *Clim. Dyn.* 44, 2787–2806. doi:10.1007/s00382-014-2164-y.
Berdahl, M., Robock, A., Ji, D., Moore, J. C., Jones, A., Kravitz, B., et al. (2014). Arctic cryosphere response in the geoengineering model intercomparison project G3 and G4 scenarios. *J. Geophys. Res.* 119, 1308–1321. doi:10.1002/2013JD020627.
Berg, A. M., Findell, K., Lintner, B. R., Giannini, A., Seneviratne, S. I., van den Hurk, B., et al. (2016). Land-atmosphere feedbacks amplify aridity increase over land under global warming. *Nat. Clim. Chang.* 6, 869–874.
Berner, J., Achatz, U., Batté, L., Bengtsson, L., Cámara, A. de la, Christensen, H. M., et al. (2017). Stochastic Parameterization: Toward a New View of Weather and Climate Models. *Bull. Am. Meteorol. Soc.* 98, 565–588. doi:10.1175/BAMS-D-15-00268.1.
Bethke, I., Outten, S., Otterå, O. H., Hawkins, E., Wagner, S., Sigl, M., et al. (2017). Potential volcanic impacts on future climate variability. *Nat. Clim. Chang.* 7, 799–805. doi:10.1038/nclimate3394.
Betts, R. A., and McNeall, D. (2018). How much CO2 at 1.5 °C and 2 °C? *Nat. Clim. Chang.* 8, 546–548. doi:10.1038/s41558-018-0199-5.
Bindoff, N. L., Stott, P. A., AchutaRao, K. M., Allen, M. R., Gillett, N., Gutzler, D., et al. (2013). “Detection and Attribution of Climate Change: from Global to Regional,” in *Climate Change 2013: The Physical Science Basis. Contribution of Working Group I to the Fifth Assessment Report of the Intergovernmental Panel on Climate Change*, eds. T. F. Stocker, D. Qin, G.-K. Plattner, M. Tignor, S. K. Allen, J. Boschung, et al. (Cambridge, United Kingdom and New York, NY, USA: Cambridge University Press), 867–952.
Bitz, C. M., Gent, P. R., Woodgate, R. A., Holland, M. M., and Lindsay, R. (2006). The influence of sea ice on ocean heat uptake in response to increasing CO2. *J. Clim.* 19, 2437–2450. doi:10.1175/JCLI3756.1.
Boe, J. (2018). Interdependency in multimodel climate projections: Component replication and result similarity. *Geophys. Res. Lett.* 45, 2771–2779. doi:10.1002/2017gl076829.
Boer, G. J., Kharin, V. V., and Merryfield, W. J. (2013). Decadal predictability and forecast skill. *Clim. Dyn.* 41, 1817–1833. doi:10.1007/s00382-013-1705-0.
Boer, G. J., Smith, D. M., Cassou, C., Doblas-Reyes, F., Danabasoglu, G., Kirtman, B., et al. (2016). The Decadal Climate Prediction Project (DCPP) contribution to CMIP6. *Geosci. Model Dev.* 9, 3751–3777. doi:10.5194/gmd-9-3751-2016.
Bollasina, M. A., Ming, Y., and Ramaswamy, V. (2011). Anthropogenic Aerosols and the Weakening of the South Asian Summer Monsoon. *Science (80-.).* 334, 502–505. doi:10.1126/science.1204994.
Bonan, D. B., Armour, K. C., Roe, G. H., Siler, N., and Feldl, N. (2018). Sources of Uncertainty in the Meridional Pattern of Climate Change. *Geophys. Res. Lett.* 45, 9131–9140. doi:10.1029/2018GL079429.
Bony, S., Bellon, G., Klocke, D., Sherwood, S., Fermepin, S., and Denvil, S. (2013). Robust direct effect of carbon dioxide on tropical circulation and regional precipitation. *Nat. Geosci.* 6, 447–451. doi:10.1038/ngeo1799.
Borodina, A., Fischer, E. M., and Knutti, R. (2017). Emergent constraints in climate projections: A case study of changes in high-latitude temperature variability. *J. Clim.* 30, 3655–3670. doi:10.1175/JCLI-D-16-0662.1.
Boucher, O., Halloran, P. R., Burke, E. J., Doutriaux-Boucher, M., Jones, C. D., Lowe, J., et al. (2012). Reversibility in an Earth System model in response to CO 2 concentration changes. *Environ. Res. Lett.* 7, 024013. doi:10.1088/1748-9326/7/2/024013.
Branstator, G., and Teng, H. Y. (2010). Two limits of initial-value decadal predictability in a CGCM. *J. Clim.* 23, 6292–6311. doi:10.1175/2010jcli3678.1.
Brogli, R., Kröner, N., Sørland, S. L., Lüthi, D., and Schär, C. (2019). The Role of Hadley Circulation and Lapse-Rate Changes for the Future European Summer Climate. *J. Clim.* 32, 385–404. doi:10.1175/JCLI-D-18-0431.1.
Bronselaer, B., Stouffer, R. J., Winton, M., Griffies, S. M., Hurlin, W. J., Russell, J. L., et al. (2018). Change in future climate due to Antarctic meltwater. *Nature* 564, 55–58. doi:10.1038/s41586-018-0712-z.
Brown, P. T., Lozier, M. S., Zhang, R., and Li, W. (2016). The necessity of cloud feedback for a basin-scale Atlantic Multidecadal Oscillation. *Geophys. Res. Lett.* 43, 3955–3963. doi:10.1002/2016GL068303.
Brown, P. T., Ming, Y., Li, W., and Hill, S. A. (2017). Change in the magnitude and mechanisms of global temperature variability with warming. *Nat. Clim. Chang.* 7, 743–748. doi:10.1038/nclimate3381.
Bürger, G., and Cubasch, U. (2015). The detectability of climate engineering. *J. Geophys. Res.* 120, 11,404-11,418. doi:10.1002/2015JD023954.
Buzan, J. R., Oleson, K., and Huber, M. (2015). Implementation and comparison of a suite of heat stress metrics within the Community Land Model version 4.5. *Geosci. Model Dev.* 8, 151–170. doi:10.5194/gmd-8-151-2015.
Byrne, M. P., and O’Gorman, P. A. (2013a). Land-ocean warming contrast over a wide range of climates: Convective

quasi-equilibrium theory and idealized simulations. *J. Clim.* 26, 4000–4016.
Byrne, M. P., and O'Gorman, P. A. (2013b). Link between land-ocean warming contrast and surface relative humidities in simulations with coupled climate models. *Geophys. Res. Lett.* 40, 5223–5227. doi:10.1002/grl.50971.
Byrne, M. P., and O'Gorman, P. A. (2015). The Response of Precipitation Minus Evapotranspiration to Climate Warming: Why the "Wet-Get-Wetter, Dry-Get-Drier'" Scaling Does Not Hold over Land." *J. Clim.* 28, 8078–8092.
Byrne, M. P., and O'Gorman, P. A. (2016). Understanding decreases in land relative humidity with global warming: conceptual model and GCM simulations. *J. Clim.* 29, 9045–9061.
Byrne, M. P., and O'Gorman, P. A. (2018). Trends in continental temperature and humidity directly linked to ocean warming. *Proc. Natl. Acad. Sci.* 115, 4863–4868. doi:10.1073/pnas.1722312115.
Byrne, M. P., and Schneider, T. (2018). Atmospheric dynamics feedback: concept, simulations and climate implications. *J. Clim.* 31, 3249–3264.
Caesar, J., Palin, E., Liddicoat, S., Lowe, J., Burke, E., Pardaens, A., et al. (2013). Response of the HadGEM2 Earth System Model to future greenhouse gas emissions pathways to the year 2300. *J. Clim.* 26, 3275–3284.
Cai, W., Santoso, A., Wang, G., Weller, E., Wu, L., Ashok, K., et al. (2014). Increased frequency of extreme Indian Ocean Dipole events due to greenhouse warming. *Nature* 510, 254–258.
Cai, W., Santoso, A., Wang, G., Yeh, S.-W., An, S.-I., Cobb, K. M., et al. (2015). ENSO and greenhouse warming. *Nat. Clim. Chang.* 5, 849–859. Available at: http://dx.doi.org/10.1038/nclimate2743.
Cai, W., Wang, G., Dewitte, B., Wu, L., Santoso, A., Takahashi, K., et al. (2018a). Increased variability of eastern Pacific El Niño under greenhouse warming. *Nature* 564, 201–206. doi:10.1038/s41586-018-0776-9.
Cai, W., Wang, G., Gan, B., Wu, L., Santoso, A., Lin, X., et al. (2018b). Stabilised frequency of extreme positive Indian Ocean Dipole under 1.5 °C warming. *Nat. Commun.* 9, 1419. doi:10.1038/s41467-018-03789-6.
Cai, W., Wu, L., Lengaigne, M., Li, T., McGregor, S., Kug, J.-S., et al. (2019). Pantropical climate interactions. *Science (80-.).* 363, eaav4236. doi:10.1126/science.aav4236.
Cai, W., Zheng, X. T., Weller, E., Collins, M., Cowan, T., Lengaigne, M., et al. (2013). Projected response of the Indian Ocean Dipole to greenhouse warming. *Nat. Geosci.* 6, 997–1007. doi:10.1038/ngeo2009.
Caian, M., Koenigk, T., Döscher, R., and Devasthale, A. (2018). An interannual link between Arctic sea-ice cover and the North Atlantic Oscillation. *Clim. Dyn.* 50, 423–441. doi:10.1007/s00382-017-3618-9.
Caldeira, K., Bala, G., and Cao, L. (2013). The science of geoengineering. *Annu. Rev. Earth Planet. Sci.* 41, 231–256. doi:10.1146/annurev-earth-042711-105548.
Cane, M. A., Clement, A. C., Murphy, L. N., and Bellomo, K. (2017). Low-Pass Filtering, Heat Flux, and Atlantic Multidecadal Variability. *J. Clim.* 30, 7529–7553. doi:10.1175/JCLI-D-16-0810.1.
Cao, L., Bala, G., and Caldeira, K. (2011). Why is there a short-term increase in global precipitation in response to diminished CO2 forcing? *Geophys. Res. Lett.* 38. doi:10.1029/2011GL046713.
Cao, L., Bala, G., and Caldeira, K. (2012). Climate response to changes in atmospheric carbon dioxide and solar irradiance on the time scale of days to weeks. *Environ. Res. Lett.* 7, 034015. doi:10.1088/1748-9326/7/3/034015.
Cao, L., Bala, G., Zheng, M., and Caldeira, K. (2015). Fast and slow climate responses to CO2 and solar forcing: A linear multivariate regression model characterizing transient climate change. *J. Geophys. Res.* 120, 12,037-12,053. doi:10.1002/2015JD023901.
Cao, L., and Caldeira, K. (2010). Atmospheric carbon dioxide removal: long-term consequences and commitment. *Environ. Res. Lett.* 5, 024011. doi:10.1088/1748-9326/5/2/024011.
Cao, L., Duan, L., Bala, G., and Caldeira, K. (2016). Simulated long-term climate response to idealized solar geoengineering. *Geophys. Res. Lett.* 43, 2209–2217. doi:10.1002/2016GL068079.
Cao, L., Duan, L., Bala, G., and Caldeira, K. (2017). Simultaneous stabilization of global temperature and precipitation through cocktail geoengineering. *Geophys. Res. Lett.* 44, 7429–7437. doi:10.1002/2017GL074281.
Caron, L.-P., Hermanson, L., Dobbin, A., Imbers, J., Lledó, L., and Vecchi, G. A. (2017). How Skillful are the Multiannual Forecasts of Atlantic Hurricane Activity? *Bull. Am. Meteorol. Soc.* 99, 403–413. doi:10.1175/BAMS-D-17-0025.1.
Carslaw, K. S., Gordon, H., Hamilton, D. S., Johnson, J. S., Regayre, L. A., Yoshioka, M., et al. (2017). Aerosols in the Pre-industrial Atmosphere. *Curr. Clim. Chang. Reports* 3, 1–15. doi:10.1007/s40641-017-0061-2.
Cassou, C., Kushnir, Y., Hawkins, E., Pirani, A., Kucharski, F., Kang, I.-S., et al. (2018). Decadal Climate Variability and Predictability: Challenges and Opportunities. *Bull. Am. Meteorol. Soc.* 99, 479–490. doi:10.1175/BAMS-D-16-0286.1.
Cattiaux, J., and Cassou, C. (2013). Opposite CMIP3/CMIP5 trends in the wintertime Northern Annular Mode explained by combined local sea ice and remote tropical influences. *Geophys. Res. Lett.* 40, 3682–3687. doi:10.1002/grl.50643.
Ceppi, P., and Hartmann, D. L. (2016). Clouds and the Atmospheric Circulation Response to Warming. *J. Clim.* 29, 783–799. doi:10.1175/JCLI-D-15-0394.1.
Ceppi, P., Hwang, Y.-T., Liu, X., Frierson, D. M. W., and Hartmann, D. L. (2013). The relationship between the ITCZ and the Southern Hemispheric eddy-driven jet. *J. Geophys. Res. Atmos.* 118, 5136–5146.
Ceppi, P., and Shepherd, T. G. (2017). Contributions of Climate Feedbacks to Changes in Atmospheric Circulation. *J.*

Clim. 30, 9097–9118. doi:10.1175/JCLI-D-17-0189.1.
Ceppi, P., Zappa, G., Shepherd, T. G., and Gregory, J. M. (2018). Fast and slow components of the extratropical atmospheric circulation response to CO2forcing. *J. Clim.* 31, 1091–1105. doi:10.1175/JCLI-D-17-0323.1.
Chadwick, R. (2016). Which aspects of CO2forcing and SST warming cause most uncertainty in projections of tropical rainfall change over land and ocean? *J. Clim.* 29, 2493–2509. doi:10.1175/JCLI-D-15-0777.1.
Chadwick, R., Boutle, I., and Martin, G. (2013). Spatial Patterns of Precipitation Change in CMIP5: Why the Rich Do Not Get Richer in the Tropics. *J. Clim.* 26, 3803–3822. doi:10.1175/JCLI-D-12-00543.1.
Chadwick, R., Good, P., and Willett, K. M. (2016). A simple moisture advection model of specific humidity change over land in response to SST warming. *J. Clim.* 29, 7613–7632.
Chalmers, N., Highwood, E. J., Hawkins, E., Sutton, R., and Wilcox, L. J. (2012). Aerosol contribution to the rapid warming of near-term climate under RCP 2.6. *Geophys. Res. Lett.* 39, 2–7. doi:10.1029/2012GL052848.
Chand, S. S., Tory, K. J., Ye, H., and Walsh, K. J. E. (2017). Projected increase in El Niño-driven tropical cyclone frequency in the Pacific. *Nat. Clim. Chang.* 7, 123–127. doi:10.1038/nclimate3181.
Chang, E. K. M. (2014). Impacts of background field removal on CMIP5 projected changes in Pacific winter cyclone activity. *J. Geophys. Res. Atmos.* 119, 4626–4639. doi:10.1002/2013JD020746.
Chang, E. K. M. (2017). Projected Significant Increase in the Number of Extreme Extratropical Cyclones in the Southern Hemisphere. *J. Clim.* 30, 4915–4935. doi:10.1175/JCLI-D-16-0553.1.
Chang, E. K. M., Ma, C.-G., Zheng, C., and Yau, A. M. W. (2016). Observed and projected decrease in Northern Hemisphere extratropical cyclone activity in summer and its impacts on maximum temperature. *Geophys. Res. Lett.* 43, 2200–2208. doi:10.1002/2016GL068172.
Cheng, L., Abraham, J., Hausfather, Z., and Trenberth, K. E. (2019). How fast are the oceans warming? *Science (80-.).* 363, 128–129. doi:10.1126/science.aav7619.
Cheng, L., Trenberth, K. E., Fasullo, J., Boyer, T., Abraham, J., and Zhu, J. (2017). Improved estimates of ocean heat content from 1960 to 2015. *Sci. Adv.* 3, e1601545. doi:10.1126/sciadv.1601545.
Chikamoto, Y., Kimoto, M., Ishii, M., Mochizuki, T., Sakamoto, T. T., Tatebe, H., et al. (2013). An overview of decadal climate predictability in a multi-model ensemble by climate model MIROC. *Clim. Dyn.* 40, 1201–1222. doi:10.1007/s00382-012-1351-y.
Chikamoto, Y., Timmermann, A., Widlansky, M. J., Balmaseda, M. A., and Stott, L. (2017). Multi-year predictability of climate, drought, and wildfire in southwestern North America. *Sci. Rep.* 7, 6568. doi:10.1038/s41598-017-06869-7.
Chiodo, G., and Polvani, L. M. (2017). Reduced Southern Hemispheric circulation response to quadrupled CO2 due to stratospheric ozone feedback. *Geophys. Res. Lett.* 44, 465–474. doi:10.1002/2016GL071011.
Choi, J., Son, S. W., and Park, R. J. (2019). Aerosol versus greenhouse gas impacts on Southern Hemisphere general circulation changes. *Clim. Dyn.* 52, 4127–4142. doi:10.1007/s00382-018-4370-5.
Christensen, H. M., Berner, J., Coleman, D. R. B., and Palmer, T. N. (2017). Stochastic parameterization and El Niño-southern oscillation. *J. Clim.* 30, 17–38. doi:10.1175/JCLI-D-16-0122.1.
Christensen, J. H., Kumar, K. K., Aldrian, E., An, S.-I., Cavalcanti, I. F. A., and M. de Castro, W. Dong, P. Goswami, A. Hall, J.K. Kanyanga, A. Kitoh, J. Kossin, N.-C. Lau, J. Renwick, D.B. Stephenson, S.-P. X. and T. Z. (2013). "Climate Phenomena and their Relevance for Future Regional Climate Change," in *Climate Change 2013 - The Physical Science Basis*, eds. T. F. Stocker, D. Qin, G.-K. Plattner, M. Tignor, S. K. Allen, J. Boschung, et al. (Cambridge: Cambridge University Press), 1217–1308. Available at: https://www.cambridge.org/core/product/identifier/CBO9781107415324A036/type/book_part.
Chu, J.-E., Ha, K.-J., Lee, J.-Y., Wang, B., Kim, B.-H., and Chung, C. E. (2014). Future change of the Indian Ocean basin-wide and dipole modes in the CMIP5. *Clim. Dyn.* 43, 535–551. doi:10.1007/s00382-013-2002-7.
Church, J. a., Clark, P. U., Cazenave, a., Gregory, J. M., Jevrejeva, S., Levermann, a., et al. (2013). Sea level change. *Clim. Chang. 2013 Phys. Sci. Basis. Contrib. Work. Gr. I to Fifth Assess. Rep. Intergov. Panel Clim. Chang.* doi:10.1017/CB09781107415315.026.
Ciais, P., Sabine, C., Bala, G., Bopp, L., Brovkin, V., Canadell, J., et al. (2013). Carbon and Other Biogeochemical Cycles 6. *Clim. Chang. 2013 - Phys. Sci. Basis*. doi:10.1017/CBO9781107415324.015.
Ciavarella, A., Stott, P., and Lowe, J. (2017). Early benefits of mitigation in risk of regional climate extremes. *Nat. Clim. Chang.* 7, 326–330. doi:10.1038/nclimate3259.
Clark, P. U., Shakun, J. D., Marcott, S. A., Mix, A. C., Eby, M., Kulp, S., et al. (2016). Consequences of twenty-first-century policy for multi-millennial climate and sea-level change. *Nat. Clim. Chang.* 6, 360–369. doi:10.1038/nclimate2923.
Claussen, M., Mysak, L. A., Weaver, A. J., Crucifix, M., Fichefet, T., Loutre, M. F., et al. (2002). Earth system models of intermediate complexity: closing the gap in the spectrum of climate system models. *Clim. Dyn.* 18, 579–586. doi:10.1007/s00382-001-0200-1.
Clement, A., Bellomo, K., Murphy, L. N., Cane, M. A., Mauritsen, T., Radel, G., et al. (2015). The Atlantic Multidecadal Oscillation without a role for ocean circulation. *Science (80-.).* 350, 320–324. doi:10.1126/science.aab3980.
Collins, J. W., Lamarque, J.-F. J. F., Schulz, M., Boucher, O., Eyring, V., Hegglin, I. M., et al. (2017). AerChemMIP:

Quantifying the effects of chemistry and aerosols in CMIP6. *Geosci. Model Dev.* 10, 585–607. doi:10.5194/gmd-10-585-2017.

Collins, M., Knutti, R., Arblaster, J., Dufresne, J.-L.-L., Fichefet, T., Friedlingstein, P., et al. (2013). “Long-term Climate Change: Projections, Commitments and Irreversibility,” in *Climate Change 2013: The Physical Science Basis. Contribution of Working Group I to the Fifth Assessment Report of the Intergovernmental Panel on Climate Change*, eds. T. F. Stocker, D. Qin, G.-K. Plattner, M. Tignor, S. K. Allen, J. Boschung, et al. (Cambridge, United Kingdom and New York, NY, USA: Cambridge University Press). doi:10.1017/CBO9781107415324.024.

COP21 (2015). Adoption of the Paris Agreement. Conference of the Parties Available at: https://unfccc.int/resource/docs/2015/cop21/eng/l09r01.pdf.

Corti, S., Palmer, T., Balmaseda, M., Weisheimer, A., Drijfhout, S., Dunstone, N., et al. (2015). Impact of initial conditions versus external forcing in decadal climate predictions: A sensitivity experiment. *J. Clim.* 28, 4454–4470. doi:10.1175/JCLI-D-14-00671.1.

Corti, S., Weisheimer, A., Palmer, T. N., Doblas-Reyes, F. J., and Magnusson, L. (2012). Reliability of decadal predictions. *Geophys. Res. Lett.* 39, L21712. doi:10.1029/2012GL053354.

Cox, P. M., Huntingford, C., and Williamson, M. S. (2018). Emergent constraint on equilibrium climate sensitivity from global temperature variability. *Nature* 553, 319–322. Available at: http://dx.doi.org/10.1038/nature25450.

Cox, P., and Stephenson, D. (2007). A Changing Climate for Prediction. *Science (80-.).* 317, 207–208. Available at: http://science.sciencemag.org/content/317/5835/207.abstract.

Crook, J. A., Forster, P. M., and Stuber, N. (2011). Spatial patterns of modeled climate feedback and contributions to temperature response and polar amplification. *J. Clim.* 24, 3575–3592. doi:10.1175/2011JCLI3863.1.

Curry, C. L., Sillmann, J., Bronaugh, D., Alterskjaer, K., Cole, J. N. S., Ji, D., et al. (2014). A multimodel examination of climate extremes in an idealized geoengineering experiment. *J. Geophys. Res. Atmos.* 119, 3900–3923. doi:10.1002/2013JD020648.

Dai, A., Fyfe, J. C., Xie, S. P., and Dai, X. (2015). Decadal modulation of global surface temperature by internal climate variability. *Nat. Clim. Chang.* 5, 555–559. doi:10.1038/nclimate2605.

Dakos, V., Scheffer, M., Nes, E. H. van, Brovkin, V., Petoukhov, V., and Held, H. (2008). Slowing down as an early warning signal for abrupt climate change. *Proc. Natl. Acad. Sci.* 105, 14308–14312. doi:10.1073/PNAS.0802430105.

Danabasoglu, G., and Gent, P. R. (2009). Equilibrium climate sensitivity: Is it accurate to use a slab ocean model? *J. Clim.* 22, 2494–2499. doi:10.1175/2008JCLI2596.1.

Davini, P., Cagnazzo, C., Gualdi, S., and Navarra, A. (2012). Bidimensional Diagnostics, Variability, and Trends of Northern Hemisphere Blocking. *J. Clim.* 25, 6496–6509. doi:10.1175/JCLI-D-12-00032.1.

Davini, P., Von Hardenberg, J., Corti, S., Christensen, H. M., Juricke, S., Subramanian, A., et al. (2017). Climate SPHINX: Evaluating the impact of resolution and stochastic physics parameterisations in the EC-Earth global climate model. *Geosci. Model Dev.* 10, 1383–1402. doi:10.5194/gmd-10-1383-2017.

Dawson, A., and Palmer, T. N. (2015). Simulating weather regimes: impact of model resolution and stochastic parameterization. *Clim. Dyn.* 44, 2177–2193. doi:10.1007/s00382-014-2238-x.

De Vries, H., Haarsma, R. J., and Hazeleger, W. (2012). Western European cold spells in current and future climate. *Geophys. Res. Lett.* 39, L04706. doi:10.1029/2011GL050665.

Deng, K., Yang, S., Ting, M., Tan, Y., and He, S. (2018). Global Monsoon Precipitation: Trends, Leading Modes, and Associated Drought and Heat Wave in the Northern Hemisphere. *J. Clim.* 31, 6947–6966. doi:10.1175/JCLI-D-17-0569.1.

Deser, C., Knutti, R., Solomon, S., and Phillips, A. S. (2012a). Communication of the role of natural variability in future North American climate. *Nat. Clim. Chang.* 2, 775–779. Available at: http://dx.doi.org/10.1038/nclimate1562.

Deser, C., and Phillips, A. (2017). An overview of decadal-scale sea surface temperature variability in the observational record. *Jt. Issue CLIVAR Exch. PAGES Mag.* 25, 2–6.

Deser, C., Phillips, A., Bourdette, V., and Teng, H. (2012b). Uncertainty in climate change projections: the role of internal variability. *Clim. Dyn.* 38, 527–546. doi:10.1007/s00382-010-0977-x.

Deser, C., Phillips, A. S., Alexander, M. A., and Smoliak, B. V. (2014). Projecting North American climate over the next 50 years: Uncertainty due to internal variability. *J. Clim.* 27, 2271–2296. doi:10.1175/JCLI-D-13-00451.1.

Deser, C., Terray, L., and Phillips, A. S. (2016). Forced and internal components of winter air temperature trends over North America during the past 50 years: Mechanisms and implications. *J. Clim.* 29, 2237–2258. doi:10.1175/JCLI-D-15-0304.1.

Deser, C., Tomas, R. A., and Sun, L. (2015). The Role of Ocean–Atmosphere Coupling in the Zonal-Mean Atmospheric Response to Arctic Sea Ice Loss. *J. Clim.* 28, 2168–2186. doi:10.1175/JCLI-D-14-00325.1.

Dhomse, S. S., Kinnison, D., Chipperfield, M. P., Salawitch, R. J., Cionni, I., Hegglin, M. I., et al. (2018). Estimates of ozone return dates from Chemistry-Climate Model Initiative simulations. *Atmos. Chem. Phys.* 18, 8409–8438. doi:10.5194/acp-18-8409-2018.

Di Lorenzo, E., Combes, V., Keister, J., Strub, P. T., Thomas, A., Franks, P., et al. (2013). Synthesis of Pacific Ocean

Climate and Ecosystem Dynamics. *Oceanography* 26, 68–81. doi:10.5670/oceanog.2013.76.
Di Lorenzo, E., Liguori, G., Schneider, N., Furtado, J. C., Anderson, B. T., and Alexander, M. A. (2015). ENSO and meridional modes: A null hypothesis for Pacific climate variability. *Geophys. Res. Lett.* 42, 9440–9448. doi:10.1002/2015GL066281.
Ding, Q., Wallace, J. M., Battisti, D. S., Steig, E. J., Gallant, A. J. E., Kim, H.-J., et al. (2014). Tropical forcing of the recent rapid Arctic warming in northeastern Canada and Greenland. *Nature* 509, 209–212. Available at: https://doi.org/10.1038/nature13260.
Doblas-Reyes, F. J., Andreu-Burillo, I., Chikamoto, Y., García-Serrano, J., Guemas, V., Kimoto, M., et al. (2013). Initialized near-term regional climate change prediction. *Nat. Commun.* 4, 1715. doi:10.1038/ncomms2704.
Dong, B., Gregory, J. M., and Sutton, R. T. (2009). Understanding land-sea warming contrast in response to increasing greenhouse gases. Part I: Transient adjustment. *J. Clim.* 22, 3079–3097.
Donohoe, A., and Battisti, D. S. (2013). The Seasonal Cycle of Atmospheric Heating and Temperature. *J. Clim.* 26, 4962–4980. doi:10.1175/JCLI-D-12-00713.1.
Dosio, A., and Fischer, E. M. (2018). Will Half a Degree Make a Difference? Robust Projections of Indices of Mean and Extreme Climate in Europe Under 1.5°C, 2°C, and 3°C Global Warming. *Geophys. Res. Lett.* 45, 935–944. doi:10.1002/2017GL076222.
Dosio, A., Mentaschi, L., Fischer, E. M., and Wyser, K. (2018). Extreme heat waves under 1.5 °C and 2 °C global warming. *Environ. Res. Lett.* 13, 054006. doi:10.1088/1748-9326/aab827.
Douville, H., Voldoire, A., and Geoffroy, O. (2015). The recent global warming hiatus: What is the role of Pacific variability? *Geophys. Res. Lett.* 42, 880–888. doi:10.1002/2014GL062775.
Drijfhout, S., Bathiany, S., Beaulieu, C., Brovkin, V., Claussen, M., Huntingford, C., et al. (2015). Catalogue of abrupt shifts in Intergovernmental Panel on Climate Change climate models. *Proc. Natl. Acad. Sci. U. S. A.* 112, E5777–E5786. doi:10.1073/pnas.1511451112.
Drost, F., Karoly, D., and Braganza, K. (2012). Communicating global climate change using simple indices: An update. *Clim. Dyn.* 39, 989–999.
Du, Y., Xie, S.-P., Yang, Y.-L., Zheng, X.-T., Liu, L., and Huang, G. (2013). Indian Ocean Variability in the CMIP5 Multimodel Ensemble: The Basin Mode. *J. Clim.* 26, 7240–7266. doi:10.1175/JCLI-D-12-00678.1.
Duan, L., Cao, L., Bala, G., and Caldeira, K. (2018). Comparison of the Fast and Slow Climate Response to Three Radiation Management Geoengineering Schemes. *J. Geophys. Res. Atmos.* 123, 11,980-12,001. doi:10.1029/2018JD029034.
Dunn-Sigouin, E., Son, S.-W., and Lin, H. (2013). Evaluation of Northern Hemisphere Blocking Climatology in the Global Environment Multiscale Model. *Mon. Weather Rev.* 141, 707–727. doi:10.1175/MWR-D-12-00134.1.
Dunne, J. P., Stouffer, R. J., and John, J. G. (2013). Reductions in labour capacity from heat stress under climate warming. *Nat. Clim. Chang.* 3, 563–566. doi:10.1038/nclimate1827.
Dunstone, N. J., Smith, D. M., and Eade, R. (2011). Multi-year predictability of the tropical Atlantic atmosphere driven by the high latitude North Atlantic Ocean. *Geophys. Res. Lett.* 38, L14701. doi:10.1029/2011GL047949.
Durack, P. J., Wijffels, S. E., and Matear, R. J. (2012). Ocean Salinities Reveal Strong Global Water Cycle Intensification During 1950 to 2000. *Science (80-.).* 336, 455–458. Available at: http://science.sciencemag.org/content/336/6080/455.abstract.
Dwyer, J. G., Biasutti, M., and Sobel, A. H. (2012). Projected Changes in the Seasonal Cycle of Surface Temperature. *J. Clim.* 25, 6359–6374. doi:10.1175/JCLI-D-11-00741.1.
Eade, R., Smith, D., Scaife, A., Wallace, E., Dunstone, N., Hermanson, L., et al. (2014). Do seasonal-to-decadal climate predictions underestimate the predictability of the real world? *Geophys. Res. Lett.* 41, 5620–5628. doi:10.1002/2014GL061146.
Eby, M., Weaver, A. J., Alexander, K., Zickfeld, K., Abe-Ouchi, A., Cimatoribus, A. A., et al. (2013). Historical and Idealized Climate Model Experiments: An EMIC Intercomparison. *Clim. Past* 9, 1111–1140.
Ehlert, D., and Zickfeld, K. (2018). Irreversible ocean thermal expansion under carbon dioxide removal. *Earth Syst. Dynam* 9, 197–210. doi:10.5194/esd-9-197-2018.
Ehlert, D., Zickfeld, K., Eby, M., and Gillett, N. (2017). The sensitivity of the proportionality between temperature change and cumulative CO2 emissions to ocean mixing. *J. Clim.* 30, 2921–2935. doi:10.1175/JCLI-D-16-0247.1.
Endo, H., and Kitoh, A. (2014). Thermodynamic and dynamic effects on regional monsoon rainfall changes in a warmer climate. *Geophys. Res. Lett.* 41, 1704–1710. doi:10.1002/2013GL059158.
Engelbrecht, F., Adegoke, J., Bopape, M.-J., Naidoo, M., Garland, R., Thatcher, M., et al. (2015). Projections of rapidly rising surface temperatures over Africa under low mitigation. *Environ. Res. Lett.* 10, 085004. doi:10.1088/1748-9326/10/8/085004.
England, M. H., McGregor, S., Spence, P., Meehl, G. A., Timmermann, A., Cai, W., et al. (2014). Recent intensification of wind-driven circulation in the Pacific and the ongoing warming hiatus. *Nat. Clim. Chang.* 4, 222. Available at: https://doi.org/10.1038/nclimate2106.
Etminan, M., Myhre, G., Highwood, E. J., and Shine, K. P. (2016). Radiative forcing of carbon dioxide, methane, and nitrous oxide: A significant revision of the methane radiative forcing. *Geophys. Res. Lett.* 43, 12,614-12,623. doi:10.1002/2016GL071930.

Exarchou, E., Kuhlbrodt, T., Gregory, J. M., and Smith, R. S. (2015). Ocean heat uptake processes: A model intercomparison. *J. Clim.* 28, 887–908. doi:10.1175/JCLI-D-14-00235.1.
Eyring, V., Arblaster, J. M., Cionni, I., Sedláček, J., Perlwitz, J., Young, P. J., et al. (2013). Long-term ozone changes and associated climate impacts in CMIP5 simulations. *J. Geophys. Res. Atmos.* 118, 5029–5060. doi:10.1002/jgrd.50316.
Eyring, V., Bony, S., Meehl, G. A., Senior, C. A., Stevens, B., Stouffer, R. J., et al. (2016a). Overview of the Coupled Model Intercomparison Project Phase 6 (CMIP6) experimental design and organization. *Geosci. Model Dev.* 9, 1937–1958. doi:10.5194/gmd-9-1937-2016.
Eyring, V., Righi, M., Lauer, A., Evaldsson, M., Wenzel, S., Jones, C., et al. (2016b). ESMValTool (v1.0) – a community diagnostic and performance metrics tool for routine evaluation of Earth system models in CMIP. *Geosci. Model Dev.* 9, 1747–1802. doi:10.5194/gmd-9-1747-2016.
Fasullo, J. T., Sanderson, B. M., and Trenberth, K. E. (2015). Recent Progress in Constraining Climate Sensitivity With Model Ensembles. *Curr. Clim. Chang. Reports* 1, 268–275. doi:10.1007/s40641-015-0021-7.
Fedorov, A., Hu, S., Wittenberg, A., Levine, A., and Deser, C. (2019). "Chapter 6 . ENSO low-frequency modulations and mean state interactions," in, ed. S. A. and C. W. McPhaden Mike (AGU Books). Available at: http://www.cgd.ucar.edu/staff/cdeser/docs/submitted.fedorov.enso_lowfrq_modulations.jan19.pdf.
Feely, R. a, Sabine, C. L., Lee, K., Berelson, W., Kleypas, J., Fabry, V. J., et al. (2004). Impact of anthropogenic CO2 on the CaCO3 system in the oceans. *Science* 305, 362–666. doi:10.1126/science.1097329.
Ferraro, A. J., Charlton-Perez, A. J., and Highwood, E. J. (2015). Stratospheric dynamics and midlatitude jets under geoengineering with space mirrors and sulfate and titania aerosols. *J. Geophys. Res. Atmos.* 120, 414–429. doi:10.1002/2014JD022734.
Ferraro, A. J., and Griffiths, H. G. (2016). Quantifying the temperature-independent effect of stratospheric aerosol geoengineering on global-mean precipitation in a multi-model ensemble. *Environ. Res. Lett.* 11, 034012. doi:10.1088/1748-9326/11/3/034012.
Ferreira, D., Marshall, J., Bitz, C. M., Solomon, S., and Plumb, A. (2015). Antarctic ocean and sea ice response to ozone depletion: A two-time-scale problem. *J. Clim.* 28, 1206–1226. doi:10.1175/JCLI-D-14-00313.1.
Fischer, E. M., Beyerle, U., and Knutti, R. (2013). Robust spatially aggregated projections of climate extremes. *Nat. Clim. Chang.* 3, 1033–1038. doi:10.1038/nclimate2051.
Fischer, E. M., and Knutti, R. (2013). Robust projections of combined humidity and temperature extremes. *Nat. Clim. Chang.* 3, 126–130. doi:10.1038/nclimate1682.
Fischer, E. M., and Knutti, R. (2014). Heated debate on cold weather. *Nat. Clim. Chang.* 4, 537–538. Available at: http://dx.doi.org/10.1038/nclimate2286.
Fischer, E. M., and Knutti, R. (2016). Observed heavy precipitation increase confirms theory and early models. *Nat. Clim. Chang.* 6, 986–991.
Fischer, E. M., Lawrence, D. M., and Sanderson, B. M. (2011). Quantifying uncertainties in projections of extremes-a perturbed land surface parameter experiment. *Clim. Dyn.* 37, 1381–1398. doi:10.1007/s00382-010-0915-y.
Fischer, E. M., Oleson, K. W., and Lawrence, D. M. (2012a). Contrasting urban and rural heat stress responses to climate change. *Geophys. Res. Lett.* 39, L03705. doi:10.1029/2011GL050576.
Fischer, E. M., Rajczak, J., and Schär, C. (2012b). Changes in European summer temperature variability revisited. *Geophys. Res. Lett.* 39, L19702. doi:10.1029/2012GL052730.
Fischer, E. M., and Schär, C. (2010). Consistent geographical patterns of changes in high-impact European heatwaves. *Nat. Geosci.* 3, 398–403. doi:10.1038/ngeo866.
Fischer, E. M., Sedláček, J., Hawkins, E., and Knutti, R. (2014). Models agree on forced response pattern of precipitation and temperature extremes. *Geophys. Res. Lett.* 41, 8554–8562. doi:10.1002/2014GL062018.
Fischer, H., Meissner, K. J., Mix, A. C., Abram, N. J., Austermann, J., Brovkin, V., et al. (2018). Palaeoclimate constraints on the impact of 2 °C anthropogenic warming and beyond. *Nat. Geosci.* 11, 474–485. doi:10.1038/s41561-018-0146-0.
Fix, M. J., Cooley, D., Sain, S. R., and Tebaldi, C. (2018). A comparison of U.S. precipitation extremes under RCP8.5 and RCP4.5 with an application of pattern scaling. *Clim. Change* 146, 335–347. doi:10.1007/s10584-016-1656-7.
Fläschner, D., Mauritsen, T., and Stevens, B. (2016). Understanding the intermodel spread in global-mean hydrological sensitivity. *J. Clim.* 29, 801–817. doi:10.1175/JCLI-D-15-0351.1.
Flato, G. M. (2011). Earth system models: an overview. *Wiley Interdiscip. Rev. Clim. Chang.* 2, 783–800. doi:10.1002/wcc.148.
Flato, G., Marotzke, J., Abiodun, B., Braconnot, P., Chou, S. C., Collins, W., et al. (2013). "Evaluation of Climate Models," in *Climate Change 2013: The Physical Science Basis. Contribution of Working Group I to the Fifth Assessment Report of the Intergovernmental Panel on Climate Change*, eds. T. F. Stocker, D. Qin, G.-K. Plattner, M. Tignor, S. K. Allen, J. Boschung, et al. (Cambridge: Cambridge University Press), 741–866. doi:10.1017/CBO9781107415324.
Fletcher, C. G., and Kushner, P. J. (2011). The Role of Linear Interference in the Annular Mode Response to Tropical SST Forcing. *J. Clim.* 24, 778–794. doi:10.1175/2010JCLI3735.1.
Folland, C. K. (2002). Relative influences of the Interdecadal Pacific Oscillation and ENSO on the South Pacific

Convergence Zone. *Geophys. Res. Lett.* 29, 1643. doi:10.1029/2001GL014201.
Foltz, G. R., Seo, K.-H., Dong, C., Chadwick, R., Jiang, J. H., Ma, J., et al. (2018). Responses of the Tropical Atmospheric Circulation to Climate Change and Connection to the Hydrological Cycle. *Annu. Rev. Earth Planet. Sci.* 46, 549–580. doi:10.1146/annurev-earth-082517-010102.
Frame, D. J., Macey, A. H., and Allen, M. R. (2014). Cumulative emissions and climate policy. *Nat. Geosci.* 7, 692–693. doi:10.1038/ngeo2254.
Francis, J. A., and Vavrus, S. J. (2012). Evidence linking Arctic amplification to extreme weather in mid-latitudes. *Geophys. Res. Lett.* 39, L06801. doi:doi:10.1029/2012GL051000.
Francis, J. A., and Vavrus, S. J. (2015). Evidence for a wavier jet stream in response to rapid Arctic warming. *Environ. Res. Lett.* 10, 014005. doi:10.1088/1748-9326/10/1/014005.
Friedlingstein, P., Meinshausen, M., Arora, V. K., Jones, C. D., Anav, A., Liddicoat, S. K., et al. (2014). Uncertainties in CMIP5 climate projections due to carbon cycle feedbacks. *J. Clim.* 27, 511–526. doi:10.1175/JCLI-D-12-00579.1.
Frieler, K., Meinshausen, M., Mengel, M., Braun, N., and Hare, W. (2012). A scaling approach to probabilistic assessment of regional climate change. *J. Clim.* 25, 3117–3144. doi:10.1175/JCLI-D-11-00199.1.
Frisch, M. (2015). Predictivism and old evidence: a critical look at climate model tuning. *Eur. J. Philos. Sci.* 5, 171–190. doi:10.1007/s13194-015-0110-4.
Frölicher, T. L., and Paynter, D. J. (2015). Extending the relationship between global warming and cumulative carbon emissions to multi-millennial timescales. *Environ. Res. Lett.* 10, 075002. doi:10.1088/1748-9326/10/7/075002.
Frölicher, T. L., Sarmiento, J. L., Paynter, D. J., Dunne, J. P., Krasting, J. P., and Winton, M. (2015). Dominance of the Southern Ocean in Anthropogenic Carbon and Heat Uptake in CMIP5 Models. *J. Clim.* 28, 862–886. doi:10.1175/jcli-d-14-00117.1.
Frolicher, T. L., Winton, M., and Sarmiento, J. L. (2014). Continued global warming after CO2 emissions stoppage. *Nat. Clim. Chang.* 4, 40–44. doi:10.1038/nclimate2060.
Fu, Q., and Feng, S. (2014). Responses of terrestrial aridity to global warming. *J. Geophys. Res. Atmos.* 119, 7863–7875.
Fučkar, N. S., Volpi, D., Guemas, V., and Doblas-Reyes, F. J. (2014). A posteriori adjustment of near-term climate predictions: Accounting for the drift dependence on the initial conditions. *Geophys. Res. Lett.* 41, 5200–5207. doi:10.1002/2014GL060815.
Fyfe, J. C., Boer, G. J., and Flato, G. M. (1999). The Arctic and Antarctic oscillations and their projected changes under global warming. *Geophys. Res. Lett.* 26, 1601–1604. doi:10.1029/1999GL900317.
Fyfe, J., Gillett, N., and Zwiers, F. (2013). Overestimated global warming over the past 20 years. *Nat. Clim. Chang.* 3, 767–769. doi:doi: 10.1038/nclimate1972.
Gabriel, C. J., Robock, A., Xia, L., Zambri, B., and Kravitz, B. (2017). The G4Foam Experiment: global climate impacts of regional ocean albedo modification. *Atmos. Chem. Phys.* 17, 595–613. doi:10.5194/acp-17-595-2017.
Gagné, M.-È., Fyfe, J. C., Gillett, N. P., Polyakov, I. V., and Flato, G. M. (2017). Aerosol-driven increase in Arctic sea ice over the middle of the twentieth century. *Geophys. Res. Lett.* 44, 7338–7346. doi:10.1002/2016GL071941.
Gagné, M.-È., Gillett, N. P., and Fyfe, J. C. (2015). Impact of aerosol emission controls on future Arctic sea ice cover. *Geophys. Res. Lett.* 42, 8481–8488. doi:10.1002/2015GL065504.
Ganopolski, A., and Rahmstorf, S. (2001). Rapid changes of glacial climate simulated in a coupled climate model. *Nature* 409, 153.
García-Serrano, J., Guemas, V., and Doblas-Reyes, F. J. (2015). Added-value from initialization in predictions of Atlantic multi-decadal variability. *Clim. Dyn.* 44, 2539–2555. doi:10.1007/s00382-014-2370-7.
Garfinkel, C. I., Waugh, D. W., and Polvani, L. M. (2015). Recent Hadley cell expansion: The role of internal atmospheric variability in reconciling modeled and observed trends. *Geophys. Res. Lett.* 42, 10824–10831. doi:10.1002/2015GL066942.
Gasparini, B., and Lohmann, U. (2016). Why cirrus cloud seeding cannot substantially cool the planet. *J. Geophys. Res. Atmos.* 121, 4877–4893. doi:10.1002/2015JD024666.
Geden, O., and Loeschel, A. (2017). Define limits for temperature overshoot targets. *Nat. Geosci.* 10, 881–882. doi:10.1038/s41561-017-0026-z.
Geng, T., Yang, Y., and Wu, L. (2019). On the Mechanisms of Pacific Decadal Oscillation Modulation in a Warming Climate. *J. Clim.* 32, 1443–1459. doi:10.1175/JCLI-D-18-0337.1.
Gidden, M. J., Riahi, K., Smith, S. J., Fujimori, S., Luderer, G., Kriegler, E., et al. (2018). Global emissions pathways under different socioeconomic scenarios for use in CMIP6: a dataset of harmonized emissions trajectories through the end of the century. *Geosci. Model Dev. Discuss.*, 1–42. doi:10.5194/gmd-2018-266.
Gillett, N. P., Arora, V. K., Matthews, D., and Allen, M. R. (2013). Constraining the Ratio of Global Warming to Cumulative CO2 Emissions Using CMIP5 Simulations. *J. Clim.* 26, 6844–6858. doi:10.1175/JCLI-D-12-00476.1.
Gillett, N. P., and Fyfe, J. C. (2013). Annular mode changes in the CMIP5 simulations. *Geophys. Res. Lett.* 40, 1189–1193. doi:10.1002/grl.50249.
Goddard, L., Kumar, A., Solomon, A., Smith, D., Boer, G., Gonzalez, P., et al. (2013). A verification framework for interannual-to-decadal predictions experiments. *Clim. Dyn.* 40, 245–272. doi:10.1007/s00382-012-1481-2.

Gong, D., and Wang, S. (1999). Definition of Antarctic Oscillation index. *Geophys. Res. Lett.* 26, 459–462. doi:10.1029/1999GL900003.

González, M. F., Ilyina, T., Sonntag, S., and Schmidt, H. (2018). Enhanced Rates of Regional Warming and Ocean Acidification After Termination of Large-Scale Ocean Alkalinization. *Geophys. Res. Lett.* 45, 7120–7129. doi:10.1029/2018GL077847.

Good, P., Booth, B. B. B., Chadwick, R., Hawkins, E., Jonko, A., and Lowe, J. A. (2016). Large differences in regional precipitation change between a first and second 2 K of global warming. *Nat. Commun.* 7, 13667. doi:10.1038/ncomms13667.

Good, P., Lowe, J. A., Andrews, T., Wiltshire, A., Chadwick, R., Ridley, J. K., et al. (2015). Nonlinear regional warming with increasing CO2concentrations. *Nat. Clim. Chang.* 5, 138–142. doi:10.1038/nclimate2498.

Goodman, J., and Marshall, J. (1999). A Model of Decadal Middle-Latitude Atmosphere–Ocean Coupled Modes. *J. Clim.* 12, 621–641. doi:10.1175/1520-0442(1999)012<0621:AMODML>2.0.CO;2.

Goodwin, P., Williams, R. G., and Ridgwell, A. (2015). Sensitivity of climate to cumulative carbon emissions due to compensation of ocean heat and carbon uptake. *Nat. Geosci.* 8, 29–34. doi:10.1038/ngeo2304.

Goosse, H., Kay, J. E., Armour, K. C., Bodas-Salcedo, A., Chepfer, H., Docquier, D., et al. (2018). Quantifying climate feedbacks in polar regions. *Nat. Commun.* 9, 1919. doi:10.1038/s41467-018-04173-0.

Goss, M., Feldstein, S. B., and Lee, S. (2016). Stationary Wave Interference and Its Relation to Tropical Convection and Arctic Warming. *J. Clim.* 29, 1369–1389. doi:10.1175/JCLI-D-15-0267.1.

Graff, L. S., and LaCasce, J. H. (2014). Changes in Cyclone Characteristics in Response to Modified SSTs. *J. Clim.* 27, 4273–4295. doi:10.1175/JCLI-D-13-00353.1.

Gregory, J. M., and Mitchell, J. F. B. (1995). Simulation of daily variability of surface temperature and precipitation over europe in the current and 2 × Co2 climates using the UKMO climate model. *Q. J. R. Meteorol. Soc.* 121, 1451–1476. doi:10.1002/qj.49712152611.

Grieger, J., Leckebusch, G. C., Donat, M. G., Schuster, M., and Ulbrich, U. (2014). Southern Hemisphere winter cyclone activity under recent and future climate conditions in multi-model AOGCM simulations. *Int. J. Climatol.* 34, 3400–3416. doi:10.1002/joc.3917.

Grise, K. M., and Polvani, L. M. (2014). The response of midlatitude jets to increased CO2: Distinguishing the roles of sea surface temperature and direct radiative forcing. *Geophys. Res. Lett.* 41, 6863–6871. doi:10.1002/2014GL061638.

Grise, K. M., and Polvani, L. M. (2017). Understanding the Time Scales of the Tropospheric Circulation Response to Abrupt CO 2 Forcing in the Southern Hemisphere: Seasonality and the Role of the Stratosphere. *J. Clim.* 30, 8497–8515. doi:10.1175/JCLI-D-16-0849.1.

Grise, K. M., Son, S.-W., Correa, G. J. P., and Polvani, L. M. (2014). The response of extratropical cyclones in the Southern Hemisphere to stratospheric ozone depletion in the 20th century. *Atmos. Sci. Lett.* 15, 29–36. doi:10.1002/asl2.458.

Guemas, V., Blanchard-Wrigglesworth, E., Chevallier, M., Day, J. J., Déqué, M., Doblas-Reyes, F. J., et al. (2016). A review on Arctic sea-ice predictability and prediction on seasonal to decadal time-scales. *Q. J. R. Meteorol. Soc.* 142, 546–561. doi:10.1002/qj.2401.

Guemas, V., Corti, S., García-Serrano, J., Doblas-Reyes, F. J., Balmaseda, M., and Magnusson, L. (2013a). The Indian Ocean: The Region of Highest Skill Worldwide in Decadal Climate Prediction. *J. Clim.* 26, 726–739. doi:10.1175/JCLI-D-12-00049.1.

Guemas, V., Doblas-Reyes, F. J., Andreu-Burillo, I., and Asif, M. (2013b). Retrospective prediction of the global warming slowdown in the past decade. *Nat. Clim. Chang.* 3, 649–653. doi:10.1038/nclimate1863.

Guilyardi, E., Wittenberg, A., Balmaseda, M., Cai, W., Collins, M., McPhaden, M. J., et al. (2016). Fourth CLIVAR Workshop on the Evaluation of ENSO Processes in Climate Models: ENSO in a Changing Climate. *Bull. Am. Meteorol. Soc.* 97, 817–820. doi:10.1175/BAMS-D-15-00287.1.

Hall, A. (2004). The Role of Surface Albedo Feedback in Climate. *J. Clim.* 17, 1550–1568. doi:10.1175/1520-0442(2004)017<1550:TROSAF>2.0.CO;2.

Hall, A., and Qu, X. (2006). Using the current seasonal cycle to constrain snow albedo feedback in future climate change. *Geophys. Res. Lett.* 33, L03502. doi:10.1029/2005GL025127.

Hansen, J., Lacis, A., Rind, D., Russell, G., Stone, P., Fung, I., et al. (1984). *Climate sensitivity: Analysis of feedback mechanisms*. doi:10.1029/GM029p0130.

Hartmann, D. L., Klein Tank, A. M. G., Rusticucci, M., Alexander, L. V., Brönnimann, S., Charabi, Y. A. R., et al. (2013). "Observations: Atmosphere and Surface," in *Climate Change 2013: The Physical Science Basis. Contribution of Working Group I to the Fifth Assessment Report of the Intergovernmental Panel on Climate Change*, eds. T. F. Stocker, D. Qin, G.-K. Plattner, M. Tignor, S. K. Allen, J. Boschung, et al. (Cambridge: Cambridge University Press), 159–254. Available at: https://www.cambridge.org/core/product/identifier/CBO9781107415324A016/type/book_part.

Harvey, B. J., Shaffrey, L. C., and Woollings, T. J. (2014). Equator-to-pole temperature differences and the extra-tropical storm track responses of the CMIP5 climate models. *Clim. Dyn.* 43, 1171–1182. doi:10.1007/s00382-013-1883-9.

Harvey, B. J., Shaffrey, L. C., and Woollings, T. J. (2015). Deconstructing the climate change response of the Northern Hemisphere wintertime storm tracks. *Clim. Dyn.* 45, 2847–2860. doi:10.1007/s00382-015-2510-8.

Hawcroft, M., Walsh, E., Hodges, K., and Zappa, G. (2018). Significantly increased extreme precipitation expected in Europe and North America from extratropical cyclones. *Environ. Res. Lett.* 13, 124006. doi:10.1088/1748-9326/aaed59.

Hawkins, E., Anderson, B., Diffenbaugh, N., Mahlstein, I., Betts, R., Hegerl, G., et al. (2014). Uncertainties in the timing of unprecedented climates. *Nature* 511, E3–E5. doi:10.1038/nature13523.

Hawkins, E., Smith, R. S., Gregory, J. M., and Stainforth, D. A. (2016). Irreducible uncertainty in near-term climate projections. *Clim. Dyn.* 46, 3807–3819. doi:10.1007/s00382-015-2806-8.

Hawkins, E., and Sutton, R. (2009). The Potential to Narrow Uncertainty in Regional Climate Predictions. *Bull. Am. Meteorol. Soc.* 90, 1095–1108. doi:10.1175/2009BAMS2607.1.

Hawkins, E., and Sutton, R. (2011). The potential to narrow uncertainty in projections of regional precipitation change. *Clim. Dyn.* 37, 407–418. doi:10.1007/s00382-010-0810-6.

Hawkins, E., and Sutton, R. (2012). Time of emergence of climate signals. *Geophys. Res. Lett.* 39, n/a-n/a. doi:10.1029/2011GL050087.

Hawkins, E., and Sutton, R. (2016). Connecting Climate Model Projections of Global Temperature Change with the Real World. *Bull. Am. Meteorol. Soc.* 97, 963–980. doi:10.1175/BAMS-D-14-00154.1.

Hazeleger, W., Guemas, V., Wouters, B., Corti, S., Andreu-Burillo, I., Doblas-Reyes, F. J., et al. (2013). Multiyear climate predictions using two initialization strategies. *Geophys. Res. Lett.* 40, 1794–1798. doi:10.1002/grl.50355.

He, J., and Soden, B. J. (2017). A re-examination of the projected subtropical precipitation decline. *Nat. Clim. Chang.* 7, 53–57. doi:10.1038/nclimate3157.

Hedemann, C., Mauritsen, T., Jungclaus, J., and Marotzke, J. (2017). The subtle origins of surface-warming hiatuses. *Nat. Clim. Chang.* 7, 336–339. doi:10.1038/nclimate3274.

Held, I. M., and Soden, B. J. (2006). Robust responses of the hydrological cycle to global warming. *J. Clim.* 19, 5686–5699. doi:10.1175/JCLI3990.1.

Held, I. M., Winton, M., Takahashi, K., Delworth, T., Zeng, F. R., and Vallis, G. K. (2010). Probing the Fast and Slow Components of Global Warming by Returning Abruptly to Preindustrial Forcing. *J. Clim.* 23, 2418–2427.

Henley, B. J., Meehl, G., Power, S. B., Folland, C. K., King, A. D., Brown, J. N., et al. (2017). Spatial and temporal agreement in climate model simulations of the Interdecadal Pacific Oscillation. *Environ. Res. Lett.* 12, 044011. doi:10.1088/1748-9326/aa5cc8.

Herger, N., Sanderson, B. M., and Knutti, R. (2015). Improved pattern scaling approaches for the use in climate impact studies. *Geophys. Res. Lett.* 42, 3486–3494. doi:10.1002/2015GL063569.

Hermanson, L., Eade, R., Robinson, N. H., Dunstone, N. J., Andrews, M. B., Knight, J. R., et al. (2014). Forecast cooling of the Atlantic subpolar gyre and associated impacts. *Geophys. Res. Lett.* 41, 5167–5174. doi:10.1002/2014gl060420.

Hewitt, A. J., Booth, B. B. B., Jones, C. D., Robertson, E. S., Wiltshire, A. J., Sansom, P. G., et al. (2016). Sources of Uncertainty in Future Projections of the Carbon Cycle. *J. Clim.* 29, 7203–7213. doi:10.1175/JCLI-D-16-0161.1.

Hezel, P. J., Fichefet, T., and Massonnet, F. (2014). Modeled Arctic sea ice evolution through 2300 in CMIP5 extended RCPs. *Cryosph.* 8, 1195–1204.

Hienola, A., Matthews, D., Korhonen, H., Pietikäinen, J.-P., O'Donnell, D., Partanen, A.-I., et al. (2018). The impact of aerosol emissions on the 1.5oC pathways. *Environ. Res. Lett.* doi:10.1088/1748-9326/aab1b2.

Hingray, B., and Saïd, M. (2014). Partitioning Internal Variability and Model Uncertainty Components in a Multimember Multimodel Ensemble of Climate Projections. *J. Clim.* 27, 6779–6798. doi:10.1175/JCLI-D-13-00629.1.

Hoegh-Guldberg, O., Jacob, D., Taylor, M., Bindi, M., Brown, S., Camilloni, I., et al. (2018). "Impacts of 1.5°C Global Warming on Natural and Human Systems," in *Global Warming of 1.5°C. An IPCC Special Report on the impacts of global warming of 1.5°C above pre-industrial levels and related global greenhouse gas emission pathways, in the context of strengthening the global response to the threat of climate change,* eds. V. Masson-Delmotte, P. Zhai, H.-O. Pörtner, D. Roberts, J. Skea, P. R. Shukla, et al. (In Press). Available at: https://www.ipcc.ch/sr15.

Hoerling, M., Hurrell, J., Kumar, A., Terray, L., Eischeid, J., Pegion, P., et al. (2011). On North American Decadal Climate for 2011–20. *J. Clim.* 24, 4519–4528. doi:10.1175/2011JCLI4137.1.

Holland, M. M., and Bitz, C. M. (2003). Polar amplification of climate change in coupled models. *Clim. Dyn.* 21, 221–232. doi:10.1007/s00382-003-0332-6.

Holmes, C. R., Woollings, T., Hawkins, E., and de Vries, H. (2016). Robust Future Changes in Temperature Variability under Greenhouse Gas Forcing and the Relationship with Thermal Advection. *J. Clim.* 29, 2221–2236. doi:10.1175/JCLI-D-14-00735.1.

Hong, Y., Moore, J. C., Jevrejeva, S., Ji, D., Phipps, S. J., Lenton, A., et al. (2017). Impact of the GeoMIP G1 sunshade geoengineering experiment on the Atlantic meridional overturning circulation. *Environ. Res. Lett.* 12. doi:10.1088/1748-9326/aa5fb8.

Horton, R. M., Mankin, J. S., Lesk, C., Coffel, E., and Raymond, C. (2016). A Review of Recent Advances in Research on Extreme Heat Events. *Curr. Clim. Chang. Reports* 2, 242–259. doi:10.1007/s40641-016-0042-x.

Hoskins, B. J., and Karoly, D. J. (1981). The Steady Linear Response of a Spherical Atmosphere to Thermal and Orographic Forcing. *J. Atmos. Sci.* 38, 1179–1196. doi:10.1175/1520-0469(1981)038<1179:TSLROA>2.0.CO;2.

Hoskins, B., and Woollings, T. (2015). Persistent Extratropical Regimes and Climate Extremes. *Curr. Clim. Chang. Reports* 1, 115–124. doi:10.1007/s40641-015-0020-8.

Houghton, R. A., Baccini, A., and Walker, W. S. (2018). Where is the residual terrestrial carbon sink? *Glob. Chang. Biol.* 24, 3277–3279. doi:10.1111/gcb.14313.

Hsu, P., Li, T., Murakami, H., and Kitoh, A. (2013). Future change of the global monsoon revealed from 19 CMIP5 models. *J. Geophys. Res. Atmos.* 118, 1247–1260. doi:10.1002/jgrd.50145.

Huang, P., Xie, S. P., Hu, K., Huang, G., and Huang, R. (2013). Patterns of the seasonal response of tropical rainfall to global warming. *Nat. Geosci.* 6, 357–361. doi:10.1038/ngeo1792.

Huntingford, C., Jones, P. D., Livina, V. N., Lenton, T. M., and Cox, P. M. (2013). No increase in global temperature variability despite changing regional patterns. *Nature* 500, 327–330. doi:10.1038/nature12310.

Hwang, Y.-T., Frierson, D. M. W., and Kang, S. M. (2013). Anthropogenic sulfate aerosol and the southward shift of tropical precipitation in the late 20th century. *Geophys. Res. Lett.* 40, 2845–2850. doi:10.1002/grl.50502.

Iles, C. E., and Hegerl, G. C. (2014). The global precipitation response to volcanic eruptions in the CMIP5 models. *Environ. Res. Lett.* 9, 104012. doi:10.1088/1748-9326/9/10/104012.

Iles, C. E., and Hegerl, G. C. (2015). Systematic change in global patterns of streamflow following volcanic eruptions. *Nat. Geosci.* 8, 838–842. doi:10.1038/ngeo2545.

Iles, C. E., Hegerl, G. C., Schurer, A. P., and Zhang, X. (2013). The effect of volcanic eruptions on global precipitation. *J. Geophys. Res. Atmos.* 118, 8770–8786. doi:10.1002/jgrd.50678.

IPCC (2014). *Climate Change 2014: Mitigation of Climate Change*. doi:10.1017/CBO9781107415416.

Irvine, P., Emanuel, K., He, J., Horowitz, L. W., Vecchi, G., and Keith, D. (2019). Halving warming with idealized solar geoengineering moderates key climate hazards. *Nat. Clim. Chang.* 9, 295–299. doi:10.1038/s41558-019-0398-8.

Irvine, P. J., Kravitz, B., Lawrence, M. G., and Muri, H. (2016). An overview of the Earth system science of solar geoengineering. *Wiley Interdiscip. Rev. Clim. Chang.* 7, 815–833. doi:10.1002/wcc.423.

Ishizaki, Y., Shiogama, H., Emori, S., Yokohata, T., Nozawa, T., Takahashi, K., et al. (2013). Dependence of precipitation scaling patterns on emission scenarios for representative concentration pathways. *J. Clim.* doi:10.1175/JCLI-D-12-00540.1.

Izumi, K., Bartlein, P. J., and Harrison, S. P. (2013). Consistent large-scale temperature responses in warm and cold climates. *Geophys. Res. Lett.* 40, 1817–1823.

Jackson, L. C., Peterson, K. A., Roberts, C. D., and Wood, R. A. (2016a). Recent slowing of Atlantic overturning circulation as a recovery from earlier strengthening. *Nat. Geosci.* 9, 518–522. doi:10.1038/ngeo2715.

Jackson, L. S., Crook, J. A., and Forster, P. M. (2016b). An intensified hydrological cycle in the simulation of geoengineering by cirrus cloud thinning using ice crystal fall speed changes. *J. Geophys. Res. Atmos.* 121, 6822–6840. doi:10.1002/2015JD024304.

Jacob, D., Kotova, L., Teichmann, C., Sobolowski, S. P., Vautard, R., Donnelly, C., et al. (2018). Climate Impacts in Europe Under +1.5°C Global Warming. *Earth's Futur.* 6, 264–285. doi:10.1002/2017EF000710.

Jahn, A. (2018). Reduced probability of ice-free summers for 1.5 °C compared to 2 °C warming. *Nat. Clim. Chang.* 8, 409–413. doi:10.1038/s41558-018-0127-8.

James, R., Washington, R., Schleussner, C.-F., Rogelj, J., and Conway, D. (2017). Characterizing half-a-degree difference: a review of methods for identifying regional climate responses to global warming targets. *Wiley Interdiscip. Rev. Clim. Chang.* 8, e457. doi:10.1002/wcc.457.

John, J. G., Stock, C. A., and Dunne, J. P. (2015). A more productive, but different, ocean after mitigation. *Geophys. Res. Lett.* 42, 9836–9845.

Johnson, J. S., Regayre, L. A., Yoshioka, M., Pringle, K. J., Lee, L. A., Sexton, D. M. H., et al. (2018). The importance of comprehensive parameter sampling and multiple observations for robust constraint of aerosol radiative forcing. *Atmos. Chem. Phys.* 18, 13031–13053. doi:10.5194/acp-18-13031-2018.

Jones, A. C., Hawcroft, M. K., Haywood, J. M., Moore, J. C., Jones, A., and Guo, X. (2018). Regional Climate Impacts of Stabilizing GlobalWarming at 1.5 K Using Solar Geoengineering. *Earth's Futur.* 6, 1–22. doi:10.1002/2017EF000720.

Jones, A., Haywood, J. M., Alterskjær, K., Boucher, O., Cole, J. N. S., Curry, C. L., et al. (2013). The impact of abrupt suspension of solar radiation management (termination effect) in experiment G2 of the Geoengineering Model Intercomparison Project (GeoMIP). *J. Geophys. Res. Atmos.* 118, 9743–9752. doi:10.1002/jgrd.50762.

Jones, C. D., Arora, V., Friedlingstein, P., Bopp, L., Brovkin, V., Dunne, J., et al. (2016a). C4MIP-The Coupled Climate-Carbon Cycle Model Intercomparison Project: experimental protocol for CMIP6. *Geosci. Model Dev.* 9, 2853–2880. doi:10.5194/gmd-9-2853-2016.

Jones, C. D., Ciais, P., Davis, S. J., Friedlingstein, P., Gasser, T., Peters, G. P., et al. (2016b). Simulating the Earth system response to negative emissions. *Environ. Res. Lett.* 11, 095012. doi:10.1088/1748-9326/11/9/095012.

Jones, J. M., Gille, S. T., Goosse, H., Abram, N. J., Canziani, P. O., Charman, D. J., et al. (2016c). Assessing recent trends in high-latitude Southern Hemisphere surface climate. *Nat. Clim. Chang.* 6, 917–926.

doi:10.1038/nclimate3103.

Joos, F., Roth, R., Fuglestvedt, J. S., Peters, G. P., Enting, I. G., von Bloh, W., et al. (2013). Carbon dioxide and climate impulse response functions for the computation of greenhouse gas metrics: a multi-model analysis. *Atmos. Chem. Phys.* 13, 2793–2825. doi:10.5194/acp-13-2793-2013.

Joshi, M., and Gregory, J. (2008). Dependence of the land-sea contrast in surface climate response on the nature of the forcing. *Geophys. Res. Lett.* 35, L24802. doi:10.1029/2008GL036234.

Joshi, M. M., Gregory, J. M., Webb, M. J., Sexton, D. M. H., and Johns, T. C. (2008). Mechanisms for the land/sea warming contrast exhibited by simulations of climate change. *Clim. Dyn.* 30, 455–465.

Joshi, M. M., Lambert, F. H., and Webb, M. J. (2013). An explanation for the difference between twentieth and twenty-first century land–sea warming ratio in climate models. *Clim. Dyn.* 41, 1853–1869. doi:10.1007/s00382-013-1664-5.

Jungclaus, J. H., Lorenz, S. J., Timmreck, C., Reick, C. H., Brovkin, V., Six, K., et al. (2010). Climate and carbon-cycle variability over the last millennium. *Clim. Past* 6, 723–737. doi:doi:10.5194/cp-6-723-2010.

Kalidindi, S., Bala, G., Modak, A., and Caldeira, K. (2015). Modeling of solar radiation management: a comparison of simulations using reduced solar constant and stratospheric sulphate aerosols. *Clim. Dyn.* 44, 2909–2925. doi:10.1007/s00382-014-2240-3.

Kamae, Y., and Watanabe, M. (2012). On the robustness of tropospheric adjustment in CMIP5 models. *Geophys. Res. Lett.* 39, L23808. doi:10.1029/2012GL054275.

Kamae, Y., and Watanabe, M. (2013). Tropospheric adjustment to increasing CO2: Its timescale and the role of land-sea contrast. *Clim. Dyn.* 41, 3007–3024. doi:10.1007/s00382-012-1555-1.

Kang, S., and Eltahir, E. A. B. (2018). North China Plain threatened by deadly heatwaves due to climate change and irrigation. *Nat. Commun.* 9, 2894. doi:10.1038/s41467-018-05252-y.

Kar-Man Chang, E. (2018). CMIP5 Projected Change in Northern Hemisphere Winter Cyclones with Associated Extreme Winds. *J. Clim.* 31, 6527–6542. doi:10.1175/JCLI-D-17-0899.1.

Karspeck, A., Yeager, S., Danabasoglu, G., and Teng, H. (2015). An evaluation of experimental decadal predictions using CCSM4. *Clim. Dyn.* 44, 907–923. doi:10.1007/s00382-014-2212-7.

Kay, J. E., Deser, C., Phillips, A., Mai, A., Hannay, C., Strand, G., et al. (2015). The Community Earth System Model (CESM) Large Ensemble project : A community resource for studying climate change in the presence of internal climate variability. *Bull. Am. Meteorol. Soc.* 96, 1333–1349. doi:10.1175/BAMS-D-13-00255.1.

Keith, D. W., and MacMartin, D. G. (2015). A temporary, moderate and responsive scenario for solar geoengineering. *Nat. Clim. Chang.* 5, 201–206. doi:10.1038/nclimate2493.

Keller, D. P., Feng, E. Y., and Oschlies, A. (2014). Potential climate engineering effectiveness and side effects during a high carbon dioxide-emission scenario. *Nat. Commun.* 5, 3304. doi:10.1038/ncomms4304 https://www.nature.com/articles/ncomms4304#supplementary-information.

Keller, D. P., Lenton, A., Scott, V., Vaughan, N. E., Bauer, N., Ji, D., et al. (2018). The Carbon Dioxide Removal Model Intercomparison Project (CDRMIP): rationale and experimental protocol for CMIP6. *Geosci. Model Dev.* 11, 1133–1160. doi:10.5194/gmd-11-1133-2018.

Kennedy, D., Parker, T., Woollings, T., Harvey, B., and Shaffrey, L. (2016). The response of high-impact blocking weather systems to climate change. *Geophys. Res. Lett.* 43, 7250–7258. doi:10.1002/2016GL069725.

Kent, C., Chadwick, R., and Rowell, D. P. (2015). Understanding Uncertainties in Future Projections of Seasonal Tropical Precipitation. *J. Clim.* 28, 4390–4413. doi:10.1175/JCLI-D-14-00613.1.

Kharin, V. V., Boer, G. J., Merryfield, W. J., Scinocca, J. F., and Lee, W. S. (2012). Statistical adjustment of decadal predictions in a changing climate. *Geophys. Res. Lett.* 39, n/a-n/a. doi:10.1029/2012GL052647.

Kharin, V. V., Flato, G. M., Zhang, X., Gillett, N. P., Zwiers, F., and Anderson, K. J. (2018). Risks from Climate Extremes Change Differently from 1.5°C to 2.0°C Depending on Rarity. *Earth's Futur.* 6, 704–715. doi:10.1002/2018EF000813.

Kim, B.-M., Son, S.-W., Min, S.-K., Jeong, J.-H., Kim, S.-J., Zhang, X., et al. (2014a). Weakening of the stratospheric polar vortex by Arctic sea-ice loss. *Nat. Commun.* 5, 4646. Available at: https://doi.org/10.1038/ncomms5646.

Kim, S. T., Cai, W., Jin, F.-F., Santoso, A., Wu, L., Guilyardi, E., et al. (2014b). Response of El Niño sea surface temperature variability to greenhouse warming. *Nat. Clim. Chang.* 4, 786–790. doi:10.1038/nclimate2326.

Kimmritz, M., Counillon, F., Bitz, C. M., Massonnet, F., Bethke, I., and Gao, Y. (2018). Optimising assimilation of sea ice concentration in an Earth system model with a multicategory sea ice model. *Tellus A Dyn. Meteorol. Oceanogr.* 70, 1–23. doi:10.1080/16000870.2018.1435945.

Kirchmeier-Young, M. C., Zwiers, F. W., and Gillett, N. P. (2017). Attribution of Extreme Events in Arctic Sea Ice Extent. *J. Clim.* 30, 553–571. doi:10.1175/JCLI-D-16-0412.1.

Kirtman, B., Power, S. B., Adedoyin, J. A., Boer, G. J., Bojariu, R., Camilloni, I., et al. (2013). "Near-term climate change: projections and predictability," in *Climate Change 2013: The Physical Science Basis. Contribution of Working Group I to the Fifth Assessment Report of the Intergovernmental Panel on Climate Change*, eds. T. F. Stocker, D. Qin, G.-K. Plattner, M. Tignor, S. K. Allen, J. Boschung, et al. (Cambridge, United Kingdom and New York, NY, USA: Cambridge University Press), 953–1028.

Kitano, Y., and Yamada, T. J. (2016). Relationship between atmospheric blocking and cold day extremes in current and

RCP8.5 future climate conditions over Japan and the surrounding area. *Atmos. Sci. Lett.* 17, 616–622. doi:10.1002/asl.711.
Kitoh, A., and Endo, H. (2016). Changes in precipitation extremes projected by a 20-km mesh global atmospheric model. *Weather Clim. Extrem.* 11, 41–52. doi:https://doi.org/10.1016/j.wace.2015.09.001.
Kitoh, A., Endo, H., Krishna Kumar, K., Cavalcanti, I. F. A., Goswami, P., and Zhou, T. (2013). Monsoons in a changing world: A regional perspective in a global context. *J. Geophys. Res. Atmos.* 118, 3053–3065. doi:10.1002/jgrd.50258.
Kjellström, E., Nikulin, G., Strandberg, G., Christensen, O. B., Jacob, D., Keuler, K., et al. (2018). European climate change at global mean temperature increases of 1.5 and 2 °C above pre-industrial conditions as simulated by the EURO-CORDEX regional climate models. *Earth Syst. Dyn.* 9, 459–478. doi:10.5194/esd-9-459-2018.
Klus, A., Prange, M., Varma, V., Tremblay, L. B., and Schulz, M. (2018). Abrupt cold events in the North Atlantic Ocean in a transient Holocene simulation. *Clim. Past* 14, 1165–1178. doi:10.5194/cp-14-1165-2018.
Knight, J. R., Andrews, M. B., Smith, D. M., Arribas, A., Colman, A. W., Dunstone, N. J., et al. (2014). Predictions of Climate Several Years Ahead Using an Improved Decadal Prediction System. *J. Clim.* 27, 7550–7567. doi:10.1175/JCLI-D-14-00069.1.
Knutson, T. R., and Ploshay, J. J. (2016). Detection of anthropogenic influence on a summertime heat stress index. *Clim. Change* 138, 25–39. doi:10.1007/s10584-016-1708-z.
Knutti, R., Furrer, R., Tebaldi, C., Cermak, J., and Meehl, G. a. (2010). Challenges in Combining Projections from Multiple Climate Models. *J. Clim.* 23, 2739–2758. doi:10.1175/2009JCLI3361.1.
Knutti, R., Masson, D., and Gettelman, A. (2013a). Climate model genealogy: Generation CMIP5 and how we got there. *Geophys. Res. Lett.* 40, 1194–1199. doi:10.1002/grl.50256.
Knutti, R., and Rugenstein, M. A. A. (2015). Feedbacks, climate sensitivity and the limits of linear models. *Philos. Trans. R. Soc. A Math. Phys. Eng. Sci.* 373, 20150146. doi:10.1098/rsta.2015.0146.
Knutti, R., Sedláček, J., Sanderson, B. M., Lorenz, R., Fischer, E. M., and Eyring, V. (2017). A climate model projection weighting scheme accounting for performance and interdependence. *Geophys. Res. Lett.* 44, 1909–1918. doi:10.1002/2016GL072012.
Knutti, R., Sedláček, J., and Sedlacek, J. (2013b). Robustness and uncertainties in the new CMIP5 climate model projections. *Nat. Clim. Chang.* 3, 369–373. doi:10.1038/nclimate1716.
Koenigk, T., Devasthale, A., and Karlsson, K. G. (2014). Summer arctic sea ice albedo in CMIP5 models. *Atmos. Chem. Phys.* 14, 1987–1998. doi:10.5194/acp-14-1987-2014.
Kohyama, T., and Hartmann, D. L. (2017). Nonlinear ENSO Warming Suppression (NEWS). *J. Clim.* 30, 4227–4251. doi:10.1175/JCLI-D-16-0541.1.
Kopp, R. E., Horton, R. M., Little, C. M., Mitrovica, J. X., Oppenheimer, M., Rasmussen, D. J., et al. (2014). Probabilistic 21st and 22nd century sea-level projections at a global network of tide-gauge sites. *Earth's Futur.* 2, 383–406. doi:10.1002/2014EF000239.
Kosaka, Y., and Xie, S.-P. (2013). Recent global-warming hiatus tied to equatorial Pacific surface cooling. *Nature* 501, 403–407. doi:10.1038/nature12534.
Kosaka, Y., and Xie, S.-P. (2016). The tropical Pacific as a key pacemaker of the variable rates of global warming. *Nat. Geosci.* 9, 669–673. doi:10.1038/ngeo2770.
Kostov, Y., Marshall, J., Hausmann, U., Armour, K. C., Ferreira, D., and Holland, M. M. (2017). Fast and slow responses of Southern Ocean sea surface temperature to SAM in coupled climate models. *Clim. Dyn.* 48, 1595–1609. doi:10.1007/s00382-016-3162-z.
Krasting, J. P., Dunne, J. P., Shevliakova, E., and Stouffer, R. J. (2014). Trajectory sensitivity of the transient climate response to cumulative carbon emissions. *Geophys. Res. Lett.* 41, 2520–2527. doi:10.1002/2013GL059141.
Kravitz, B., Caldeira, K., Boucher, O., Robock, A., Rasch, P. J., Alterskjær, K., et al. (2013a). Climate model response from the Geoengineering Model Intercomparison Project (GeoMIP). *J. Geophys. Res. Atmos.* 118, 8320–8332. doi:10.1002/jgrd.50646.
Kravitz, B., Forster, P. M., Jones, A., Robock, A., Alterskjaer, K., Boucher, O., et al. (2013b). Sea spray geoengineering experiments in the geoengineering model intercomparison project (GeoMIP): Experimental design and preliminary results. *J. Geophys. Res. Atmos.* 118, 11,175-11,186. doi:10.1002/jgrd.50856.
Kravitz, B., MacMartin, D. G., Mills, M. J., Richter, J. H., Tilmes, S., Lamarque, J.-F., et al. (2017). First Simulations of Designing Stratospheric Sulfate Aerosol Geoengineering to Meet Multiple Simultaneous Climate Objectives. *J. Geophys. Res. Atmos.* 122, 12,616-12,634. doi:10.1002/2017JD026874.
Kravitz, B., Robock, A., Tilmes, S., Boucher, O., English, J. M., Irvine, P. J., et al. (2015). The Geoengineering Model Intercomparison Project Phase 6 (GeoMIP6): simulation design and preliminary results. *Geosci. Model Dev.* 8, 3379–3392. doi:10.5194/gmd-8-3379-2015.
Krishnan, R., Sabin, T. P., Vellore, R., Mujumdar, M., Sanjay, J., Goswami, B. N., et al. (2016). Deciphering the desiccation trend of the South Asian monsoon hydroclimate in a warming world. *Clim. Dyn.* 47, 1007–1027. doi:10.1007/s00382-015-2886-5.
Kristjánsson, J. E., Muri, H., and Schmidt, H. (2015). The hydrological cycle response to cirrus cloud thinning. *Geophys. Res. Lett.* 42, 10807–10815. doi:10.1002/2015GL066795.

Kröger, J., Pohlmann, H., Sienz, F., Marotzke, J., Baehr, J., Köhl, A., et al. (2018). Full-field initialized decadal predictions with the MPI Earth system model: an initial shock in the North Atlantic. *Clim. Dyn.* 51, 2593–2608. doi:10.1007/s00382-017-4030-1.
Kröner, N., Kotlarski, S., Fischer, E., Lüthi, D., Zubler, E., and Schär, C. (2017). Separating climate change signals into thermodynamic, lapse-rate and circulation effects: theory and application to the European summer climate. *Clim. Dyn.* 48, 3425–3440. doi:10.1007/s00382-016-3276-3.
Kruschke, T., Rust, H. W., Kadow, C., Müller, W. A., Pohlmann, H., Leckebusch, G. C., et al. (2016). Probabilistic evaluation of decadal prediction skill regarding Northern Hemisphere winter storms. *Meteorol. Zeitschrift* 25, 721–738. doi:10.1127/metz/2015/0641.
Lambert, F. H., and Allen, M. R. (2009). Are changes in global precipitation constrained by the tropospheric energy budget? *J. Clim.* 22, 499–517. doi:10.1175/2008JCLI2135.1.
Lambert, F. H., and Chiang, J. C. H. (2007). Control of land-ocean temperature contrast by ocean heat uptake. *Geophys. Res. Lett.* 34, n/a-n/a. doi:10.1029/2007GL029755.
Lambert, F. H., Ferraro, A. J., and Chadwick, R. (2017). Land–Ocean Shifts in Tropical Precipitation Linked to Surface Temperature and Humidity Change. *J. Clim.* 30, 4527–4545. doi:10.1175/JCLI-D-16-0649.1.
Lambert, F. H., Webb, M. J., and Joshi, M. M. (2011). The relationship between land-ocean surface temperature contrast and radiative forcing. *J. Clim.* 24, 3239–3256.
Langenbrunner, B., Neelin, J. D., Lintner, B. R., and Anderson, B. T. (2015). Patterns of Precipitation Change and Climatological Uncertainty among CMIP5 Models, with a Focus on the Midlatitude Pacific Storm Track. *J. Clim.* 28, 7857–7872. doi:10.1175/JCLI-D-14-00800.1.
Lapp, S. L., St. Jacques, J.-M., Barrow, E. M., and Sauchyn, D. J. (2012). GCM projections for the Pacific Decadal Oscillation under greenhouse forcing for the early 21st century. *Int. J. Climatol.* 32, 1423–1442. doi:10.1002/joc.2364.
Latham, J., Bower, K., Choularton, T., Coe, H., Connolly, P., Cooper, G., et al. (2012). Marine cloud brightening. *Philos. Trans. R. Soc. A Math. Phys. Eng. Sci.* 370, 4217–4262. doi:10.1098/rsta.2012.0086.
Lawrence, D. M., Hurtt, G. C., Arneth, A., Brovkin, V., Calvin, K. V, Jones, A. D., et al. (2016). The Land Use Model Intercomparison Project (LUMIP) contribution to CMIP6: rationale and experimental design. *Geosci. Model Dev.* 9, 2973–2998. doi:10.5194/gmd-9-2973-2016.
Leduc, M., Matthews, H. D., and De Elía, R. (2015). Quantifying the limits of a linear temperature response to cumulative CO2 emissions. *J. Clim.* 28, 9955–9968. doi:10.1175/JCLI-D-14-00500.1.
Lee, C.-J., Liao, Y.-C., Lan, C.-W., Chiang, J. C. H., Chung, C.-H., and Chou, C. (2013). Increase in the range between wet and dry season precipitation. *Nat. Geosci.* 6, 263–267. doi:10.1038/ngeo1744.
Lee, D. Y., and Ahn, J.-B. (2017). Future change in the frequency and intensity of wintertime North Pacific blocking in CMIP5 models. *Int. J. Climatol.* 37, 2765–2781. doi:10.1002/joc.4878.
Lee, H. J., Kwon, M. O., Yeh, S.-W., Kwon, Y.-O., Park, W., Park, J.-H., et al. (2017). Impact of Poleward Moisture Transport from the North Pacific on the Acceleration of Sea Ice Loss in the Arctic since 2002. *J. Clim.* 30, 6757–6769. doi:10.1175/JCLI-D-16-0461.1.
Lee, J. Y., and Wang, B. (2014). Future change of global monsoon in the CMIP5. *Clim. Dyn.* 42, 101–119. doi:10.1007/s00382-012-1564-0.
Lee, L. A., Reddington, C. L., and Carslaw, K. S. (2016). On the relationship between aerosol model uncertainty and radiative forcing uncertainty. *Proc. Natl. Acad. Sci.* 113, 5820–5827. doi:10.1073/pnas.1507050113.
Lee, S., Gong, T., Johnson, N., Feldstein, S. B., and Pollard, D. (2011). On the Possible Link between Tropical Convection and the Northern Hemisphere Arctic Surface Air Temperature Change between 1958 and 2001. *J. Clim.* 24, 4350–4367. doi:10.1175/2011JCLI4003.1.
Lee, S., Woods, C., and Caballero, R. (2019). Relation Between Arctic Moisture Flux and Tropical Temperature Biases in CMIP5 Simulations and Its Fingerprint in RCP8.5 Projections. *Geophys. Res. Lett.* 46, 1088–1096. doi:10.1029/2018GL080562.
Lehmann, J., Coumou, D., Frieler, K., Eliseev, A. V, and Levermann, A. (2014). Future changes in extratropical storm tracks and baroclinicity under climate change. *Environ. Res. Lett.* 9, 084002. doi:10.1088/1748-9326/9/8/084002.
Lehner, F., Deser, C., and Sanderson, B. M. (2018). Future risk of record-breaking summer temperatures and its mitigation. *Clim. Change* 146, 363–375. doi:10.1007/s10584-016-1616-2.
Lehner, F., Deser, C., and Terray, L. (2017). Toward a new estimate of "Time of Emergence" of anthropogenic warming: Insights from dynamical adjustment and a large initial-condition model ensemble. *J. Clim.* 30, 7739–7756. doi:10.1175/JCLI-D-16-0792.1.
Lelieveld, J., Klingmüller, K., Pozzer, A., Burnett, R. T., Haines, A., and Ramanathan, V. (2019). Effects of fossil fuel and total anthropogenic emission removal on public health and climate. *Proc. Natl. Acad. Sci.* 0, 201819989. doi:10.1073/pnas.1819989116.
Lenderink, G., van den Hurk, B. J. J. M., Klein Tank, A. M. G., van Oldenborgh, G. J., van Meijgaard, E., de Vries, H., et al. (2014). Preparing local climate change scenarios for the Netherlands using resampling of climate model output. *Environ. Res. Lett.* 9, 115008. doi:10.1088/1748-9326/9/11/115008.
Levy, H., Horowitz, L. W., Schwarzkopf, M. D., Ming, Y., Golaz, J.-C., Naik, V., et al. (2013). The roles of aerosol

direct and indirect effects in past and future climate change. *J. Geophys. Res. Atmos.* 118, 4521–4532. doi:10.1002/jgrd.50192.

Li, C., Michel, C., Seland Graff, L., Bethke, I., Zappa, G., Bracegirdle, T. J., et al. (2018a). Midlatitude atmospheric circulation responses under 1.5 and 2.0 °C warming and implications for regional impacts. *Earth Syst. Dyn.* 9, 359–382. doi:10.5194/esd-9-359-2018.

Li, C., von Storch, J.-S., and Marotzke, J. (2013). Deep-ocean heat uptake and equilibrium climate response. *Clim. Dyn.* 40, 1071–1086. doi:10.1007/s00382-012-1350-z.

Li, C., Zhang, X., Zwiers, F., Fang, Y., and Michalak, A. M. (2017). Recent Very Hot Summers in Northern Hemispheric Land Areas Measured by Wet Bulb Globe Temperature Will Be the Norm Within 20 Years. *Earth's Futur.* 5, 1203–1216. doi:10.1002/2017EF000639.

Li, G., Xie, S.-P., and Du, Y. (2016a). A Robust but Spurious Pattern of Climate Change in Model Projections over the Tropical Indian Ocean. *J. Clim.* 29, 5589–5608. doi:10.1175/JCLI-D-15-0565.1.

Li, H., Ilyina, T., Müller, W. A., and Landschützer, P. (2019). Predicting the variable ocean carbon sink. *Sci. Adv.*, in press.

Li, H., Ilyina, T., Müller, W. A., and Sienz, F. (2016b). Decadal predictions of the North Atlantic CO2 uptake. *Nat. Commun.* 7, 10.1038/ncomms11076. doi:10.1038/ncomms11076.

Li, J., Chen, Y. D., Gan, T. Y., and Lau, N.-C. (2018b). Elevated increases in human-perceived temperature under climate warming. *Nat. Clim. Chang.* 8, 43–47. doi:10.1038/s41558-017-0036-2.

Li, J., and Wang, J. X. L. (2003). A modified zonal index and its physical sense. *Geophys. Res. Lett.* 30. doi:10.1029/2003GL017441.

Li, M., Woollings, T., Hodges, K., and Masato, G. (2014). Extratropical cyclones in a warmer, moister climate: A recent Atlantic analogue. *Geophys. Res. Lett.* 41, 8594–8601. doi:10.1002/2014GL062186.

Li, W., Ciais, P., Wang, Y., Peng, S., Broquet, G., Ballantyne, A. P., et al. (2016c). Reducing uncertainties in decadal variability of the global carbon budget with multiple datasets. *Proc. Natl. Acad. Sci.* 113, 13104–13108. doi:10.1073/pnas.1603956113.

Lin, R., Zhou, T., and Qian, Y. (2014). Evaluation of Global Monsoon Precipitation Changes based on Five Reanalysis Datasets. *J. Clim.* 27, 1271–1289. doi:10.1175/JCLI-D-13-00215.1.

Liu, C., Becker, A., Kendon, E. J., Arkin, P. A., Zhang, X., Ingram, W. J., et al. (2014). Challenges in Quantifying Changes in the Global Water Cycle. *Bull. Am. Meteorol. Soc.* 96, 1097–1115. doi:10.1175/bams-d-13-00212.1.

Liu, L., Shawki, D., Voulgarakis, A., Kasoar, M., Samset, B. H., Myhre, G., et al. (2018a). A PDRMIP Multimodel Study on the Impacts of Regional Aerosol Forcings on Global and Regional Precipitation. *J. Clim.* 31, 4429–4447. doi:10.1175/JCLI-D-17-0439.1.

Liu, W., Lu, J., Xie, S.-P., and Fedorov, A. (2018b). Southern Ocean Heat Uptake, Redistribution, and Storage in a Warming Climate: The Role of Meridional Overturning Circulation. *J. Clim.* 31, 4727–4743. doi:10.1175/JCLI-D-17-0761.1.

Liu, W., Xie, S.-P., Liu, Z., and Zhu, J. (2017). Overlooked possibility of a collapsed Atlantic Meridional Overturning Circulation in warming climate. *Sci. Adv.* 3, e1601666. doi:10.1126/sciadv.1601666.

Liu, Y., Hallberg, R., Sergienko, O., Samuels, B. L., Harrison, M., and Oppenheimer, M. (2018c). Climate response to the meltwater runoff from Greenland ice sheet: evolving sensitivity to discharging locations. *Clim. Dyn.* 51, 1733–1751. doi:10.1007/s00382-017-3980-7.

Liu, Z. (2012). Dynamics of Interdecadal Climate Variability: A Historical Perspective*. *J. Clim.* 25, 1963–1995. doi:10.1175/2011JCLI3980.1.

Liu, Z., and Di Lorenzo, E. (2018). Mechanisms and Predictability of Pacific Decadal Variability. *Curr. Clim. Chang. Reports* 4, 128–144. doi:10.1007/s40641-018-0090-5.

Lo, Y. T. E., Charlton-Perez, A. J., Lott, F. C., and Highwood, E. J. (2016). Detecting sulphate aerosol geoengineering with different methods. *Sci. Rep.* 6, 1–10. doi:10.1038/srep39169.

Lopez, A., Suckling, E. B., and Smith, L. A. (2014). Robustness of pattern scaled climate change scenarios for adaptation decision support. *Clim. Change* 122, 555–566. doi:10.1007/s10584-013-1022-y.

Losada, T., and Rodríguez-Fonseca, B. (2016). Tropical atmospheric response to decadal changes in the Atlantic Equatorial Mode. *Clim. Dyn.* 47, 1211–1224. doi:10.1007/s00382-015-2897-2.

Lovenduski, N. S., McKinley, G. A., Fay, A. R., Lindsay, K., and Long, M. C. (2016). Partitioning uncertainty in ocean carbon uptake projections: Internal variability, emission scenario, and model structure. *Global Biogeochem. Cycles* 30, 1276–1287. doi:10.1002/2016GB005426.

Lübbecke, J. F., Rodríguez-Fonseca, B., Richter, I., Martín-Rey, M., Losada, T., Polo, I., et al. (2018). Equatorial Atlantic variability-Modes, mechanisms, and global teleconnections. *Wiley Interdiscip. Rev. Clim. Chang.* 9, e527. doi:10.1002/wcc.527.

MacDougall, A. H. (2013). Reversing climate warming by artificial atmospheric carbon-dioxide removal: Can a Holocene-like climate be restored? *Geophys. Res. Lett.* 40, 5480–5485.

MacDougall, A. H. (2016). The Transient Response to Cumulative CO2 Emissions: a Review. *Curr. Clim. Chang. Reports* 2, 39–47. doi:10.1007/s40641-015-0030-6.

MacMartin, D. G., Kravitz, B., Tilmes, S., Richter, J. H., Mills, M. J., Lamarque, J.-F., et al. (2017). The Climate

Response to Stratospheric Aerosol Geoengineering Can Be Tailored Using Multiple Injection Locations. *J. Geophys. Res. Atmos.* 122, 12,574-12,590. doi:10.1002/2017JD026868.

MacMartin, D. G., Ricke, K. L., and Keith, D. W. (2018). Solar geoengineering as part of an overall strategy for meeting the 1.5°C Paris target. *Philos. Trans. R. Soc. A Math. Phys. Eng. Sci.* 376, 20160454. doi:10.1098/rsta.2016.0454.

MacMartin, D. G., Wang, W., Kravitz, B., Tilmes, S., Richter, J. H., and Mills, M. J. (2019). Timescale for Detecting the Climate Response to Stratospheric Aerosol Geoengineering. *J. Geophys. Res. Atmos.* 124, 1233–1247. doi:10.1029/2018JD028906.

Magnusson, L., Alonso-Balmaseda, M., Corti, S., Molteni, F., and Stockdale, T. (2013). Evaluation of forecast strategies for seasonal and decadal forecasts in presence of systematic model errors. *Clim. Dyn.* 41, 2393–2409. doi:10.1007/s00382-012-1599-2.

Maher, N., Matei, D., Milinski, S., and Marotzke, J. (2018). ENSO Change in Climate Projections: Forced Response or Internal Variability? *Geophys. Res. Lett.* 45, 11,390-11,398. doi:10.1029/2018GL079764.

Maher, N., McGregor, S., England, M. H., and Gupta, A. Sen (2015). Effects of volcanism on tropical variability. *Geophys. Res. Lett.* 42, 6024–6033. doi:10.1002/2015GL064751.

Maher, N., Milinski, S., Suarez-Gutierrez, L., Botzet, M., Kornblueh, L., Takano, Y., et al. (2019). The Max Planck Institute Grand Ensemble – enabling the exploration of climate system variability. *J. Adv. Model. Earth Syst.*, submitted.

Mahlstein, I., and Knutti, R. (2011). Ocean Heat Transport as a Cause for Model Uncertainty in Projected Arctic Warming. *J. Clim.* 24, 1451–1460. doi:10.1175/2010JCLI3713.1.

Man, W., Zhou, T., and Jungclaus, J. H. (2014). Effects of Large Volcanic Eruptions on Global Summer Climate and East Asian Monsoon Changes during the Last Millennium: Analysis of MPI-ESM Simulations. *J. Clim.* 27, 7394–7409. doi:10.1175/JCLI-D-13-00739.1.

Manabe, S., and Stouffer, R. J. (1980). Sensitivity of a global climate model to an increase of CO 2 concentration in the atmosphere. *J. Geophys. Res.* 85, 5529–5554. doi:10.1029/JC085iC10p05529.

Manabe, S., Stouffer, R. J., Spelman, M. J., and Bryan, K. (1991). Transient responses of a coupled ocean-atmosphere model to gradual changes of atmospheric CO2. Part I: Annual Mean Response. *J. Clim.* 4, 785–818.

Manabe, S., and Wetherald, R. T. (1975). The Effects of Doubling the CO 2 Concentration on the climate of a General Circulation Model. *J. Atmos. Sci.* 32, 3–15. doi:10.1175/1520-0469(1975)032<0003:TEODTC>2.0.CO;2.

Manabe, S., and Wetherald, R. T. (1980). On the Distribution of Climate Change Resulting from an Increase in CO 2 Content of the Atmosphere. *J. Atmos. Sci.* 37, 99–118. doi:10.1175/1520-0469(1980)037<0099:OTDOCC>2.0.CO;2.

Mantua, N. J., Hare, S. R., Zhang, Y., Wallace, J. M., and Francis, R. C. (1997). A Pacific Interdecadal Climate Oscillation with Impacts on Salmon Production. *Bull. Am. Meteorol. Soc.* 78, 1069–1079. doi:10.1175/1520-0477(1997)078<1069:APICOW>2.0.CO;2.

Manzini, E., Karpechko, A. Y., Anstey, J., Baldwin, M. P., Black, R. X., Cagnazzo, C., et al. (2014). Northern winter climate change: Assessment of uncertainty in CMIP5 projections related to stratosphere-troposphere coupling. *J. Geophys. Res. Atmos.* 119, 7979–7998. doi:10.1002/2013JD021403.

Marini, C., Polkova, I., Köhl, A., and Stammer, D. (2016). A Comparison of Two Ensemble Generation Methods Using Oceanic Singular Vectors and Atmospheric Lagged Initialization for Decadal Climate Prediction. *Mon. Weather Rev.* 144, 2719–2738. doi:10.1175/MWR-D-15-0350.1.

Marotzke, J. (2019). Quantifying the irreducible uncertainty in near-term climate projections. *Wiley Interdiscip. Rev. Clim. Chang.* 10, e563. doi:doi:10.1002/wcc.563.

Marotzke, J., and Forster, P. M. (2015). Forcing, feedback and internal variability in global temperature trends. *Nature* 517, 565–570. doi:10.1038/nature14117.

Marotzke, J., Müller, W. A., Vamborg, F. S. E., Becker, P., Cubasch, U., Feldmann, H., et al. (2016). MiKlip: A national research project on decadal climate prediction. *Bull. Am. Meteorol. Soc.* 97, 2379–2394. doi:10.1175/BAMS-D-15-00184.1.

Marshall, G. J. (2003). Trends in the Southern Annular Mode from Observations and Reanalyses. *J. Clim.* 16, 4134–4143. doi:10.1175/1520-0442(2003)016<4134:TITSAM>2.0.CO;2.

Marshall, J., Armour, K. C., Scott, J. R., Kostov, Y., Hausmann, U., Ferreira, D., et al. (2014). The ocean's role in polar climate change: asymmetric Arctic and Antarctic responses to greenhouse gas and ozone forcing. *Philos. Trans. R. Soc. A Math. Phys. Eng. Sci.* 372, 20130040–20130040. doi:10.1098/rsta.2013.0040.

Marshall, J., Scott, J. R., Armour, K. C., Campin, J.-M., Kelley, M., and Romanou, A. (2015). The ocean's role in the transient response of climate to abrupt greenhouse gas forcing. *Clim. Dyn.* 44, 2287–2299. doi:10.1007/s00382-014-2308-0.

Martín-Rey, M., Polo, I., Rodríguez-Fonseca, B., Losada, T., and Lazar, A. (2017). Is There Evidence of Changes in Tropical Atlantic Variability Modes under AMO Phases in the Observational Record? *J. Clim.* 41, 3071–3089. doi:10.1007/s00382-015-2471-y.

Martín-Rey, M., Rodríguez-Fonseca, B., Polo, I., and Kucharski, F. (2014). On the Atlantic–Pacific Niños connection: a multidecadal modulated mode. *Clim. Dyn.* 43, 3163–3178. doi:10.1007/s00382-014-2305-3.

Martin, E. R., and Thorncroft, C. (2014a). Sahel rainfall in multimodel CMIP5 decadal hindcasts. *Geophys. Res. Lett.* 41, 2169–2175. doi:10.1002/2014GL059338.
Martin, E. R., and Thorncroft, C. D. (2014b). The impact of the AMO on the West African monsoon annual cycle. *Q. J. R. Meteorol. Soc.* 140, 31–46. doi:10.1002/qj.2107.
Masato, G., Hoskins, B. J., and Woollings, T. (2013). Winter and Summer Northern Hemisphere Blocking in CMIP5 Models. *J. Clim.* 26, 7044–7059. doi:10.1175/JCLI-D-12-00466.1.
Masson-Delmotte, V. M., Schulz, A. A.-O., Beer, J., Ganopolski, A., González-Rouco, J. F., Jansen, E., et al. (2013). "Information from Paleoclimate Archives," in *Climate Change 2013 - The Physical Science Basis*, eds. T. F. Stocker, D. Qin, G.-K. Plattner, M. Tignor, S. K. Allen, J. Boschung, et al. (Cambridge: Cambridge University Press), 383–464. doi:10.1017/CBO9781107415324.013.
Masson-Delmotte, V., Zhai, P., Pörtner, H.-O., Roberts, D., Skea, J., Shukla, P. R., et al. (2018). Global warming of 1.5°C An IPCC Special Report. *Rep. Intergov. Panel Clim. Chang.* 265, 37–46. Available at: https://report.ipcc.ch/sr15/pdf/sr15_spm_final.pdf.
Massonnet, F., Bellprat, O., Guemas, V., and Doblas-Reyes, F. J. (2016). Using climate models to estimate the quality of global observational data sets. *Science (80-.).* 354, 452–455. doi:10.1126/science.aaf6369.
Matsueda, M., and Endo, H. (2017). The robustness of future changes in Northern Hemisphere blocking: A large ensemble projection with multiple sea surface temperature patterns. *Geophys. Res. Lett.* 44, 5158–5166. doi:10.1002/2017GL073336.
Matthews, H. D. (2010). Can carbon cycle geoengineering be a useful complement to ambitious climate mitigation ? *Management* 1, 135–144.
Matthews, H. D. (2011). Radiative forcing and climate response to zeroed emissions of greenhouse gases and aerosols. *Geophys. Res. Abstr.* 13, 3898–3898.
Matthews, H. D., and Caldeira, K. (2007). Transient climate carbon simulations of planetary geoengineering. *Proc. Natl. Acad. Sci.* 104, 9949–9954. doi:10.1073/pnas.0700419104.
Matthews, H. D., and Caldeira, K. (2008). Stabilizing climate requires near-zero emissions. *Geophys. Res. Lett.* 35, L04705. doi:10.1029/2007GL032388.
Matthews, H. D., Gillett, N. P., Stott, P. A., and Zickfeld, K. (2009). The proportionality of global warming to cumulative carbon emissions. *Nature* 459, 829–832. doi:10.1038/nature08047.
Matthews, H. D., Zickfeld, K., Knutti, R., and Allen, M. R. (2018). Focus on cumulative emissions, global carbon budgets and the implications for climate mitigation targets. *Environ. Res. Lett.* 13, 010201. doi:10.1088/1748-9326/aa98c9.
May, W. (2012). Assessing the strength of regional changes in near-surface climate associated with a global warming of 2°C. *Clim. Change* 110, 619–644. doi:10.1007/s10584-011-0076-y.
Maycock, A. C., Joshi, M. M., Shine, K. P., and Scaife, A. A. (2013). The Circulation Response to Idealized Changes in Stratospheric Water Vapor. *J. Clim.* 26, 545–561. doi:10.1175/JCLI-D-12-00155.1.
Mbengue, C., and Schneider, T. (2017). Storm-Track Shifts under Climate Change: Toward a Mechanistic Understanding Using Baroclinic Mean Available Potential Energy. *J. Atmos. Sci.* 74, 93–110. doi:10.1175/JAS-D-15-0267.1.
McCusker, K. E., Armour, K. C., Bitz, C. M., and Battisti, D. S. (2014). Rapid and extensive warming following cessation of solar radiation management. *Environ. Res. Lett.* 9, 024005. doi:10.1088/1748-9326/9/2/024005.
McCusker, K. E., Fyfe, J. C., and Sigmond, M. (2016). Twenty-five winters of unexpected Eurasian cooling unlikely due to Arctic sea-ice loss. *Nat. Geosci.* 9, 838–842. doi:10.1038/ngeo2820.
McCusker, K. E., Kushner, P. J., Fyfe, J. C., Sigmond, M., Kharin, V. V, and Bitz, C. M. (2017). Remarkable separability of circulation response to Arctic sea ice loss and greenhouse gas forcing. *Geophys. Res. Lett.* 44, 7955–7964. doi:10.1002/2017GL074327.
McKenna, C. M., Bracegirdle, T. J., Shuckburgh, E. F., Haynes, P. H., and Joshi, M. M. (2018). Arctic Sea Ice Loss in Different Regions Leads to Contrasting Northern Hemisphere Impacts. *Geophys. Res. Lett.* 45, 945–954. doi:10.1002/2017GL076433.
McKinnon, K. A., Poppick, A., Dunn-Sigouin, E., and Deser, C. (2017). An "Observational Large Ensemble" to Compare Observed and Modeled Temperature Trend Uncertainty due to Internal Variability. *J. Clim.* 30, 7585–7598. doi:10.1175/JCLI-D-16-0905.1.
McSweeney, C. F., and Jones, R. G. (2013). No consensus on consensus: the challenge of finding a universal approach to measuring and mapping ensemble consistency in GCM projections. *Clim. Change* 119, 617–629. doi:10.1007/s10584-013-0781-9.
Mearns, L. O., Rosenzweig, C., and Goldberg, R. (1997). Mean and variance change in climate scenarios: Methods, agricultural applications, and measures of uncertainty. *Clim. Change* 35, 367–396. doi:10.1023/A:100535813.
Meehl, G. A., Arblaster, J. M., Fasullo, J. T., Hu, A., and Trenberth, K. E. (2011). Model-based evidence of deep-ocean heat uptake during surface-temperature hiatus periods. *Nat. Clim. Chang.* 1, 360–364. doi:10.1038/nclimate1229.
Meehl, G. A., Goddard, L., Boer, G., Burgman, R., Branstator, G., Cassou, C., et al. (2014). Decadal climate prediction an update from the trenches. *Bull. Am. Meteorol. Soc.* 95, 243–267. doi:10.1175/BAMS-D-12-00241.1.
Meehl, G. A., Hu, A., and Teng, H. (2016). Initialized decadal prediction for transition to positive phase of the

Interdecadal Pacific Oscillation. *Nat. Commun.* 7, 11718. doi:10.1038/ncomms11718.
Meehl, G. A., and Teng, H. (2012). Case studies for initialized decadal hindcasts and predictions for the Pacific region. *Geophys. Res. Lett.* 39, n/a-n/a. doi:10.1029/2012GL053423.
Meehl, G. A., Teng, H., Maher, N., and England, M. H. (2015). Effects of the Mount Pinatubo eruption on decadal climate prediction skill of Pacific sea surface temperatures. *Geophys. Res. Lett.* 42, 10,840-10,846. doi:10.1002/2015GL066608.
Meinshausen, M., Meinshausen, N., Hare, W., Raper, S. C. B., Frieler, K., Knutti, R., et al. (2009). Greenhouse-gas emission targets for limiting global warming to 2°C. *Nature* 458, 1158–1162. doi:10.1038/nature08017.
Meinshausen, M., Smith, S. J., Calvin, K., Daniel, J. S., Kainuma, M. L. T., Lamarque, J.-F., et al. (2011). The RCP greenhouse gas concentrations and their extensions from 1765 to 2300. *Clim. Change* 109, 213–241. doi:10.1007/s10584-011-0156-z.
Menary, M. B., and Hermanson, L. (2018). Limits on determining the skill of North Atlantic Ocean decadal predictions. *Nat. Commun.* 9, 1694. doi:10.1038/s41467-018-04043-9.
Menary, M. B., Hodson, D. L. R., Robson, J. I., Sutton, R. T., Wood, R. A., and Hunt, J. A. (2015). Exploring the impact of CMIP5 model biases on the simulation of North Atlantic decadal variability. *Geophys. Res. Lett.* 42, 5926–5934. doi:10.1002/2015GL064360.
Mengel, M., Levermann, A., Frieler, K., Robinson, A., Marzeion, B., and Winkelmann, R. (2016). Future sea level rise constrained by observations and long-term commitment. *Proc. Natl. Acad. Sci.* 113, 2597–2602. doi:10.1073/pnas.1500515113.
Michaelis, A. C., Willison, J., Lackmann, G. M., and Robinson, W. A. (2017). Changes in Winter North Atlantic Extratropical Cyclones in High-Resolution Regional Pseudo–Global Warming Simulations. *J. Clim.* 30, 6905–6925. doi:10.1175/JCLI-D-16-0697.1.
Mignot, J., García-Serrano, J., Swingedouw, D., Germe, A., Nguyen, S., Ortega, P., et al. (2016). Decadal prediction skill in the ocean with surface nudging in the IPSL-CM5A-LR climate model. *Clim. Dyn.* 47, 1225–1246. doi:10.1007/s00382-015-2898-1.
Millar, R. J., and Friedlingstein, P. (2018). The utility of the historical record for assessing the transient climate response to cumulative emissions. *Philos. Trans. R. Soc. A Math. Phys. Eng. Sci.* 376, 20160449. doi:10.1098/rsta.2016.0449.
Millar, R. J., Fuglestvedt, J. S., Friedlingstein, P., Rogelj, J., Grubb, M. J., Matthews, H. D., et al. (2017). Emission budgets and pathways consistent with limiting warming to 1.5 degrees C. *Nat. Geosci.* 10, 741–748. doi:10.1038/ngeo3031.
Millar, R. J., Fuglestvedt, J. S., Friedlingstein, P., Rogelj, J., Grubb, M. J., Matthews, H. D., et al. (2018a). Author Correction: Emission budgets and pathways consistent with limiting warming to 1.5°C (Nature Geoscience (2017) DOI: 10.1038/ngeo3031). *Nat. Geosci.* 11, 454–455. doi:10.1038/s41561-018-0153-1.
Millar, R. J., Fuglestvedt, J. S., Friedlingstein, P., Rogelj, J., Grubb, M. J., Matthews, H. D., et al. (2018b). Reply to "Interpretations of the Paris climate target." *Nat. Geosci.* 11, 222. doi:10.1038/s41561-018-0087-7.
Mitchell, D., AchutaRao, K., Allen, M., Bethke, I., Beyerle, U., Ciavarella, A., et al. (2017). Half a degree additional warming, prognosis and projected impacts (HAPPI): background and experimental design. *Geosci. Model Dev.* 10, 571–583. doi:10.5194/gmd-10-571-2017.
Mitchell, D. L., and Finnegan, W. (2009). Modification of cirrus clouds to reduce global warming. *Environ. Res. Lett.* 4, 045102. doi:10.1088/1748-9326/4/4/045102.
Mitchell, T. D. (2003). Pattern Scaling: An Examination of the Accuracy of the Technique for Describing Future Climates. *Clim. Change* 60, 217–242. doi:10.1023/A:1026035305597.
Miyama, T., and Kawamiya, M. (2009). Estimating allowable carbon emission for CO 2 concentration stabilization using a GCM-based Earth system model. *Geophys. Res. Lett.* 36, L19709. doi:10.1029/2009GL039678.
Mizuta, R., Arakawa, O., Ose, T., Kusunoki, S., Endo, H., and Kitoh, A. (2014). Classification of CMIP5 Future Climate Responses by the Tropical Sea Surface Temperature Changes. *SOLA* 10, 167–171. doi:10.2151/sola.2014-035.
Mochizuki, T., Chikamoto, Y., Kimoto, M., Ishii, M., Tatebe, H., Komuro, Y., et al. (2012). Decadal Prediction Using a Recent Series of MIROC Global Climate Models. *J. Meteorol. Soc. Japan* 90A, 373–383. doi:10.2151/jmsj.2012-A22.
Mochizuki, T., Ishii, M., Kimoto, M., Chikamoto, Y., Watanabe, M., Nozawa, T., et al. (2010). Pacific decadal oscillation hindcasts relevant to near-term climate prediction. *Proc. Natl. Acad. Sci.* 107, 1833–1837. doi:10.1073/pnas.0906531107.
Modak, A., Bala, G., Cao, L., and Caldeira, K. (2016). Why must a solar forcing be larger than a CO2 forcing to cause the same global mean surface temperature change? *Environ. Res. Lett.* 11, 044013. doi:10.1088/1748-9326/11/4/044013.
Mohino, E., Keenlyside, N., and Pohlmann, H. (2016). Decadal prediction of Sahel rainfall: where does the skill (or lack thereof) come from? *Clim. Dyn.* 47, 3593–3612. doi:10.1007/s00382-016-3416-9.
Mohino, E., and Losada, T. (2015). Impacts of the Atlantic Equatorial Mode in a warmer climate. *Clim. Dyn.* 45, 2255–2271. doi:10.1007/s00382-015-2471-y.

Monerie, P.-A., Coquart, L., Maisonnave, É., Moine, M.-P., Terray, L., and Valcke, S. (2017). Decadal prediction skill using a high-resolution climate model. *Clim. Dyn.* 49, 3527–3550. doi:10.1007/s00382-017-3528-x.
Moore, J. C., Rinke, A., Yu, X., Ji, D., Cui, X., Li, Y., et al. (2014). Arctic sea ice and atmospheric circulation under the GeoMIP G1 scenario. *J. Geophys. Res. Atmos.* 119, 567–583. doi:10.1002/2013JD021060.
Mora, C., Frazier, A. G., Longman, R. J., Dacks, R. S., Walton, M. M., Tong, E. J., et al. (2013). The projected timing of climate departure from recent variability. *Nature* 502, 183–187. doi:10.1038/nature12540.
Mori, M., Watanabe, M., Shiogama, H., Inoue, J., and Kimoto, M. (2014). Robust Arctic sea-ice influence on the frequent Eurasian cold winters in past decades. *Nat. Geosci.* 7, 869–873. doi:10.1038/ngeo2277.
Morice, C. P., Kennedy, J. J., Rayner, N. A., and Jones, P. D. (2012). Quantifying uncertainties in global and regional temperature change using an ensemble of observational estimates: The HadCRUT4 data set. *J. Geophys. Res. Atmos.* 117, n/a-n/a. doi:10.1029/2011JD017187.
Msadek, R., Vecchi, G. A., Winton, M., and Gudgel, R. G. (2014). Importance of initial conditions in seasonal predictions of Arctic sea ice extent. *Geophys. Res. Lett.* 41, 5208–5215. doi:10.1002/2014GL060799.
Müller, W. A., Jungclaus, J. H., Mauritsen, T., Baehr, J., Bittner, M., Budich, R., et al. (2018). A Higher-resolution Version of the Max Planck Institute Earth System Model (MPI-ESM1.2-HR). *J. Adv. Model. Earth Syst.* 10, 1383–1413. doi:10.1029/2017MS001217.
Muri, H., Tjiputra, J., Otterå, O. H., Adakudlu, M., Lauvset, S. K., Grini, A., et al. (2018). Climate Response to Aerosol Geoengineering: A Multimethod Comparison. *J. Clim.* 31, 6319–6340. doi:10.1175/JCLI-D-17-0620.1.
Murphy, J. M., Sexton, D. M. H., Barnett, D. N., Jones, G. S., Webb, M. J., Collins, M., et al. (2004). Quantification of modelling uncertainties in a large ensemble of climate change simulations. *Nature* 430, 768–772. Available at: http://dx.doi.org/10.1038/nature02771.
Muthyala, R., Bala, G., and Nalam, A. (2018a). Regional Scale Analysis of Climate Extremes in an SRM Geoengineering Simulation, Part 1:Precipitation Extremes. *Curr. Sci.* 114, 1024–1035. doi:10.18520/cs/v114/i05/1024-1035.
Muthyala, R., Bala, G., and Nalam, A. (2018b). Regional Scale Analysis of Climate Extremes in an SRM Geoengineering Simulation, Part 2:Temperature Extremes. *Curr. Sci.* 114, 1036–1045. doi:10.18520/cs/v114/i05/1036-1045.
Myhre, G., Forster, P. M., Samset, B. H., Hodnebrog, Ø., Sillmann, J., Aalbergsjø, S. G., et al. (2017). PDRMIP: A Precipitation Driver and Response Model Intercomparison Project—Protocol and Preliminary Results. *Bull. Am. Meteorol. Soc.* 98, 1185–1198. doi:10.1175/BAMS-D-16-0019.1.
Myhre, G., Kramer, R. J., Smith, C. J., Hodnebrog, Ø., Forster, P., Soden, B. J., et al. (2018). Quantifying the Importance of Rapid Adjustments for Global Precipitation Changes. *Geophys. Res. Lett.* 45, 11,399-11,405. doi:10.1029/2018GL079474.
Najafi, M. R., Zwiers, F. W., and Gillett, N. P. (2015). Attribution of Arctic temperature change to greenhouse-gas and aerosol influences. *Nat. Clim. Chang.* 5, 246–249. doi:10.1038/nclimate2524.
Nakashiki, N., Kim, D.-H., Bryan, F. O., Yoshida, Y., Tsumune, D., Maruyama, K., et al. (2006). Recovery of thermohaline circulation under CO2 stabilization and overshoot scenarios. *Ocean Model.* 15, 200–217.
National Research Council (2015a). *Climate Intervention: Carbon Dioxide Removal and Reliable Sequestration*. Washington, DC: The National Academies Press doi:10.17226/18805.
National Research Council (2015b). *Climate Intervention: Reflecting Sunlight to Cool Earth*. Washington, DC: The National Academies Press doi:10.17226/18988.
Nauels, A., Meinshausen, M., Mengel, M., Lorbacher, K., and Wigley, T. M. L. (2017). Synthesizing long-Term sea level rise projections-The MAGICC sea level model v2.0. *Geosci. Model Dev.* 10, 2495–2524. doi:10.5194/gmd-10-2495-2017.
Neely, R. R., Marsh, D. R., Smith, K. L., Davis, S. M., and Polvani, L. M. (2014). Biases in southern hemisphere climate trends induced by coarsely specifying the temporal resolution of stratospheric ozone. *Geophys. Res. Lett.* 41, 8602–8610. doi:10.1002/2014GL061627.
Newman, M., Alexander, M. A., Ault, T. R., Cobb, K. M., Deser, C., Di Lorenzo, E., et al. (2016). The Pacific Decadal Oscillation, Revisited. *J. Clim.* 29, 4399–4427. doi:10.1175/JCLI-D-15-0508.1.
Nguyen, H., Lucas, C., Evans, A., Timbal, B., and Hanson, L. (2015). Expansion of the Southern Hemisphere Hadley Cell in Response to Greenhouse Gas Forcing. *J. Clim.* 28, 8067–8077. doi:10.1175/JCLI-D-15-0139.1.
Niederdrenk, A. L., and Notz, D. (2018). Arctic Sea Ice in a 1.5°C Warmer World. *Geophys. Res. Lett.* 45, 1963–1971. doi:10.1002/2017GL076159.
Niemeier, U., and Schmidt, H. (2017). Changing transport processes in the stratosphere by radiative heating of sulfate aerosols. *Atmos. Chem. Phys.* 17, 14871–14886. doi:10.5194/acp-17-14871-2017.
Niemeier, U., and Timmreck, C. (2015). What is the limit of climate engineering by stratospheric injection of SO2? *Atmos. Chem. Phys.* 15, 9129–9141. doi:10.5194/acp-15-9129-2015.
Nisbet, E. G., Manning, M. R., Dlugokencky, E. J., Fisher, R. E., Lowry, D., Michel, S. E., et al. (2019). Very Strong Atmospheric Methane Growth in the 4 Years 2014–2017: Implications for the Paris Agreement. *Global Biogeochem. Cycles*, 2018GB006009. doi:10.1029/2018GB006009.
Nohara, D., Tsutsui, J., Watanabe, S., Tachiiri, K., Hajima, T., Okajima, H., et al. (2015). Examination of a climate

stabilization pathway via zero-emissions using Earth system models. *Environ. Res. Lett.* 10, 095005. doi:10.1088/1748-9326/10/9/095005.

Notz, D. (2015). How well must climate models agree with observations? *Philos. Trans. R. Soc. A Math. Phys. Eng. Sci.* 373, 20140164. doi:10.1098/rsta.2014.0164.

Notz, D., and Marotzke, J. (2012). Observations reveal external driver for Arctic sea-ice retreat. *Geophys. Res. Lett.* 39, n/a-n/a. doi:10.1029/2012GL051094.

Notz, D., and Stroeve, J. (2016). Observed Arctic sea-ice loss directly follows anthropogenic CO2 emission. *Science (80-.).* 354, 747–750. doi:10.1126/science.aag2345.

Notz, D., and Stroeve, J. (2018). The Trajectory Towards a Seasonally Ice-Free Arctic Ocean. *Curr. Clim. Chang. Reports* 4, 407–416. doi:10.1007/s40641-018-0113-2.

Nowack, P. J., Luke Abraham, N., Maycock, A. C., Braesicke, P., Gregory, J. M., Joshi, M. M., et al. (2015). A large ozone-circulation feedback and its implications for global warming assessments. *Nat. Clim. Chang.* 5, 41–45. doi:10.1038/nclimate2451.

Nummelin, A., Li, C., and Hezel, P. J. (2017). Connecting ocean heat transport changes from the midlatitudes to the Arctic Ocean. *Geophys. Res. Lett.* 44, 1899–1908. doi:10.1002/2016GL071333.

O'Gorman, P. A., Allan, R. P., Byrne, M. P., and Previdi, M. (2012). Energetic Constraints on Precipitation Under Climate Change. *Surv. Geophys.* 33, 585–608. doi:10.1007/s10712-011-9159-6.

O'Neill, B. C., Oppenheimer, M., Warren, R., Hallegatte, S., Kopp, R. E., Pörtner, H. O., et al. (2017). IPCC reasons for concern regarding climate change risks. *Nat. Clim. Chang.* 7, 28–37. doi:10.1038/nclimate3179.

O'Neill, B. C., Tebaldi, C., van Vuuren, D. P., Eyring, V., Friedlingstein, P., Hurtt, G., et al. (2016). The Scenario Model Intercomparison Project (ScenarioMIP) for CMIP6. *Geosci. Model Dev.* 9, 3461–3482. doi:10.5194/gmd-9-3461-2016.

O'Reilly, C. H., Huber, M., Woollings, T., and Zanna, L. (2016). The signature of low-frequency oceanic forcing in the Atlantic Multidecadal Oscillation. *Geophys. Res. Lett.* 43, 2810–2818. doi:10.1002/2016GL067925.

Oldenburg, D., Armour, K. C., Thompson, L., and Bitz, C. M. (2018). Distinct Mechanisms of Ocean Heat Transport Into the Arctic Under Internal Variability and Climate Change. *Geophys. Res. Lett.* 45, 7692–7700. doi:10.1029/2018GL078719.

Oleson, K. W., Anderson, G. B., Jones, B., McGinnis, S. A., and Sanderson, B. (2018). Avoided climate impacts of urban and rural heat and cold waves over the U.S. using large climate model ensembles for RCP8.5 and RCP4.5. *Clim. Change* 146, 377–392. doi:10.1007/s10584-015-1504-1.

Olonscheck, D., and Notz, D. (2017). Consistently Estimating Internal Climate Variability from Climate Model Simulations. *J. Clim.* 30, 9555–9573. doi:10.1175/JCLI-D-16-0428.1.

Olson, R., An, S.-I., Fan, Y., Evans, J. P., and Caesar, L. (2018). North Atlantic observations sharpen meridional overturning projections. *Clim. Dyn.* 50, 4171–4188. doi:10.1007/s00382-017-3867-7.

Osborn, T. J., Wallace, C. J., Lowe, J. A., and Bernie, D. (2018). Performance of Pattern-Scaled Climate Projections under High-End Warming. Part I: Surface Air Temperature over Land. *J. Clim.* 31, 5667–5680. doi:10.1175/JCLI-D-17-0780.1.

Oschlies, A., Pahlow, M., Yool, A., and Matear, R. J. (2010). Climate engineering by artificial ocean upwelling: Channelling the sorcerer's apprentice. *Geophys. Res. Lett.* 37, 1–5. doi:10.1029/2009GL041961.

Oudar, T., Sanchez-Gomez, E., Chauvin, F., Cattiaux, J., Terray, L., and Cassou, C. (2017). Respective roles of direct GHG radiative forcing and induced Arctic sea ice loss on the Northern Hemisphere atmospheric circulation. *Clim. Dyn.* 49, 3693–3713. doi:10.1007/s00382-017-3541-0.

Pal, J. S., and Eltahir, E. A. B. (2016). Future temperature in southwest Asia projected to exceed a threshold for human adaptability. *Nat. Clim. Chang.* 6, 197–200. doi:10.1038/nclimate2833.

Palmer, M. D., Harris, G. R., and Gregory, J. M. (2018). Extending CMIP5 projections of global mean temperature change and sea level rise due to thermal expansion using a physically-based emulator. *Environ. Res. Lett.* 13, 84003.

Palter, J. B., Frölicher, T. L., Paynter, D., and John, J. G. (2018). Climate, ocean circulation, and sea level changes under stabilization and overshoot pathways to 1.5 K warming. *Earth Syst. Dyn.* 9, 817–828. doi:10.5194/esd-9-817-2018.

Parker, W. S. (2009). Confirmation and adequacy-for-purpose in climate modelling. *Aristot. Soc. Suppl. Vol.* 83, 233–249. doi:10.1111/j.1467-8349.2009.00180.x.

Parsons, S., Renwick, J. A., and McDonald, A. J. (2016). An Assessment of Future Southern Hemisphere Blocking Using CMIP5 Projections from Four GCMs. *J. Clim.* 29, 7599–7611. doi:10.1175/JCLI-D-15-0754.1.

Peings, Y., Simpkins, G., and Magnusdottir, G. (2016). Multidecadal fluctuations of the North Atlantic Ocean and feedback on the winter climate in CMIP5 control simulations. *J. Geophys. Res. Atmos.* 121, 2571–2592. doi:10.1002/2015JD024107.

Pendergrass, A. G., and Hartmann, D. L. (2014). The Atmospheric Energy Constraint on Global-Mean Precipitation Change. *J. Clim.* 27, 757–768. doi:10.1175/JCLI-D-13-00163.1.

Perlwitz, J., Hoerling, M., and Dole, R. (2015). Arctic Tropospheric Warming: Causes and Linkages to Lower Latitudes. *J. Clim.* 28, 2154–2167. doi:10.1175/JCLI-D-14-00095.1.

Pfahl, S., O'Gorman, P. A., and Singh, M. S. (2015). Extratropical Cyclones in Idealized Simulations of Changed Climates. *J. Clim.* 28, 9373–9392. doi:10.1175/JCLI-D-14-00816.1.
Pitari, G., Aquila, V., Kravitz, B., Robock, A., Watanabe, S., Cionni, I., et al. (2014). Stratospheric ozone response to sulfate geoengineering: Results from the geoengineering model intercomparison project (GeoMip). *J. Geophys. Res.* 119, 2629–2653. doi:10.1002/2013JD020566.
Pithan, F., and Mauritsen, T. (2014). Arctic amplification dominated by temperature feedbacks in contemporary climate models. *Nat. Geosci.* 7, 181–184. doi:10.1038/ngeo2071.
Pohlmann, H., Jungclaus, J. H., Köhl, A., Stammer, D., and Marotzke, J. (2009). Initializing decadal climate predictions with the GECCO oceanic synthesis: Effects on the North Atlantic. *J. Clim.* 22, 3926–3938.
Pohlmann, H., Kröger, J., Greatbatch, R. J., and Müller, W. A. (2017). Initialization shock in decadal hindcasts due to errors in wind stress over the tropical Pacific. *Clim. Dyn.* 49, 2685–2693. doi:10.1007/s00382-016-3486-8.
Pohlmann, H., Müller, W. A., Kulkarni, K., Kameswarrao, M., Matei, D., Vamborg, F. S. E., et al. (2013). Improved forecast skill in the tropics in the new MiKlip decadal climate predictions. *Geophys. Res. Lett.* 40, 5798–5802. doi:10.1002/2013GL058051.
Polkova, I., Köhl, A., and Stammer, D. (2014). Impact of initialization procedures on the predictive skill of a coupled ocean–atmosphere model. *Clim. Dyn.* 42, 3151–3169. doi:10.1007/s00382-013-1969-4.
Polson, D., Bollasina, M., Hegerl, G. C., and Wilcox, L. J. (2014). Decreased monsoon precipitation in the Northern Hemisphere due to anthropogenic aerosols. *Geophys. Res. Lett.* 41, 6023–6029. doi:10.1002/2014GL060811.
Power, S. B., Delage, F., Colman, R., and Moise, A. (2012). Consensus on Twenty-First-Century Rainfall Projections in Climate Models More Widespread than Previously Thought. *J. Clim.* 25, 3792–3809. doi:10.1175/JCLI-D-11-00354.1.
Power, S., Delage, F., Chung, C., Kociuba, G., and Keay, K. (2013). Robust twenty-first-century projections of El Niño and related precipitation variability. *Nature* 502, 541–545. doi:10.1038/nature12580.
Pugh, T. A. M., Jones, C. D., Huntingford, C., Burton, C., Arneth, A., Brovkin, V., et al. (2018). A Large Committed Long-Term Sink of Carbon due to Vegetation Dynamics. *Earth's Futur.* 6, 1413–1432. doi:10.1029/2018EF000935.
Rahmstorf, S., and Ganopolski, A. (1999). Long-term global warming scenarios computed with an efficient coupled climate model. *Clim. Change* 43, 353–367.
Ramanathan, V., Chung, C., Kim, D., Bettge, T., Buja, L., Kiehl, J. T., et al. (2005). Atmospheric brown clouds: Impacts on South Asian climate and hydrological cycle. *Proc. Natl. Acad. Sci.* 102, 5326–5333. doi:10.1073/pnas.0500656102.
Raphael, M. N. (2004). A zonal wave 3 index for the Southern Hemisphere. *Geophys. Res. Lett.* 31, 1–4. doi:10.1029/2004GL020365.
Regayre, L. A., Johnson, J. S., Yoshioka, M., Pringle, K. J., Sexton, D. M. H., Booth, B. B. B., et al. (2018). Aerosol and physical atmosphere model parameters are both important sources of uncertainty in aerosol ERF. *Atmos. Chem. Phys.* 18, 9975–10006. doi:10.5194/acp-18-9975-2018.
Riahi, K., van Vuuren, D. P., Kriegler, E., Edmonds, J., O'Neill, B. C., Fujimori, S., et al. (2017). The Shared Socioeconomic Pathways and their energy, land use, and greenhouse gas emissions implications: An overview. *Glob. Environ. Chang.* 42, 153–168. doi:10.1016/j.gloenvcha.2016.05.009.
Richardson, T. B., Forster, P. M., Andrews, T., Boucher, O., Faluvegi, G., Fläschner, D., et al. (2018). Drivers of Precipitation Change: An Energetic Understanding. *J. Clim.* 31, 9641–9657. doi:10.1175/JCLI-D-17-0240.1.
Richardson, T. B., Forster, P. M., Andrews, T., and Parker, D. J. (2016). Understanding the Rapid Precipitation Response to CO 2 and Aerosol Forcing on a Regional Scale*. *J. Clim.* 29, 583–594. doi:10.1175/JCLI-D-15-0174.1.
Richardson, T., Forster, P. M., Smith, C. J., Maycock, A. C., Wood, T., Andrews, T., et al. (2019). Efficacy of climate forcings in PDRMIP models. *J. Geophys. Res.* submitted.
Richter Jadwiga, H., Simone, T., Anne, G., Ben, K., G., M. D., J., M. M., et al. (2018). Stratospheric Response in the First Geoengineering Simulation Meeting Multiple Surface Climate Objectives. *J. Geophys. Res. Atmos.* 123, 5762–5782. doi:10.1029/2018JD028285.
Ricke, K. L., and Caldeira, K. (2014). Maximum warming occurs about one decade after a carbon dioxide emission. *Environ. Res. Lett.* 9, 124002. doi:10.1088/1748-9326/9/12/124002.
Rickels, W., Reith, F., Keller, D., Oschlies, A., and Quaas, M. F. (2018). Integrated Assessment of Carbon Dioxide Removal. *Earth's Futur.* 6, 565–582. doi:10.1002/2017EF000724.
Ridley, H. E., Asmerom, Y., Baldini, J. U. L., Breitenbach, S. F. M., Aquino, V. V, Prufer, K. M., et al. (2015). Aerosol forcing of the position of the intertropical convergence zone since ad 1550. *Nat. Geosci.* 8, 195–200. doi:10.1038/ngeo2353.
Robock, A. (1983). Ice and snow feedbacks and the latitudinal and seasonal distribution of climate sensitivity. *J. Atmos. Sci.* 40, 986–997.
Robock, A., Bunzl, M., Kravitz, B., and Stenchikov, G. L. (2010). A Test for Geoengineering ? *Science (80-.).* 38, 9–10.
Robson, J. I., Sutton, R. T., and Smith, D. M. (2012). Initialized decadal predictions of the rapid warming of the North

Atlantic Ocean in the mid 1990s. *Geophys. Res. Lett.* 39, n/a-n/a. doi:10.1029/2012GL053370.
Robson, J., Sutton, R., and Smith, D. (2014). Decadal predictions of the cooling and freshening of the North Atlantic in the 1960s and the role of ocean circulation. *Clim. Dyn.* 42, 2353–2365. doi:10.1007/s00382-014-2115-7.
Rodgers, K. B., Lin, J., and Frölicher, T. L. (2015). Emergence of multiple ocean ecosystem drivers in a large ensemble suite with an Earth system model. *Biogeosciences* 12, 3301–3320. doi:10.5194/bg-12-3301-2015.
Rogelj, J., Schaeffer, M., Meinshausen, M., Shindell, D. T., Hare, W., Klimont, Z., et al. (2014). Disentangling the effects of CO2 and short-lived climate forcer mitigation. *Proc. Natl. Acad. Sci.* 111, 16325–16330. doi:10.1073/pnas.1415631111.
Rogelj, J., Shindell, D., Jiang, K., Fifita, S., Forster, P., Ginzburg, V., et al. (2018). "Mitigation Pathways Compatible with 1.5°C in the Context of Sustainable Development," in *Global Warming of 1.5°C. An IPCC Special Report on the impacts of global warming of 1.5°C above pre-industrial levels and related global greenhouse gas emission pathways, in the context of strengthening the global response to the threat of climate change,* eds. V. Masson-Delmotte, P. Zhai, H.-O. Pörtner, D. Roberts, J. Skea, P. R. Shukla, et al. (In Press).
Rotstayn, L. D. (2013). Projected effects of declining anthropogenic aerosols on the southern annular mode. *Environ. Res. Lett.* 8, 044028. doi:10.1088/1748-9326/8/4/044028.
Ruiz-Barradas, A., Nigam, S., and Kavvada, A. (2013). The Atlantic Multidecadal Oscillation in twentieth century climate simulations: uneven progress from CMIP3 to CMIP5. *Clim. Dyn.* 41, 3301–3315. doi:10.1007/s00382-013-1810-0.
Ruprich-Robert, Y., and Cassou, C. (2015). Combined influences of seasonal East Atlantic Pattern and North Atlantic Oscillation to excite Atlantic multidecadal variability in a climate model. *Clim. Dyn.* 44, 229–253. doi:10.1007/s00382-014-2176-7.
Russo, S., Sillmann, J., and Sterl, A. (2017). Humid heat waves at different warming levels. *Sci. Rep.* 7, 7477. doi:10.1038/s41598-017-07536-7.
Russotto, R. D., and Ackerman, T. P. (2018). Changes in clouds and thermodynamics under solar geoengineering and implications for required solar reduction. *Atmos. Chem. Phys.* 18, 11905–11925. doi:10.5194/acp-18-11905-2018.
Saffioti, C., Fischer, E. M., and Knutti, R. (2017). Improved Consistency of Climate Projections over Europe after Accounting for Atmospheric Circulation Variability. *J. Clim.* 30, 7271–7291. doi:10.1175/JCLI-D-16-0695.1.
Samset, B. H., Myhre, G., Forster, P. M., Hodnebrog, Ø., Andrews, T., Boucher, O., et al. (2018a). Weak hydrological sensitivity to temperature change over land, independent of climate forcing. *npj Clim. Atmos. Sci.* 1, 20173. doi:10.1038/s41612-017-0005-5.
Samset, B. H., Myhre, G., Forster, P. M., Hodnebrog, Ø., Andrews, T., Faluvegi, G., et al. (2016). Fast and slow precipitation responses to individual climate forcers: A PDRMIP multimodel study. *Geophys. Res. Lett.* 43, 2782–2791. doi:10.1002/2016GL068064.
Samset, B. H., Sand, M., Smith, C. J., Bauer, S. E., Forster, P. M., Fuglestvedt, J. S., et al. (2018b). Climate Impacts From a Removal of Anthropogenic Aerosol Emissions. *Geophys. Res. Lett.* 45, 1020–1029. doi:10.1002/2017GL076079.
Sanchez, C., Williams, K. D., and Collins, M. (2016). Improved stochastic physics schemes for global weather and climate models. *Q. J. R. Meteorol. Soc.* 142, 147–159. doi:10.1002/qj.2640.
Sanchez, D. J., and Simon, M. C. (2018). Transcriptional control of kidney cancer. *Science (80-.).* 361, 226–227. doi:10.1126/science.aau4385.
Sand, M., Berntsen, T. K., von Salzen, K., Flanner, M. G., Langner, J., and Victor, D. G. (2016). Response of Arctic temperature to changes in emissions of short-lived climate forcers. *Nat. Clim. Chang.* 6, 286–289. doi:10.1038/nclimate2880.
Sanderson, B. M., Knutti, R., and Caldwell, P. (2015). Addressing Interdependency in a Multimodel Ensemble by Interpolation of Model Properties. *J. Clim.* 28, 5150–5170. doi:10.1175/JCLI-D-14-00361.1.
Sanderson, B. M., Oleson, K. W., Strand, W. G., Lehner, F., and O'Neill, B. C. (2018). A new ensemble of GCM simulations to assess avoided impacts in a climate mitigation scenario. *Clim. Change* 146, 303–318. doi:10.1007/s10584-015-1567-z.
Sanderson, B. M., Wehner, M., and Knutti, R. (2017a). Skill and independence weighting for multi-model assessments. *Geosci. Model Dev.* 10, 2379–2395. doi:10.5194/gmd-10-2379-2017.
Sanderson, B. M., Xu, Y., Tebaldi, C., Wehner, M., O'Neill, B., Jahn, A., et al. (2017b). Community climate simulations to assess avoided impacts in 1.5 and 2 °C futures. *Earth Syst. Dyn.* 8, 827–847. doi:10.5194/esd-8-827-2017.
Santer, B. D., Bonfils, C., Painter, J. F., Zelinka, M. D., Mears, C., Solomon, S., et al. (2014). Volcanic contribution to decadal changes in tropospheric temperature. *Nat. Geosci.* 7, 185–189. doi:10.1038/ngeo2098.
Santer, B. D., Fyfe, J. C., Pallotta, G., Flato, G. M., Meehl, G. A., England, M. H., et al. (2017). Causes of differences in model and satellite tropospheric warming rates. *Nat. Geosci.* 10, 478–485. doi:10.1038/ngeo2973.
Santer, B. D., Po-Chedley, S., Zelinka, M. D., Cvijanovic, I., Bonfils, C., Durack, P. J., et al. (2018). Human influence on the seasonal cycle of tropospheric temperature. *Science (80-.).* 361, eaas8806. doi:10.1126/science.aas8806.
Scaife, A. A., and Smith, D. (2018). A signal-to-noise paradox in climate science. *npj Clim. Atmos. Sci.* 1, 28. doi:10.1038/s41612-018-0038-4.

Scaife, A. A., Spangehl, T., Fereday, D. R., Cubasch, U., Langematz, U., Akiyoshi, H., et al. (2012). Climate change projections and stratosphere–troposphere interaction. *Clim. Dyn.* 38, 2089–2097. doi:10.1007/s00382-011-1080-7.

Scheff, J., and Frierson, D. (2012). Twenty-First-Century Multimodel Subtropical Precipitation Declines Are Mostly Midlatitude Shifts. *J. Clim.* 25, 4330–4347. doi:10.1175/JCLI-D-11-00393.1.

Schleussner, C.-F., Pfleiderer, P., and Fischer, E. M. (2017). In the observational record half a degree matters. *Nat. Clim. Chang.* 7, 460–462. doi:10.1038/nclimate3320.

Schmidt, H., Alterskjær, K., Alterskjær, K., Bou Karam, D., Boucher, O., Jones, A., et al. (2012). Solar irradiance reduction to counteract radiative forcing from a quadrupling of CO_2: Climate responses simulated by four earth system models. *Earth Syst. Dyn.* 3, 63–78. doi:10.5194/esd-3-63-2012.

Schneider, S. H. (2001). What is “dangerous” climate change? *Nature* 411, 17–19.

Schneider, T., O’Gorman, P. A., and Levine, X. J. (2010). Water vapor and the dynamics of climate changes. *Rev. Geophys.* 48, RG3001.

Schurer, A. P., Cowtan, K., Hawkins, E., Mann, M. E., Scott, V., and Tett, S. F. B. (2018). Interpretations of the Paris climate target. *Nat. Geosci.* 11, 220–221. doi:10.1038/s41561-018-0086-8.

Schuur, E. A. G., Bockheim, J., Canadell, J. G., Euskirchen, E., Field, C. B., Goryachkin, S. V, et al. (2008). Vulnerability of permafrost carbon to climate change: Implications for the global carbon cycle. *Bioscience* 58, 701–714.

Schuur, E. A. G., McGuire, A. D., Schädel, C., Grosse, G., Harden, J. W., Hayes, D. J., et al. (2015). Climate change and the permafrost carbon feedback. *Nature* 520, 171–179. doi:10.1038/nature14338.

Schwierz, C., Croci-Maspoli, M., and Davies, H. C. (2004). Perspicacious indicators of atmospheric blocking. *Geophys. Res. Lett.* 31, n/a-n/a. doi:10.1029/2003GL019341.

Screen, J. A. (2014). Arctic amplification decreases temperature variance in northern mid- to high-latitudes. *Nat. Clim. Chang.* 4, 577–582. doi:10.1038/nclimate2268.

Screen, J. A. (2018). Arctic sea ice at 1.5 and 2 °C. *Nat. Clim. Chang.* 8, 362–363. doi:10.1038/s41558-018-0137-6.

Screen, J. A., Bracegirdle, T. J., and Simmonds, I. (2018a). Polar Climate Change as Manifest in Atmospheric Circulation. *Curr. Clim. Chang. Reports* 4, 383–395. doi:10.1007/s40641-018-0111-4.

Screen, J. A., Deser, C., Smith, D. M., Zhang, X., Blackport, R., Kushner, P. J., et al. (2018b). Consistency and discrepancy in the atmospheric response to Arctic sea-ice loss across climate models. *Nat. Geosci.* 11, 155–163. doi:10.1038/s41561-018-0059-y.

Screen, J. A., and Williamson, D. (2017). Ice-free Arctic at 1.5 °C? *Nat. Clim. Chang.* 7, 230–231.

Seager, R., Liu, H., Henderson, N., Simpson, I., Kelley, C., Shaw, T., et al. (2014). Causes of increasing aridification of the {M}editerranean region in response to rising greenhouse gases. *J. Clim.* 27, 4655–4676.

Seiffert, R., and von Storch, J.-S. (2008). Impact of atmospheric small-scale fluctuations on climate sensitivity. *Geophys. Res. Lett.* 35, L10704. doi:10.1029/2008GL033483.

Seiler, C., and Zwiers, F. W. (2016). How will climate change affect explosive cyclones in the extratropics of the Northern Hemisphere? *Clim. Dyn.* 46, 3633–3644. doi:10.1007/s00382-015-2791-y.

Selten, F. M., Branstator, G. W., Dijkstra, H. A., and Kliphuis, M. (2004). Tropical origins for recent and future Northern Hemisphere climate change. *Geophys. Res. Lett.* 31, L21205. doi:10.1029/2004GL020739.

Seneviratne, S. I., Donat, M. G., Pitman, A. J., Knutti, R., and Wilby, R. L. (2016). Allowable CO_2 emissions based on regional and impact-related climate targets. *Nature* 529, 477–483. doi:10.1038/nature16542.

Seneviratne, S. I., Lüthi, D., Litschi, M., and Schär, C. (2006). Land–atmosphere coupling and climate change in Europe. *Nature* 443, 205–209. doi:10.1038/nature05095.

Seneviratne, S. I., Phipps, S. J., Pitman, A. J., Hirsch, A. L., Davin, E. L., Donat, M. G., et al. (2018a). Land radiative management as contributor to regional-scale climate adaptation and mitigation. *Nat. Geosci.* 11, 88–96. doi:10.1038/s41561-017-0057-5.

Seneviratne, S. I., Wartenburger, R., Guillod, B. P., Hirsch, A. L., Vogel, M. M., Brovkin, V., et al. (2018b). Climate extremes, land–climate feedbacks and land-use forcing at 1.5°C. *Philos. Trans. R. Soc. A Math. Phys. Eng. Sci.* 376, 20160450. doi:10.1098/rsta.2016.0450.

Serreze, M. C., and Barry, R. G. (2011). Processes and impacts of Arctic amplification: A research synthesis. *Glob. Planet. Change* 77, 85–96. doi:10.1016/j.gloplacha.2011.03.004.

Servain, J., Caniaux, G., Kouadio, Y. K., McPhaden, M. J., and Araujo, M. (2014). Recent climatic trends in the tropical Atlantic. *Clim. Dyn.* 43, 3071–3089. doi:10.1007/s00382-014-2168-7.

Shaffrey, L. C., Hodson, D., Robson, J., Stevens, D. P., Hawkins, E., Polo, I., et al. (2017). Decadal predictions with the HiGEM high resolution global coupled climate model: description and basic evaluation. *Clim. Dyn.* 48, 297–311. doi:10.1007/s00382-016-3075-x.

Shaw, T. A., Baldwin, M., Barnes, E. A., Caballero, R., Garfinkel, C. I., Hwang, Y.-T., et al. (2016). Storm track processes and the opposing influences of climate change. *Nat. Geosci.* 9, 656–664. doi:10.1038/ngeo2783.

Shaw, T. A., and Voigt, A. (2015). Tug of war on summertime circulation between radiative forcing and sea surface warming. *Nat. Geosci.* 8, 560–566. doi:10.1038/ngeo2449.

Sheen, K. L., Smith, D. M., Dunstone, N. J., Eade, R., Rowell, D. P., and Vellinga, M. (2017). Skilful prediction of

Sahel summer rainfall on inter-annual and multi-year timescales. *Nat. Commun.* 8, 14966. Available at: http://dx.doi.org/10.1038/ncomms14966.

Shepherd, T. G. (2014). Atmospheric circulation as a source of uncertainty in climate change projections. *Nat. Geosci.* 7, 703–708. doi:10.1038/ngeo2253.

Shepherd, T. G., Boyd, E., Calel, R. A., Chapman, S. C., Dessai, S., Dima-West, I. M., et al. (2018). Storylines: an alternative approach to representing uncertainty in physical aspects of climate change. *Clim. Change* 151, 555–571. doi:10.1007/s10584-018-2317-9.

Sherwood, S. C., Bony, S., Boucher, O., Bretherton, C., Forster, P. M., Gregory, J. M., et al. (2015). Adjustments in the Forcing-Feedback Framework for Understanding Climate Change. *Bull. Am. Meteorol. Soc.* 96, 217–228. doi:10.1175/BAMS-D-13-00167.1.

Shindell, D., Borgford-Parnell, N., Brauer, M., Haines, A., Kuylenstierna, J. C. I., Leonard, S. A., et al. (2017). A climate policy pathway for near- and long-term benefits. *Science (80-.).* 356, 493–494. doi:10.1126/science.aak9521.

Shu, Q., Song, Z., and Qiao, F. (2015). Assessment of sea ice simulations in the CMIP5 models. *Cryosph.* 9, 399–409. doi:10.5194/tc-9-399-2015.

Sigmond, M., and Fyfe, J. C. (2016). Tropical Pacific impacts on cooling North American winters. *Nat. Clim. Chang.* 6, 970–974. doi:10.1038/nclimate3069.

Sigmond, M., Fyfe, J. C., and Swart, N. C. (2018). Ice-free Arctic projections under the Paris Agreement. *Nat. Clim. Chang.* 8, 404–408. doi:10.1038/s41558-018-0124-y.

Sime, L. C., Hopcroft, P. O., and Rhodes, R. H. (2019). Impact of abrupt sea ice loss on Greenland water isotopes during the last glacial period. *Proc. Natl. Acad. Sci. U. S. A.* 116, 4099–4104. doi:10.1073/pnas.1807261116.

Simpson, I. R., Hitchcock, P., Seager, R., Wu, Y., and Callaghan, P. (2018). The Downward Influence of Uncertainty in the Northern Hemisphere Stratospheric Polar Vortex Response to Climate Change. *J. Clim.* 31, 6371–6391. doi:10.1175/JCLI-D-18-0041.1.

Simpson, I. R., Shaw, T. A., and Seager, R. (2014). A Diagnosis of the Seasonally and Longitudinally Varying Midlatitude Circulation Response to Global Warming*. *J. Atmos. Sci.* 71, 2489–2515. doi:10.1175/JAS-D-13-0325.1.

Singh, H. A., Rasch, P. J., and Rose, B. E. J. (2017). Increased Ocean Heat Convergence Into the High Latitudes With CO 2 Doubling Enhances Polar-Amplified Warming. *Geophys. Res. Lett.* 44, 10,583-10,591. doi:10.1002/2017GL074561.

Smith, D. M., Eade, R., and Pohlmann, H. (2013a). A comparison of full-field and anomaly initialization for seasonal to decadal climate prediction. *Clim. Dyn.* 41, 3325–3338. doi:10.1007/s00382-013-1683-2.

Smith, D. M., Scaife, A. A., Boer, G. J., Caian, M., Doblas-Reyes, F. J., Guemas, V., et al. (2013b). Real-time multi-model decadal climate predictions. *Clim. Dyn.* 41, 2875–2888. doi:10.1007/s00382-012-1600-0.

Smith, D. M., Scaife, A. A., Hawkins, E., Bilbao, R., Boer, G. J., Caian, M., et al. (2018). Predicted Chance That Global Warming Will Temporarily Exceed 1.5 °C. *Geophys. Res. Lett.* 45, 11,895-11,903. doi:10.1029/2018GL079362.

Smith, S. J., and Mizrahi, A. (2013). Near-term climate mitigation by short-lived forcers. *Proc. Natl. Acad. Sci.* 110, 14202–14206. doi:10.1073/pnas.1308470110.

Solomon, A., and Polvani, L. M. (2016). Highly Significant Responses to Anthropogenic Forcings of the Midlatitude Jet in the Southern Hemisphere. *J. Clim.* 29, 3463–3470. doi:10.1175/JCLI-D-16-0034.1.

Solomon, S., Plattner, G.-K., Knutti, R., and Friedlingstein, P. (2009). Irreversible climate change due to carbon dioxide emissions. *Proc. Natl. Acad. Sci.* 106, 1704–1709. doi:10.1073/pnas.0812721106.

Steffen, W., Broadgate, W., Deutsch, L., Gaffney, O., and Ludwig, C. (2015). The trajectory of the Anthropocene: The Great Acceleration. *Anthr. Rev.* 2, 81–98. doi:10.1177/2053019614564785.

Steffen, W., Rockström, J., Richardson, K., Lenton, T. M., Folke, C., Liverman, D., et al. (2018). Trajectories of the Earth System in the Anthropocene. *Proc. Natl. Acad. Sci.* 115, 8252–8259. doi:10.1073/pnas.1810141115.

Steinacher, M., and Joos, F. (2016). Transient Earth system responses to cumulative carbon dioxide emissions: Linearities, uncertainties, and probabilities in an observation-constrained model ensemble. *Biogeosciences* 13, 1071–1103. doi:10.5194/bg-13-1071-2016.

Steinman, B. A., Mann, M. E., and Miller, S. K. (2015). Atlantic and Pacific multidecadal oscillations and Northern Hemisphere temperatures. *Science (80-.).* 347, 988–991. doi:10.1126/science.1257856.

Steptoe, H., Wilcox, L. J., and Highwood, E. J. (2016). Is there a robust effect of anthropogenic aerosols on the Southern Annular Mode? *J. Geophys. Res. Atmos.* 121, 10,029-10,042. doi:10.1002/2015JD024218.

Stjern, C. W., Muri, H., Ahlm, L., Boucher, O., Cole, J. N. S., Ji, D., et al. (2018). Response to marine cloud brightening in a multi-model ensemble. *Atmos. Chem. Phys.* 18, 621–634. doi:10.5194/acp-18-621-2018.

Stocker, T. F., Qin, D., Plattner, G.-K. G.-K. G.-K., Alexander, L. V., Allen, S. K., Bindoff, N. L., et al. (2013). "TS: Technical Summary," in *Climate Change 2013: The Physical Science Basis. Contribution of Working Group I to the Fifth Assessment Report of the Intergovernmental Panel on Climate Change*, eds. T. F. Stocker, D. Qin, G.-K. Plattner, M. Tignor, S. K. Allen, J. Boschung, et al. (Cambridge, United Kingdom and New York, NY, USA), 33–115. doi:10.1017/CBO9781107415324.

Stohl, A., Aamaas, B., Amann, M., Baker, L. H., Bellouin, N., Berntsen, T. K., et al. (2015). Evaluating the climate and air quality impacts of short-lived pollutants. *Atmos. Chem. Phys.* 15, 10529–10566. doi:10.5194/acp-15-10529-2015.
Stolpe, M. B., Medhaug, I., Sedláček, J., and Knutti, R. (2018). Multidecadal Variability in Global Surface Temperatures Related to the Atlantic Meridional Overturning Circulation. *J. Clim.* 31, 2889–2906. doi:10.1175/jcli-d-17-0444.1.
Storelvmo, T., Boos, W. R., and Herger, N. (2014). Cirrus cloud seeding: a climate engineering mechanism with reduced side effects? *Philos. Trans. R. Soc. A Math. Phys. Eng. Sci.* 372, 20140116. doi:10.1098/rsta.2014.0116.
Stott, P. A., and Jones, G. S. (2012). Observed 21st century temperatures further constrain likely rates of future warming. *Atmos. Sci. Lett.* 13, 151–156. doi:10.1002/asl.383.
Stott, P., Good, P., Jones, G., Gillett, N., and Hawkins, E. (2013). The upper end of climate model temperature projections is inconsistent with past warming. *Environ. Res. Lett.* 8, 014024. doi:10.1088/1748-9326/8/1/014024.
Stroeve, J., Barrett, A., Serreze, M., and Schweiger, A. (2014). Using records from submarine, aircraft and satellites to evaluate climate model simulations of Arctic sea ice thickness. *Cryosph.* 8, 1839–1854. doi:10.5194/tc-8-1839-2014.
Stroeve, J., and Notz, D. (2015). Insights on past and future sea-ice evolution from combining observations and models. *Glob. Planet. Change* 135, 119–132. doi:10.1016/J.GLOPLACHA.2015.10.011.
Strømmen, K., Christensen, H. M., Berner, J., and Palmer, T. N. (2018). The impact of stochastic parametrisations on the representation of the Asian summer monsoon. *Clim. Dyn.* 50, 2269–2282. doi:10.1007/s00382-017-3749-z.
Strømmen, K., Watson, P. A. G., and Palmer, T. N. (2019). The impact of stochastic physics on climate sensitivity in EC-Earth. *J. Geophys. Res. Atmos.*, submitted.
Stuecker, M. F., Bitz, C. M., Armour, K. C., Proistosescu, C., Kang, S. M., Xie, S.-P., et al. (2018). Polar amplification dominated by local forcing and feedbacks. *Nat. Clim. Chang.* 8, 1076–1081. doi:10.1038/s41558-018-0339-y.
Stuecker, M. F., Timmermann, A., Jin, F.-F., Chikamoto, Y., Zhang, W., Wittenberg, A. T., et al. (2017). Revisiting ENSO/Indian Ocean Dipole phase relationships. *Geophys. Res. Lett.* 44, 2481–2492. doi:10.1002/2016GL072308.
Suarez-Gutierrez, L., Li, C., Müller, W. A., and Marotzke, J. (2018). Internal variability in European summer temperatures at 1.5 °C and 2 °C of global warming. *Environ. Res. Lett.* 13, 064026. doi:10.1088/1748-9326/aaba58.
Suárez-Gutiérrez, L., Li, C., Thorne, P. W., and Marotzke, J. (2017). Internal variability in simulated and observed tropical tropospheric temperature trends. *Geophys. Res. Lett.* 44, 5709–5719. doi:10.1002/2017GL073798.
Sugiyama, M., Arino, Y., Kosugi, T., Kurosawa, A., and Watanabe, S. (2018). Next steps in geoengineering scenario research: limited deployment scenarios and beyond. *Clim. Policy* 18, 681–689. doi:10.1080/14693062.2017.1323721.
Sun, L., Deser, C., and Tomas, R. A. (2015). Mechanisms of Stratospheric and Tropospheric Circulation Response to Projected Arctic Sea Ice Loss. *J. Clim.* 28, 7824–7845. doi:10.1175/JCLI-D-15-0169.1.
Sutton, R. T. (2018). ESD Ideas: a simple proposal to improve the contribution of IPCC WGI to the assessment and communication of climate change risks. *Earth Syst. Dyn.* 9, 1155–1158. doi:10.5194/esd-9-1155-2018.
Sutton, R. T., Dong, B., and Gregory, J. M. (2007). Land/sea warming ratio in response to climate change: IPCC AR4 model results and comparison with observations. *Geophys. Res. Lett.* 34, L02701. doi:10.1029/2006GL028164.
Svendsen, L., Hetzinger, S., Keenlyside, N., and Gao, Y. (2014). Marine-based multiproxy reconstruction of Atlantic multidecadal variability. *Geophys. Res. Lett.* 41, 1295–1300. doi:10.1002/2013GL059076.
Swart, N. C., Gille, S. T., Fyfe, J. C., and Gillett, N. P. (2018). Recent Southern Ocean warming and freshening driven by greenhouse gas emissions and ozone depletion. *Nat. Geosci.* 11, 836–841. doi:10.1038/s41561-018-0226-1.
Tachiiri, K., Hajima, T., and Kawamiya, M. (2015). Increase of uncertainty in transient climate response to cumulative carbon emissions after stabilization of atmospheric CO2 concentration. *Environ. Res. Lett.* 10, 125018. doi:10.1088/1748-9326/10/12/125018.
Tamarin-Brodsky, T., and Kaspi, Y. (2017). Enhanced poleward propagation of storms under climate change. *Nat. Geosci.* 10, 908–913. doi:10.1038/s41561-017-0001-8.
Tao, W., Huang, G., Hu, K., Qu, X., Wen, G., and Gong, H. (2015). Interdecadal modulation of ENSO teleconnections to the Indian Ocean Basin Mode and their relationship under global warming in CMIP5 models. *Int. J. Climatol.* 35, 391–407. doi:10.1002/joc.3987.
Taylor, K. E., Stouffer, R. J., and Meehl, G. A. (2012). An Overview of CMIP5 and the Experiment Design. *Bull. Am. Meteorol. Soc.* 93, 485–498. doi:10.1175/BAMS-D-11-00094.1.
Tebaldi, C., and Arblaster, J. M. (2014). Pattern scaling: Its strengths and limitations, and an update on the latest model simulations. *Clim. Change* 122, 459–471. doi:10.1007/s10584-013-1032-9.
Tebaldi, C., Arblaster, J. M., and Knutti, R. (2011). Mapping model agreement on future climate projections. *Geophys. Res. Lett.* 38, n/a-n/a. doi:10.1029/2011GL049863.
Tebaldi, C., and Friedlingstein, P. (2013). Delayed detection of climate mitigation benefits due to climate inertia and variability. *Proc. Natl. Acad. Sci.* 110, 17229–17234. doi:10.1073/pnas.1300005110.
Tebaldi, C., O'Neill, B., and Lamarque, J.-F. (2015). Sensitivity of regional climate to global temperature and forcing.

Environ. Res. Lett. 10, 74001. doi:10.1088/1748-9326/10/7/074001.
Tebaldi, C., and Wehner, M. F. (2018). Benefits of mitigation for future heat extremes under RCP4.5 compared to RCP8.5. *Clim. Change* 146, 349–361. doi:10.1007/s10584-016-1605-5.
Teng, H., Meehl, G. A., Branstator, G., Yeager, S., and Karspeck, A. (2017). Initialization Shock in CCSM4 Decadal Prediction Experiments. *Past Glob. Chang. Mag.* 25, 41–46. doi:10.22498/pages.25.1.41.
Thoma, M., Gerdes, R., Greatbatch, R. J., and Ding, H. (2015a). Partially coupled spin-up of the MPI-ESM: implementation and first results. *Geosci. Model Dev.* 8, 51–68. doi:10.5194/gmd-8-51-2015.
Thoma, M., Greatbatch, R. J., Kadow, C., and Gerdes, R. (2015b). Decadal hindcasts initialized using observed surface wind stress: Evaluation and prediction out to 2024. *Geophys. Res. Lett.* 42, 6454–6461. doi:10.1002/2015GL064833.
Thompson, D. W. J., Barnes, E. A., Deser, C., Foust, W. E., and Phillips, A. S. (2015). Quantifying the Role of Internal Climate Variability in Future Climate Trends. *J. Clim.* 28, 6443–6456. doi:10.1175/JCLI-D-14-00830.1.
Tilmes, S., Fasullo, J., Lamarque, J. F., Marsh, D. R., Mills, M., Alterskjær, K., et al. (2013). The hydrological impact of geoengineering in the Geoengineering Model Intercomparison Project (GeoMIP). *J. Geophys. Res. Atmos.* 118, 11036–11058. doi:10.1002/jgrd.50868.
Tilmes, S., Richter, J. H., Kravitz, B., MacMartin, D. G., Mills, M. J., Simpson, I. R., et al. (2018). CESM1(WACCM) Stratospheric Aerosol Geoengineering Large Ensemble Project. *Bull. Am. Meteorol. Soc.* 99, 2361–2371. doi:10.1175/BAMS-D-17-0267.1.
Tilmes, S., Richter, J. H., Mills, M. J., Kravitz, B., MacMartin, D. G., Vitt, F., et al. (2017). Sensitivity of aerosol distribution and climate response to stratospheric SO_2 injection locations. *J. Geophys. Res. Atmos.* doi:10.1002/2017JD026888.
Tilmes, S., Sanderson, B. M., and O'Neill, B. C. (2016). Climate impacts of geoengineering in a delayed mitigation scenario. *Geophys. Res. Lett.* 43, 8222–8229. doi:10.1002/2016GL070122.
Timmermann, A., An, S.-I., Kug, J.-S., Jin, F.-F., Cai, W., Capotondi, A., et al. (2018). El Niño–Southern Oscillation complexity. *Nature* 559, 535–545. doi:10.1038/s41586-018-0252-6.
Timmreck, C., Pohlmann, H., Illing, S., and Kadow, C. (2016). The impact of stratospheric volcanic aerosol on decadal-scale climate predictions. *Geophys. Res. Lett.* 43, 834–842. doi:10.1002/2015GL067431.
Tokarska, K. B., and Zickfeld, K. (2015). The effectiveness of net negative carbon dioxide emissions in reversing anthropogenic climate change. *Environ. Res. Lett.* 10, 094013. doi:10.1088/1748-9326/10/9/094013.
Tsutsui, J., Yoshida, Y., Kim, D.-H., Kitabata, H., Nishizawa, K., Nakashiki, N., et al. (2007). Long-term climate response to stabilized and overshoot anthropogenic forcings beyond the twenty-first century. *Clim. Dyn.* 28, 199–214.
Tung, K.-K., Chen, X., Zhou, J., and Li, K.-F. (2019). Interdecadal variability in pan-Pacific and global SST, revisited. *Clim. Dyn.* 52, 2145–2157. doi:10.1007/s00382-018-4240-1.
UNEP (2011). *Near-term climate protection and clean air benefits: actions for controlling shortlived climate forcers. A UNEP synthesis report*.
Valdes, P. (2011). Built for stability. *Nat. Geosci.* 4, 414–416. doi:10.1038/ngeo1200.
Vallis, G. K., Zurita-Gotor, P., Cairns, C., and Kidston, J. (2015). Response of the large-scale structure of the atmosphere to global warming. *Q. J. R. Meteorol. Soc.* 141, 1479–1501. doi:10.1002/qj.2456.
van Oldenborgh, G. J., Doblas-Reyes, F. J., Wouters, B., and Hazeleger, W. (2012). Decadal prediction skill in a multi-model ensemble. *Clim. Dyn.* 38, 1263–1280. doi:10.1007/s00382-012-1313-4.
van Vuuren, D. P., Edmonds, J., Kainuma, M., Riahi, K., Thomson, A., Hibbard, K., et al. (2011). The representative concentration pathways: an overview. *Clim. Change* 109, 5–31. doi:10.1007/s10584-011-0148-z.
Vautard, R., Gobiet, A., Sobolowski, S., Kjellström, E., Stegehuis, A., Watkiss, P., et al. (2014). The European climate under a 2 °C global warming. *Environ. Res. Lett.* 9, 034006. doi:10.1088/1748-9326/9/3/034006.
Vecchi, G. A., Delworth, T., Gudgel, R., Kapnick, S., Rosati, A., Wittenberg, A. T., et al. (2014). On the Seasonal Forecasting of Regional Tropical Cyclone Activity. *J. Clim.* 27, 7994–8016. doi:10.1175/JCLI-D-14-00158.1.
Vecchi, G. A., and Soden, B. J. (2007). Global warming and the weakening of the tropical circulation. *J. Clim.* 20, 4316–4340. doi:10.1175/JCLI4258.1.
Vial, J., Dufresne, J.-L., and Bony, S. (2013). On the interpretation of inter-model spread in CMIP5 climate sensitivity estimates. *Clim. Dyn.* 41, 3339–3362.
Vicente-Serrano, S. M., Nieto, R., Gimeno, L., Azorin-Molina, C., Drumond, A., El Kenawy, A., et al. (2018). Recent changes of relative humidity: regional connections with land and ocean processes. *Earth Syst. Dyn.* 9, 915–937. doi:10.5194/esd-9-915-2018.
Vogel, M. M., Orth, R., Cheruy, F., Hagemann, S., Lorenz, R., van den Hurk, B. J. J. M., et al. (2017). Regional amplification of projected changes in extreme temperatures strongly controlled by soil moisture-temperature feedbacks. *Geophys. Res. Lett.* 44, 1511–1519. doi:10.1002/2016GL071235.
Voigt, A., Pincus, R., Stevens, B., Bony, S., Boucher, O., Bellouin, N., et al. (2017). Fast and slow shifts of the zonal-mean intertropical convergence zone in response to an idealized anthropogenic aerosol. *J. Adv. Model. Earth Syst.* 9, 870–892. doi:10.1002/2016MS000902.
Voigt, A., and Shaw, T. A. (2016). Impact of regional atmospheric cloud radiative changes on shifts of the extratropical

jet stream in response to global warming. *J. Clim.* 29, 8399–8421. doi:10.1175/JCLI-D-16-0140.1.

Walters, D., Baran, A., Boutle, I., Brooks, M., Earnshaw, P., Edwards, J., et al. (2017). The Met Office Unified Model Global Atmosphere 7.0/7.1 and JULES Global Land 7.0 configurations. *Geosci. Model Dev. Discuss.*, 1–78. doi:10.5194/gmd-2017-291.

Wang, B., and Ding, Q. (2008). Global monsoon: Dominant mode of annual variation in the tropics. *Dyn. Atmos. Ocean.* 44, 165–183. doi:10.1016/j.dynatmoce.2007.05.002.

Wang, B., Li, J., Cane, M. A., Liu, J., Webster, P. J., Xiang, B., et al. (2018a). Toward Predicting Changes in the Land Monsoon Rainfall a Decade in Advance. *J. Clim.* 31, 2699–2714. doi:10.1175/JCLI-D-17-0521.1.

Wang, B., Liu, J., Kim, H.-J., Webster, P. J., Yim, S.-Y., and Xiang, B. (2013). Northern Hemisphere summer monsoon intensified by mega-El Niño/southern oscillation and Atlantic multidecadal oscillation. *Proc. Natl. Acad. Sci.* 110, 5347 LP-5352. Available at: http://www.pnas.org/content/110/14/5347.abstract.

Wang, G., Cai, W., Gan, B., Wu, L., Santoso, A., Lin, X., et al. (2017a). Continued increase of extreme El Niño frequency long after 1.5 °C warming stabilization. *Nat. Clim. Chang.* 7, 568–572. doi:10.1038/nclimate3351.

Wang, G., Cai, W., and Purich, A. (2014). Trends in Southern Hemisphere wind-driven circulation in CMIP5 models over the 21st century: Ozone recovery versus greenhouse forcing. *J. Geophys. Res. Ocean.* 119, 2974–2986. doi:10.1002/2013JC009589.

Wang, J., Kim, H.-M., and Chang, E. K. M. (2017b). Changes in Northern Hemisphere Winter Storm Tracks under the Background of Arctic Amplification. *J. Clim.* 30, 3705–3724. doi:10.1175/JCLI-D-16-0650.1.

Wang, P. X., Wang, B., Cheng, H., Fasullo, J., Guo, Z., Kiefer, T., et al. (2017c). The global monsoon across time scales: Mechanisms and outstanding issues. *Earth-Science Rev.* 174, 84–121. doi:10.1016/j.earscirev.2017.07.006.

Wang, X., Li, J., Sun, C., and Liu, T. (2017d). NAO and its relationship with the Northern Hemisphere mean surface temperature in CMIP5 simulations. *J. Geophys. Res. Atmos.* 122, 4202–4227. doi:10.1002/2016JD025979.

Wang, Y., Jiang, J. H., Su, H., Choi, Y.-S., Huang, L., Guo, J., et al. (2018b). Elucidating the Role of Anthropogenic Aerosols in Arctic Sea Ice Variations. *J. Clim.* 31, 99–114. doi:10.1175/JCLI-D-17-0287.1.

Wang, Y., Zhang, G. J., and Craig, G. C. (2016). Stochastic convective parameterization improving the simulation of tropical precipitation variability in the NCAR CAM5. *Geophys. Res. Lett.* 43, 6612–6619. doi:10.1002/2016GL069818.

Watanabe, M., Kug, J.-S., Jin, F.-F., Collins, M., Ohba, M., and Wittenberg, A. T. (2012). Uncertainty in the ENSO amplitude change from the past to the future. *Geophys. Res. Lett.* 39, L20703. doi:10.1029/2012GL053305.

Watanabe, M., Shiogama, H., Tatebe, H., Hayashi, M., Ishii, M., and Kimoto, M. (2014). Contribution of natural decadal variability to global warming acceleration and hiatus. *Nat. Clim. Chang.* 4, 893–897. Available at: https://doi.org/10.1038/nclimate2355.

Watson, P. A. G., Berner, J., Corti, S., Davini, P., von Hardenberg, J., Sanchez, C., et al. (2017). The impact of stochastic physics on tropical rainfall variability in global climate models on daily to weekly time scales. *J. Geophys. Res. Atmos.* 122, 5738–5762. doi:10.1002/2016JD026386.

Webb, M. J., Andrews, T., Bodas-Salcedo, A., Bony, S., Bretherton, C. S., Chadwick, R., et al. (2017). The Cloud Feedback Model Intercomparison Project (CFMIP) contribution to CMIP6. *Geosci. Model Dev.* 10, 359–384. doi:10.5194/gmd-10-359-2017.

Weigel, A. P., Knutti, R., Liniger, M. A., and Appenzeller, C. (2010). Risks of Model Weighting in Multimodel Climate Projections. *J. Clim.* 23, 4175–4191. doi:10.1175/2010JCLI3594.1.

Wen, Q., Yao, J., Döös, K., and Yang, H. (2018). Decoding Hosing and Heating Effects on Global Temperature and Meridional Circulations in a Warming Climate. *J. Clim.* 31, 9605–9623. doi:10.1175/JCLI-D-18-0297.1.

Westra, S., Alexander, L. V, and Zwiers, F. W. (2013). Global Increasing Trends in Annual Maximum Daily Precipitation. *J. Clim.* 26, 3904–3918. doi:10.1175/JCLI-D-12-00502.1.

Williams, R. G., Roussenov, V., Frölicher, T. L., and Goodwin, P. (2017). Drivers of Continued Surface Warming After Cessation of Carbon Emissions. *Geophys. Res. Lett.* 44, 10,610-633,642. doi:10.1002/2017GL075080.

Willison, J., Robinson, W. A., and Lackmann, G. M. (2015). North Atlantic Storm-Track Sensitivity to Warming Increases with Model Resolution. *J. Clim.* 28, 4513–4524. doi:10.1175/JCLI-D-14-00715.1.

Winton, M. (2006). Amplified Arctic climate change: What does surface albedo feedback have to do with it? *Geophys. Res. Lett.* 33, L03701. doi:10.1029/2005GL025244.

Wittenberg, A. T. (2009). Are historical records sufficient to constrain ENSO simulations? *Geophys. Res. Lett.* 36, L12702. doi:10.1029/2009GL038710.

Wobus, C., Flanner, M., Sarofim, M. C., Moura, M. C. P., and Smith, S. J. (2016). Future Arctic temperature change resulting from a range of aerosol emissions scenarios. *Earth's Futur.* 4, 270–281. doi:10.1002/2016EF000361.

Woods, C., and Caballero, R. (2016). The Role of Moist Intrusions in Winter Arctic Warming and Sea Ice Decline. *J. Clim.* 29, 4473–4485. doi:10.1175/JCLI-D-15-0773.1.

Woollings, T., Barriopedro, D., Methven, J., Son, S.-W., Martius, O., Harvey, B., et al. (2018). Blocking and its Response to Climate Change. *Curr. Clim. Chang. Reports* 4, 287–300. doi:10.1007/s40641-018-0108-z.

Wouters, B., Hazeleger, W., Drijfhout, S., Oldenborgh, G. J., and Guemas, V. (2013). Multiyear predictability of the North Atlantic subpolar gyre. *Geophys. Res. Lett.* 40, 3080–3084. doi:10.1002/grl.50585.

Wu, P., Ridley, J., Pardaens, A., Levine, R., and Lowe, J. (2015). The reversibility of CO 2 induced climate change. *Clim. Dyn.* 45, 745–754.
Xie, S.-P., Deser, C., Vecchi, G. A., Collins, M., Delworth, T. L., Hall, A., et al. (2015). Towards predictive understanding of regional climate change. *Nat. Clim. Chang.* 5, 921–930. doi:10.1038/nclimate2689.
Xie, S.-P., Hu, K., Hafner, J., Tokinaga, H., Du, Y., Huang, G., et al. (2009). Indian Ocean Capacitor Effect on Indo–Western Pacific Climate during the Summer following El Niño. *J. Clim.* 22, 730–747. doi:10.1175/2008JCLI2544.1.
Xie, S.-P., Lu, B., and Xiang, B. (2013). Similar spatial patterns of climate responses to aerosol and greenhouse gas changes. *Nat. Geosci.* 6, 828–832.
Xu, Y., and Hu, A. (2017). How Would the Twenty-First-Century Warming Influence Pacific Decadal Variability and Its Connection to North American Rainfall: Assessment Based on a Revised Procedure for the IPO/PDO. *J. Clim.* 31, 1547–1563. doi:10.1175/JCLI-D-17-0319.1.
Yang, C., Christensen, H. M., Corti, S., von Hardenberg, J., and Davini, P. (2019). The impact of stochastic physics on the El Niño Southern Oscillation in the EC-Earth coupled model. *Clim. Dyn.* doi:10.1007/s00382-019-04660-0.
Yeager, S. G., Danabasoglu, G., Rosenbloom, N. A., Strand, W., Bates, S. C., Meehl, G. A., et al. (2018). Predicting Near-Term Changes in the Earth System: A Large Ensemble of Initialized Decadal Prediction Simulations Using the Community Earth System Model. *Bull. Am. Meteorol. Soc.* 99, 1867–1886. doi:10.1175/BAMS-D-17-0098.1.
Yeager, S. G., Karspeck, A. R., and Danabasoglu, G. (2015). Predicted slowdown in the rate of Atlantic sea ice loss. *Geophys. Res. Lett.* 42, 10,704-10,713. doi:10.1002/2015GL065364.
Yeager, S. G., and Robson, J. I. (2017). Recent Progress in Understanding and Predicting Atlantic Decadal Climate Variability. *Curr. Clim. Chang. Reports* 3, 112–127. doi:10.1007/s40641-017-0064-z.
Yettella, V., and Kay, J. E. (2017). How will precipitation change in extratropical cyclones as the planet warms? Insights from a large initial condition climate model ensemble. *Clim. Dyn.* 49, 1765–1781. doi:10.1007/s00382-016-3410-2.
Young, P. J., Davis, S. M., Hassler, B., Solomon, S., and Rosenlof, K. H. (2014). Modeling the climate impact of Southern Hemisphere ozone depletion: The importance of the ozone data set. *Geophys. Res. Lett.* 41, 9033–9039. doi:10.1002/2014GL061738.
Young, P. J., Maycock, A. C., Wild, O., Kinnison, D. E., Rap, A., and Iglesias-Suarez, F. (2018). Key drivers of ozone change and its radiative forcing over the 21st century. *Atmos. Chem. Phys.* 18, 6121–6139. doi:10.5194/acp-18-6121-2018.
Zanchettin, D., Khodri, M., Timmreck, C., Toohey, M., Schmidt, A., Gerber, E. P., et al. (2016). The Model Intercomparison Project on the climatic response to Volcanic forcing (VolMIP): experimental design and forcing input data for CMIP6. *Geosci. Model Dev.* 9, 2701–2719. doi:10.5194/gmd-9-2701-2016.
Zappa, G., Hoskins, B. J., and Shepherd, T. G. (2015). Improving Climate Change Detection through Optimal Seasonal Averaging: The Case of the North Atlantic Jet and European Precipitation. *J. Clim.* 28, 6381–6397. doi:10.1175/JCLI-D-14-00823.1.
Zappa, G., Masato, G., Shaffrey, L., Woollings, T., and Hodges, K. (2014). Linking Northern Hemisphere blocking and storm track biases in the CMIP5 climate models. *Geophys. Res. Lett.* 41, 135–139. doi:10.1002/2013GL058480.
Zappa, G., and Shepherd, T. G. (2017). Storylines of Atmospheric Circulation Change for European Regional Climate Impact Assessment. *J. Clim.* 30, 6561–6577. doi:10.1175/JCLI-D-16-0807.1.
Zhang, H., and Delworth, T. L. (2018). Robustness of anthropogenically forced decadal precipitation changes projected for the 21st century. *Nat. Commun.* 9, 1150. doi:10.1038/s41467-018-03611-3.
Zhang, L., and Delworth, T. L. (2016). Simulated Response of the Pacific Decadal Oscillation to Climate Change. *J. Clim.* 29, 5999–6018. doi:10.1175/JCLI-D-15-0690.1.
Zhang, R., Sutton, R., Danabasoglu, G., Delworth, T. L., Kim, W. M., Robson, J., et al. (2016). Comment on "The Atlantic Multidecadal Oscillation without a role for ocean circulation." *Science (80-.).* 352, 1527–1527. doi:10.1126/science.aaf1660.
Zhang, W., Zhou, T., Zou, L., Zhang, L., and Chen, X. (2018). Reduced exposure to extreme precipitation from 0.5 °C less warming in global land monsoon regions. *Nat. Commun.* 9, 3153. doi:10.1038/s41467-018-05633-3.
Zhang, X., Zwiers, F. W., and Stott, P. A. (2006). Multimodel Multisignal Climate Change Detection at Regional Scale. *J. Clim.* 19, 4294–4307. doi:10.1175/JCLI3851.1.
Zhang, Y., Wallace, J. M., and Battisti, D. S. (1997). ENSO-like Interdecadal Variability: 1900–93. *J. Clim.* 10, 1004–1020. doi:10.1175/1520-0442(1997)010<1004:ELIV>2.0.CO;2.
Zhao, Y., Ducharne, A., Sultan, B., Braconnot, P., and Vautard, R. (2015). Estimating heat stress from climate-based indicators: present-day biases and future spreads in the CMIP5 global climate model ensemble. *Environ. Res. Lett.* 10, 084013. doi:10.1088/1748-9326/10/8/084013.
Zheng, F., Li, J., Clark, R. T., and Nnamchi, H. C. (2013a). Simulation and Projection of the Southern Hemisphere Annular Mode in CMIP5 Models. *J. Clim.* 26, 9860–9879. doi:10.1175/JCLI-D-13-00204.1.
Zheng, X.-T., Hui, C., and Yeh, S.-W. (2018). Response of ENSO amplitude to global warming in CESM large ensemble: uncertainty due to internal variability. *Clim. Dyn.* 50, 4019–4035. doi:10.1007/s00382-017-3859-7.
Zheng, X.-T., Xie, S.-P., Du, Y., Liu, L., Huang, G., and Liu, Q. (2013b). Indian Ocean Dipole Response to Global

Warming in the CMIP5 Multimodel Ensemble. *J. Clim.* 26, 6067–6080. doi:10.1175/JCLI-D-12-00638.1.
Zheng, X.-T., Xie, S.-P., Lv, L.-H., and Zhou, Z.-Q. (2016). Intermodel Uncertainty in ENSO Amplitude Change Tied to Pacific Ocean Warming Pattern. *J. Clim.* 29, 7265–7279. doi:10.1175/JCLI-D-16-0039.1.
Zickfeld, K., Eby, M., Weaver, A. J., Alexander, K., Crespin, E., Edwards, N. R., et al. (2013). Long-Term Climate Change Commitment and Reversibility: An EMIC Intercomparison. *J. Clim.* 26, 5782–5809. doi:10.1175/JCLI-D-12-00584.1.
Zickfeld, K., and Herrington, T. (2015). The time lag between a carbon dioxide emission and maximum warming increases with the size of the emission. *Environ. Res. Lett.* 10, 31001. doi:10.1088/1748-9326/10/3/031001.
Zickfeld, K., MacDougall, A. H., and Matthews, H. D. (2016). On the proportionality between global temperature change and cumulative CO2 emissions during periods of net negative CO2 emissions. *Environ. Res. Lett.* 11, 055006. doi:10.1088/1748-9326/11/5/055006.
Zickfeld, K., Solomon, S., and Gilford, D. M. (2017). Centuries of thermal sea-level rise due to anthropogenic emissions of short-lived greenhouse gases. *Proc. Natl. Acad. Sci.* 114, 657–662. doi:10.1073/pnas.1612066114.
Zuo, M., Man, W., Zhou, T., and Guo, Z. (2018). Different Impacts of Northern, Tropical, and Southern Volcanic Eruptions on the Tropical Pacific SST in the Last Millennium. *J. Clim.* 31, 6729–6744. doi:10.1175/JCLI-D-17-0571.1.

Figures

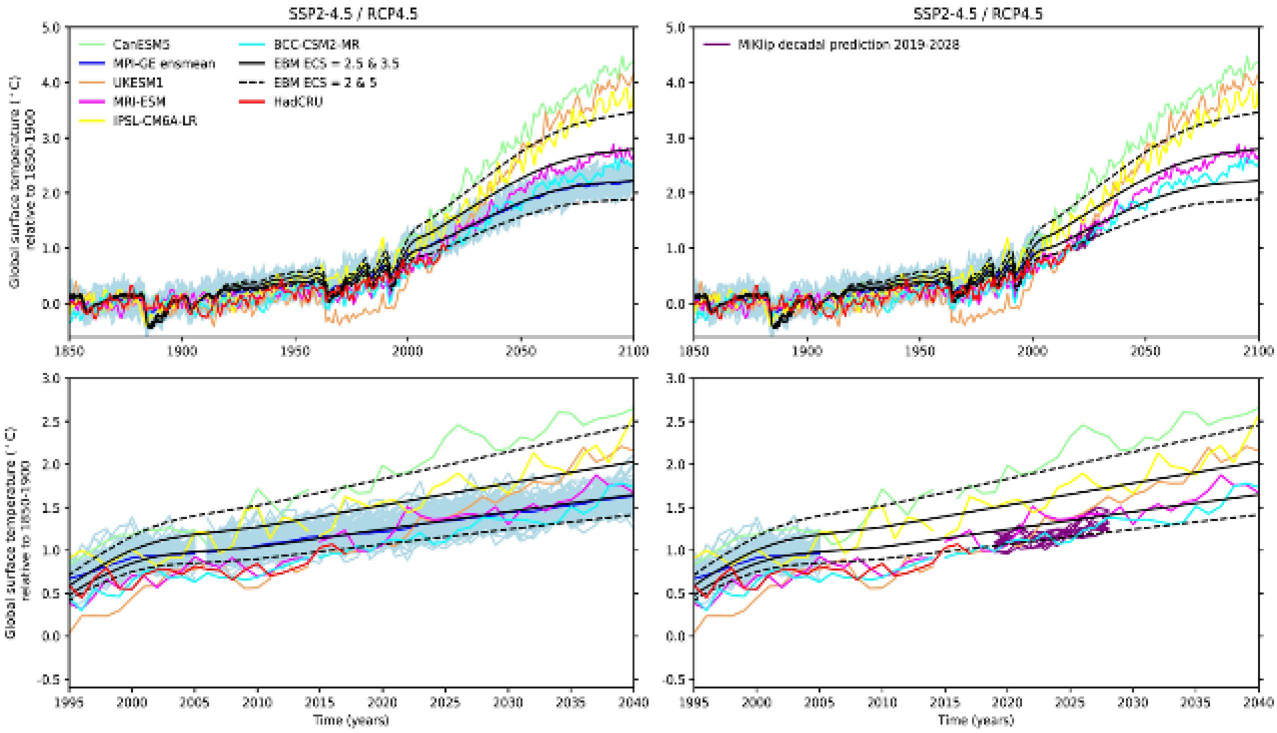

Box 4.1, Figure 1: CMIP6 GSAT simulations and various contributions to uncertainty in the projections ensemble. The top row shows the period 1850–2100, referenced to 1850–1900; the bottom row shows a cut-out for the period 1995–2040, which encompasses the most recent past in CMIP6 (1995–2014) and the near-term future (2021–2040). All panels show for 1850–2100 one CMIP6-forced simulation each with BCC-CSM2-MR (cyan), CanESM5 (light green), IPSL-CM6A-LR (yellow), MRI-ESM2-0 (light purple), and UKESM1 (ochre); and GSAT simulated with an emulator driven by the AR5 radiative forcing, using RCP4.5 from the WGI AR5 Annex II after 2005 (black). The emulator is a two-layer time-dependent energy-balance model (EBM) following (Held et al., 2010), with ocean heat uptake efficiency $\kappa = 0.8$ W m^{-2} $°C^{-1}$ and efficacy 1.0. Results are shown for ECS = 2.5°C and 3.5°C, the lower and upper limits, respectively, of the Chapter 7 ECS *likely* range (solid black), as well as for 2°C and 5°C, the lower and upper limits, respectively, of the Chapter 7 ECS *very likely* range (dashed black). For the historical period, all panels show the observations (HadCRUT4, (Morice et al., 2012), red) and the CMIP5-forced simulations from the 100-member Max Planck Institute Grand Ensemble (MPI-GE, (Maher et al., 2019), dark blue for ensemble mean, light blue for individual realizations), Left: The MPI-GE simulations are extended from 2006–2100 following the RCP4.5 scenario. Right: For the years 2019–2028, the initialized-prediction ensemble from the CMIP6 model MPI-ESM-HR (Müller et al., 2018) is shown (dark purple), produced through the MiKlip project (Marotzke et al., 2016) and contributing to DCPP (Boer et al., 2016). The MiKlip results are drift-removed and referenced to the time-averaged hindcasts for 1995–2014 lead-year by lead-year; then the HadCRUT4 difference between the means over 1995–2014 and 1850–1900 is added. [Placeholder figure, to be updated with the full CMIP6 ensemble and CMIP6/AR6/SSP forcing for the EBM.]

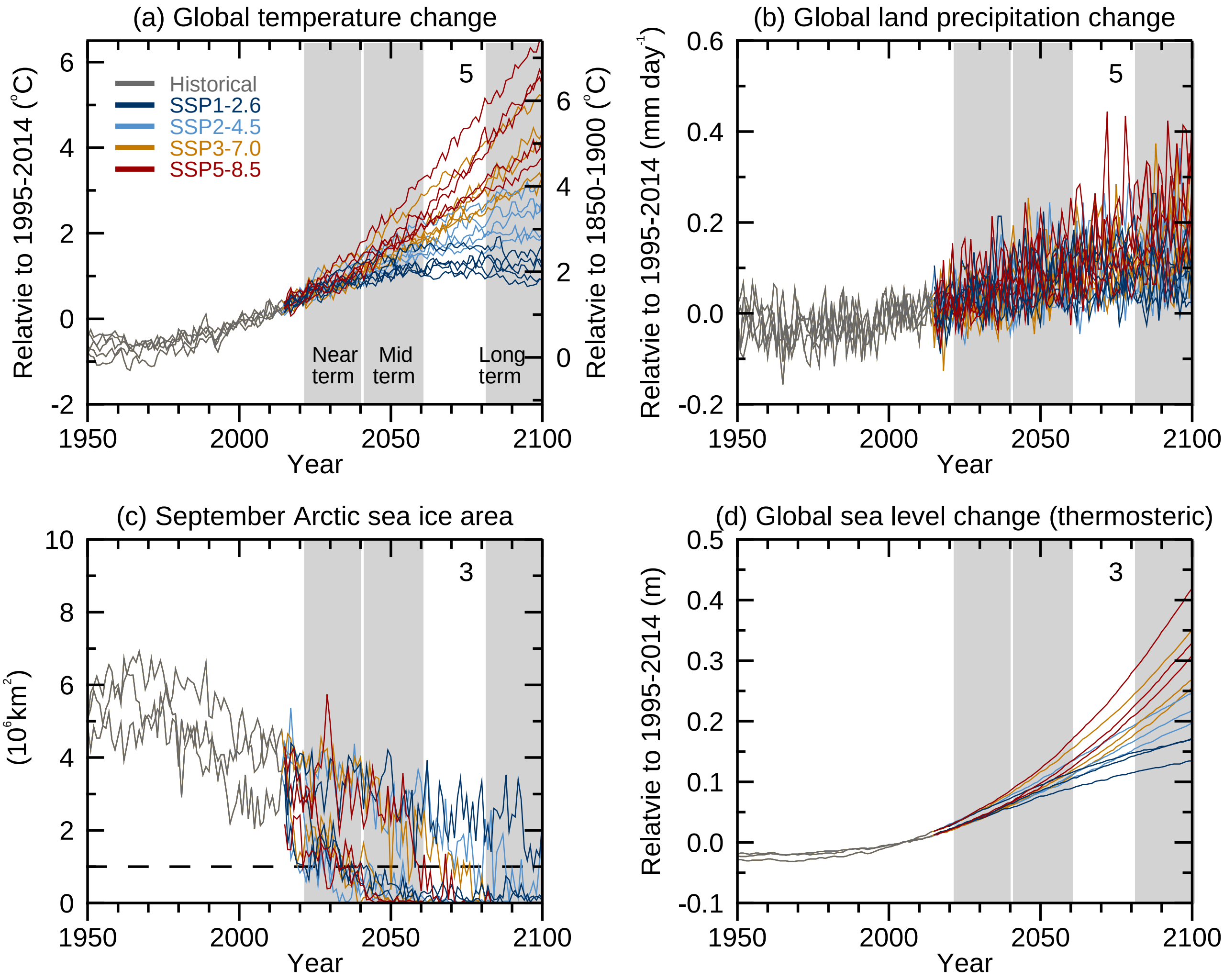

Figure 4.1: Selected indicators of global climate change from historical and scenario simulations. (a) Global surface air temperature changes relative to averages from 1995–2014 (left axis) and relative to averages from 1850–1900 (right axis). (b) Arctic sea-ice area. (c) Global land precipitation changes relative to averages from 1995–2014. (d) Global sea level change (due to thermal expansion alone) relative to averages from 1995-2014. (a), (b) and (d) are annual averages, (c) are September averages. The curves plotted here are based on results from the models that have thus far contributed to the CMIP6 exercise. In (a) and (b), the models are BCC-CSM2-MR, CanESM5, CNRM-CM6-1, IPSL-CM6A-LR, and MRI-ESM2-0. In (c) and (d), the models are CanESM5, CNRM-CM6-1, and IPSL-CM6A-LR. The number inside panel indicates the total number of models used. Eventually this figure will be updated using single simulations from the full CMIP6 ensemble plotted as ensemble means with shaded uncertainties.

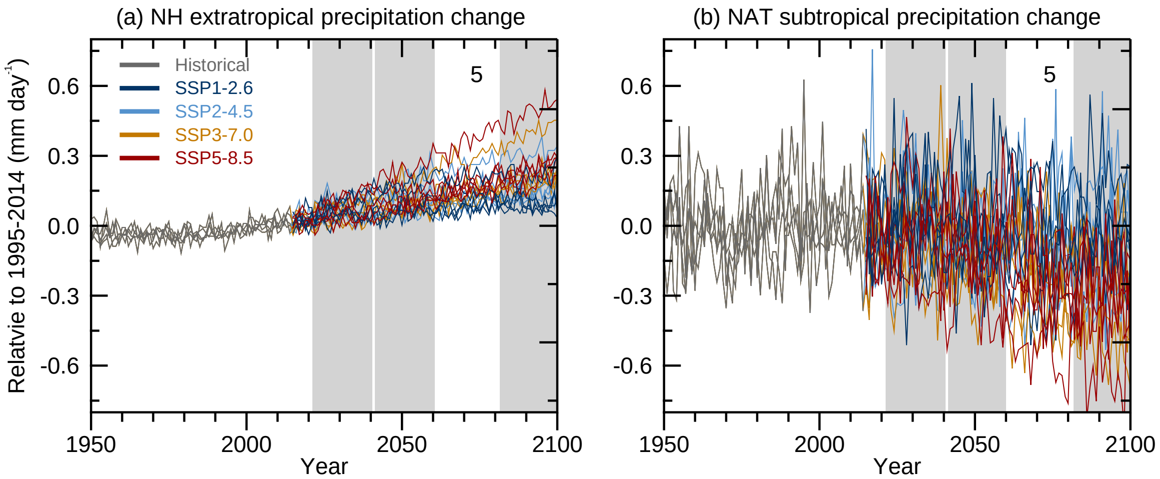

Figure 4.2: Annual mean precipitation changes from historical and scenario simulations. (a) Northern Hemisphere (NH) extratropics (30°N–90°N). (b) North Atlantic (NAT) subtropics (5°N–30°N, 80°W–0°). Changes are relative to averages from 1995–2014. The number inside panel indicates the total number of models used. The curves here are for single simulations from the five CMIP 6 models including BCC-CSM2-MR, CanESM5, CNRM-CM6-1, IPSL-CM6A-LR, and MRI-ESM2-0. Eventually this figure will be updated using single simulations from the full CMIP6 ensemble plotted as ensemble means with shaded uncertainties.

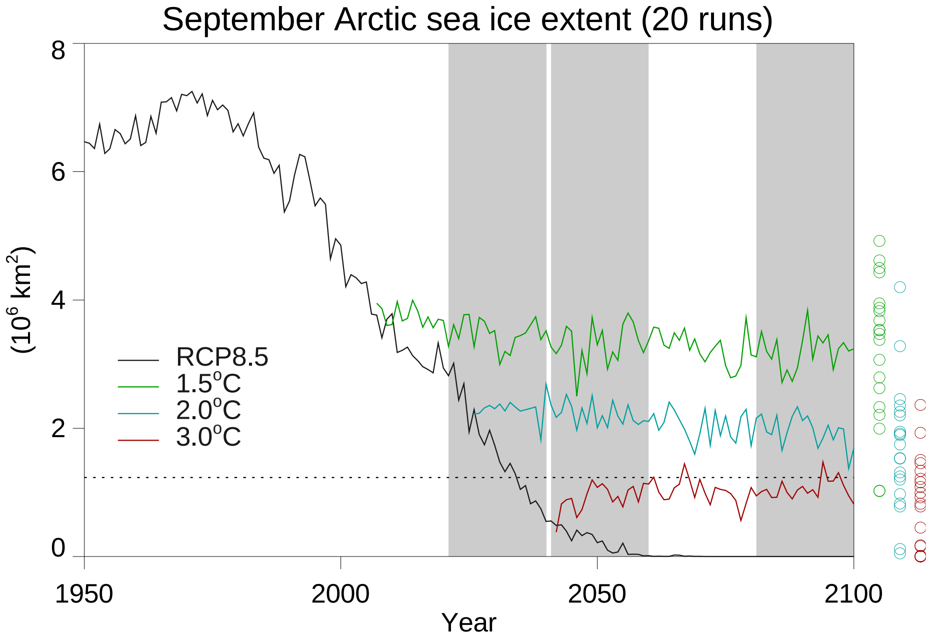

Figure 4.3: Arctic sea ice extent in September in a large initial-condition ensemble of observationally-constrained simulations of an Earth System Model (CanESM2). The black curve is the average over twenty simulations following historical forcings to 2015 and RCP8.5 extensions to 2100. The coloured curves are averages over twenty simulations after GSAT has been stabilized at the indicated degrees of warming relative to preindustrial. The coloured circles on the right are individual values at 2100. On an individual simulation basis, the probability of the Arctic becoming ice free (i.e. with less than 1 million km^2 coverage) is significantly higher for 2°C warming than for 1.5°C warming (Sigmond et al., 2018).

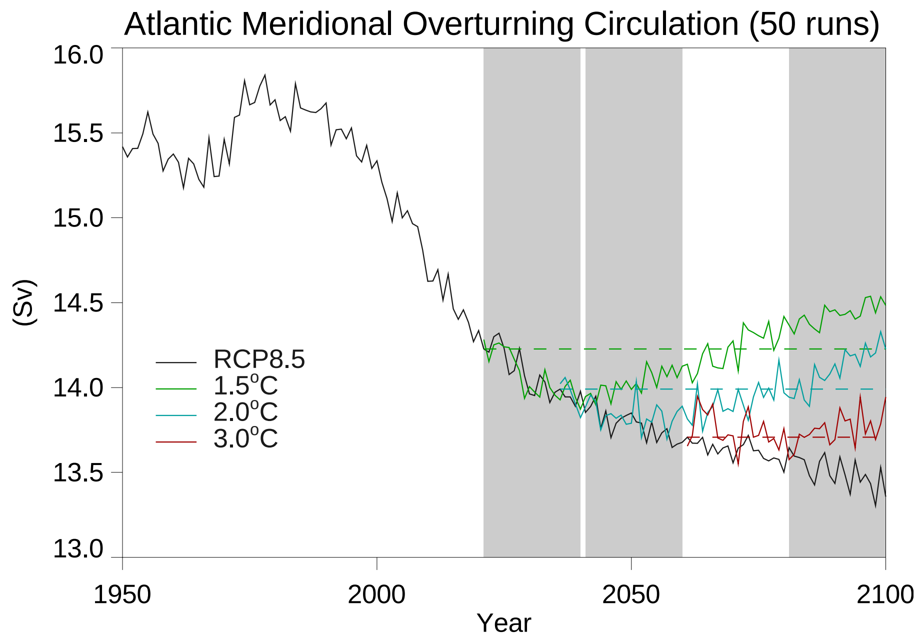

Figure 4.4: AMOC in large initial-condition ensembles of simulations of an Earth System Model (CanESM2). The black curve is the average over fifty simulations following historical forcings to 2005 and RCP8.5 extensions to 2100. The coloured curves are averages over fifty simulations (each) after GSAT has been stabilized at the indicated degree of warming relative to pre-industrial (Sigmond et al., 2018). The dashed lines indicate the AMOC strength at the point of emissions cessation.

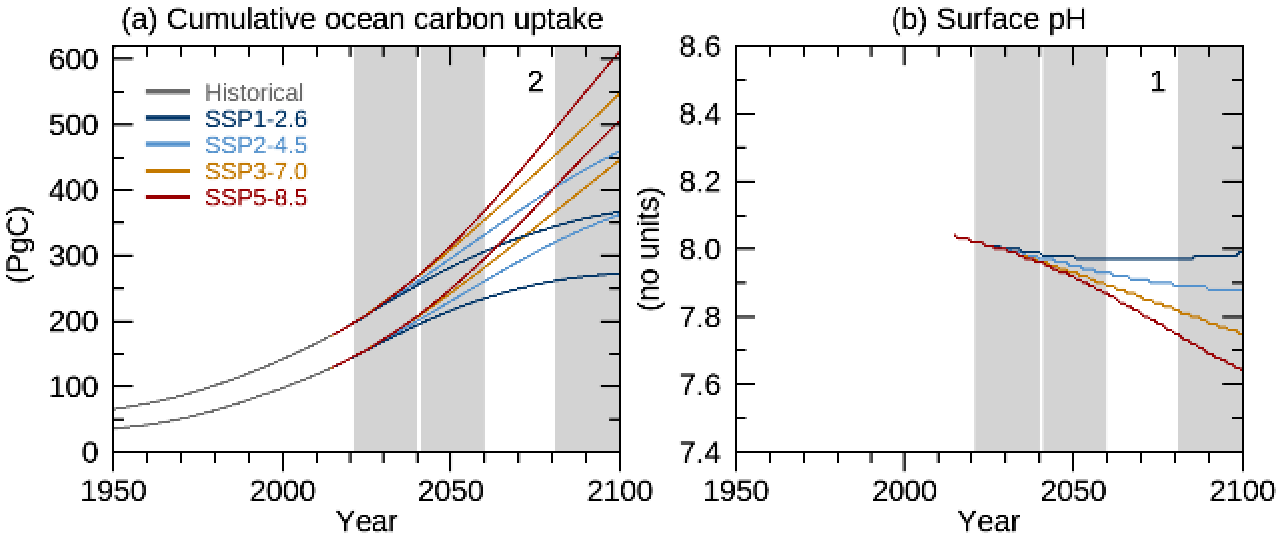

Figure 4.5: Cumulative ocean carbon uptake and surface pH from historical and scenario simulations. (a) Cumulative ocean carbon uptake since 1850. (b) Surface pH. The curves plotted here are for single simulations from (a) two CMIP6 models (IPSL-CM6A-LR and CanESM5) and (b) one model (IPSL-CM6A-LR). Eventually the figure will be updated using single simulations from the full CMIP6 ensemble, plotted as ensemble means with shading.

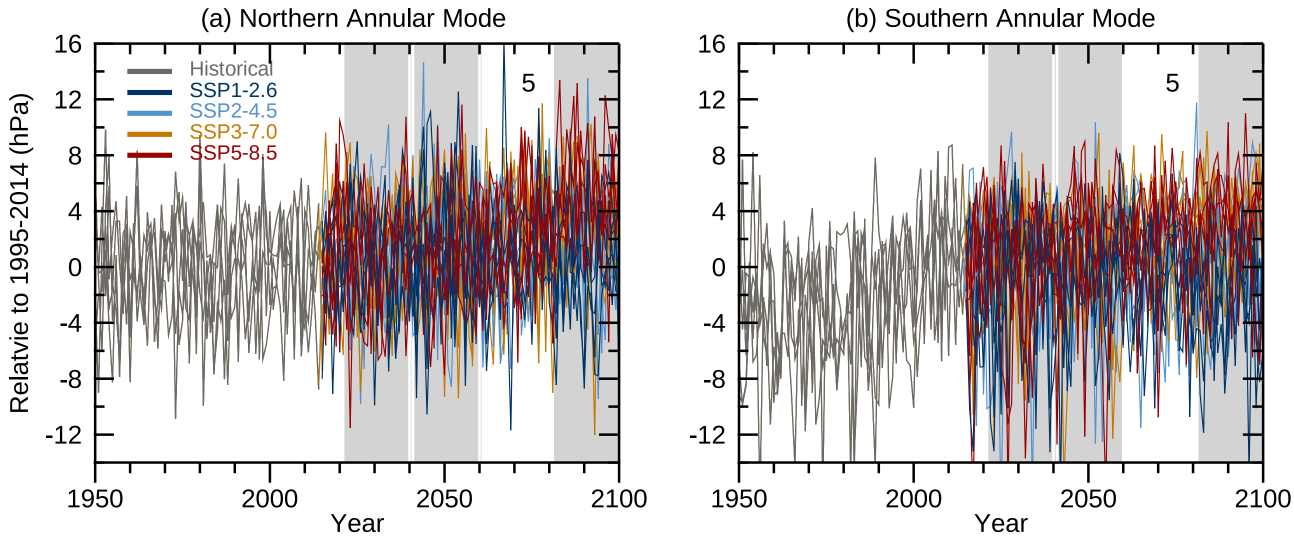

Figure 4.6: Simulations of boreal wintertime Annular Mode indices: (a) NAM and (b) SAM. The NAM is defined as the difference in zonal mean SLP at 35°N and 65°N (Li and Wang, 2003) and the SAM as the difference in zonal mean SLP at 40°S and 65°S (Gong and Wang, 1999). All anomalies are relative to averages from 1850 to 1900. The curves here are for single simulations from the five CMIP6 models that are BCC-CSM2-MR, CanESM5, CNRM-CM6-1, IPSL-CM6A-LR, and MRI-ESM2-0. Eventually this figure will be updated using single simulations from the full CMIP6 ensemble, and ensemble means and shaded uncertainties will be displayed.

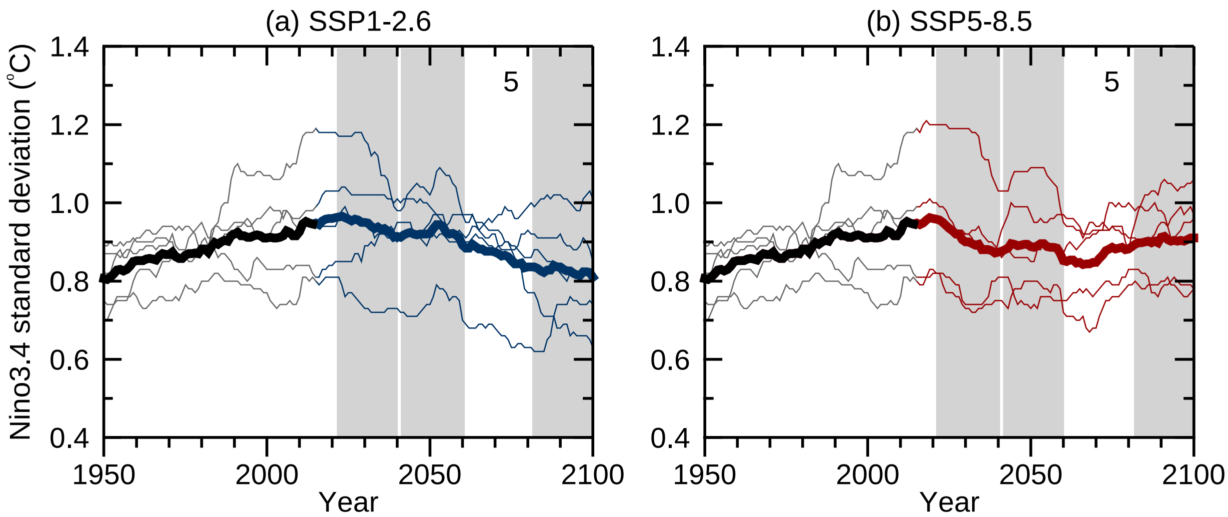

Figure 4.7: Historical simulation and future projection of the amplitude of the ENSO under (a) SSP1-2.6 and (b) SSP5-8.5. The amplitude is defined as the standard deviation of the monthly Niño 3.4 index after removing climatological monthly mean and long-term trend. The amplitude is shown for maximally-overlapping fifty-year periods with the end-year shown on the horizontal axis. The thick curves are the mean of individual model's ENSO amplitude. The curves here are for single simulations from the five CMIP6 models that are BCC-CSM2-MR, CanESM5, CNRM-CM6-1, IPSL-CM6A-LR, and MRI-ESM2-0. Eventually this figure will be updated using single simulations from the full CMIP6 ensemble, and ensemble means and shaded uncertainties will be displayed.

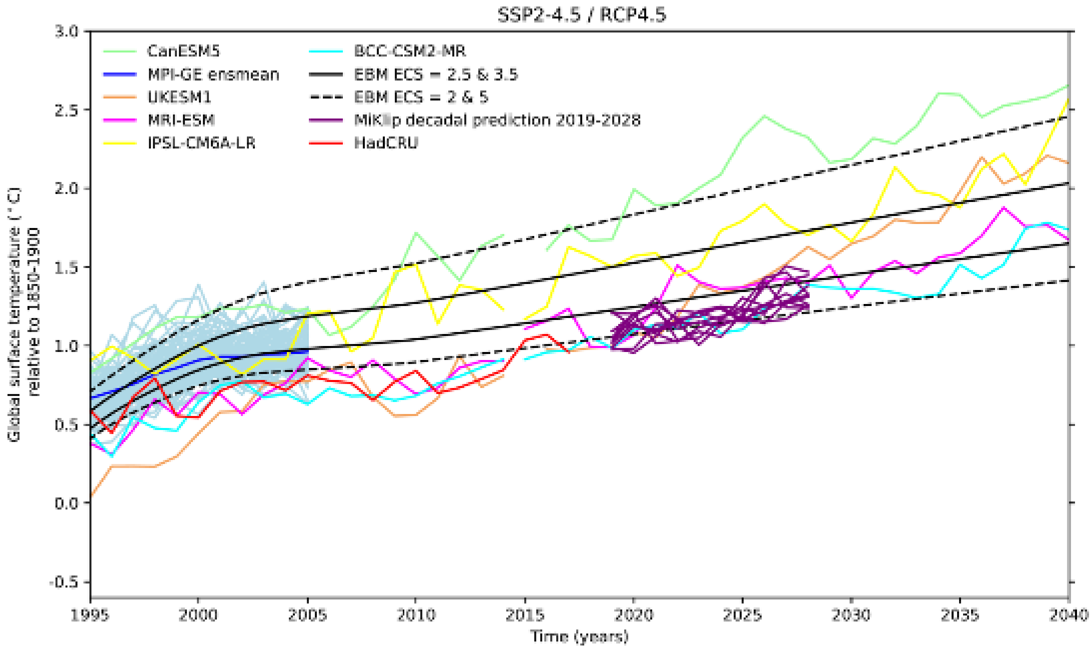

Figure 4.8: Projections and predictions of global-mean annual-mean surface air temperature, referenced to 1850–1900. The figure shows for 1995–2040 one CMIP6-forced simulation each with BCC-CSM2-MR (cyan), CanESM5 (light green), IPSL-CM6A-LR (yellow), MRI-ESM2-0 (light purple), and UKESM1 (ochre); and GSAT simulated with an emulator driven by the AR5 radiative forcing, using RCP4.5 from the WGI AR5 Annex II after 2005 (black). The emulator is a two-layer time-dependent energy-balance model (EBM) following (Held et al., 2010), with ocean heat uptake efficiency $\kappa = 0.8$ W m^{-2} $°C^{-1}$ and efficacy 1.0. Results are shown for ECS = 2.5°C and 3.5°C, the lower and upper limits, respectively, of the Chapter 7 ECS *likely* range (solid black), as well as for 2°C and 5°C, the lower and upper limits, respectively, of the Chapter 7 ECS *very likely* range (dashed black). For the historical period, all panels show the observations (HadCRUT4, (Morice et al., 2012), red) and the CMIP5-forced simulations from the 100-member Max Planck Institute Grand Ensemble (MPI-GE, (Maher et al., 2019), dark blue for ensemble mean, light blue for individual realizations), For the years 2019–2028, the initialized-prediction ensemble from the CMIP6 model MPI-ESM-HR (Müller et al., 2018) is shown (dark purple), produced through the MiKlip project (Marotzke et al., 2016) and contributing to DCPP (Boer et al., 2016). The MiKlip results are drift-removed and referenced to the time-averaged hindcasts for 1995–2014 lead-year by lead-year; then the HadCRUT4 difference between the means over 1995–2014 and 1850–1900 is added. [Placeholder figure, copied from Box 4.1, Figure 1, bottom right; to be updated with the full CMIP6 ensemble and CMIP6/AR6/SSP forcing for the EBM.]

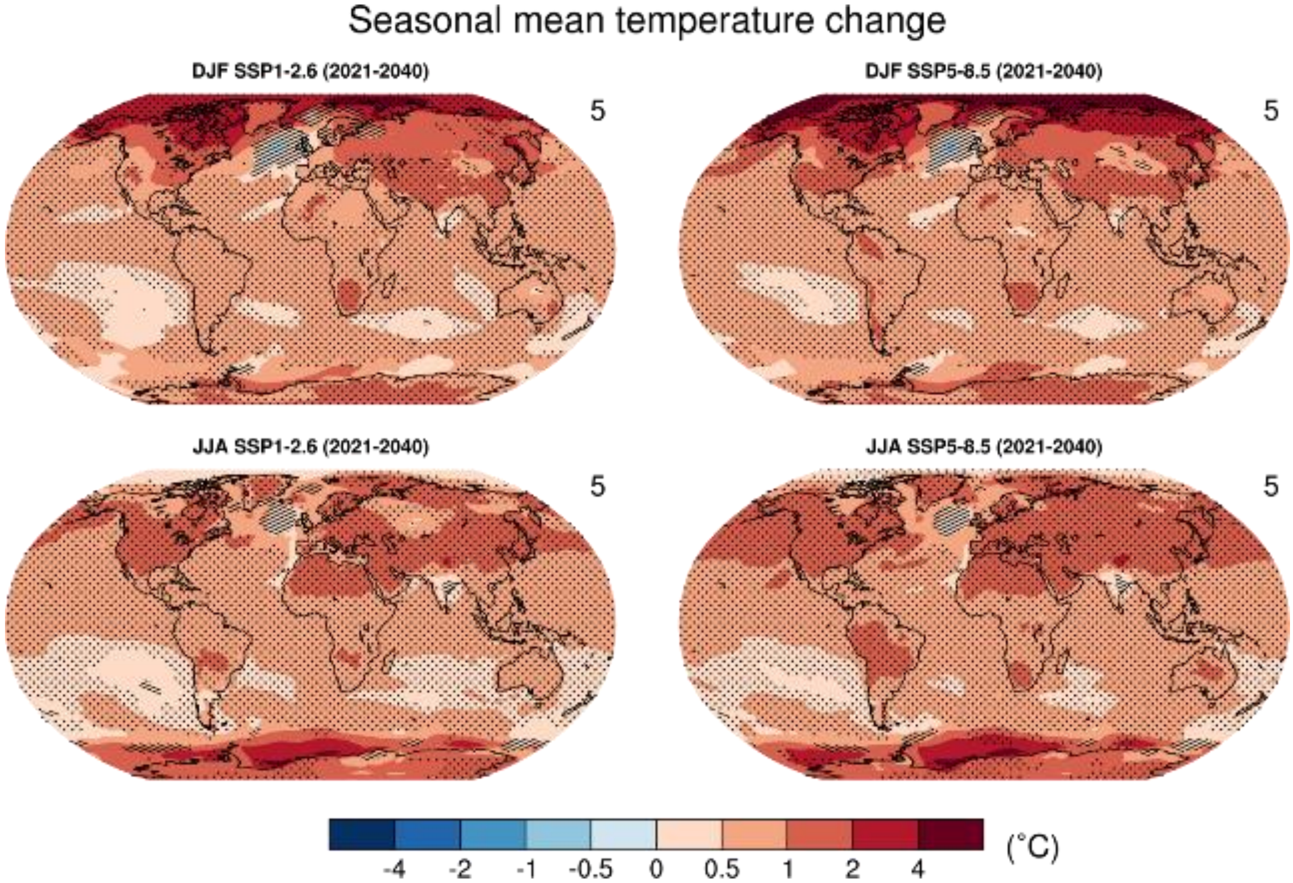

Figure 4.9: CMIP6 multi-model mean change (°C) in (top) DJF and (bottom) JJA near-surface air temperature in 2021–2040 from SSP1-2.6 and SSP5-8.5 relative to 1995–2014 [Figure produced with ESMValTool (Eyring et al., 2016b) based on the five CMIP6 models: BCC-CSM2-MR, CanESM5, CNRM-CM6-1, IPSL-CM6A-LR, and MRI-ESM2-0. Figure will be updated with more CMIP6 models]

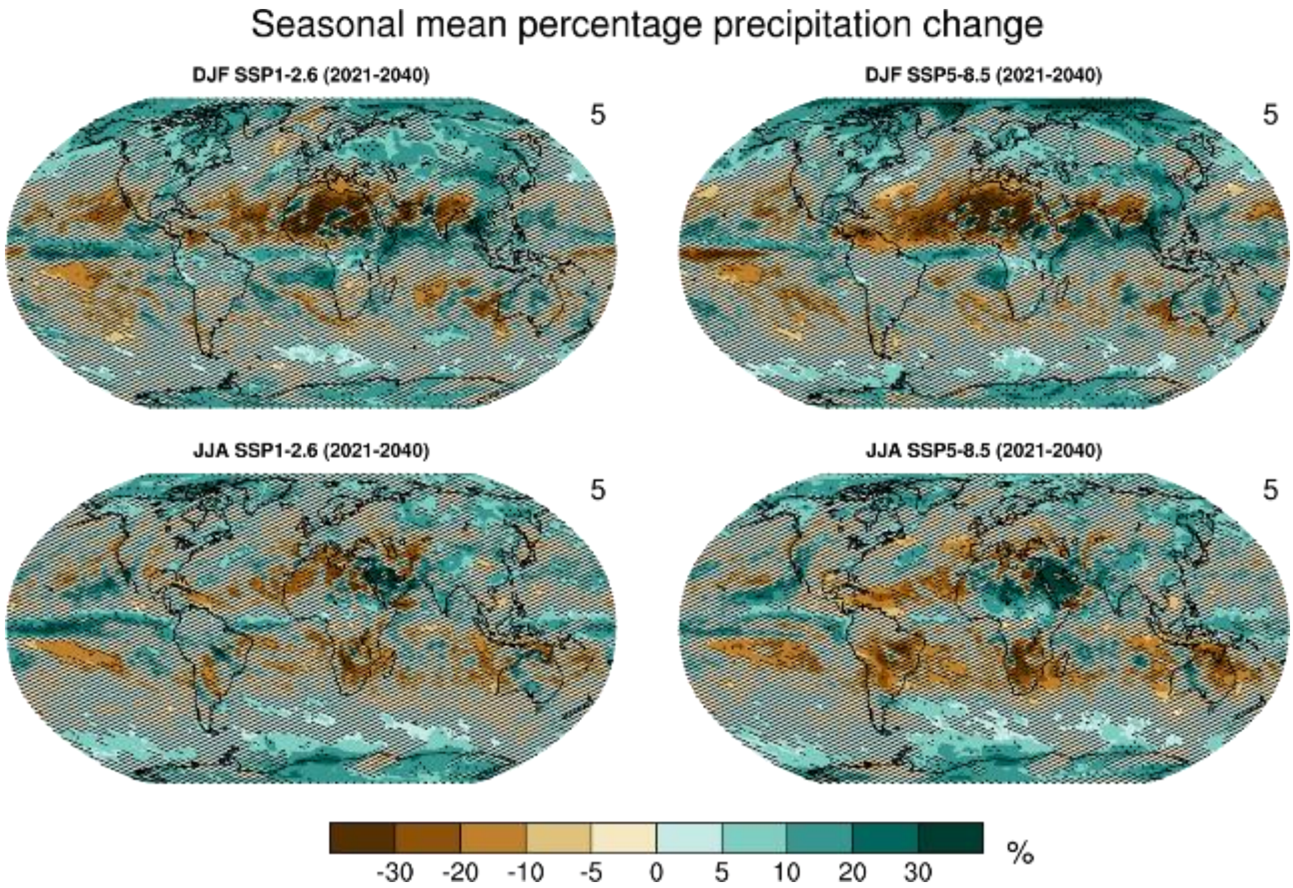

Figure 4.10: CMIP6 multi-model mean change (%) in (top) DJF and (bottom) JJA precipitation in 2021-2040 from SSP1-2.6 and SSP5-8.5 relative to 1995-2014 [Figure produced with ESMValTool (Eyring et al., 2016b) based on the five CMIP6 models: BCC-CSM2-MR, CanESM5, CNRM-CM6-1, IPSL-CM6A-LR, and MRI-ESM2-0. Figure will be updated with more CMIP6 models. Figure will be updated with more CMIP6 models]

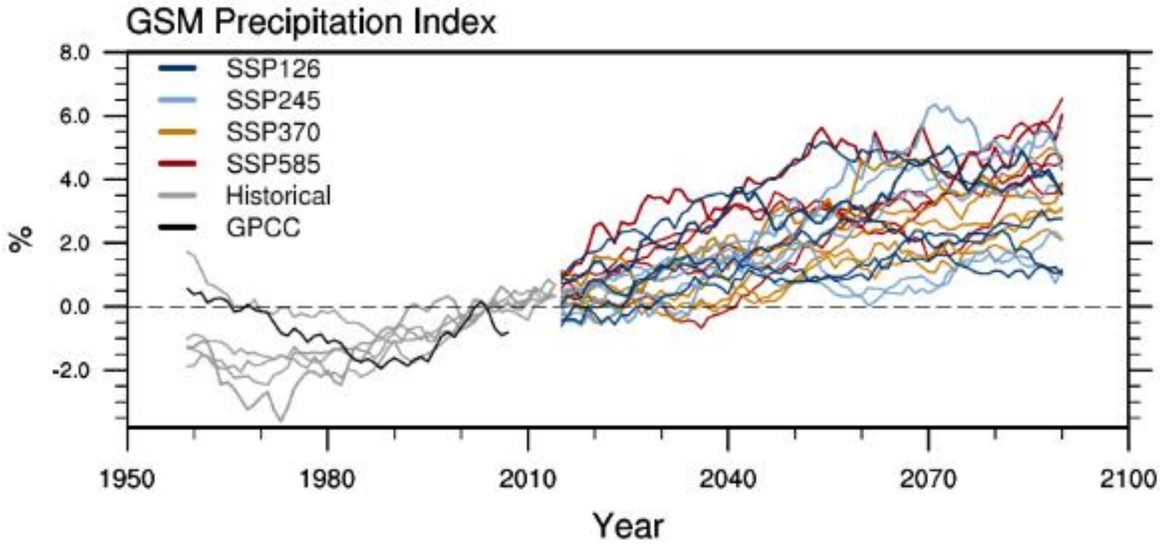

Figure 4.11: Changes of global land monsoon precipitation index (defined as the accumulated precipitation falling in the global land monsoon domain as defined by (Wang et al., 2013) in the historical climate simulation and four SSPs projections of five CMIP6 (BCC-CSM2-MR, CanESM5, CNRM-CM6-1, IPSL-CM6A-LR, MRI-ESM2-0) models. Each line in each SSP represents one model realization. Anomalies are relative to the 1995–2014 mean. Time series are normalized by climate mean values and smoothed with a 20-yr running-mean filter (Unit: %). Eventually this figure will be updated using single simulations from the full CMIP6 models, plotted as multi-model ensemble with shading of model spread.

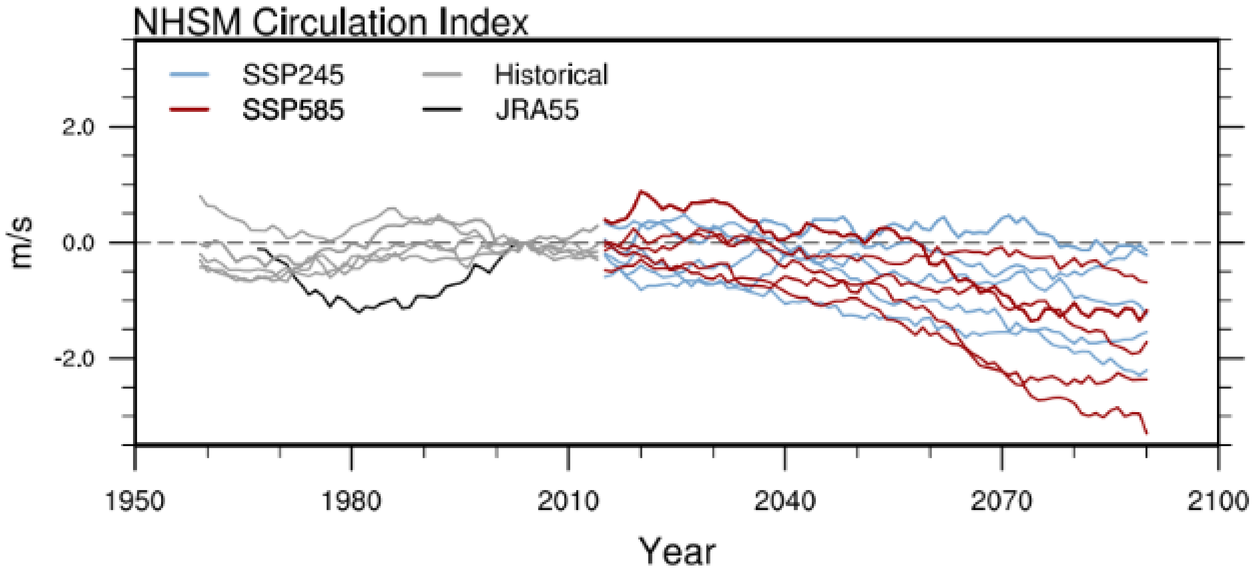

Figure 4.12: Changes of tropical monsoon circulation index (defined as the vertical shear of zonal winds between 850 and 200 hPa averaged in a zone stretching from Mexico eastward to the Philippines (0°–20°N, 120°W–120°E) (Wang et al., 2013)in the historical climate simulation and two SSPs projection of five CMIP6 (BCC-CSM2-MR, CanESM5, CNRM-CM6-1, IPSL-CM6A-LR, MRI-ESM2-0). Each line in each SSP represents one model realization. Anomalies are relative to the 1995–2014 mean. Anomalies are relative to the 1995–2014 mean. Time series are smoothed with a 20-yr running-mean filter (Unit: m/s). Eventually this figure will be updated using single simulations from the full CMIP6 models, plotted as multi-model ensemble with shading of model spread.

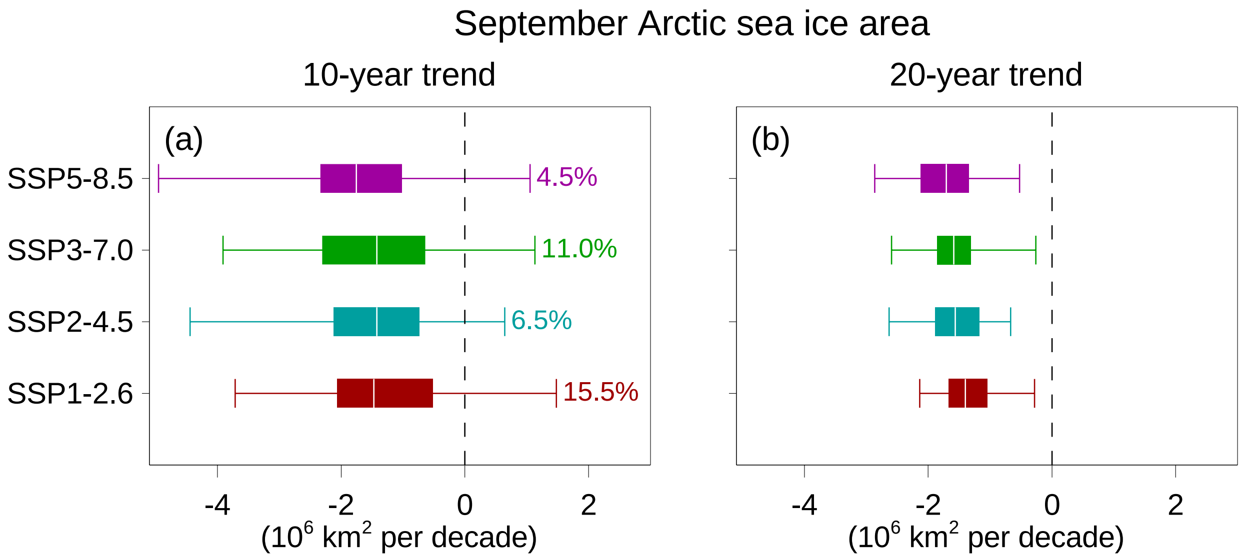

Figure 4.13: September Arctic sea ice area trends for periods ending in the near-term period from 2021-2040 following the various priority SSPs. (a) 10-year periods. (b) 20-year periods. Plotted are the minimum and maximum trends, the lower and higher trend quartiles and the median trend. The percentage of positive trend values are indicated to the right of the maximum value. [The values plotted here are for 10 simulations from one CMIP6 model, CanESM5. Eventually the figure will be updated using single simulations from the full CMIP6 ensemble.]

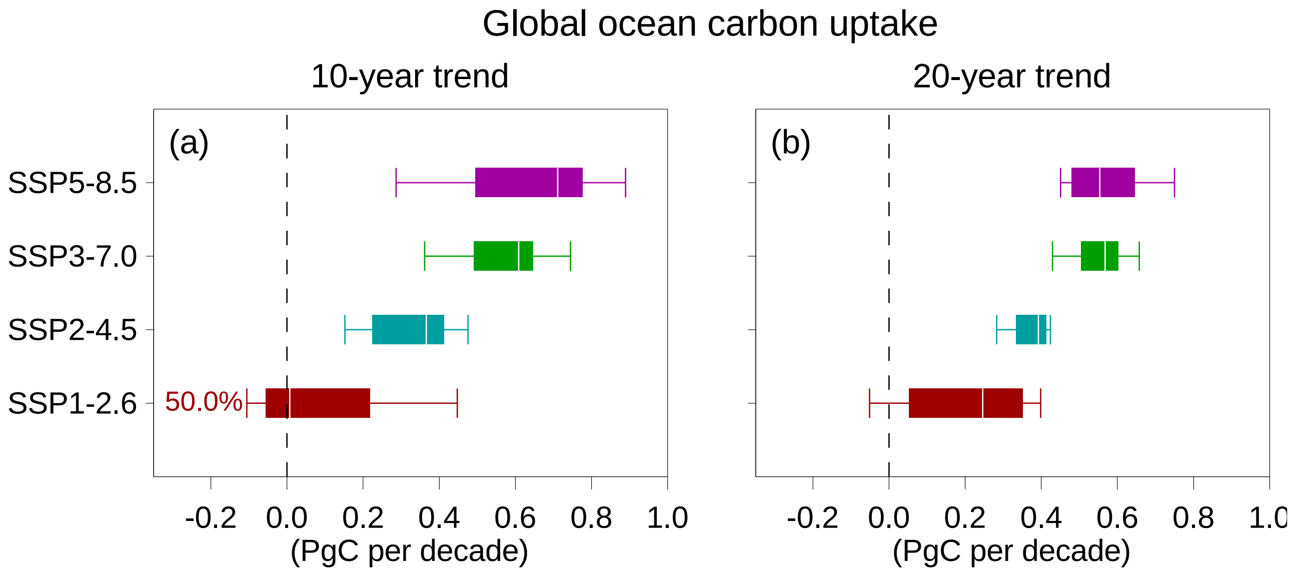

Figure 4.14: Annual-mean ocean carbon uptake trends for all periods ending in the near-term (2021-2040). (a) 10-year periods. (b) 20-year periods. Plotted are the minimum and maximum trends, the lower and higher trend quartiles and the median trend. The percentage of positive trend values are indicated to the right of the maximum value. [The values plotted here are for 10 simulations from on CMIP6 model, CanESM5. Eventually the figure will be updated using single simulations from the full CMIP6 ensemble.]

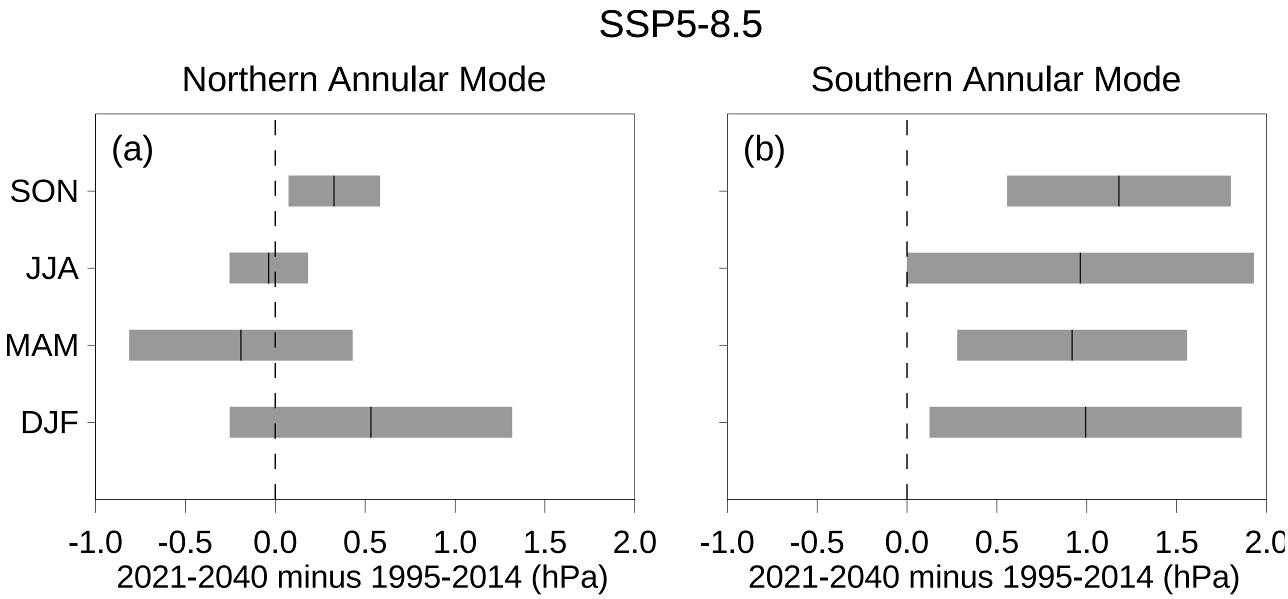

Figure 4.15: Simulated Annular Mode index change (hPa) from present-day to the near-term: (a) NAM and (b) SAM. The NAM is defined as the difference in zonal mean sea-level pressure (SLP) at 35°N and 65°N (Li and Wang, 2003) and the SAM as the difference in zonal mean SLP at 40°S and 65°S (Gong and Wang, 1999). Present-day values are averages over the period from 1995-2014. Near-term values are averages over the period from 2021-2040. The vertical lines are ensemble-means and the shaded bars are 5-95% confidence intervals on the ensemble means. [These calculations are based on a ten-member ensemble of simulations from one CMIP6 model, CanESM5. Eventually, the figure will be updated using single simulations from the full CMIP6 ensemble.]

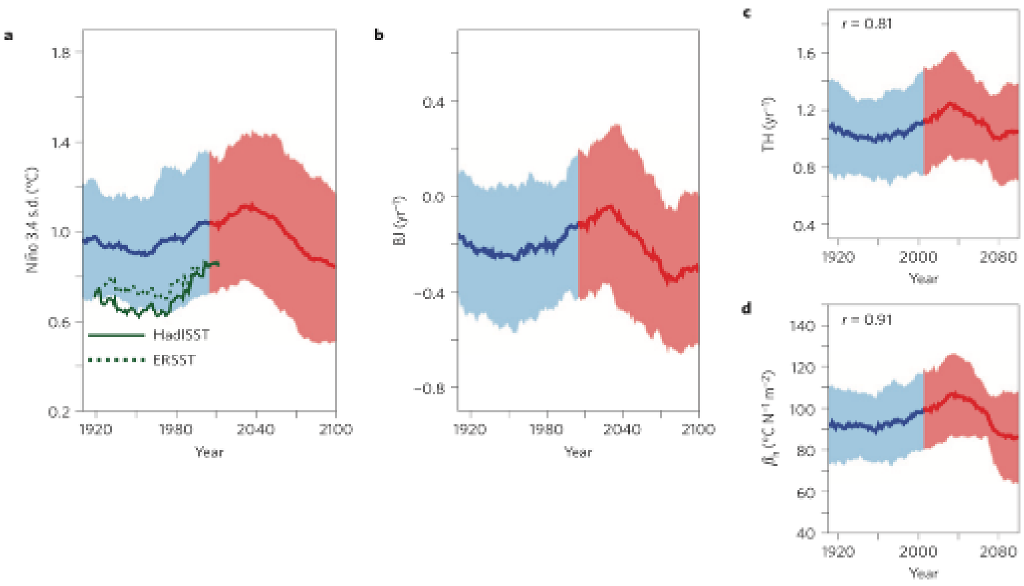

Figure 2 | Time variation of simulated ENSO amplitude and ENSO stability. a, The MME of the ENSO amplitude from the BEST9 computed over 50-year running periods from 1861 to 2100. The 50-year running ENSO amplitudes from HadISST (ref. 11) and ERSST (ref. 12) over the period 1870–2012 are also shown. There is significant correlation between the MME and observations ($r = 0.90$ for HadISST and $r = 0.87$ for ERSST). **b–d**, The MME of the 50-year running ENSO stability estimated using the BJ index (**b**), the MME thermocline feedback term (**c**), and MME response sensitivity coefficient for anomalous zonal thermocline slope response to wind stress anomalies (β_h; **d**) from the BEST9. In **c**, correlation coefficient with the BJ index, and in **d**, correlation coefficient with the thermocline feedback are shown. In **a–d**, the light blue shading and light red shading represent inter-model spread or uncertainty range, which is estimated with the inter-model standard deviations, in the historical run and the RCP8.5 run, respectively. The last year of each 50-year running period is plotted on the *x* axis.

Figure 4.16: Time variation of simulated ENSO amplitude and ENSO stability [Placeholder figure from (Kim et al., 2014b), to be replaced in later drafts].

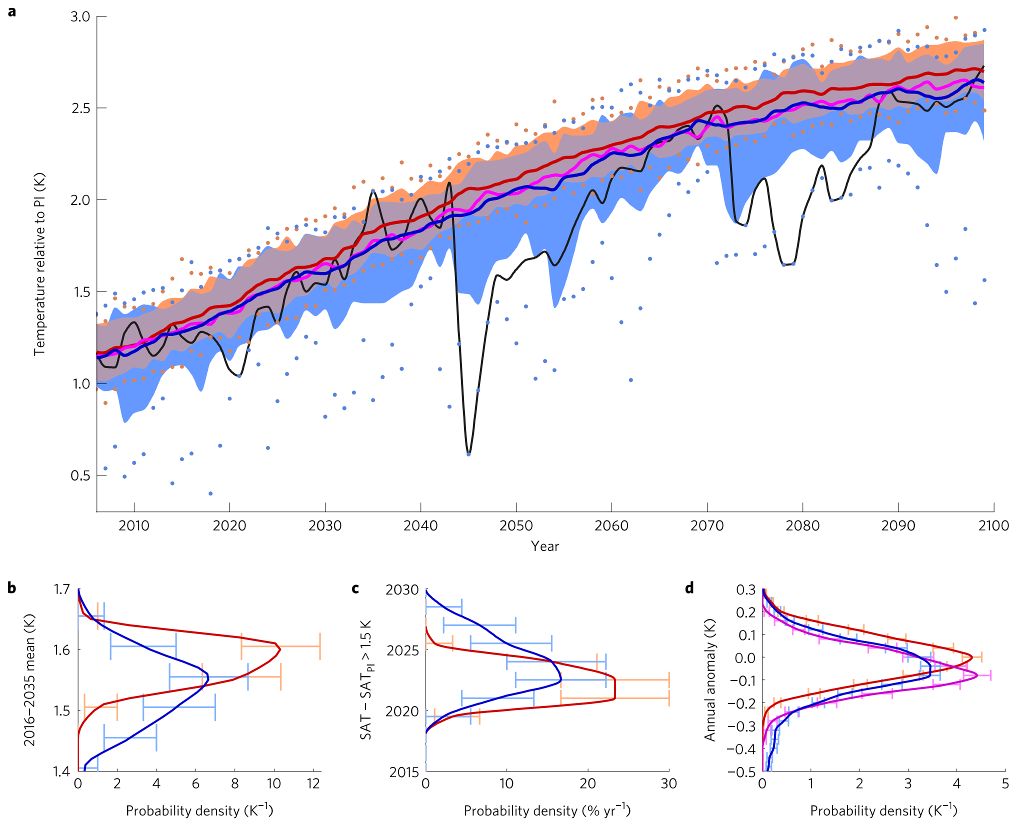

Figure 4.17: Annual-mean GSAT. a, Ensemble mean (solid) of VOLC (blue), VOLC-CONST (magenta) and NO-VOLC (red/orange) with 5–95% range (shading) and ensemble minima/maxima (dots) for VOLC and NO-VOLC; evolution of the most extreme member (black). b, Probability density function (PDF) of the 2016–2035 mean relative to pre-industrial (PI), with 5–95% bootstrap confidence bounds. c, PDF of the time when GSAT change relative to PI (20-year running average) exceeds 1.5°C. d, PDF of annual anomalies with anthropogenic trend removed. The spread of VOLC-CONST is linearly shifted relative to NO-VOLC, and therefore not shown in a–c. These calculations are based on three 21st-century simulation ensembles with the Norwegian Earth System Model (NorESM), which use the same mid-range anthropogenic forcing scenario RCP4.5 but differ in their volcanic forcing: a 60-member ensemble using plausible stochastic volcanic forcing (VOLC); a 60-member reference ensemble using zero volcanic forcing (NO-VOLC); and a 20-member ensemble using 1850–2000 averaged volcanic forcing (VOLC-CONST). [This figure is adopted from (Bethke et al., 2017).]

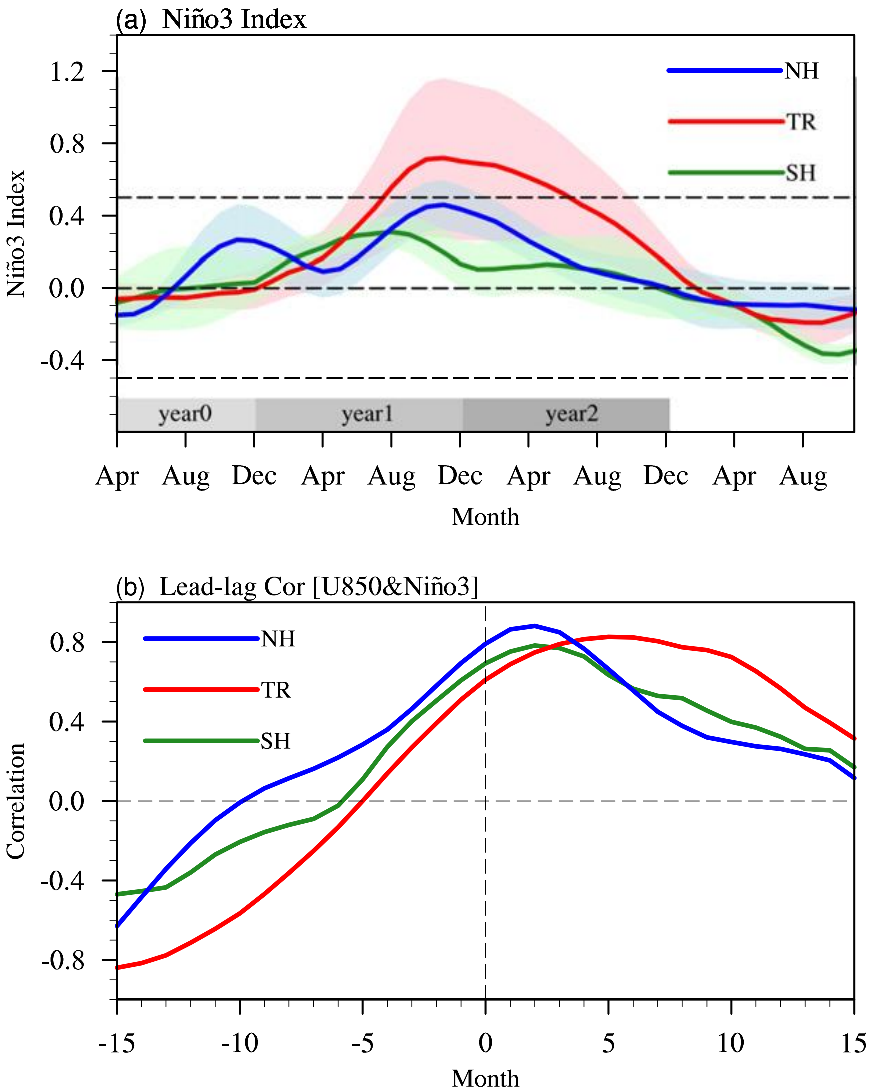

Figure 4.18: (a) Evolution of the composite Niño-3 index with zonal mean removed (units: 8°C) after northern eruptions (blue line), tropical eruptions (red line), and southern eruptions (green line). The spreads of the individual volcanic eruptions are denoted by the blue, red, and green shading, respectively. (b) The lead–lag correlation between the Niño-3 index (5°S–5°N, 150°–90°W) and the 850-hPa zonal wind in the western-to-central equatorial Pacific (5°S–5°N, 110°E–150°W) following northern (blue line), tropical (red line), and southern eruptions (green line). The positive value of the horizontal axis indicates that the Niño-3 index lags the 850-hPa zonal wind. [This figure is adopted from (Zuo et al., 2018).]

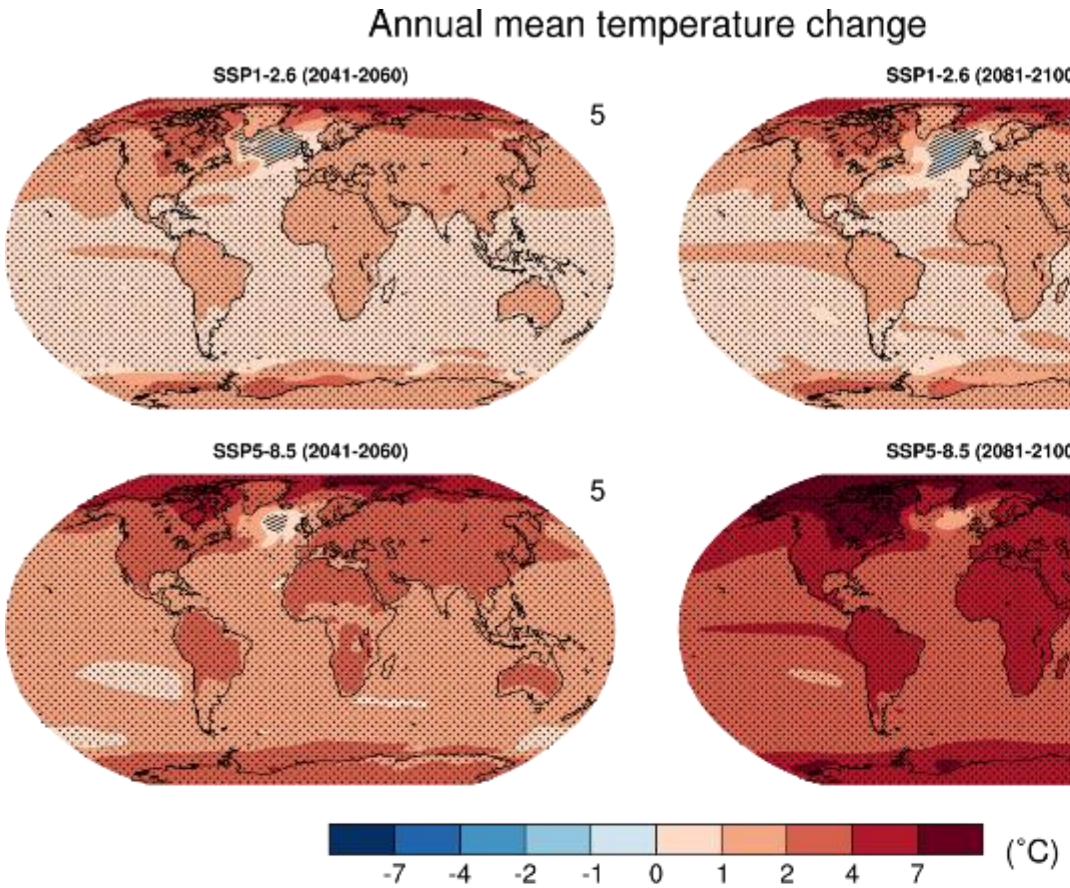

Figure 4.19: Multi-model mean change in annual mean near-surface air temperature (°C) in 2041–2060 and 2081–2100 in (top) SSP1-2.6 and (bottom) SSP5-8.5 relative to 1995–2014. [Figure produced with ESMValTool (Eyring et al., 2016b) based on the five CMIP6 models, BCC-CSM2-MR, CanESM5, CNRM-CM6-1, IPSL-CM6A-LR, and MRI-ESM2-0 will be updated with more CMIP6 models.]

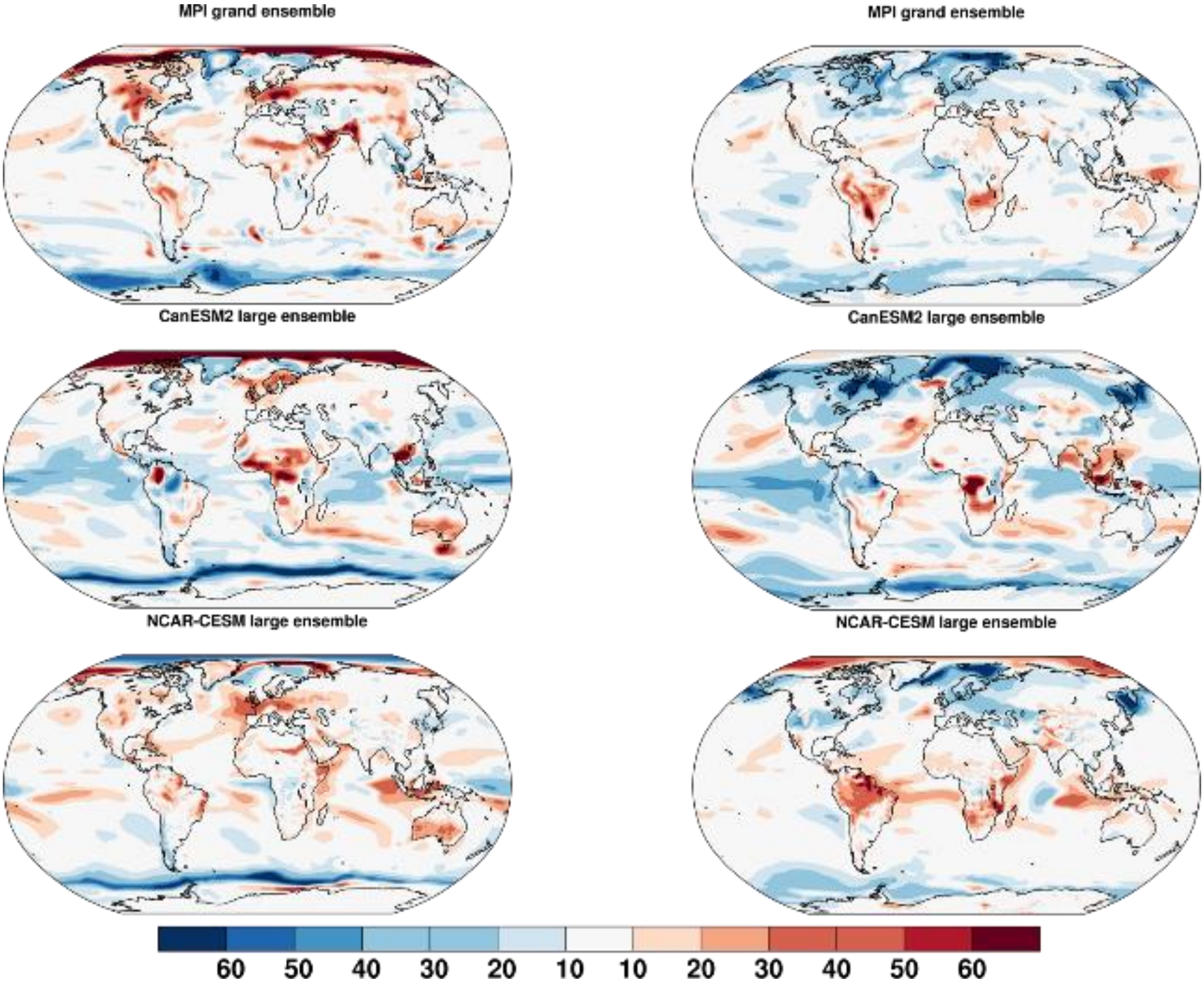

Figure 4.20: Relative change in variability of (left) JJA and (right) DFJ mean temperature in three large initial condition ensembles. Changes are shown as percentage changes of standard deviation across local seasonal mean temperatures. Changes are shown MPI 100-member grand ensemble by 2081–2100 (Maher et al., 2019), CanESM2 50-member ensemble (Kirchmeier-Young et al., 2017) and NCAR-CESM 30-member ensemble (Kay et al., 2015) for RCP8.5. [Figure may later be updated based on large initial-condition ensembles or large multi-model ensembles such as CMIP6 showing changes in standard deviation of seasonal mean temperatures in 2081–2100 (SSP5-8.5) relative to 1995–2014].

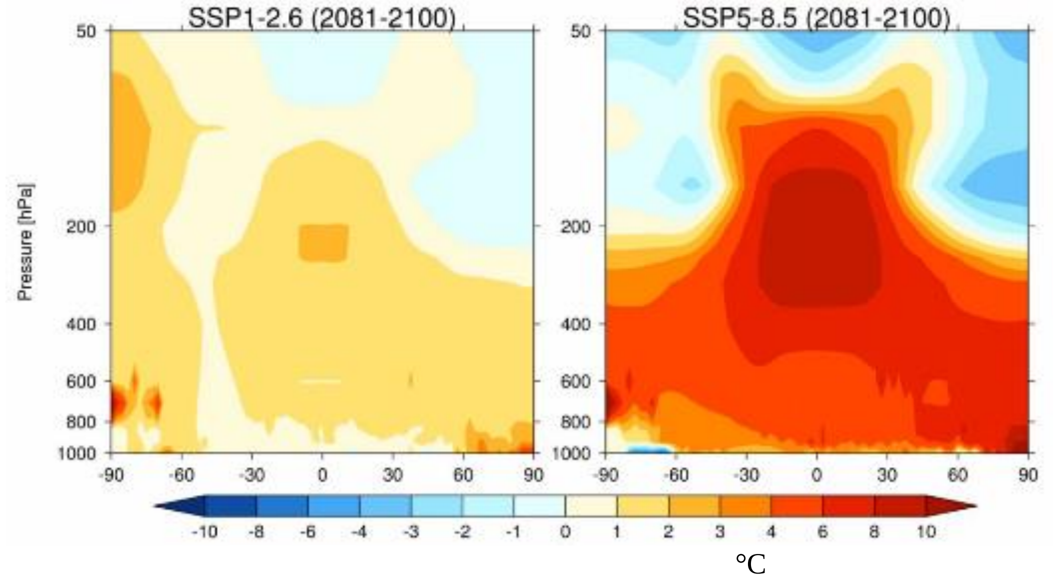

Figure 4.21: Change in annual atmospheric temperature (°C) in 2081–2100 in (left) SSP1-2.6 and (right) SSP5-8.5 relative to 1995–2014 for the IPSL-CM6A-LR model from CMIP6. [To be updated with more CMIP6 models as they become available].

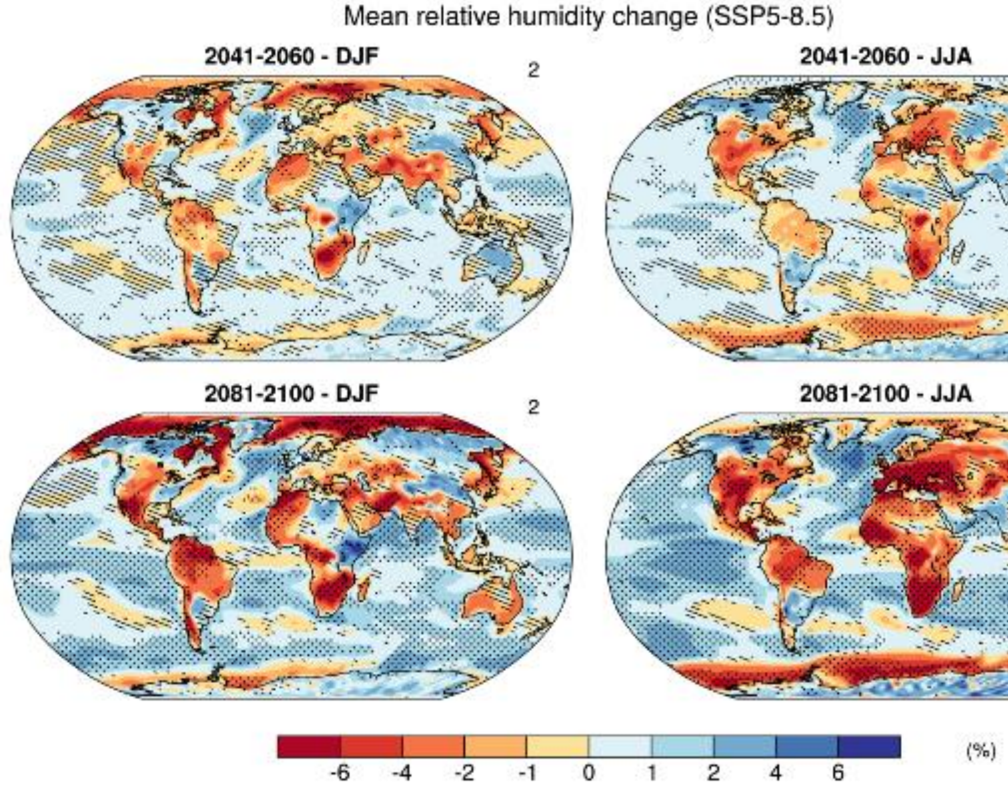

Figure 4.22: Multi-model mean change (%) in seasonal (left) DJF and (right) JJA mean near-surface relative humidity in 2041–2060 and 2081–2100 in SSP5-8.5 relative to 1995–2014 based on two CMIP6 models, IPSL-CM6A-LR and MRI-ESM2-0. [Figure to be updated.]

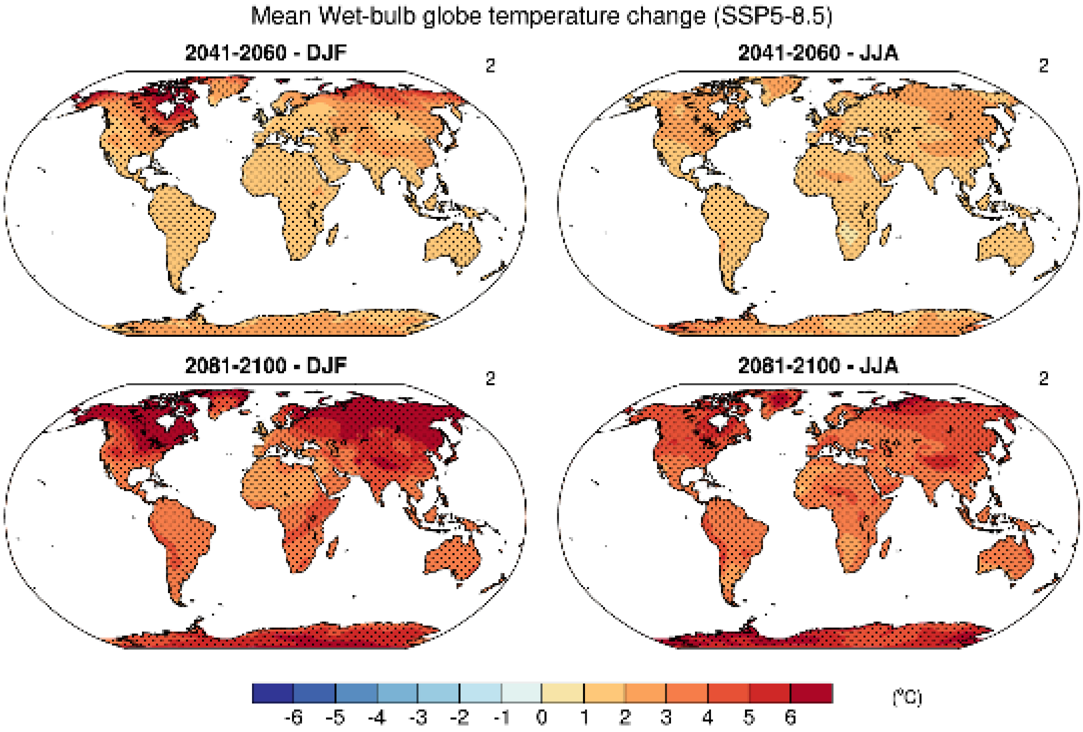

Figure 4.23: Multi-model mean change (°C) in seasonal (left) DJF and (right) JJA mean wet-bulb globe temperature in 2041-2060 and 2081-2100 in SSP5-8.5 relative to 1995-2014 based on two CMIP6 models:IPSL-CM6A-LR and MRI-ESM2-0. [Figure to be updated.]

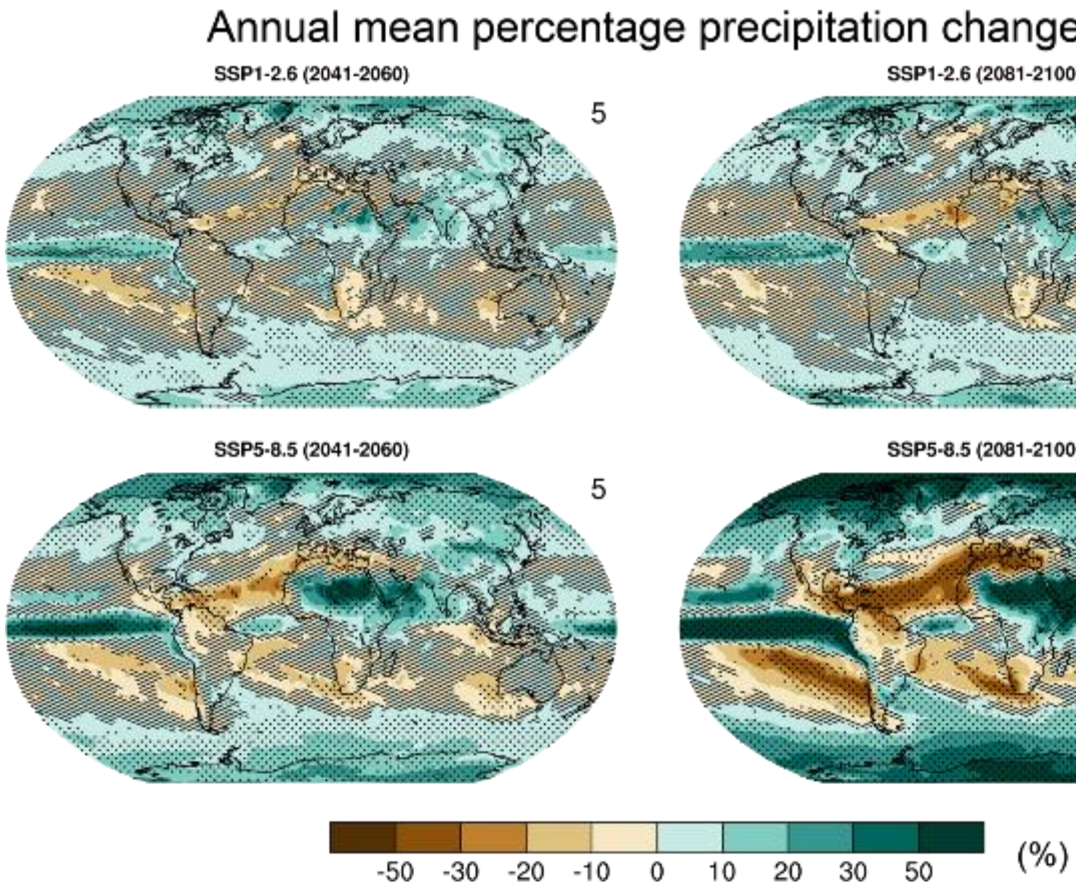

Figure 4.24: Multi-model mean change (%) in annual mean precipitation in 2041-2060 (left) and 2081-2100 (right) relative to 1995-2014 from (top) SSP1-2.6 and (bottom) SSP5-8.5. [Figure produced with ESMValTool (Eyring et al., 2016b) based on the five CMIP6 models BCC-CSM2-MR, CanESM5, CNRM-CM6-1, IPSL-CM6A-LR, and MRI-ESM2-0. Figure to be updated with more CMIP6 models for JJA and DJF season.]

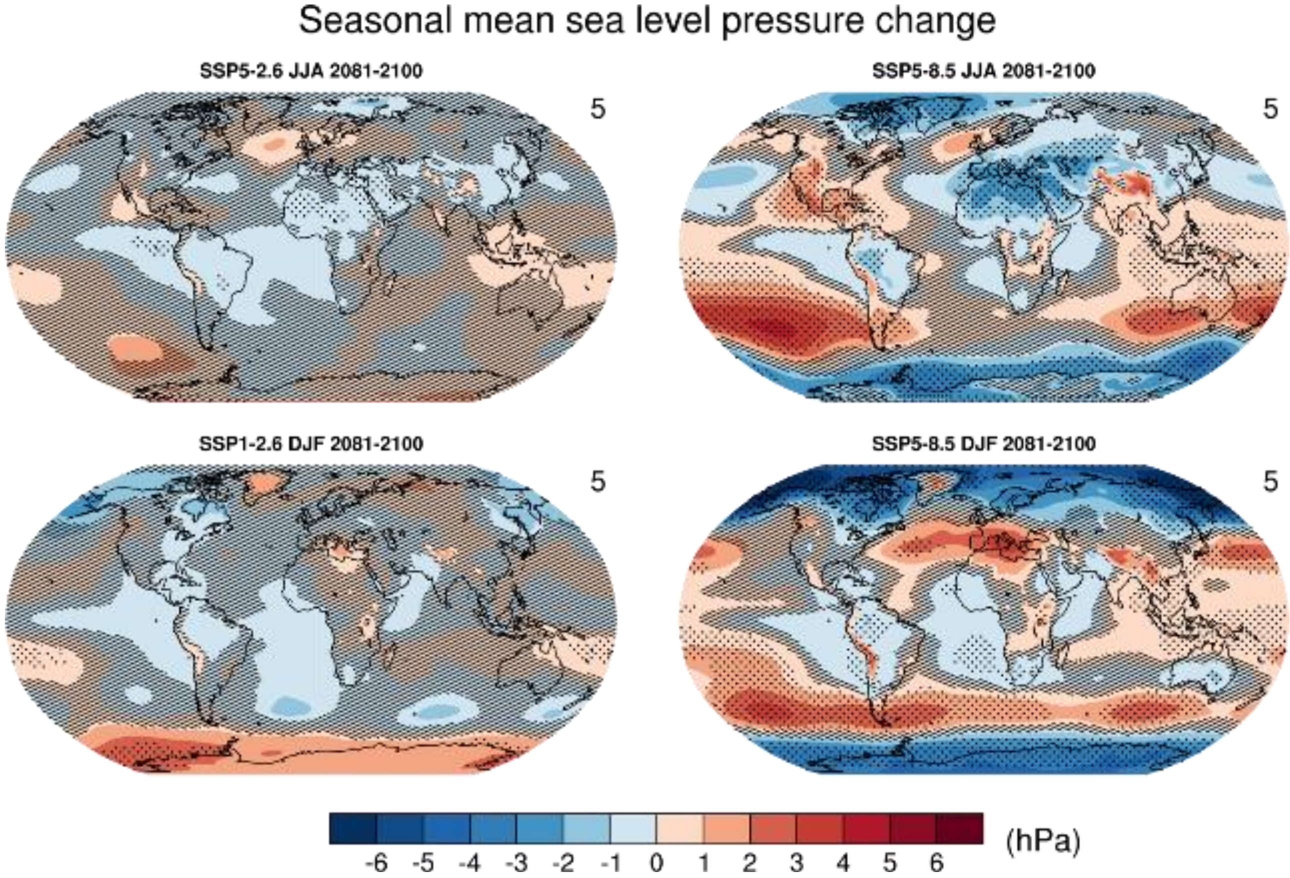

Figure 4.25: Multi-model mean change (hPa) in JJA and DJF mean sea level pressure in 2081-2100 in SSP1-2.6 and SSP5-8.5 relative to 1995-2014 [Figure produced with ESMValTool (Eyring et al., 2016b) based on the five CMIP6 models BCC-CSM2-MR, CanESM5, CNRM-CM6-1, IPSL-CM6A-LR, and MRI-ESM2-0. More CMIP6 models will be added as they become available.]

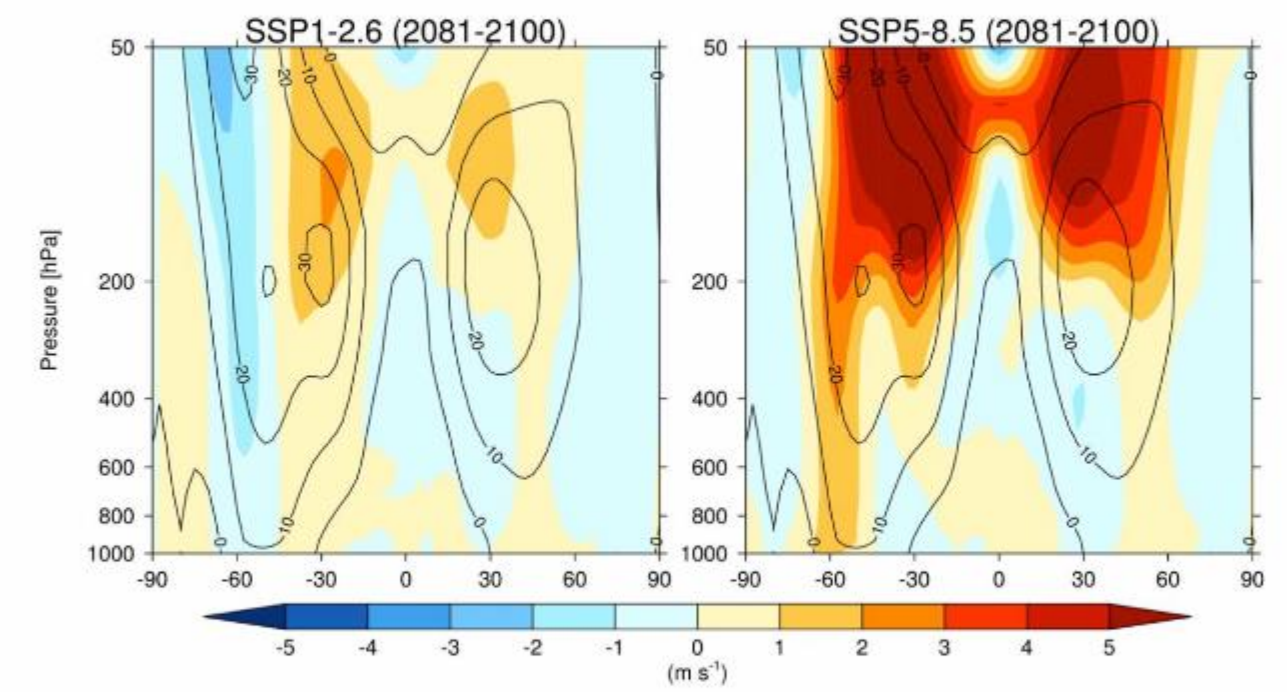

Figure 4.26: Multi-model mean annual mean zonal wind change (m s^{-1}) in 2081-2100 in (left) SSP1-2.6 and (right) SSP5-8.5 relative to 1995-2014. Results are based on the IPSL-CM6A-LR and BCC-CSM models. The 1995-2014 climatology is shown in contours with spacing 10 m s^{-1}. [More CMIP6 models to be added as they become available.]

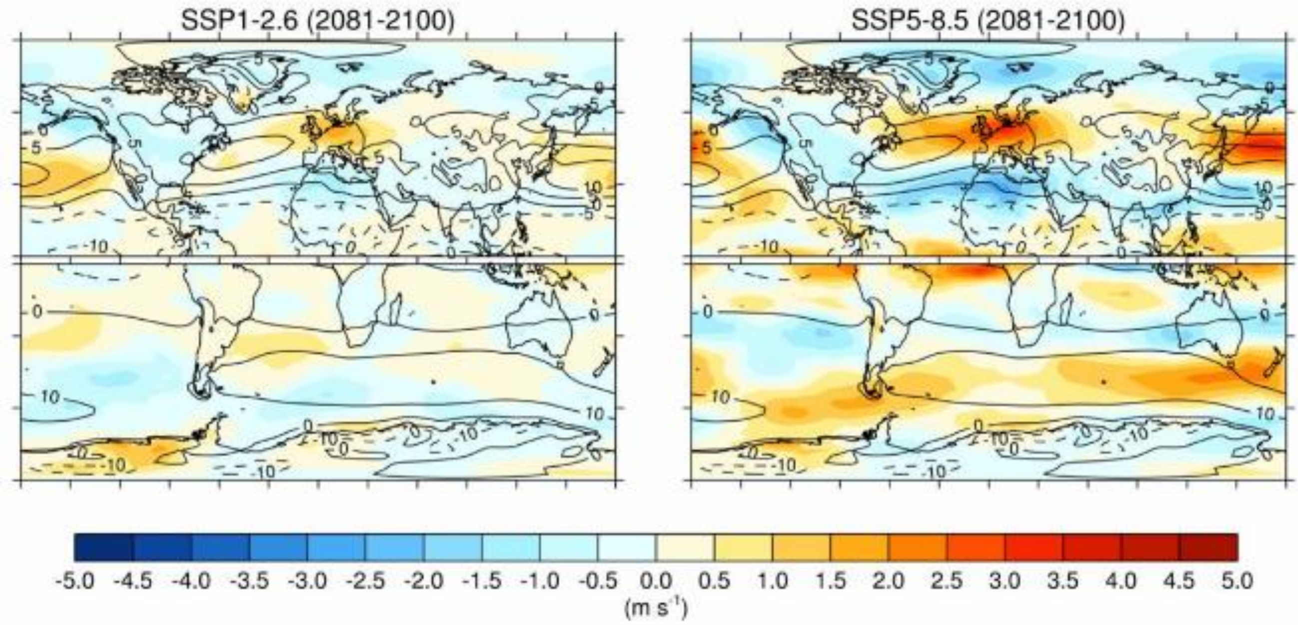

Figure 4.27: Multi-model mean change in winter (NH DJF, SH JJA) zonal wind at 850 hPa (*u850*) in 2081-2100 in (left) SSP1-2.6 and (right) SSP5-8.5 relative to 1995-2014. The 1995-2014 climatology is shown in contours with spacing 10 m s^{-1}. [More CMIP6 models to be added as they become available.]

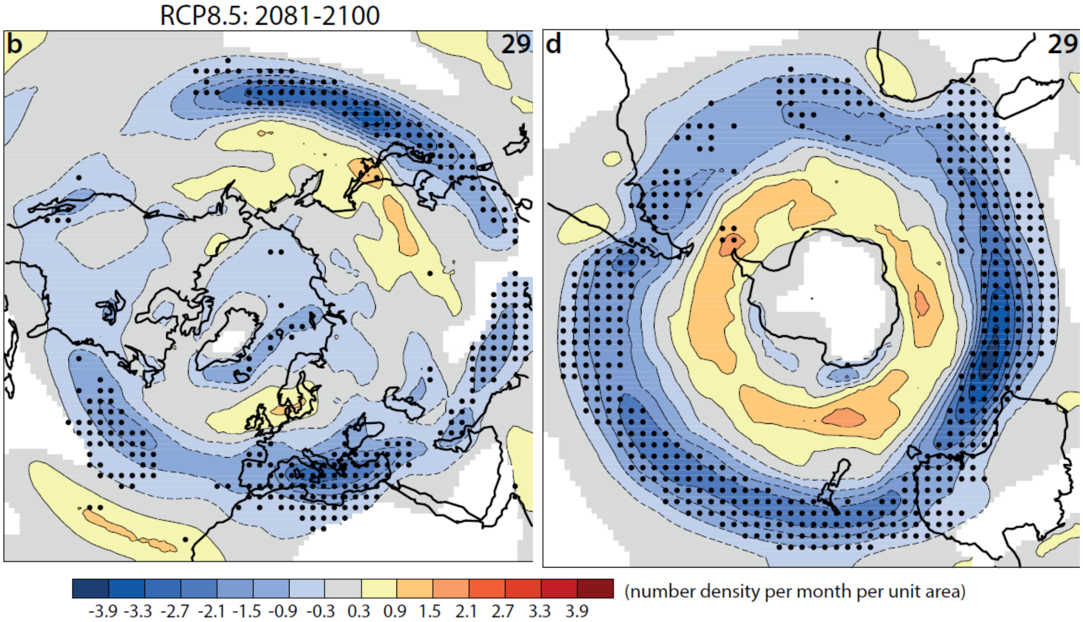

Figure 4.28: Multi-model mean change in winter, extratropical storm track density (NH DJF, SH JJA in 2081-2100 in SSP5-8.5 relative to 1995-2014. [The AR5 Figure 12.20, to be updated when high frequency output becomes available from CMIP6].

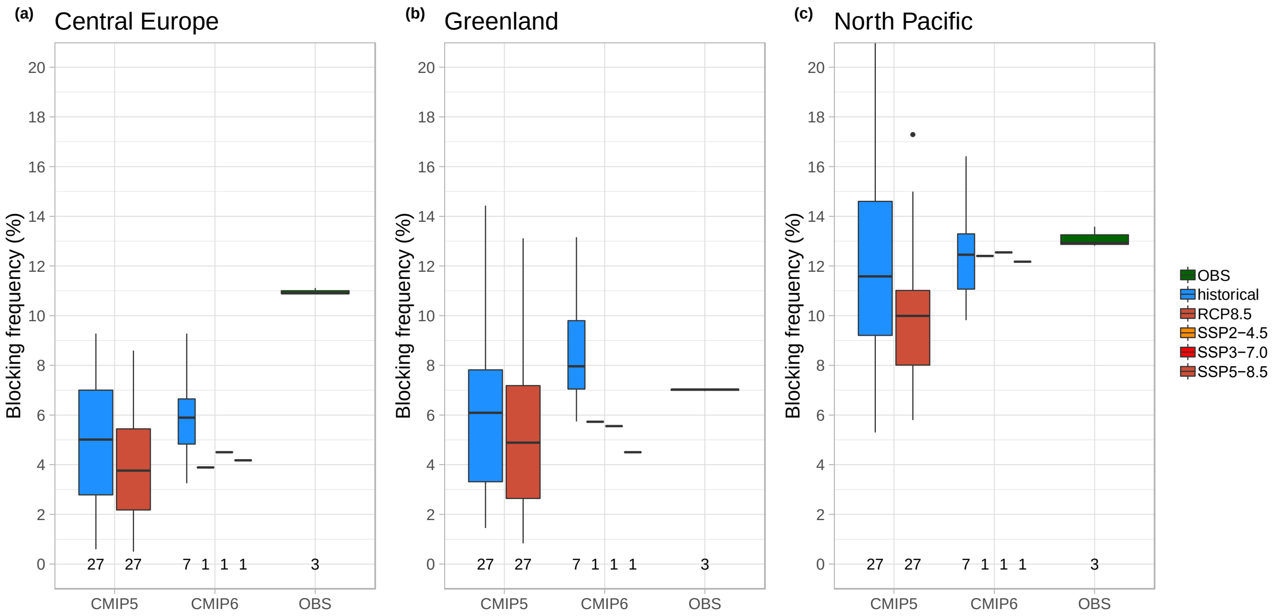

Figure 4.29: Box plot showing wintertime (December to March) present-day (1986-2005) and future climate (2081-2100) atmospheric blocking frequencies over (a) the Greenland region (65W-20W, 62.5N-72.5N), (b) the Central European region (20W-20E, 45N-65N), (c) the North Pacific region (130E-150W, 60N-75N). Values show the percentage of blocked days per season following the (Davini et al., 2012) index. Median values are the black horizontal bar. The numbers below each bar report the number of models included. Observations are obtained as the average of the ERA-Interim Reanalysis, the JRA-55 Reanalysis and the NCEP/NCAR Reanalysis.

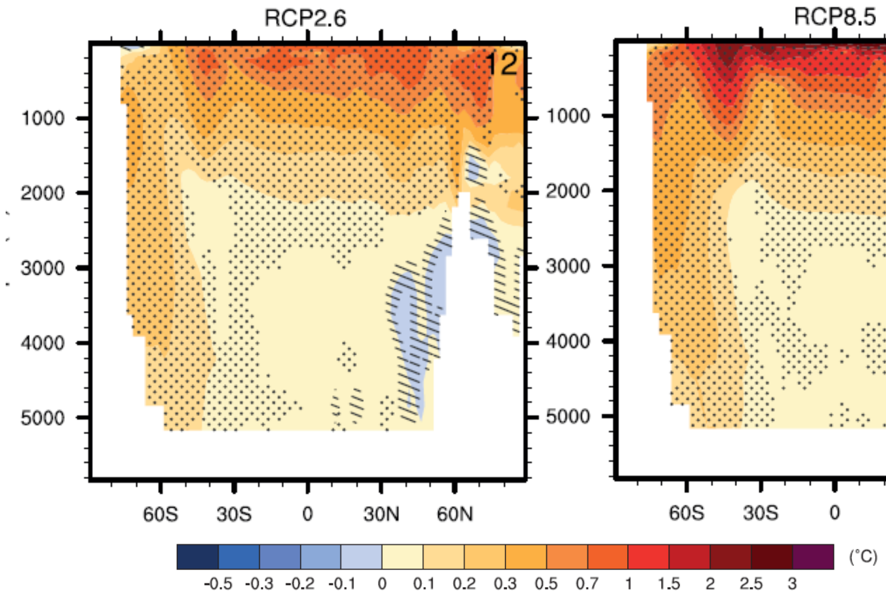

Figure 4.30: Multi-model mean change (°C) in annual mean ocean temperature in 2081–2100 in (left) SSP1-2.6 and (right) SSP5-8.5 relative to 1995–2014. [The AR5 Figure 12.12 lower panels, to be updated for FOD].

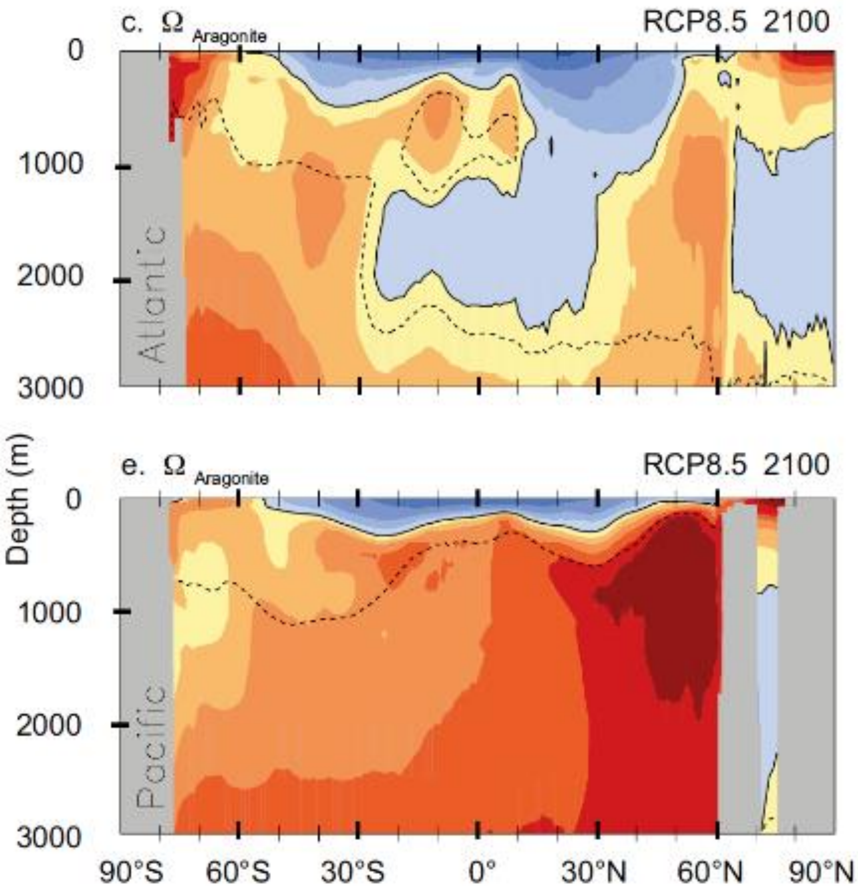

Figure 4.31: Latitude-depth distribution of aragonite saturation state under RCP 8.5 in year 2100 for the Atlantic (upper panel) and Pacific Ocean (lower panel). Overplotted is the aragonite saturation horizon at year 2010 (dotted lines) and 2100 (solid lines). Result are shown for the median projection of CMIP5 model results (taken from Figure 6.29 of the AR5, to be updated with CMIP6 SSP1-2.6 and SSP5-8.5 restuls relative to 1995-2014).

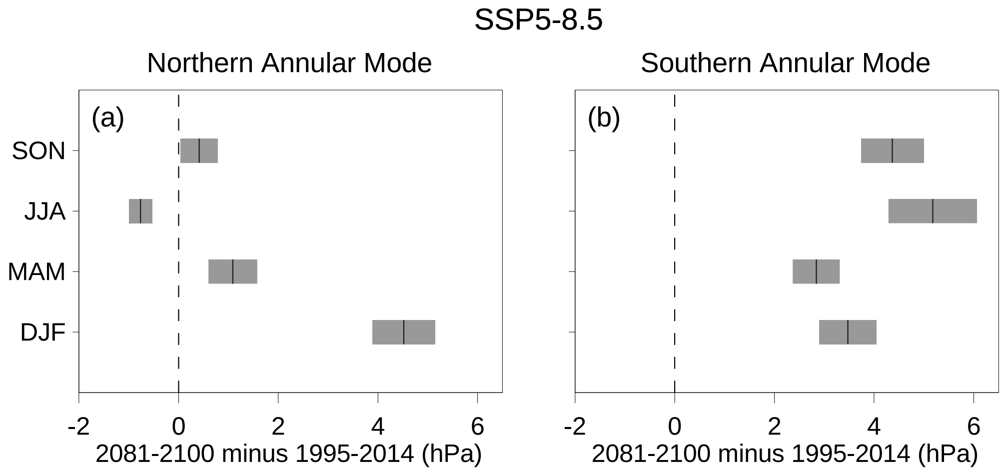

Figure 4.32: Simulated Annular Mode index change from present-day to the long-term: (a) NAM and (b) SAM. The NAM is defined as the difference in zonal mean SLP at 35°N and 65°N (Li and Wang, 2003) and the SAM as the difference in zonal mean SLP at 40°S and 65°S (Gong and Wang, 1999). Present-day values are averages over the period from 1995-2014. Near-term values are averages over the period from 2081-2100. The vertical lines are ensemble-means and the shaded bars are 5-95% confidence intervals on the ensemble means. [These calculations are based on a ten-member ensemble of simulations from one CMIP6 model, CanESM5. Eventually, the figure will be updated using single simulations from the full CMIP6 ensemble.]

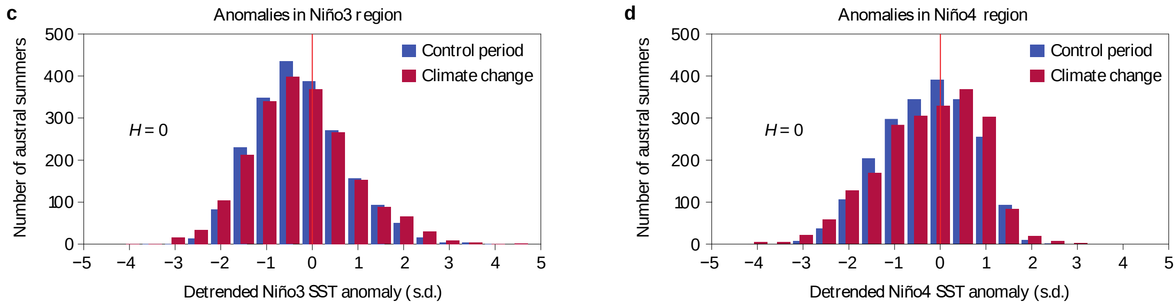

Figure 2 | Greenhouse-**warming-induced changes in ENSO properties.** The plots shown are based on outputs from CMIP5 experiments under historical and RCP8.5 scenarios using 21 models (out of 34 in total), focusing on austral summer (DJF). **a**,**b**, Comparison of Niño3 and Niño4 standard deviation (s.d) in the 'Control' period (1900–1999) (horizontal axis) and 'Climate change' period (2000–2099) (vertical axis). Numbers in the upper left indicate the number of models that produce an increase in s.d., and in the lower right, number of models that produce a decrease in s.d. **c**,**d**, Histogram of quadratically detrended Niño3 and Niño4 SST anomalies in s.d. for 'Control' period (1900–1999; blue) and 'Climate change' period (2000–2099; red). There is a tendency for each index to be more extreme in the 'Climate change' period, but the two histograms in each panel are not statistically different ($H = 0$) about the 95% confidence interval, according to a two-sided Student's t-test.

Figure 4.33: Comparison between past and future probability distributions of ENSO SST anomalies computed using two different ENSO indices (Cai et al., 2015), namely Niño3 and Niño4 Indices. [A similar analysis based on the CMIP6 multi-model ensemble potentially will be shown in this subsection. Additionally, a figure for ENSO-associated hydroclimate changes will be shown.]

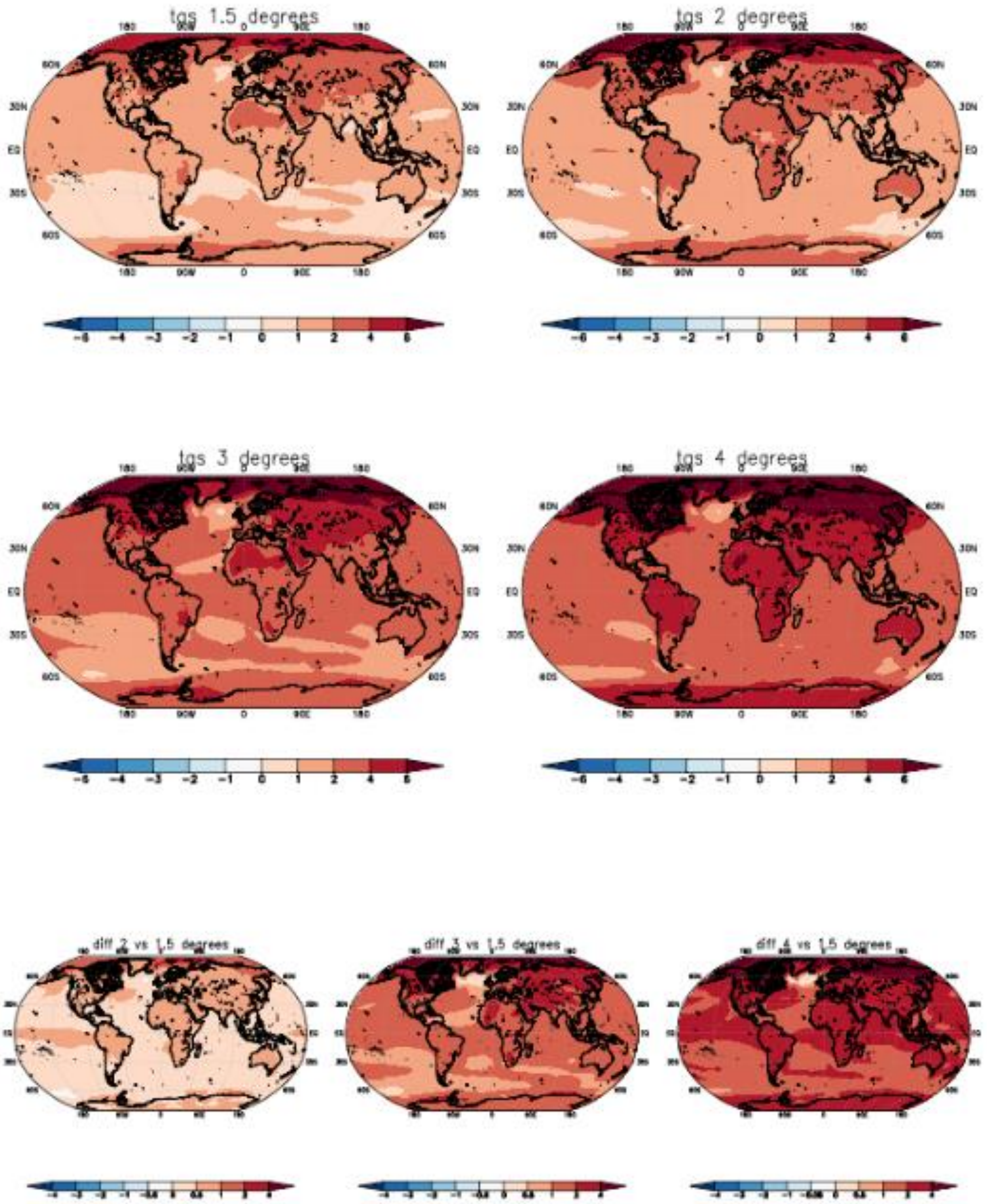

Figure 4.34: Projected spatial patterns of changes in annual mean temperature (°C) at 1.5, 2, 3 and 4 °C of global warming compared to the pre-industrial period (1850–1900) (top), and the spatial differences of temperature change between 2, 3 and 4 °C of global warming relative to 1.5 °C of global warming (bottom). Cross-hatching highlights areas where at least two-thirds of the models (2 out of 3 models at the time of the FOD) agree on the sign of change, as a measure of robustness. Values were assessed from the transient response over a 21-year period at a given warming level, based on SSP5-8.5 in CMIP6. Note that the responses for stabilization scenarios at 1.5°C and 2 °C of global warming are similar (see Atlas, Section X.1). Maps depicting the effects of differential aerosol forcing on spatial patterns of temperature change at different levels of global warming are shown in Section X.2 of the Atlas.

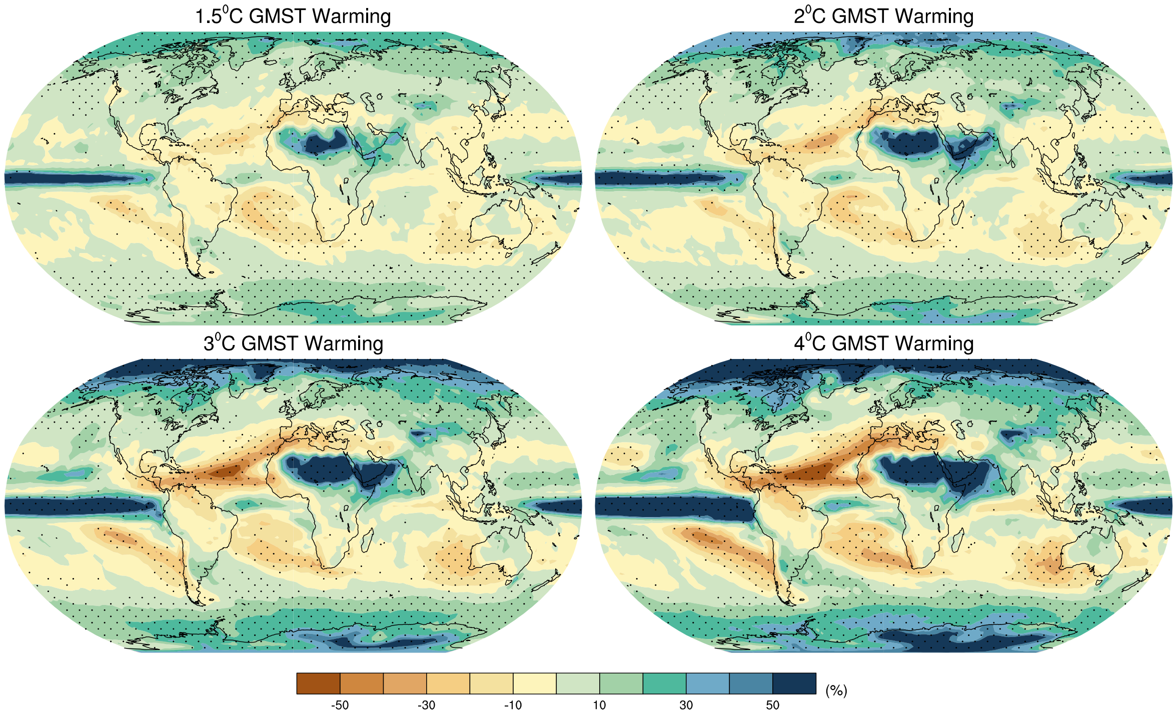

Figure 4.35: Projected spatial patterns of changes in annual precipitation (expressed as a % change) at 1.5, 2, 3 and 4 °C of global warming compared to the pre-industrial period (1850–1900). Stippling highlights areas where at least two-thirds of the models (2 out of 3 models at the time of the FOD) agree on the sign of change, as a measure of robustness. Values were assessed from the transient response over a 21-year period at a given warming level, based on SSP5-8.5 in CMIP6. Note that the responses for stabilization scenarios at 1.5°C and 2 °C of global warming are similar (see Atlas, Section X.1). Maps depicting the effects of differential aerosol forcing on spatial patterns of temperature change at different levels of global warming are shown in Section X.2 of the Atlas.

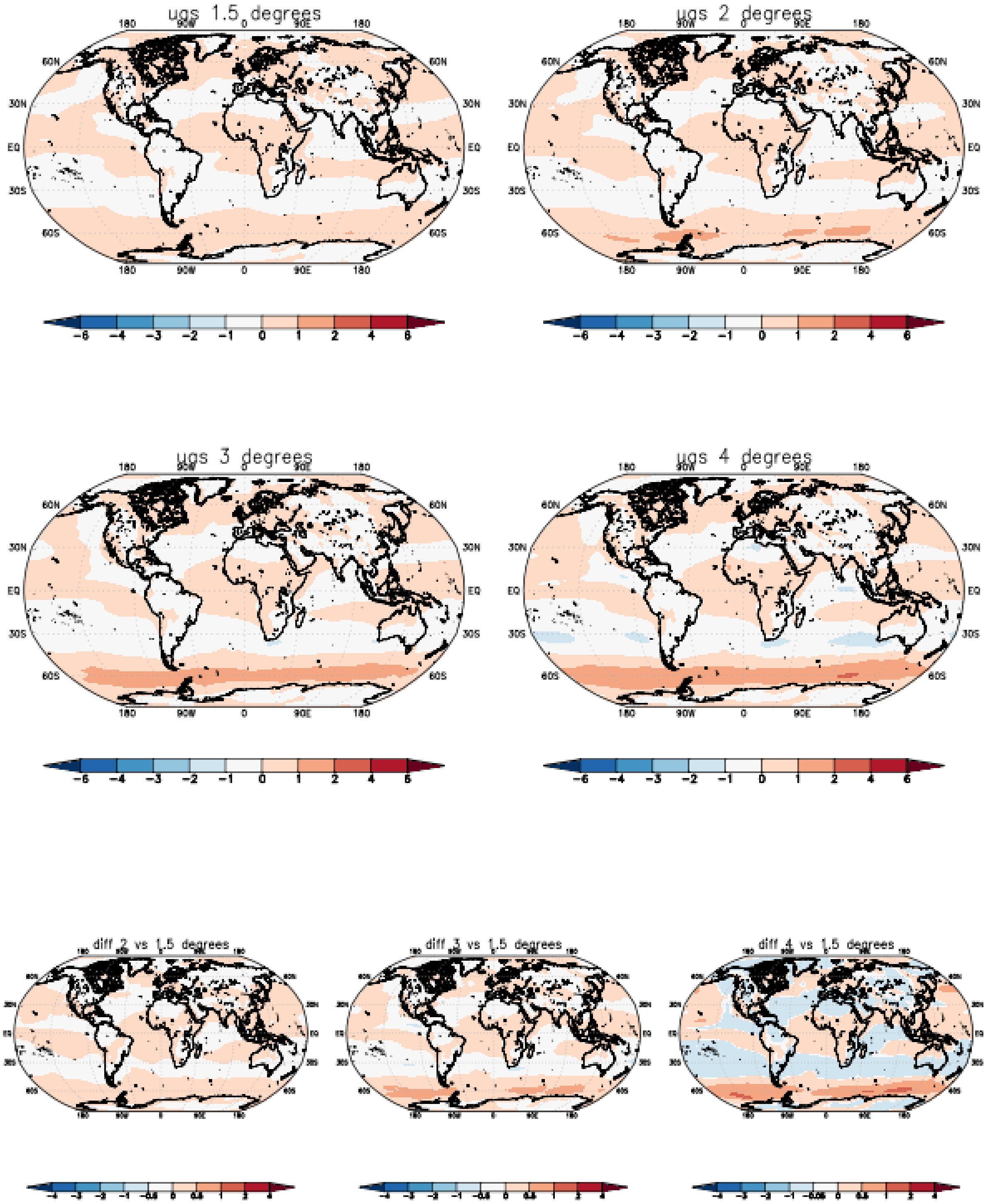

Figure 4.36: Projected spatial patterns of change in near-surface winter zonal winds (m/s, 1000 hPa) at 1.5°C, 2°C, 3°C and 4°C of global warming compared to the pre-industrial period (1850–1900) for the SH (Panels a to d), and NH (Panels e to h). Cross-hatching highlights areas where at least two-thirds of the models (2 out of 3 models at the time of the FOD) agree on the sign of change, as a measure of robustness. Values were assessed from the transient response over a 21-year period at a given warming level, based on SSP5-8.5 in CMIP6 model simulations. Note that the responses for stabilization scenarios at 1.5°C and 2°C of global warming are similar (see Atlas, Section X.1). Maps depicting the effects of differential aerosol forcing on spatial patterns of temperature change at different levels of global warming are shown in Section X.2 of the Atlas.

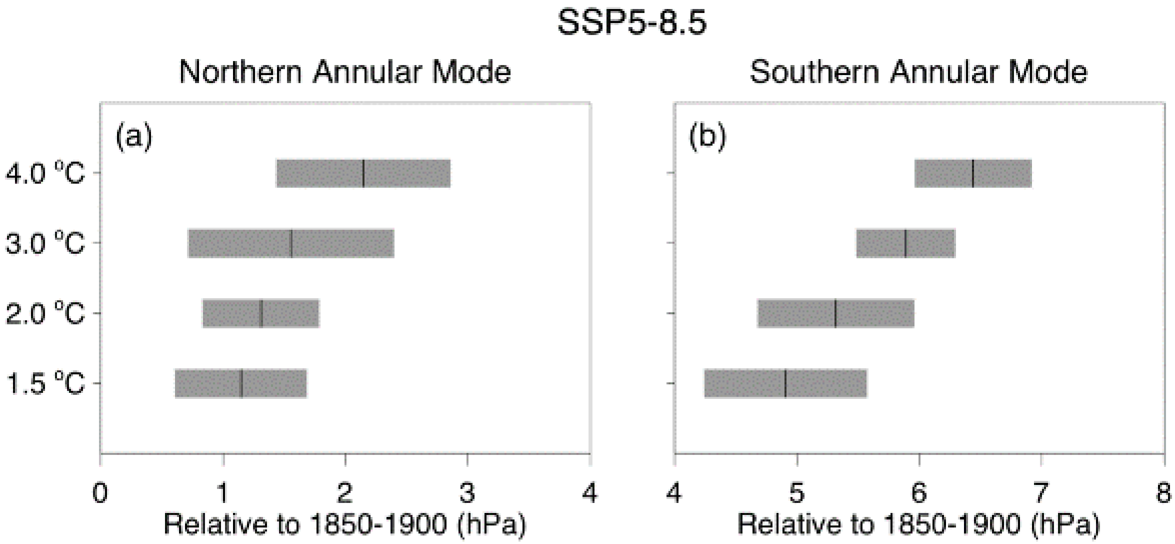

Figure 4.37: Simulated Annular Mode index change under 1.5, 2, 3 and 4 °C of global warming. (a) Northern Annular Mode (NAM). (b) Southern Annular Mode (SAM). The NAM is defined as the difference in zonal mean sea-level pressure (SLP) at 35°N and 65°N (Li and Wang, 2003) and the SAM as the difference in zonal mean SLP at 40°S and 65°S (Gong and Wang, 1999). Values were assessed from the transient response over a 21-year period at a given warming level, based on SSP5-8.5 in CMIP6. The vertical lines are ensemble-means and the shaded bars are 5-95% confidence intervals on the ensemble means. [These calculations are based on a ten-member ensemble of simulations from one CMIP6 model, CanESM5. Eventually, the figure will be updated using single simulations from the full CMIP6 ensemble.]

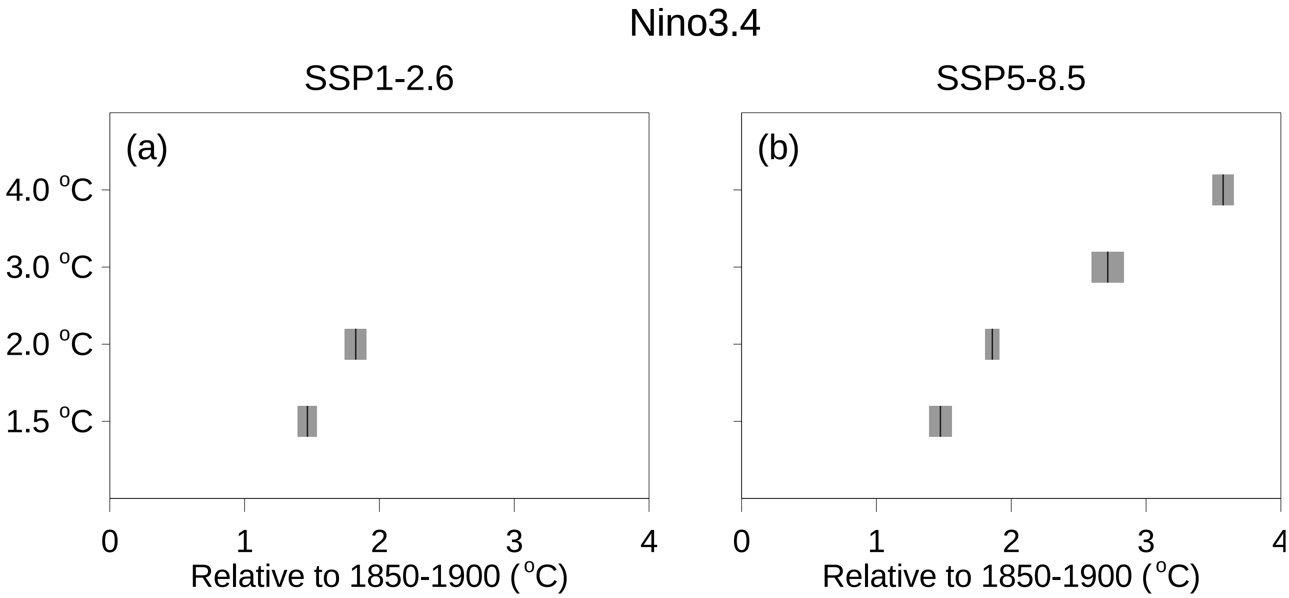

Figure 4.38: Projected mean change of ENSO SST under 1.5, 2, 3 and 4 °C of global warming relative to the pre-industrial period (1850-1900). Values were assessed from the transient response over a 21-year period at a given warming level, based on SSP1-2.6 and SSP5-8.5 from one CMIP6 model. The vertical lines are ensemble-means and the shaded bars are 5-95% confidence intervals on the ensemble means. [These calculations are based on a ten-member ensemble of simulations from one CMIP6 model, CanESM5. Eventually, the figure will be updated using single simulations from the full CMIP6 ensemble.]

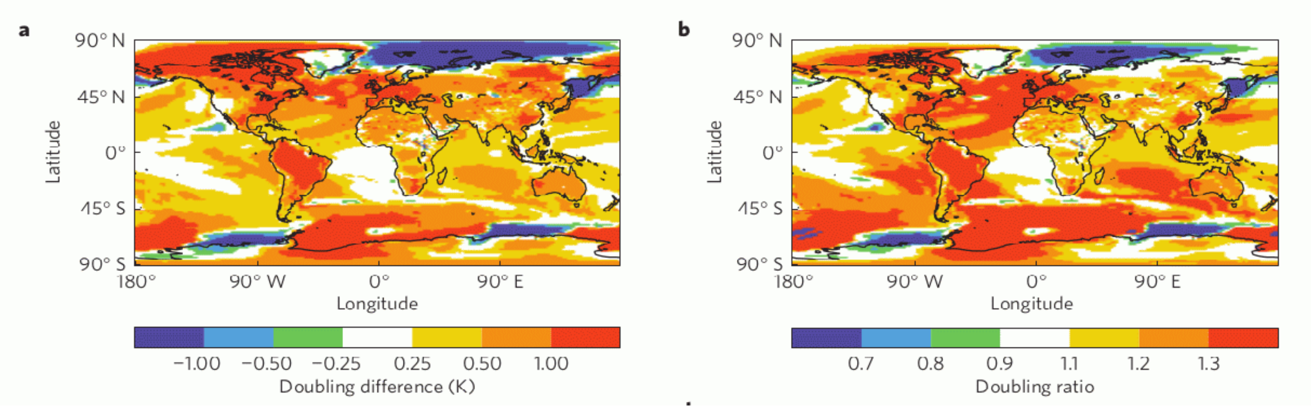

Figure 4.39: Projected changes in the global pattern of near-surface temperature and precipitation associated with a 2ºC increase in global temperature achieved by different pathways. Example above shows the doubling difference and ratio from experiments to 2x and 4x CO_2 taken from (Good et al., 2016).

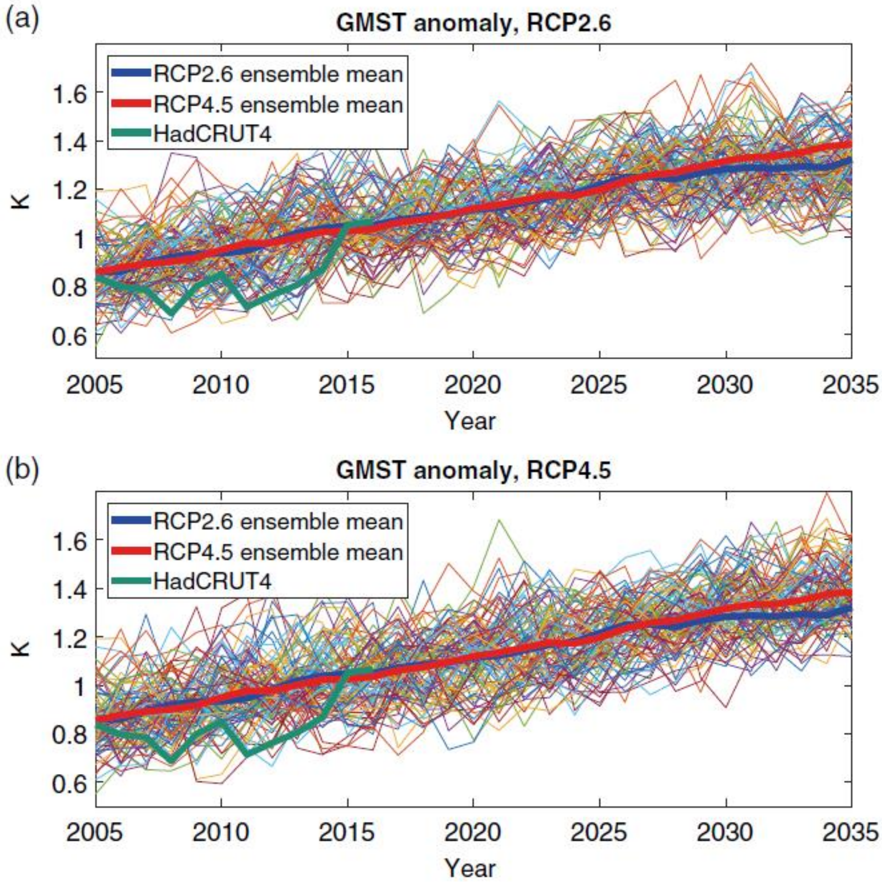

Figure 4.40: Near-term GSAT anomalies relative to the pre-industrial period (here, 1861–1880) in the 100-member Max Planck Institute Grand Ensemble (MPI-GE). (a) GSAT time series for each realization, scenario RCP2.6. (b) As (a) but for scenario RCP4.5. The thick blue, red, and green lines show, respectively, the RCP2.6 and RCP4.5 ensemble means and the observations. The climate response to RCP2.6 and RCP4.5 is nearly indistinguishable in the near term, here 2005–2035, indicating the irreducible uncertainty due to internal variability. [Placeholder figure from (Marotzke, 2019); will be updated using CMIP6.]

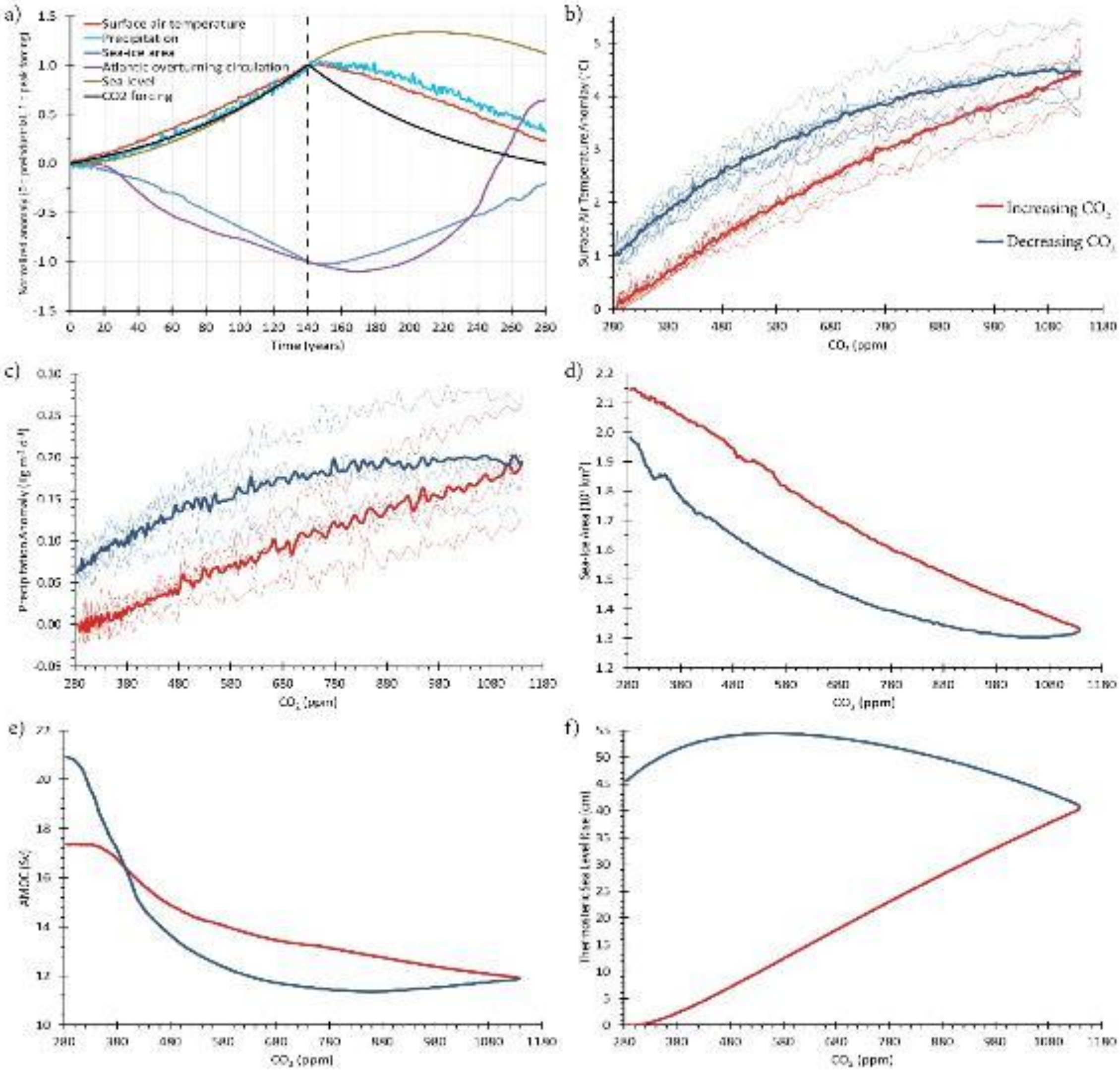

Figure 4.41: Simulated lag and irrversibility in global and annual mean climate variables against atmospheric CO_2. a) normalized anomaly for key climate variables, b) surface air temperature, c) precipitation, d) Arctic sea ice area, e) Atlantic meridional overturning circulation, and f) thermosteric sea level rise as a function of atmospheric CO_2. Atmospheric CO_2 concentration increases at 1% per year to 4×CO2 and then decreases at 1% per year again to return to pre-industrial levels. Multi-model mean (solid lines) and individual model results (thin lines) that participated in CDRMIP are shown. For surface air temperature, results are shown for 7 models (ACCESS1, BNU-ESM, CNRM1-ESM, Mk3L-COAL, NorESM, UVic, and OSCAR). For precipitation, results are shown for 4 models (ACCESS1, BNU-ESM, CNRM1-ESM, and NorESM). For sea ice, AMOC, and sea level rise, only Uvic model reults are shown.

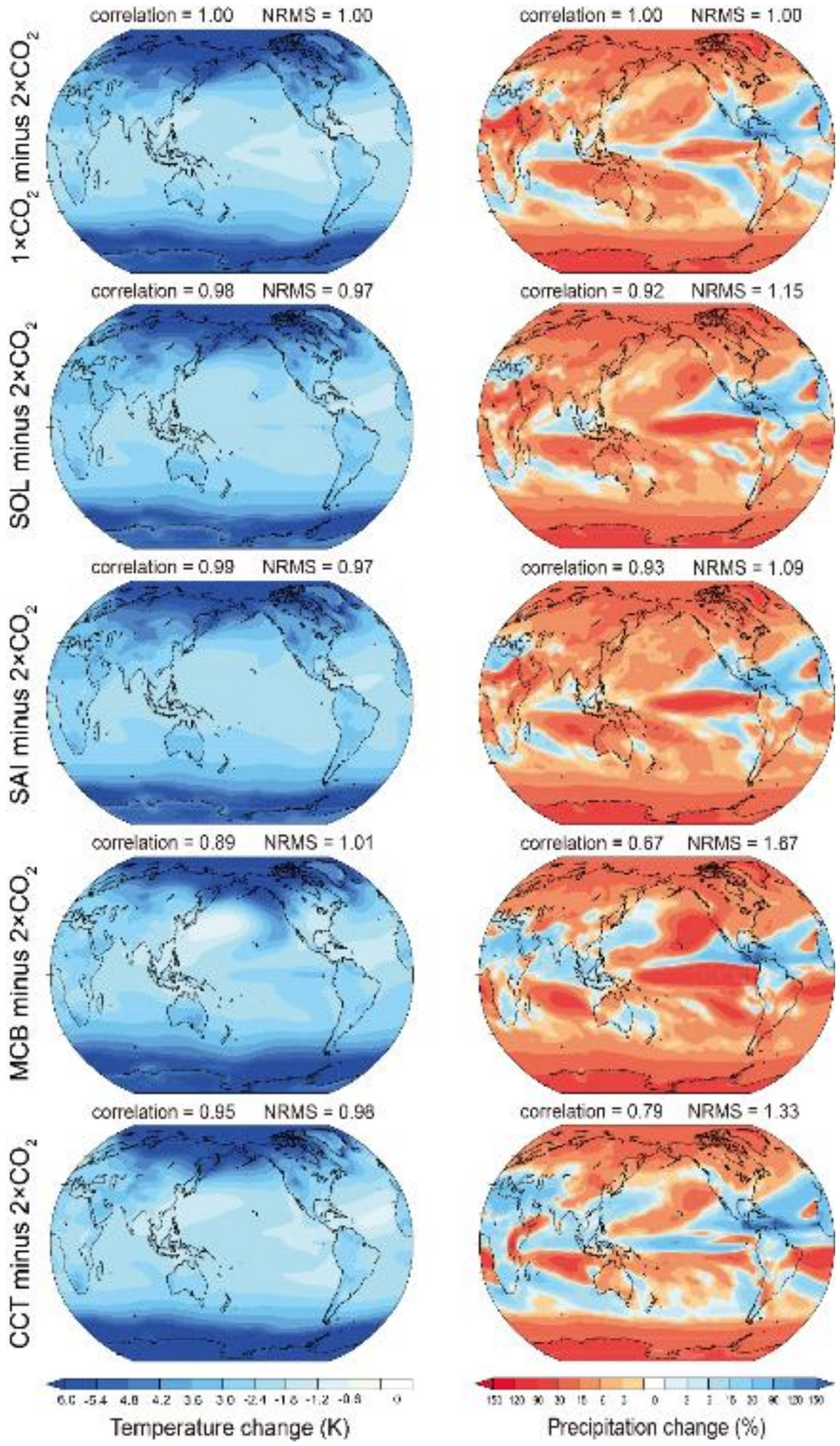

Figure 4.42: The spatial pattern of changes in annual mean temperature (left panels) and precipitation (right panels) from CO_2 reduction, solar constant reduction, stratospheric sulphate aerosols, marine cloud brightening and cirrus cloud thinning experiments. The results are obtained from CESM slab ocean simulations. All geoengineering simulations are designed to offset global mean warming from an abrupt doubling of atmospheric CO_2. All results are shown relative to $2\times CO_2$. Correlation coefficient represent the spatial correlation between geoengineering case and $1\times CO_2$ case, and NRMS is the root-mean-square difference of geoengineering case normalized by that of $1\times CO_2$ case. The departure of the spatial patterns, relative to CO_2 change, are larger for marine cloud brightening and cirrus cloud thinning and less for solar constant reduction and stratospheric sulphate aerosols.

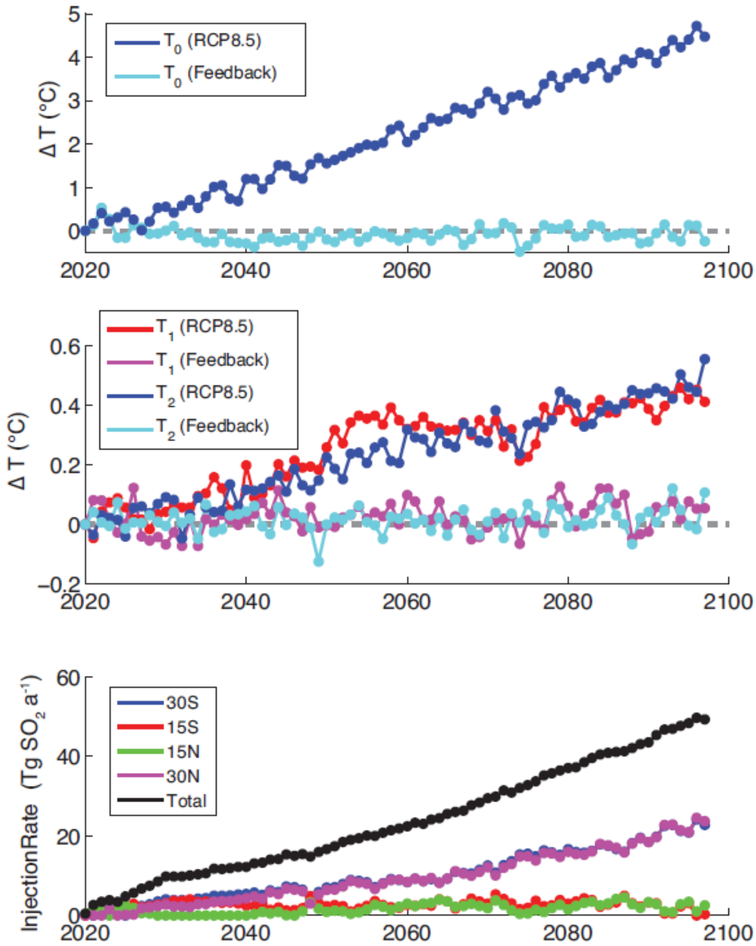

Figure 4.43: Demonstration of the ability to meet three simultaneous temperature objectives in the state-of-the-art model CESM1(WACCM) via SO_2 injection at four independent locations (30°N, 15°N, 15°S, and 30°S, all at 180°E and 5 km above the annual mean tropopause), where the injection rate is adjusted every year based on feedback of the "observed" climate state. The objectives are to maintain, at 2020 levels, global mean temperature (ΔT0), the interhemispheric temperature gradient (ΔT1), and the equator-to-pole temperature gradient (ΔT2). Top and middle panels show comparisons between the base state (RCP8.5) and the model with geoengineering implemented (referred to as "feedback"); 2020 values, which are the objectives, are indicated by dashed gray lines. Bottom panel shows the injection rate at each location, as well as the sum of all injections. Figure is reproduced from (Kravitz et al., 2017)

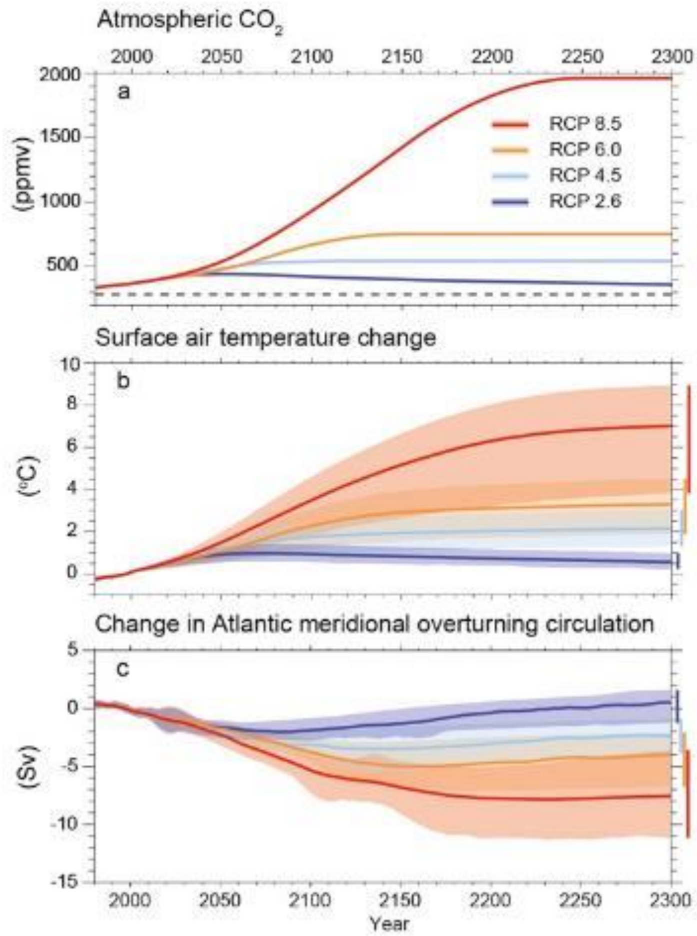

Figure 4.44: (a) Atmospheric CO_2 and projected (b) GSAT change and (c) AMOC change as simulated by EMICs for four RCPs up to 2300 [Placeholder Figure 12.42 from the AR5 – will be updated using more comprehensive EMIC and, if available, simulations with comprehensive ESMs. Other global climate indices may be included further.].

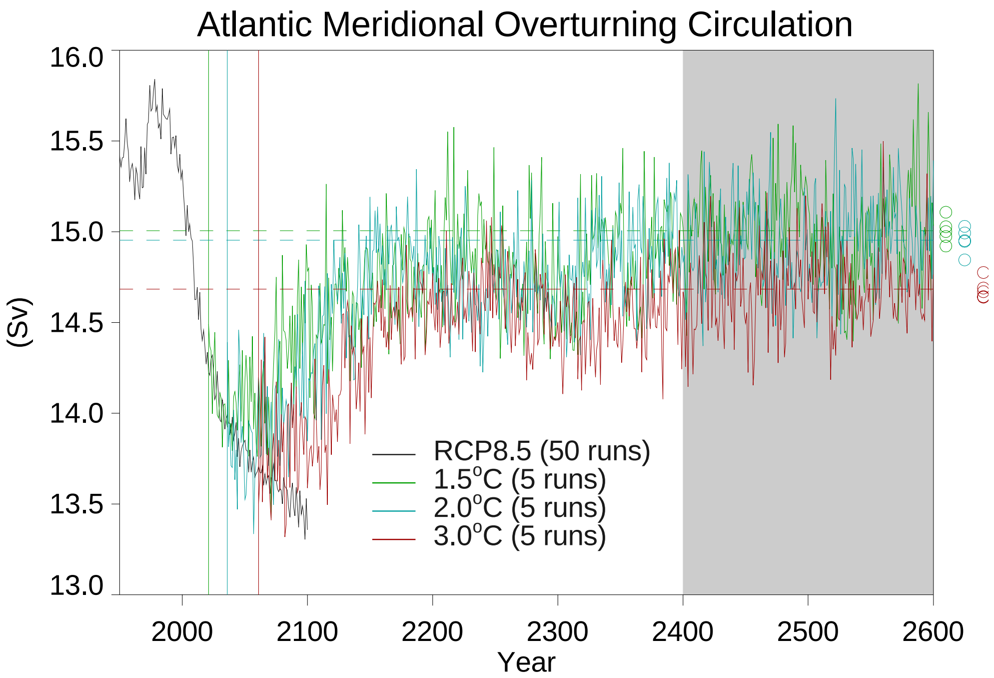

Figure 4.45: Atlantic Meridional Overturning Circulation (AMOC) in ensembles of simulations of an Earth System Model (CanESM2). The black curve is the average over fifty simulations following historical forcings to 2005 and RCP8.5 extensions to 2100. The colored curves are averages over five simulations (each) after global mean surface temperature (GMST) has been stabilized at the indicated degree of warming relative to pre-industrial. The vertical solid lines are the year at which all anthropogenic emissions were terminated and surface temperatures approximately stabilized. The dashed lines are ensemble-means averaged over 2400-2600. The open circles are individual averages over 2400-2600. Data based on (Sigmond et al., 2018a).

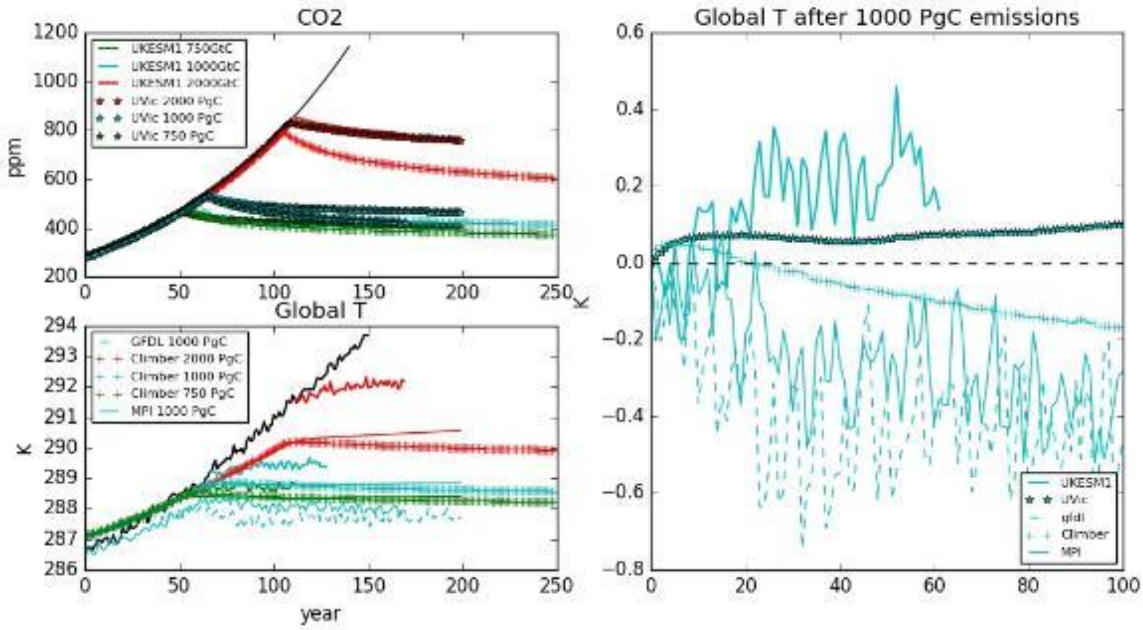

Figure 4.46: Global CO_2 (left top) and temperature response (left lower) following a sudden cessation of emissions at three points on the 1% per year trajectory. Right hand panel shows collated temperature response from the point of departure after 1000 PgC cumulative emissions (hence year varies for each model). Figure compiled from preliminary data from UKESM1, MPI-ESM, GFDL-ESM2M, CLIMBER and UVic simulations. Results to be updated from further ESMs and EMICs under the new ZEC-MIP activity quantifying the Zero-emissions commitment consistent with TCRE estimates. This will be a key input to Ch.5 assessment of carbon budgets.

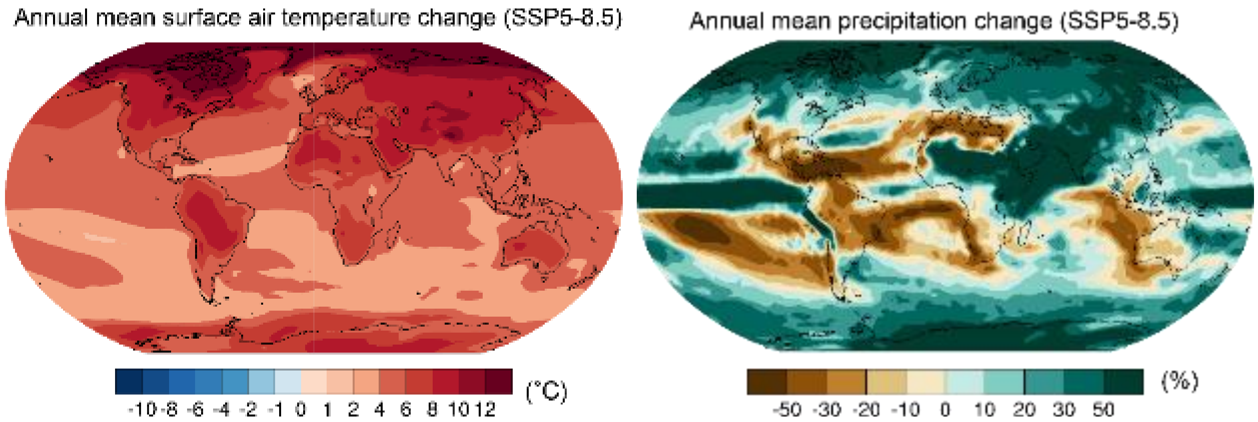

Figure 4.47: Changes in annual mean temperature and precipitation in 2081-2100 relative to 1995-2014) in SSP5-8.5 and SSP1-2.6 for a storyline representing a physically plausible high-global-warming storyline.

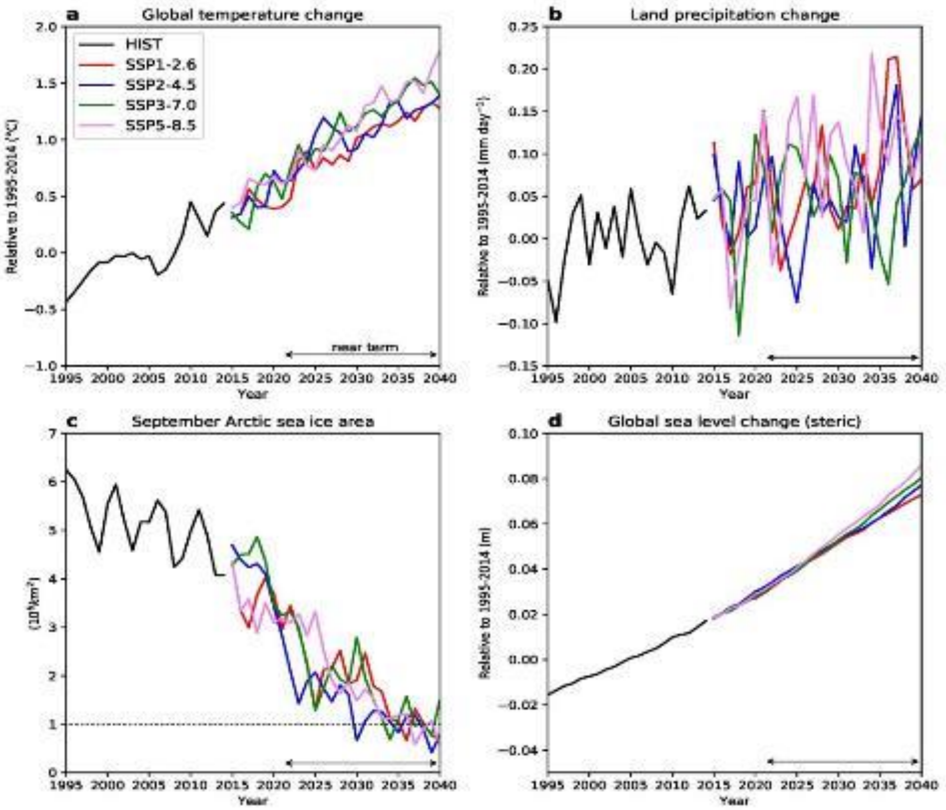

FAQ 4.1, Figure 1: Simulations over the period 1995–2040, encompassing the recent past and the near-term future, of four icons of global climate change, (a) globally averaged near-surface air temperature, (b) precipitation averaged globally over land, (c) the area of Arctic sea ice in September, and (d) globally averaged steric sea-level change, which arises purely from ocean warming. All quantities except the Arctic sea-ice area are shown as deviations from the average over the period 1995–2014. The black curves are for the historical period ending in 2014; the colours refer to various SSP scenarios as shown in the inlet. In (c), the dashed horizontal line is at 1 million km^2, the threshold conventionally used for designating an ice-free Arctic. [Placeholder figure, based on the CMIP6 model CanESM5. To be updated with other CMIP6 models and shading for indicating uncertainty. Sea-level change to be augmented by contributions from land-ice melt, something that is not included in the CMIP6 models.]

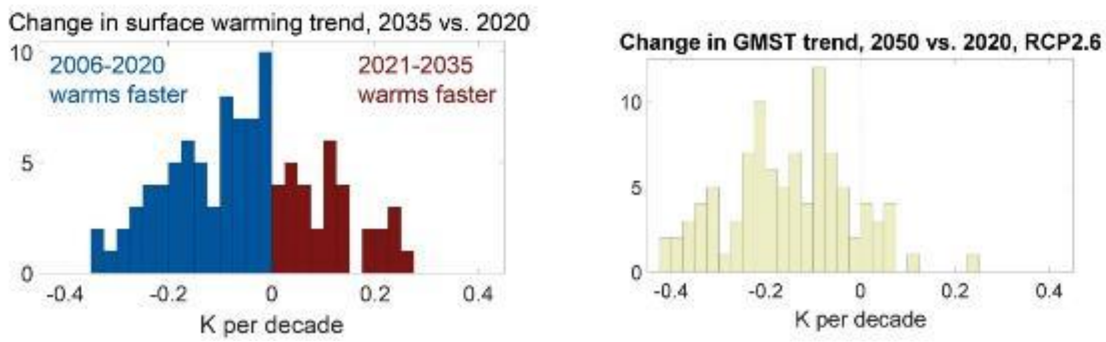

FAQ 4.2, Figure 1: Illustrating the difficulty of discerning mitigation benefit in the near term: Shown are results from 100 simulations with the same climate model that all assume the same reduction in greenhouse-gas emissions from 2020 onward. The difference between individual simulations arises solely through different manifestations of natural internal variability and represents an irreducible uncertainty. We want to assess quantitatively to what extent emissions reductions lead to a reduction in warming trend. Thus we compare, in each simulation separately, how the warming trend differs between the periods 2021–2035 and 2005–2020 (left), and between the periods 2036–2050 and 2005–2020 (right). The length of each bar indicates how often a trend difference of a certain size occurs among the 100 simulations. In the near term (left), we already see a preponderance of a slowdown in surface warming, occurring in two-thirds of the simulations. But as many as one-third of the simulations show faster warming in the near term, despite emissions reductions. By the mid-term (right), almost 90% of the simulations show a slowdown in warming compared to 2005–2020. [Placeholder figure, based on (Marotzke, 2019). Suggest replacing by 20-year trends and using the AR6 WGI definitions of near term and mid-term, as well as by CMIP6 results.]

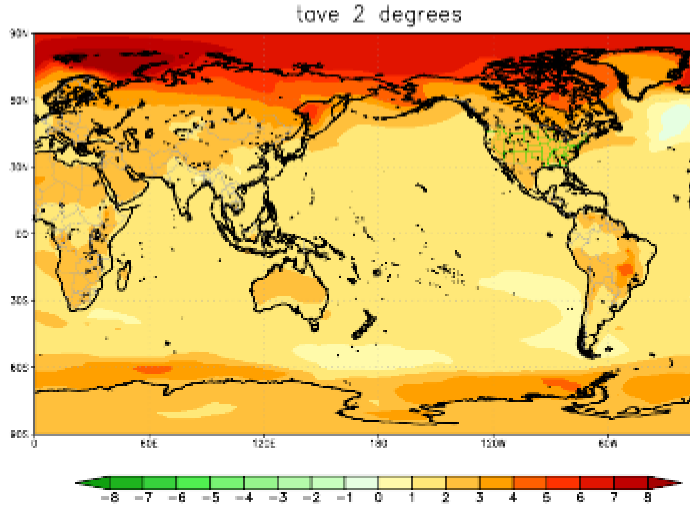

FAQ 4.3, Figure 1: Example for a robust warming pattern, which is presented here for the CMIP6 model MRI-ESM2 and calculated from the scenario SSP3-7.0. Surface warming relative to 1850–1900 is shown here for time periods over which the globally averaged surface warming is 2°C. We recognise the strong warming over the Arctic, generally stronger warming over land than over the ocean, and a slight cooling over the central subpolar North Atlantic. [Placeholder figure, to be replaced by the average over more CMIP6 models.]